Settling of particles in quiescent and turbulent flows. From ground conditions to micro-gravity

Facundo Ezequiel Cabrera

Numéro National de Thèse : 2021LYSEN081

THESE DE DOCTORAT DE L'UNIVERSITE DE LYON

opérée par

l'Ecole Normale Supérieure de Lyon

Ecole Doctorale N° 206

Physique et Astrophysique de Lyon (PHAST)

Discipline : PHYSIQUE

Soutenue publiquement le 16/12/2021, par :

Facundo Ezequiel CABRERA

Settling of particles in quiescent and turbulent flows.

From ground conditions to micro-gravity.

Sedimentation des particules dans les écoulements calmes et turbulents.

Des conditions du sol à la microgravité.

Devant le jury composé de :

COLETTI, Filippo	Prof.	ETH Zürich	Rapporteur
UHLMANN, Markus	Prof.	KIT	Rapporteur
CAL, Bayoán	Prof.	Portland State University	Examinateur
ERN, Patricia	DR	IMFT	Examinatrice
NASO, Aurore	CR	École Centrale de Lyon	Examinatrice
BOURGOIN, Mickaël	DR	ENS de Lyon	Directeur de thèse
PLIHON, Nicolas	DR	ENS de Lyon	Co-encadrant

Acknowledgements

I would like to warmly thank my supervisors Nicolas Plihon and Mickaël Bourgoin. It was a genuinely pleasure to work with you and the things I got from our exchanges are innumerable. Aside from the things I mention in what follows, I had one of the greatest times of my life working with you and I am proud of the work we were able to do. Just to mention one of the many good attitudes you have: you were extremely open with new ideas. One of those ideas led to a collaboration with Alain Pumir, Aurore Naso, Muhammad Zubair Sheikh (a fellow PhD student at the time), and Bernhard Mehlig. I had a great time collaborating with you and I am thankful for your time and the work we did.
I would like to thank Alain in particular, not only for our scientific discussions but also for the many hours he spent giving me advice and answering my questions about the professional (and sometimes personal) life of a scientist.

I have also had the chance to see other research communities than the LPENSL, in addition to the many conferences and schools that Nicolas and Mickaël have allowed me to attend. In particular, the collaboration with our American colleagues from Portland that shaped this thesis. I had the chance to stay for a few months at Portland State University enjoying very interesting scientific exchanges but also the best convivial moments, so I would like to thank Dr. Bayoán Cal.

I thank the mechanics and electronics for their advice and help on the experiments, but also for their good humor and predisposition. I would like to thank in particular Olivier Razebassia for his excellent predisposition and excellent work quality, and Pascal Metz and Mathurin Picoul that spent a considerable amount of time fixing issues regarding the electronic control of the Drop Tower Experiment. Additionally, I am grateful for the exchanges I had with Artyom over countless subjects.
I am also grateful to Richard Pedurand (a postdoc at the time) for moving forward the complex task of producing an experiment with a turbulent flow in the very restrictive conditions inside the Dryden Drop Tower.

I would like to thank the entire secretariat team: Fatiha, Laurence and Nadine who know how to combine efficiency, kindness and a lot of patience to help us with the administrative procedures. The different experiments and prototypes we did resulted in a tremendous number of purchase orders.

If I know parts of the beautiful region of “Auvergne Rhône Alpes”, and of France in general, is thanks to Philippe Odier who took me to discover a number of places and was always happy to include me. In particular, Philippe and I rode approximately 1200 km, what corresponds to around 60 h (without counting the traveling time). We spent a little less than three full days riding together!
In the athletic domain I am also very thankful with Thierry Dauxois that introduced me to triathlon and took me to my first event of that kind. I embraced it and now I am still doing it!
Last but not least, I would like to thank Marc Geiller, with whom I did one stage of the Tour the France, for including me in his sports life.

I am also glad and thankful I could find far-from-home friendship in Simon, Bianca and Florencia, with whom I had very interesting talks, not necessarily in the scientific domain.

Contents

Notation

The notation used for the different magnitudes that appear in this thesis is outlined in what follows.

d_p	Spherical Particle Diameter.
$\mathbf{v}$	Directly measured particle's settling velocity.
v_s or V_z	Particle vertical settling velocity.
ρ_p	Particle mass density.
ρ_f	Fluid mass density.
μ	Fluid Dynamic Viscosity.
ν	Fluid Kinematic Viscosity.
Γ	Particle-to-fluid density ratio.
$\mathbf{g}$	Gravity vector.
g	Gravity vector norm.
u_g	Buoyancy velocity.
Ga	Galileo number.
τ_p^0	Particle response time without non-linear drag correction.
τ_p	Particle response time.
C_D	Drag coefficient.
l	Rod length.
a	Rod diameter.
β	Slender particle aspect ratio.
η	Kolmogorov scale.
L	Integral Scale.
Ro	Rouse number.
St	Stokes number based on the dissipation scale η.
St_{d_p}	Stokes number at the scale of the particle.
St_L	Stokes number based on the integral scale.
Re	Reynolds number.
$\mathbf{u}$	Eulerian velocity field.
$\langle \mathbf{u} \cdot \hat{z} \rangle$	Mean vertical Eulerian velocity field.
$\langle \mathbf{u} \cdot \hat{z} \rangle^{@P}$	Mean vertical Eulerian velocity field at the particle's positions.
σ_u	Standard deviation of the Eulerian velocity field.
$\langle \sigma_u \rangle^{@P}$	Averaged standard deviation of the Eulerian velocity field at the particle's positions.
U	Incoming fluid velocity in the study of the wakes of fixed objects.
A	Reference area in the drag force.
$\mathbf{x}$	Particle position in 3D.
V	Particle volume.
λ	Taylor's scale.
ϵ	Energy dissipation rate.

τ_L	Time integral scale.
τ_η	Time dissipation scale.
m_p	Particle mass.
m_f	Fluid mass.
$\mathbf{W}$	Slip velocity.
F_r	Froude number.
$\mathbf{a}$	Fluid acceleration field.
σ_v	Standard deviation of particle velocity distribution.
N	Coil's number of turns.
R	Coil's radius.
R_Ω	Coil's electrical resistance.
σ	Coil's cross-section.
fps	Frames per second.
$\mathbf{B}$	Magnetic induction field.
B	Magnetic induction field norm.
B_i	Magnetic induction field component in the direction i.
I	Electrical current.
$\dot{\gamma}$	Shear Rate.
τ	Shear stress.
Ra	Arithmetical mean height.
$\mathbf{M}$	Spherical particles magnetic moment.
M	Spherical particles magnetic moment norm.
D_0	Particle pair initial separation.
S_p	Structure function of order p.
$S_p^{\parallel}$	p-order parallel structure function.
$S_p^{\perp}$	p-order perpendicular structure function.
px	Pixels.
δ_u	Velocity increment.
$R^{\parallel}$	Parallel fluid autocorrelation.
$\tilde{g}$	Effective gravity.
g^*	Adimensional gravity: ratio between the effective gravity and 9.8 m/s^2.
fr	Image frame.
F^M	Magnetic force.
T^M	Magnetic torque.
χv	Volumetric magnetic susceptibility.
μ_0	Magnetic permeability of vacuum.
B_{rem}	Permanent magnet's remanent field.
ψ	Angle between $\mathbf{M}$ and $\mathbf{B}$.
	In the context of Slender Bodies, the horizontal angle of the rod.
G_z	Magnetic induction gradient evaluated at $r = z = 0$.
B_0	Magnetic induction evaluated at $r = z = 0$.
T_c	Curie's temperature.
ω	Particle's angular velocity.
C_ω	Rotational drag coefficient.
θ	In the context of Slender Bodies, the angle between the rod and the horizontal plane.
	In the context of path instability, the trajectory angle with the vertical.
$\hat{n}$	3D direction of the rod.
$\hat{p}$	Vector orthogonal to the projection of $\hat{n}$ onto the horizontal plane.
$\mathbf{x}$	Particle's center of mass position.

$\mathbf{f}_S$	Stokes force in the context of Slender Bodies.
$\mathbf{f}_I$	Inertial force in the context of Slender Bodies.
$\mathbb{A}$	Resistance tensor.
I_p	Moment of inertia of rods.
$\mathbf{T}_S$	Stokes torque on slender bodies.
$\mathbf{T}_I$	Inertial torque on slender bodies.
$\boldsymbol{\Omega}$	Vorticity.
C_S	Resistance coefficient.
$F(\beta)$	Shape factor.
ϕ	Pitch angle.
w_g	Vertical velocity of slender bodies.
w_h	Horizontal velocity of slender bodies.
L_{ref}	Reference length.
T_{ref}	Reference time.
V_{ref}	Reference velocity.
f_{ref}	Reference frequency.
$\mathbf{v}_\perp$	Perpendicular (to gravity) settling velocity.
$\mathbf{v}_\parallel$	Parallel (to gravity) settling velocity.
h	Height of visualisation volume.
$\sigma_a^{\mathrm{tracer}}$	Standard deviation of tracers from Heisenberg-Yaglom relation.
$R_v(\tau)$	Lagrangian auto-correlation function of particle velocity.
T_L	Lagrangian correlation time.
T_L^*	Large scale Lagrangian time.
T_2	Small scale Lagrangian time.
τ_λ	Lagrangian taylor microscale.

Chapter 1

State of the art

1.1 Motivation

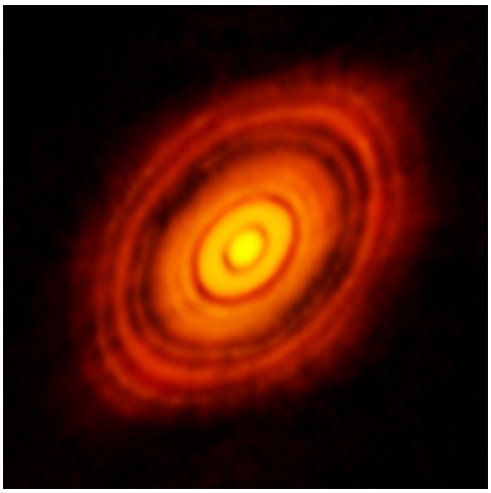

Figure 1.1: HL Tauri star taken by the ALMA telescope. The star is at the center and an accretion disk surrounds it. The gaps in the disk are due to particles that have clustered to form larger objects. Credit: ALMA (ESO/NAOJ/NRAO)

In spite of its apparent simplicity, the problem of particles in a fluid hides a whole hierarchy of rich intricate phenomena, a number of them are still shrouded in mystery. The problem impacts numerous situations in nature, such as the atmospheric dispersion of pollutants, dynamics of dust in proto-planetary accretion disks (planet formation), transport of grains in geophysical flows and sprays in industrial processes are just a few examples.

Although one may naively think that a problem as simple as the settling of a sphere under gravity on Earth is solved since Newton's apple, the problem is indeed far more complex than it seems. Actually, it is still not possible nowadays to predict even such a simple thing as the speed of a falling raindrop. The reason of this is that the problem is trivial only if the sphere falls in vacuum, while in most real situations, the falling particle is embedded in a fluid (liquid, gas, or plasma) with which it interacts. The motion of the fluid and of the particles then becomes extremely intricate. As a consequence of these couplings, even in the simplest situation where the surrounding fluid is quiescent, the settling can exhibit complex behaviors where a sphere would not always fall in a vertical straight line, but may follow oblique, oscillating, chaotic, etc.

trajectories, as wake instabilities develop. The situation is even more complex when the surrounding fluid is itself moving, eventually in turbulent conditions. This problem is of extreme importance for numerous fields in several branches of science and human activities. Settling particles are ubiquitous and play a crucial role in a series of phenomena around us and up to the evolution of the Universe. Planet formation is an emblematic example. Figure 1.1 presents an image from the "Atacama Large Millimeter Array" (ALMA) telescope, of the "HL Tauri" star at 450 light-years from us. It is the first image ever recorded of a star at the centre of an accretion disk composed of small dust particles coupled with a gas. Note that the gaps in the disk are due to particles that have clustered to form larger objects (i.e. an early stage of planet formation). Planet formation requires the growth of sub-micron dust grains in a dense gaseous phase, over many orders of magnitude: the dust feeding the disk had grown from sub-micron grains up to micron sized particles in the dense regions of molecular clouds. Once incorporated into the accretion disk, the grains must grow from micron-sized to centimetre-sized, and ultimately kilometre-sized bodies. The dust drifts towards the accretion disk driven by the star gravity is thought to have a dominant hydrodynamical (or magneto-hydrodynamical) nature as the dust particles interact with the surrounding turbulent gas, at least in the first stages when the dust is micron-sized and their small mass renders gravitational attraction ineffective between dust particles. Understanding the coupling between the dust and the gas around the forming star has become a priority for astrophysicists. The settling of particles is also believed to be crucial in the formation of giant gaseous planets, due to the presence of Helium and Neon rain. It is also crucial for the differentiation and crystallisation process of telluric planet interiors, as the Earth, during their formation. At the surface of our planet, settling particles are also everywhere, volcanic ashes, sand from deserts, water drops and droplets, pollen, marine snow and, since the industrial revolution, tons of pollutant particles travelling in the atmosphere, rivers and seas. Understanding the planetary transport and the deposition processes of such particles has become one of the biggest challenges for environmental and climate issues. All these fascinating and challenging problems suffer today from a lack of understanding. The weakness of available particle/turbulence interaction models became flagrant during the recent pandemics (COVID-19) and limited for instance the capacity to accurately model and predict the aerial virus propagation via physiological aerosol dispersion and deposition. Such a modelling is mandatory, for instance, to develop relevant social distancing or ventilation strategies.

It is interesting to remark that while in previous examples the surrounding flows are generally turbulent, relevant unsolved problems still remain even in the absence of turbulence. Although the flow might be turbulent at some scales, all turbulent flows can be considered laminar at sufficiently small scales (dissipative scales). Understanding the coupling of particles with a flow in such laminar conditions is often a pre-requisite to the modeling of the global coupling with turbulence. For instance, a problem tackled in this thesis is that of the rotational and translational dynamics of rods in a quiescent highly viscous flow (i.e. very far from turbulent). This problem is indeed crucial to develop accurate models for small ice crystals in atmospheric clouds.

This thesis investigates several aspects of the couplings between settling particles (spheres, cubes, and rods) in quiescent and turbulent conditions, with a particular effort to identify and explore the relevant control parameters of the problem.

1.2 Introduction

The problem of a particle (assumed spherical in this first introduction) of diameter d_p and density ρ_p settling in a quiescent fluid of density ρ_f and viscosity ν under a gravitational field $\mathbf{g}$

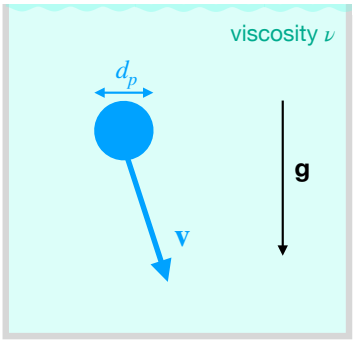

Figure 1.2: Sketch of the basic type of experiment done in this thesis. A sphere of diameter d_p settles with velocity $\mathbf{v}$ in a fluid with viscosity ν.

is controlled by two dimensionless parameters. Indeed, the Π theorem yields two dimensionless parameters: there are 5 independent variables $(d_p, \rho_f, \rho_p, g, \nu)$ and 3 units (meters, seconds, kilograms), then there are 5-3=2 dimensionless parameters that are usually chosen to be particle-to-fluid density ratio $\Gamma = \rho_p/\rho_f$ and Galileo number $Ga = u_g d_p/\nu$, with $u_g = \sqrt{|\Gamma - 1| g d_p}$ the buoyancy velocity (see Eq. 1.3). As it will be further discussed, these two parameters control for instance the settling regimes, which are typically vertical at low valued of Ga and become more complex (oblique, oscillating and chaotic) as Ga increases, the detailed dynamics also depending on the density ratio Γ. If beyond the nature of the settling trajectory, one is also interested in the terminal settling velocity v_s as a variable of the problem, an additional dimensionless parameter, called particle Reynolds number appears: $Re_p = v_s d_p/\nu$. Note that Ga is an input (control) parameter of the problem, which can be computed *a priori* by simply knowing the above mentioned physical properties of the particles, fluid and gravity, while Re_p is a response parameter, which needs to determine the settling velocity that has to be measured or computed with a model. Nevertheless, it is not unusual that Re_p is used in the literature rather than Ga to classify the settling regimes. So it may be done in this manuscript when discussing existing studies using *Re_p-classification* rather than *Ga-classification*

The problem of a single sphere settling in a quiescent creeping flow, where the settling velocity is *slow* (i.e. $Re_p \lesssim 1$) was solved by Stokes, who determined that in this situation the particle trajectory is rectilinear in the direction of gravity and the settling velocity is $v_s = \frac{g}{18\nu}(\Gamma - 1)d_p^2 = \tau_p^0 g$, with $\tau_p^0 = \frac{1}{18\nu}(\Gamma - 1)d_p^2$ (Stokes, 1851). Note that in this Stokes flow approximation, Ga and Re_p are simply related by $Re_p = Ga^2/18$.

As Ga (and hence Re_p) increase, wake instabilities start to develop leading to a more complex dynamics where the trajectories are no longer vertical but can for instance oscillate or be oblique (Jenny et al., 2004; Zhou and Dusek, 2015). No exact solution for the settling velocity of the type $Re_p = f(Ga, \Gamma)$ is known in this case. The solution (i.e. the function f) depends on the hydrodynamical drag F_D (the terminal settling velocity v_s, hence Re_p, resulting from the balance between gravity, buoyancy, and drag), which adds an extra dimensionless parameter (C_D, the drag coefficient) to the problem. Note that C_D depends on the control parameters of the problem Γ and Ga (or Γ and Re_p if the relation between Re_p, Γ, and Ga is determined). Formulae to compute the drag coefficient (and hence v_s) from the control parameters are however not known from first principles and have to be obtained empirically (Brown and Lawler, 2003; Clift et al., 1978a). The settling regimes for spheres at moderate Ga (or Re_p) are detailed in Section 1.4.

If the particles are not spherical, new dimensionless control parameters must be considered, as a new set of independent variables that represents the particle's shape influences the translational and rotational dynamics. For slender rods or ellipsoidal particles the aspect ratio $\beta = l/a$ is

usually considered, where l and a are, for instance, the length and diameter of a cylindrical particle (as it will be the case here).

If the surrounding fluid is not quiescent but turbulent, the situation becomes more intricate as the interaction of the particle with the multiscale structures (eddies) of turbulence affects its dynamics (the literature on the topic is immense, the reader can for instance refer to some review articles as Bourgoin and Xu (2014); Toschi and Bodenschatz (2009). As a consequence, even seemingly simple questions remain unsolved, for instance the particle settling velocity enhancement/hindering problem where, depending on the particle's inertia, the addition of turbulence can enhance or hinder the settling velocity compared to the quiescent Flow case.
Going back to the case of spherical particles for which the shape variable β is not pertinent, new independent variables related to turbulence have to be included to the previous Π-theorem analysis to determine the control parameters of the problem. A minimalistic characterization of the multi-scale nature of turbulence requires at least two scales to be given (a more detailed description of the phenomenology of turbulence will be given in Subsection 1.5.1): L – the scale at which the energy is injected, for instance by stirring the flow with an impeller of typical size L, and η – the scale at which the energy is dissipated by viscosity, which corresponds to the scale of the smallest turbulent eddies. Two extra dimensionless parameters come out from the Π-theorem which can for instance be taken as: $Re = (L/\eta)^{4/3}$ – the turbulent Reynolds number that measures the separation between the larger and smaller scale; and d_p/η – that represents the relation between the particle size and the smallest turbulent scale.
This analysis yields the following set of dimensionless control parameters: $\{Ga, \Gamma, Re, d_p/\eta\}$. As it will be discussed later, it is common in the literature to use another set of parameters (namely $\{\Gamma, St, Ro, Re\}$, with St and Ro respectively the Stokes and Rouse numbers) which are simple combinations of $\{Ga, \Gamma, Re, d_p/\eta\}$ (see Section 1.5).

This thesis explores experimentally several aspects related to the couplings between settling particles and fluids when these different control parameters $\{\beta, Ga, \Gamma, Re, d_p/\eta\}$ are varied over a certain range completing previous existing numerical and experimental works. For the case of spheres ($\beta = 1$), the creeping flow case will not be considered as it has a well-known analytical solution. The study is organised as follows:

1. Settling of single slender bodies in a Quiescent Creeping Flow at low particle Reynolds number – $Re_p \lesssim 1$.
   Relevance of torque and forces models on a finite size slender particle are yet unsolved.

2. Settling of single spheres and cubes in a Quiescent Flow at moderate Galileo number – $Ga \sim \mathcal{O}(100)$.
   Questions remain about the (non-vertical) trajectories that such particles undergo as a function of Ga and Γ, in particular in the high Γ regimes which are experimentally unexplored.

3. Spheres in an Homogeneous and Isotropic Turbulent HIT Flow – $Ga \approx \mathcal{O}(100), Re_\lambda \approx \mathcal{O}(100)$.
   Among others, the problem of particle settling velocity enhancement/hindering and the competition of particle inertia and gravity in particle/turbulence interactions are to be elucidated. An important and original aspect of the work achieved during this thesis concerns the implementation of strategies to disentangle inertial and gravitational effects by modifying the effective gravity experienced by the particles.

The following section of this introductory chapter details the state of the art of the knowledge on this different questions and the associated challenges related to the work done during this thesis.

1.3 Anisotropic particles in quiescent creeping flow

Anisotropic particles are important in several fields. This includes for instance, in an engineering context, problems involving paper fibers (Lundell et al., 2011). The question is also particularly relevant in the environmental sciences, consider for example the settling of planktons in the oceans (Durham et al., 2013; Pedley and Kessler, 1992; Ruiz et al., 2004), or ice crystals settling in clouds (Gustavsson et al., 2017, 2019; Jucha et al., 2018; Pruppacher and Klett, 1980; Sheikh et al., 2020; Siewert et al., 2014). In most of these situations of practical interest the flow surrounding the particles is agitated and even turbulent. However, if the particle size is comparable to the dissipative scales of turbulence, resulting in a particle Reynolds number smaller than one, i.e. the particles experience a creeping flow at that scale. The state of the art numerical simulations for small fibers in turbulence are based on such a creeping flow approximation to model the particle/fluid coupling at such dissipative scale. Even in this case there is no consensus yet on a proper model. In this thesis, this question is experimentally addressed by investigating the settling of rods in creeping flows. In particular, the settling of tungsten cylinders with $\Gamma = 12.1$, and aspect ratio $\beta = 8$ and 16, in a very viscous Quiescent flow with dynamic viscosity $\mu \approx 1\ Pa \cdot s$ is studied in order to test the validity of the models that will be presented in what follows.

It has been known for a long time that describing the angular degrees of freedom with the Stokes approximation (i.e. no fluid inertia) leads to an indeterminacy in the settling angle: the particle may settle at any angle with respect to the vertical. This degeneracy, however, is lifted by the action of the inertia of the fluid, already in the limit of a small but non-zero particle Reynolds number Re_p. Whereas the correction to the translational velocity has been understood for a long time, the torque acting on a non-spherical particle is not as well understood. Cox (1965) determined the fluid inertia torque acting on spheroids in the limit of *small* Re_p and $1/\log(\beta)$. Later, Khayat and Cox (1989) expanded this effort to determine the fluid inertia torque for very slender rods, in the limit of $Re_p/\log(\beta) \ll 1$. More recently, the fluid inertia torque acting on spheroids was determined for arbitrary aspect ratio (Dabade et al., 2015).
To summarize, the limits on which each model is constructed are:

Rod model (Khayat and Cox, 1989) $\rightarrow Re_p/\log(\beta) \ll 1$ & $1/\log(\beta) \ll 1$;
Spheroid model (Dabade et al., 2015) $\rightarrow Re_p \ll 1$.

Because of the importance of the problem, many contributions have been devoted to its numerical solution, to determine approximate torque parameterisations as a function of the particle Reynolds number Re_p and particle shape (Andersson and Jiang, 2019; Fröhlich et al., 2020; Hölzer and Sommerfeld, 2009; Jiang et al., 2014; Ouchene et al., 2015, 2016; Zastawny et al., 2012). The effect of small to moderate Reynolds numbers for spheroids over a large range of aspect ratios β was recently analysed by means of numerical simulations (Jiang et al., 2021), allowing a direct comparison with the small-Re_p theory (Dabade et al., 2015) in the limit of small Re_p. It was found that the theory (Dabade et al., 2015) generally provides the correct functional form and the correct magnitude for the torque. However, it tends to over predict the numerically determined values when $Re_p \gtrsim 1$.

The hydrodynamic loads on a fixed finite-length circular cylinder in a uniform flow have also been obtained numerically, from creeping-flow conditions to strongly inertial regimes (Kharrouba et al., 2021). Semi-empirical models based on theoretical predictions and incorporating finite-length and inertial corrections extracted from the numerical data were then derived. There have been, in comparison, far fewer experimental studies.

		Rod model		Spheroid model
		$Re_p/\log\beta$	$1/\log\beta$	Re_p
Present work	$\beta = 8$	0.07	0.48	0.15
	$\beta = 16$	0.14	0.36	0.4
Roy et al	$\beta = 20$	0.5	0.33	1.6
	$\beta = 100$	1.8	0.22	8.5

Table 1.1: Regimens reached in the present work and those in the literature.

In experiments where rods settle through a simple vortical flow, it was shown that the effect of fluid inertia could not be ignored (Lopez and Guazzelli, 2017). More recently, the force and torque measured in experiments of symmetric and asymmetric fibers settling were qualitatively well described by the model of Khayat and Cox (Roy et al., 2019). The expression of torque by Khayat and Cox for symmetric fibers, with $\Gamma \approx 3$, overpredicts (i.e. the prediction is higher than the experimental data) the experimentally measured torque for $\beta = 20$ and $Re_p = 1.6$, while it underpredicts (i.e. the prediction is lower than the experimental data) the measurements for $\beta = 100$ and $Re_p = 8.5$ – however the origin was argued to lie in the defects in fibers which produce slight asymmetries (Roy et al., 2019) (see also Candelier and Mehlig (2016)).

As these models are constructed in the limit of $Re_p \ll 1$ and $\Gamma \gg 1$, it is important to experimentally validate them at lower Re_p and larger Γ values than those currently present in the literature. Moreover, it is interesting to test their performance in a creeping flow when $1/log(\beta) \not\ll 1$. To fill this gap, Chapter 3 in this thesis focuses on the measurement of the rotational and translational dynamics of rods settling in a quiescent creeping flow, in a regime of high particle-to-fluid density ratios $\Gamma = 14.8$ and low Re_p of about 0.3. Two particles, with aspect ratios $\beta = 8$ and $\beta = 16$ were considered.
In particular, Table 1.1 shows the regimens attained in the present work and that of Roy et al. (2019), with a focus on the proximity to the limits where the Rod and Spheroid models are valid.
The Re_p values attained in this thesis are approximately one order of magnitude smaller than those of Roy et al. (2019). Whereas the values of $\log(\beta)$ are about 30% larger.
Note that it is experimentally impossible to attain the limit $1/\log(\beta) \ll 1$. For instance, to obtain $1/\log(\beta) = 0.1$, $\beta = 10^{10}$ is needed. Thus it is crucial to test the rigidity of the condition in β as it is hard to imagine a situation in nature where such elongated particles exist.

The theoretical framework and the experimental results are presented in Chapter 3.

1.4 Particle settling in a quiescent flow at moderate Reynolds numbers

Although the problem of a single spherical particle settling in a quiescent flow might seem somewhat simple, a very rich dynamics, not yet totally understood, is present. The settling regimes are controlled by two dimensionless parameters (as already discussed in Section 1.2): Ga and Γ. The terminal settling velocity v_s yield the definition of $Re_p = v_s d_p/\nu$.
The trajectories of single particles settling in these conditions are generally not vertical (Jenny et al., 2004; Zhou and Dusek, 2015). A series of trajectory regimes where the trajectory can, for instance, have a non-zero angle with the vertical and/or periodically oscillate have been found. These are the result of the different wake bifurcations that appear as Galileo (or, equivalently Reynolds) numbers increase. The bifurcations yield wake instabilities that transfer momentum to the settling particle, thus modifying its trajectory.

In particular, the analytical calculation of the different bifurcations that said dynamics undergoes is only available for the first bifurcation (Fabre et al., 2008, 2012), i.e. when the vertical

trajectories disappear. Furthermore, the community relays on data from numerical simulations that is often not conclusively validated by experiments. Note that the last sentence is also valid in the case of slender bodies in creeping flow presented in the previous Section.
Although not studied here, besides of the inherent interest on single particle dynamics, one particle settling is the first step to understand suspensions, as a number of collective effects are found to be directly related to the ones of single particle settling. In this sense, experimental (Huisman et al., 2016) and numerical (Fornari et al., 2016; Seyed-Ahmadi and Wachs, 2021; Uhlmann and Doychev, 2014) studies have shed light on a number of suspension properties, such as: the modification of settling velocities compared to the single particle case, caused by entrainment; or particle clustering effects. Moreover, although in this thesis only spheres and cubes are studied (at moderate Ga), it is interesting to remark that there has been a growing interest in studying anisotropic particles in the context here presented, see for example Toupoint et al. (2019); Will et al. (2021) or, for a comprehensive review, Ern et al. (2012) and references therein.

1.4.1 Fixed object wake dynamics

As the particle settling path instabilities are caused by wake bifurcations, it is interesting to start studying the nature of wake instabilities alone. This is achieved by having the particle fixed in an incoming laminar flow with velocity U. In this case, the dynamics is dominated by only one dimensionless parameter, in particular the Π-theorem reads: 4 independent variables (d_p, ν, U) and 3 units (m, s, kg) thus 1 parameter. The only dimensionless parameter that can be constructed is a Reynolds number: $Re_f = Ud_p/\nu$ (the subscript 'f' recalls here that this Reynolds number refers to the case of *fixed* spheres). Furthermore, experiments in this configuration are simpler as it is not necessary to track a particle moving but it suffices to image the wake in a fixed region in space.

Fixed sphere wake

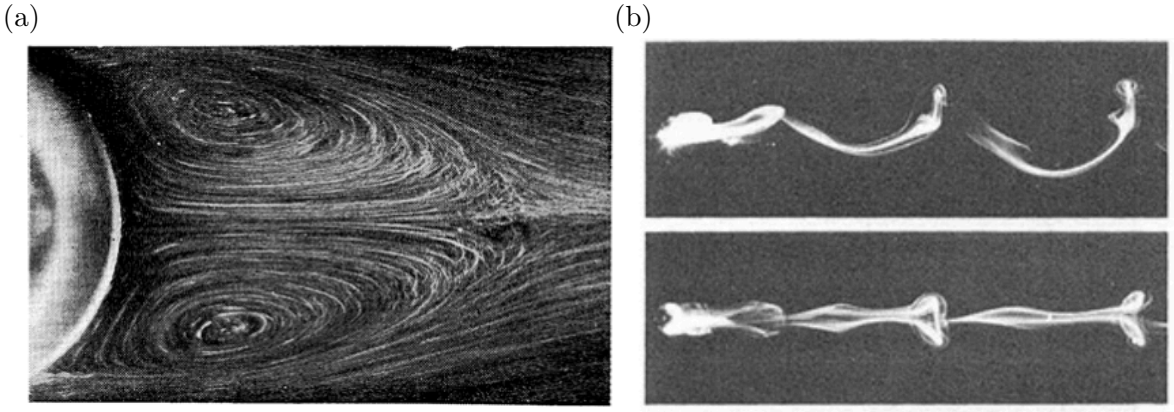

Figure 1.3: Wakes behind a fixed sphere. (a) Stationary vortex pair behind a sphere at $212 \lesssim Re_f \lesssim 274$, taken from (Taneda, 1956). (b) The vortex in (a) periodically shed when $274 \lesssim Re_f \lesssim 325$, taken from (Sakamoto and Haniu, 1990).

All the conventional objects' shapes present a wake with a number of bifurcations as Re_f increases before it converges to a final chaotic state at large Re_f. For the case of a spherical particle, numerical/theoretical (Bouchet et al., 2006; Fabre et al., 2008; Ghidersa and Dusek, 2000; Natarajan and Acrivos, 1993; Pier, 2008; Tomboulides and Orszag, 2000) and experimental (Gumowski et al., 2008; Johnson and Patel, 1999; Nakamura, 1976; Ormières and Provansal,

1999; Przadka et al., 2008; Sakamoto and Haniu, 1990; Taneda, 1956) studies have characterised the wake transitions, and its relative onsets, as a function of a Reynolds number based on the sphere diameter and the velocity of the incoming laminar flow. Note that in the literature there is some disagreement about the onset values for each wake transition.
In what follows a summary of the different transitions of the wake behind a sphere in the Re_f ranges of interest in this thesis are laid out, following the more recent onset values in the literature:

- ($Re_f \lesssim 200$) Axisymmetric, planar, and steady wake.
- ($200 \lesssim Re_f \lesssim 274$) Non-axisymmetric, planar, and steady wake.
  A spontaneous symmetry breaking generates a pair of vortex-rings (that do not detach) in the wake – see Figure 1.3(a). It is worth to remark the contrast with the wake behind a cylinder where the analogous transition occurs at $Re \approx 50$.
- ($274 \lesssim Re_f \lesssim 325$) Non-axisymmetric, planar, and unsteady wake.
  The vortex pair becomes unsteady and the vortical structures start to shed – see Figure 1.3(b). In particular, the vortex are shed periodically.
- ($325 \lesssim Re_f$) Non-axisymmetric, non-planar, and unsteady wake.
  The unsteady wake is quasi-periodic and it is called chaotic.

The wake dynamics of a fixed sphere is then composed of the following consecutive states: steady, axisymmetric, planar; steady, non axisymmetric, planar; periodic, non-axisymmetric, planar; quasi-periodic, non-axisymmetric, non-planar.

Drag

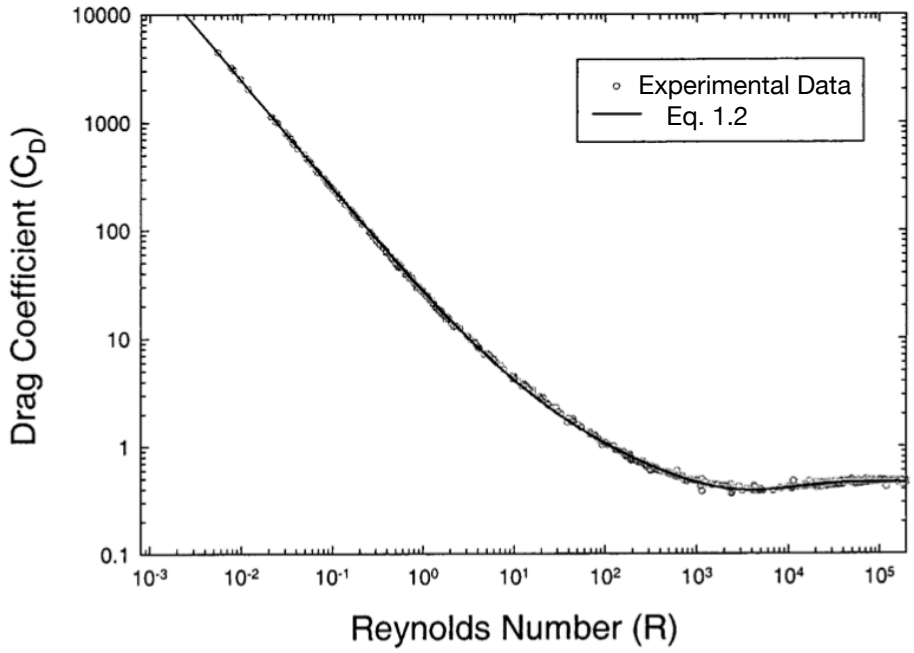

Figure 1.4: Drag coefficient measured and Equation 1.2 (taken from Brown and Lawler (2003)).

If besides the nature of the wake regimes, one is interested in aero/hydrodynamic drag exerted by the flow on the particle, an additional parameter appears: the drag coefficient ($C_D(Re_f)$)

such that the drag force follows:

$$F_D = \frac{1}{2}\rho_f C_D(Re_f) A U^2, \tag{1.1}$$

with A the reference area.

In the case of an anisotropic particle both $C_D(Re_f)$ and A are dependant on the particle orientation, although in some first order approximations the deviation from the spherical shape is taken as a parameter (see Section 4.3). In particular, the reference area takes a simple value of $A = \pi d_p^2/4$ in the spherical case. Furthermore, in the simplest case the drag coefficient of a sphere $C_D(Re_f)$ reduces to $24/Re_f$, i.e. the Stokes approximation. Otherwise, the drag coefficient is only empirically known and it strongly depends on the object's shape (Hoerner, 1965). For a fixed sphere, Brown and Lawler (2003) proposed a single equation for drag coefficient prediction over a larger range of Reynolds number from 1×10^{-2} to 1×10^5 that reads:

$$C_D^{\text{Brown}}(Re_f) = \frac{24}{Re_f}(1 + 0.150 Re_f^{0.681}) + \frac{0.407}{1 + \frac{8.710}{Re_f}}. \tag{1.2}$$

Figure 1.4 presents the drag coefficient measured (circles) and Equation 1.2 (taken from (Brown and Lawler, 2003)). It can be seen that the Equation models well the dynamics, in particular, the model is seen to capture all the experimental points with a maximum discrepancy of 15%.

Note that, interestingly, the work by Brown and Lawler (2003) is partially based on measurements for settling spheres (rather than fixed), what brings the question of the impact (or not) of the motion of the spheres (and hence of the density ration Γ) on the drag coefficient. While Brown study does not consider this eventuality, this point is actually not trivial. It will be discussed in next subsection and explored experimentally in Subsection 4.1.4, where the usual approximation that C_D does not depend on Γ will be contrasted to experimental results form this thesis.

Fixed cube wake

The study of cubic particles' wakes started roughly 10 years after the analogous studies were made for spheres. This is partly because the sphere is the canonical shape: due to its symmetries it often simplifies the analysis. On the other hand, modelling the sharp edges of a cube is an additional difficulty that could not be tackled yet: consider, for instance, the difficulties in the modelling of a cylinder edges in a creeping flow (Section 1.3). Moreover, a new degree of freedom is added to the problem as the orientation of the particle has to be taken into account.
Regarding the literature, the first study of the wake behind a fixed cube is a numerical simulation from 1990 that explored the wakes in the range $10 \lesssim Re_{\text{side}} \lesssim 100$ (Raul et al., 1990), with Re_{side} is now the Reynolds number based on the length of the sides of the cube. Furthermore, in the last two decades, a number of studies focused on this question from the numerical (Khan et al., 2019; Meng et al., 2021; Rahmani and Wachs, 2014; Richter and Nikrityuk, 2012; Saha, 2004, 2006; Seyed-Ahmadi and Wachs, 2019; Wang et al., 2019, 2020) and experimental (Khan et al., 2018, 2021; Klotz et al., 2014; Zhao et al., 2019) point of view. Because of how recent these studies are, there is still some disagreement between them, especially in the Re_{side} value of the wake instability onsets. Figure 1.5 presents the three first transitions that a cube undergoes, measured experimentally by Klotz et al. (2014). A qualitative description of the different wake bifurcations and onsets of a fixed cube with its face perpendicular to the incoming flow (see Fig. 1.5) in the range $1 \lesssim Re_{\text{side}} \lesssim 400$ follows:

- ($Re_{\text{side}} \lesssim 215$) Orthogonal symmetry and steady wake.
  Four pairs of vortices form behind the cube – Fig. 1.5(a,b).

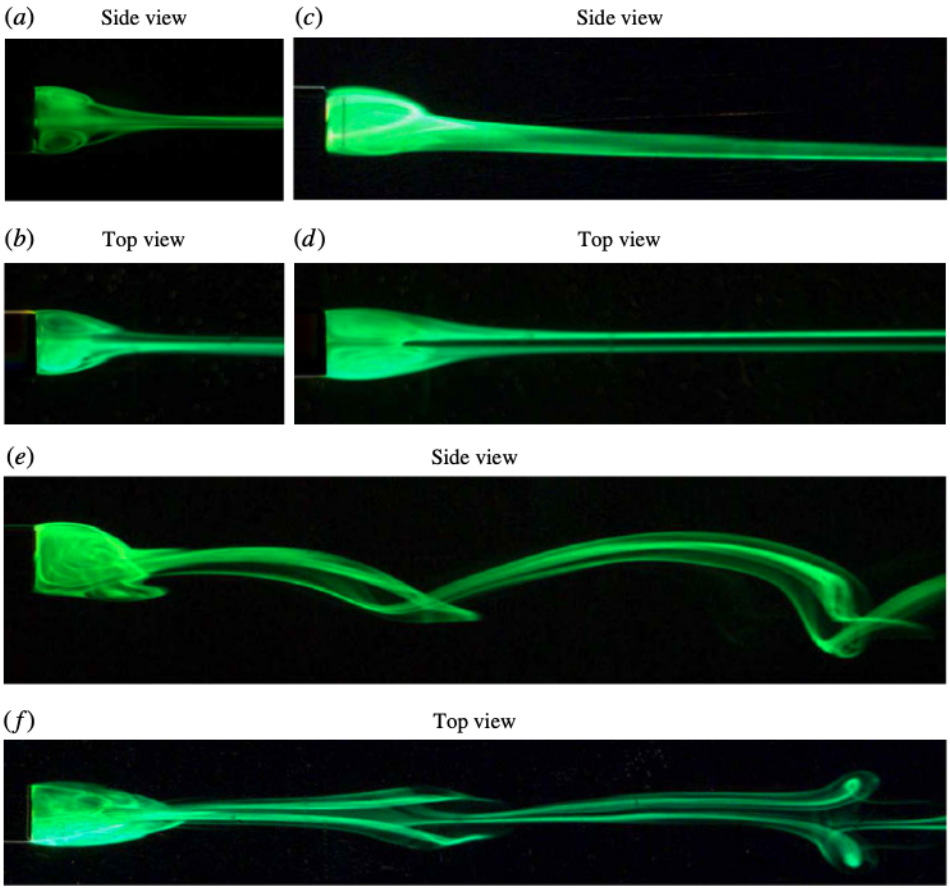

Figure 1.5: Visualisations of the first three wake regimes of a cube: (a,b) the steady wake at $Re_{\text{side}} = 100$, (c,d) the pair of counter-rotating vortex-rings that do not detach at $Re_{\text{side}} = 250$, and (e,f) the periodic vortex shedding regime at $Re_{\text{side}} = 300$ (taken from Klotz et al. (2014)).

- ($215 \lesssim Re_{\text{side}} \lesssim 276$) Planar symmetry and steady wake.
  A spontaneous symmetry breaking generates a pair of counter-rotating vortex-rings that do not detach – Fig. 1.5(c,d).

- ($276 \lesssim Re_{\text{side}} \lesssim 315$) Planar symmetry and unsteady wake.
  Periodic vortex shedding – Fig. 1.5(e,f).

- ($315 \lesssim Re_{\text{side}}$) Axisymmetric and unsteady wake.
  Chaotic vortex shedding.

1.4.2 Free particle settling: path instabilities, settling velocity and drag

Questions arise immediately from the previous Section: how will the wake behave if the sphere were settling in a quiescent fluid instead of being fixed in an incoming laminar flow? It is clear that the sphere is subjected to transfers of linear and angular momentum each time a vortex is detached from its wake, how would then the trajectory of the particles be affected by the different wake instabilities?

Besides the trajectory geometry, the question also applies to the drag coefficient: is the drag coefficient of a settling object the same as for a fixed object at the same Reynolds number ? And can the terminal settling velocity be determined from the knowledge of fixed drag coefficients ?

The last question is *a priori* not so straightforward, even for a sphere. Indeed, while there is only one control parameter for the fixed sphere case (Re_f), the settling case has two control parameters Γ and Ga. It is therefore expected that in the settling case $C_D(\Gamma, Ga)$. Since the terminal settling velocity, hence the terminal particle Reynolds number Re_p also depends on Γ and Ga ($Re_p(\Gamma, Ga)$), one could eventually consider a dependency $C_D(\Gamma, Re_p)$ for the drag coefficient, which would not only be determined by Re_p but would also depend on Γ.

Note that the terminal settling velocity and the drag coefficient are simply related by the balance between hydrodynamical drag and gravity. For spheres, this yields to the relation

$$\mathbf{v_s}(\Gamma, Ga) = \sqrt{\frac{4|\Gamma - 1|d_p|\mathbf{g}|}{3C_D(\Gamma, Ga)}}\frac{\mathbf{g}}{|\mathbf{g}|}. \tag{1.3}$$

This relation allows to determine the drag coefficient from the measurement of settling velocities, as done in the study by Brown and Lawler (2003). When projected onto the vertical coordinate (aligned with gravity), this relation can be simply expressed in terms of the terminal particle Reynolds number $Re_p = v_s d_p/\nu$ (v_s is now the vertical component of the terminal velocity) as

$$Re_p(\Gamma, Ga) = \sqrt{\frac{4}{3C_D(\Gamma, Ga)}}Ga \tag{1.4}$$

Note that, in the limit of creeping flow approximation, where the Stokes drag applies C_D is analytically related to Re_p by $C_D = 24/Re_p$, what yields in this case to the aforementioned relation $Re_p = Ga^2/18$ (only valid for spheres in the Stokes regime). The next subsections detail some important features of path instabilities and drag considerations for spheres and cubes, which will be explored experimentally in this thesis.

Sphere

It is only in the past 30 years that the interplay between drag law and path instabilities has been tackled. A pioneer work regarding fluidised beds shed light on the non-applicability of Newton's free settling law on rising particles ($\Gamma < 1$) caused by the aforementioned wake effect on the particle trajectory which modify the drag coefficient compared to the fixed spheres case

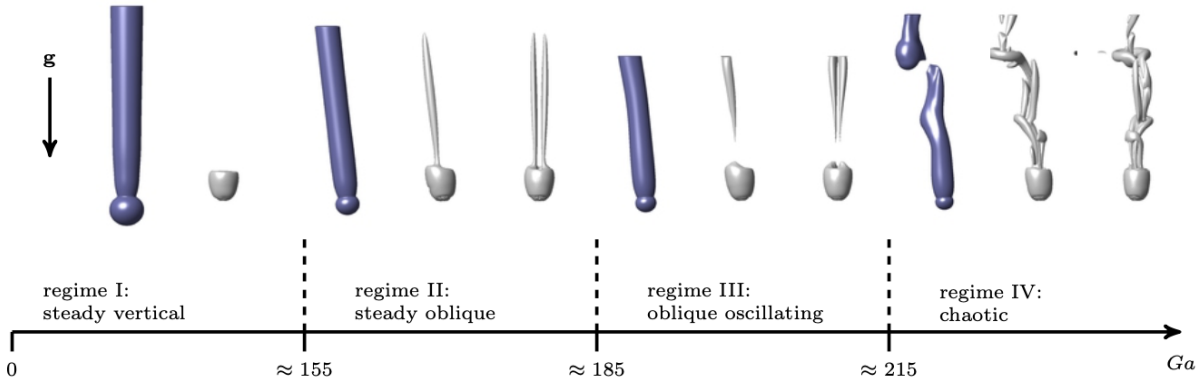

Figure 1.6: The four main regimes that a sphere settling in a quiescent flow undergoes as a function of the Galileo number for a density ratio = 1.5. The typical wake structure is shown for each regime. The regime boundaries $Ga = \{155, 185, 215\}$ correspond to particle Reynolds numbers of approximately $\{203, 253, 304\}$, respectively. (Taken from (Uhlmann and Doychev, 2014))

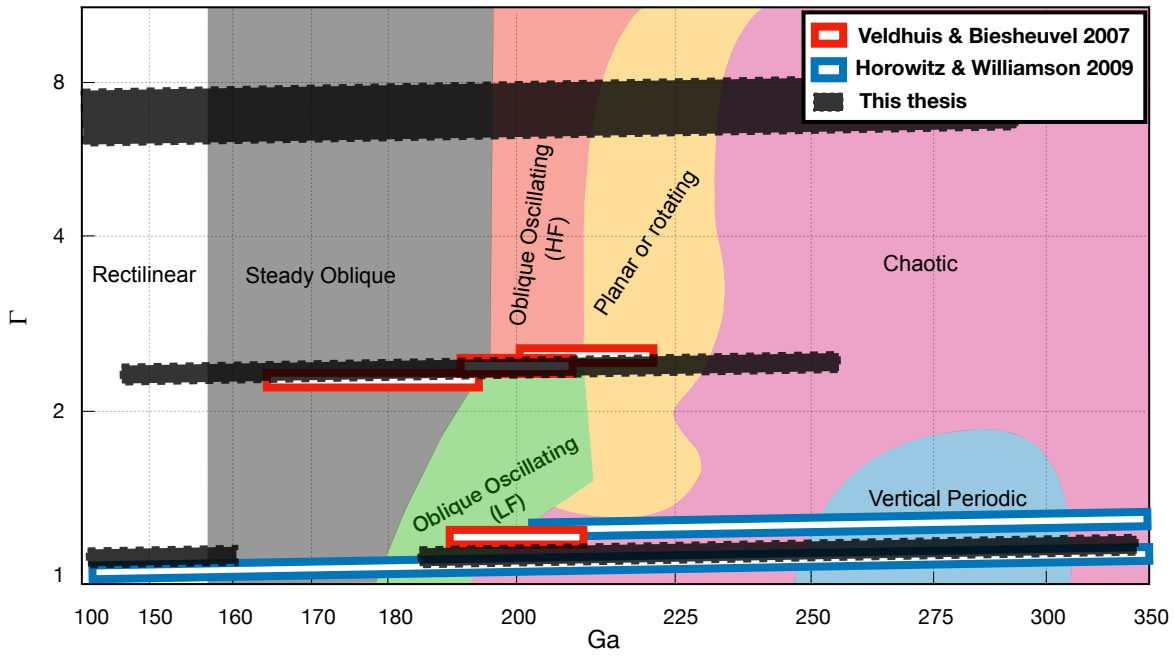

Figure 1.7: The particle-to-fluid density ratio – Galileo number parameters space for the settling of spheres, built from the numerical simulation findings of Zhou and Dusek (2015). The red and blue boxes show the regions that Veldhuis and Biesheuvel (2007) and Horowitz and Williamson (2010) have explored. Furthermore, the black regions represent the parameters ranges studied in this thesis.

(Karamanev and Nikolov, 1992). This study therefore already pointed to the joint Γ, Ga dependency of C_D and its connection to path instabilities. The dependency of the drag coefficient on density ratio for light buoyant spheres ($\Gamma < 1$), has been further investigated in a recent numerical study which exhibits a systematic increase of the drag coefficient as the density ratio decreases (Auguste and Magnaudet, 2018). For the case of dense particles ($\Gamma > 1$), Brown and Lawler (2003) used measurements of settling spheres to establish a generic law for the Reynolds number dependency of the drag coefficient (generally associated to fixed spheres), not addressing a possible dependency of C_D on Γ. Their results seem to corroborate this hypothesis, although a scatter of the order of 15% is mentioned when comparing the accuracy of the empirical drag law 1.2 compared to the large dataset of experimental drag coefficients derived from settling velocities. This therefore raises the question of a possible dependency $C_D(\Gamma, Ga)$, not explored for the case of heavy particles. It is also interesting to point out that while most empirical correlations for the drag coefficient give $C_D(Re_p)$, where Re_p is not known *a priori* because it is a response parameter. It would be interesting to establish the direct empirical correlations $C_D(\Gamma, Ga)$ and $Re_p(\Gamma, Ga)$, useful to rapidly determine drag and settling from the actual control parameters. Interestingly, Brown and Lawler (2003) do give a relation of the type $Re_p(Ga)$ (which actually turns out to be more accurate than the proposed relation $C_D(Re_p)$) although the eventual Γ dependency is not addressed.

Regarding the path instability problem, Jenny et al. (2003) made the first numerical study that explored the trajectory dynamics, as a function of Galileo number and particle-to-fluid density ratio, of a single spherical particle settling or rising in a quiescent unconfined flow. Particularly, they studied the first three wake bifurcations critical Galileo number values and the trajectory characteristics on each regime. In this way they were able to construct a particle-to-fluid density ratio - Galileo number number map showing the different regimes for a single sphere settling or rising in a quiescent flow. The trajectories were characterised by their angle, spectral content and planarity, leading to four main regimes: Vertical, Steady Oblique, Oblique Oscillating and Chaotic. In particular, Figure 1.6 (taken from Uhlmann and Doychev (2014)), shows the results of one set of numerical simulations in the literature that studied these path regimes and the corresponding wakes. The four wakes dynamics and their bifurcations can be seen, as it was introduced in the previous Section under the names 0-3. It is worth to remark that the onsets are different than those of the fixed sphere.
More recently, Zhou and Dusek (2015) have studied more systematically the dynamics around the bifurcations. They have narrowed down the position, in both Galileo and particle-to-fluid density ratio, of the delimitations between regimes. Furthermore, they have quantified a number of trajectory parameters such as angle, velocities and spectral content, for example. Moreover, they have identified an interesting new regime, that is found surrounded by the Chaotic Regime, whose existence is verified experimentally in this thesis: the Vertical Periodic Regime that has zero angle with the vertical and periodic oscillations.
This problem has also been studied from the theoretical point of view by a weakly non-linear expansion of the flow around the particle: the onset of the first bifurcation, that delimitates the rectilinear and steady oblique regimes, was derived analytically and found to be independent of particle-to-fluid density ratio (Fabre et al., 2012). Additionally, this physical phenomena has been used as a benchmark for numerical simulation codes that aim to explore collective particle effects (Fornari et al., 2016; Uhlmann and Doychev, 2014). Furthermore, this dynamics was the starting point for studies concerning liquid metals and impurities that are needed for the production of clean metal (Pan et al., 2019).

As far as 2021, only two experimental studies (Horowitz and Williamson, 2010; Veldhuis and Biesheuvel, 2007) have explored the predictions made by simulations.
Figure 1.7 presents the $\Gamma - Ga$ parameters space taken from (Zhou and Dusek, 2015), while the red and blue boxes show the regions that Veldhuis and Biesheuvel (2007) and Horowitz

and Williamson (2010) have explored. The black regions are the parameters ranges studied in this thesis. In numerical simulations the High frequency and Low frequency-Planar or Rotating regimes are very slim in Ga (just a few percents), what renders its distinction extremely difficult in experimental studies as uncertainties in Ga are comparable to its width. The planar and rotating regime will then be considered here as a single *tri-stable* regime where Low Frequency, High Frequency and Chaotic regimes can eventually co-exist. While in numerical simulations two slim bi-stable regimes are distinguished (Chaotic plus High Frequency) followed by another slim bi-stable region (Chaotic plus Low Frequency), before settling on the Chaotic regime (Zhou and Dusek, 2015).
The work of Veldhuis and Biesheuvel (2007), although with some discrepancies, has been able to validate part of the parameters space for the dynamics described in the numerical simulations. The regimes therein observed are: oblique trajectory with no significant frequencies (Steady Oblique regime); oblique with oscillations at three significant non dimensional frequencies 0.07, 0.017 and 0.025 (Oblique Oscillating regime), whose apparition depends on the particle-to-fluid density ratio; oblique chaotic regime with no dominant frequencies and trajectory curvature (Chaotic regime). The experiments performed by Veldhuis and Biesheuvel (2007) were targeted to identify the Oblique Oscillating regimes and their onsets, up to a particle-fluid density ratio of 2.3.
On the other hand, Horowitz and Williamson (2010) were mostly interested in rising spheres and Galileo numbers smaller than 1×10^4 whereas the aforementioned numerical simulations explore the dynamics up to $Ga = 350$. In particular, they studied the trajectory angle and the drag (following the work of Karamanev and Nikolov (1992)). It is worth to remark that some of their results are not in quantitative agreement with the experimental Veldhuis and Biesheuvel (2007) and numerical literature (Jenny et al., 2004, 2003; Zhou and Dusek, 2015), or the present work. For instance, Horowitz and Williamson (2010) measure trajectories corresponding to the Steady Oblique Regime up to $Ga \approx 300$, whereas this thesis and all the other studies in the literature agree in a Steady Oblique regime that ends at $Ga \approx 200$.

A number of important regions in the parameters space and trajectory characteristics observed in numerical simulations by Zhou and Dusek (2015) have to be still corroborated, such as: trajectory angle as a function of Galileo number; dynamics at particle-to-fluid density ratio higher than 3; the new Vertical Periodic Regime identified in simulations; planarity lose threshold (Chaotic Regime onset); among others. These questions motivate the experimental work presented in Chapter 4.

Cube

An analogous behaviour to that described for spheres can be anticipated for cubic particles, as their wakes also present bifurcations that lead to instabilities. As briefly mentioned before, the study of cubic particles is behind that of spheres for approximately 10 years. In this context, in 2014 the first work regarding the path dynamics of cubic particles settling in a quiescent flow has been published (Rahmani and Wachs, 2014), and in 2021 a more thorough study was made by the same group (Seyed-Ahmadi and Wachs, 2019). Nonetheless, the literature focus is mostly, as it is the case for many non-spherical particles, on finding drag correlations (Haider and Levenspiel, 1989; Hölzer and Sommerfeld, 2008; Tran-Cong et al., 2004b). In this case the objective is to absorb the shape of the particle in a shape factor that would be another parameter to take into account in the drag coefficient (Lau and Chuah, 2013; Paul et al., 2017). The shape factor ϕ is defined as $\phi = s/S$, with s and S the surface of a sphere with the same volume as the anisotropic particle and S the actual particle surface. It is worth to remark that the two main works regarding this problem (Rahmani and Wachs, 2014; Seyed-Ahmadi and Wachs, 2019) are numerical. In particular, the different regimes found numerically by (Seyed-Ahmadi and Wachs,

2019) for the settling of cubes do not differ much from those of a sphere. The trajectories are characterised by their trajectory angle; spectral content; planarity; and, differently from the case of a sphere, the particle's orientation. In this sense, four main regimes have been identified: oblique, vertical, helical and chaotic. Note some of the differences with the case of a sphere: (1) the first two regimes are oblique-vertical, instead of vertical-oblique; (2) instabilities happen at much lower Galileo number; (3) these regimes are present for all particle-to-fluid density ratios (Γ) in the range $(1.2, 7)$, i.e. there is no discrimination by Γ.

The settling regimes predicted by simulations for cubic particles therefore still need to be confronted to experimental evidence. This is part of the work achieved during this thesis and will be presented in Chapter 4.

1.5 Spherical particles settling in turbulence

In the precedent, situations where particles settle in a Quiescent Fluid were discussed, which already revealed rich dynamical behaviours emerging from coupling between particle and fluid dynamics. Such coupling becomes even more intricate when the surrounding fluid is not at rest, and specifically when it exhibits turbulence and the inertia of the particle interplays with that of the turbulence. The multiscale nature of turbulence also strongly impacts the particle dynamics as, depending on their size, the particles may preferentially interact with turbulent structures at different scales and have a dynamics that deviates more or less from that of a fluid parcel. As a consequence, particles in turbulent flows tend to be divided into two categories: tracers which behave as fluid particles, and inertial particles which do not. Ideally, a tracer particle has a mass density equal to that of the flow and a size smaller than the flow's smaller scale (Kolmogorov scale η). Thus it would react to the fluid pressure gradients in the same manner as a fluid parcel, *i.e.* it will follow the flow. On the other hand, inertial particles do not have the same density as the fluid and/or a size larger than the smallest scale of the flow. These produce a longer response time to momentum transfer from the fluid (compared to a fluid parcel), together, eventually, with a spatial filtering of turbulent eddies eventually smaller than the particle which will not significantly contribute to its transport. Overall, this results in the necessity to consider the effects of forces that affect inertial particles differently than a fluid parcel. This section will present some of the phenomena that an inertial particle in a flow presents. Essentially, the case of *one-way coupling*, where the flow transports the particles without being modified by their presence, is considered.

It is worth to mention that the velocity of a tracer particle can be computed from the Navier-Stokes equations, whereas empirical models are needed to describe the motion of an inertial particle. At the moment, only the case of point-particles (detailed in Section 1.5.2) has a rigorous theoretical framework.

1.5.1 Phenomenology of turbulence

Turbulence is a state of fluid motion which is characterised by apparently random and chaotic three-dimensional vorticity (informally, a set of different sized eddies). When turbulence is present, it usually results in increased energy dissipation, mixing, heat transfer, and drag (George, 2013). Although its ruling equations have been known for centuries (mainly the Navier-Stokes equations) their non-linearity and non-locality yields a complexity that apart from some few analytical results (such as the kinetic energy balance or the Karman-Howarth relation for energy cascade) most of the knowledge of turbulence remains empirical and derived from experimental observations and Direct Numerical Simulations (DNS).

The cornerstone of such empirical description relies on the idea of energy cascade and on a phenomenology based on dimensional analysis, which essentially applied to homogeneous and

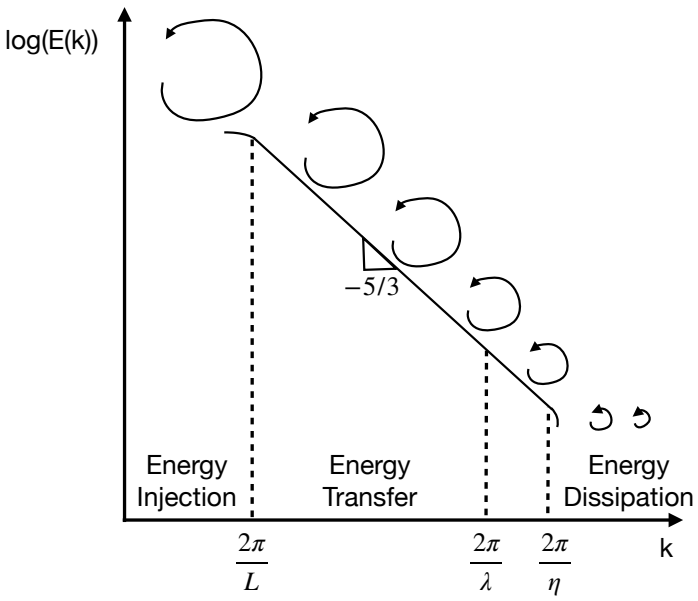

Figure 1.8: Spectrum of turbulent kinetic energy versus wake number. When a flow is forced at a scale L (for instance by stirring it with an impeller of typical size L), if the power ϵ injected per unit of mass is too large for viscosity to dissipate it at the forcing scale, energy will be non-linearly transferred to smaller scales (hence generating eddies at scales $l < L$) up to a scale η where velocity gradients become sufficient for viscosity to dissipate the injected energy.

isotropic turbulence, developed by Kolmogorov (1941) – for a modern version of these see, for example, (Frisch, 1995).
An important concept behind turbulence relies on its multi-scale nature and is known as the energy cascade: when a flow is forced at a scale L (for instance by stirring it with an impeller of typical size L), if the power ϵ injected per unit of mass is too large for the viscosity to dissipate it through the flow gradients at the forcing scale, energy will be non-linearly transferred to smaller scales (hence generating eddies at scales $l < L$) up to a scale η where velocity gradients become sufficiently intense for viscosity to efficiently dissipate the injected energy. In this sense, the energy cascade is intimately related to energy conservation. In this context, three main scale regimes of turbulence can be defined, in decreasing order:

- $L \ll l$
  the large scales range, for scales larger than the energy injection scale L. It corresponds to uncorrelated dynamics;

- $\eta \ll l \ll L$
  the inertial range, where the energy is non-linearly transferred to smaller scales with no major dissipation: this leads to a correlated multi-scale dynamics;

- $l \ll \eta$
  the dissipation range, where the energy is dissipated by viscosity in form of heat: viscous friction. At this scales the flow is smooth and can be considered as laminar.

The energy cascade in Fourier space is sketched in Figure 1.8, where the celebrated five-thirds *Kolmogorov* law for the inertial range is presented Pope (2011).

In the homogeneous and isotropic case, the multi-scale turbulent dynamics is mainly described by two parameters: the energy injection scale L and the energy dissipation scale η. This

results in a single dimensionless parameter, the Reynolds number: $Re = \left(\frac{L}{\eta}\right)^{4/3}$. Reynolds number can also be introduced from the Navier-Stokes equations, as the ratio between the non-linear term (which drives the energy transfer across scales), and the viscous term (which controls the energy dissipation). In its dimensionless form, Navier-Stokes equation indeed carries the Reynolds number as its single dimensionless parameter. From L and η other important characteristics of turbulence can be derived from dimensional analysis, involving other (*a priori* Reynolds number dependent) dimensionless numbers.

For instance, the energy dissipation rate ϵ relates to η and to the viscosity of the fluid by $\eta = \nu^3/\eta^4$. Note that in practice L (the energy injection scale), ϵ (the energy dissipation rate, which ought to energy conservation equals the energy injection rate) and ν are generally the actual control variables (turbulence is generated by stirring a fluid of viscosity ν with an impeller of size L driven by an engine able to deliver an power per unit mass ϵ). If this set of parameters is chosen, then the Reynolds number writes $Re = \epsilon^{1/3}L^{4/3}/\nu$, and the dissipation scale is then defined as $\eta = (\nu^3/\epsilon)^{1/4}$. The previous relation shall include a dimensionless parameter, which is generally taken as 1, making this relation the practical definition of the dissipation scale.

Another important response parameter of the turbulence is the fluctuating velocity of the fluid, whose *rms* value σ_u dimensionally relates to the control variables by $\epsilon = C_\epsilon \frac{\sigma_u^3}{L}$ where C_ϵ is a dimensionless number of order one (Pearson et al., 2002; Sreenivasan, 1998; Vassilicos, 2015).

The knowledge of σ_u allows to rewrite the turbulent Reynolds number as $Re = \sigma_u L/\nu$ (taking $C_\epsilon = 1$).

Other parameters are often also considered to describe the dynamics, which are combinations of the previous. For instance, the integral time scale $T_E = L/\sigma_u$, the dissipation time scale $\tau_\eta = (\nu/\epsilon)^{1/2}$, the Taylor microscale $\lambda = (15\nu/\epsilon)^{1/2}\sigma_u$, among others. The Taylor microscale, although it has no clear physical meaning, is often used to defined the Taylor based Reynolds number of turbulence $Re_\lambda : \sigma_u\lambda/\nu = (L/\eta)^{2/3} = (T_E/\tau_\eta) = (15Re)^{1/2}$.

In the experiments performed during this thesis, turbulence will be characterized using Particle Image Velocimetry (PIV) from which the triad of parameters σ_u - L - ϵ is measured. All the other relevant quantities are estimated according the previous relations which are summarized in Table 1.2.

Spatial scales	$\eta = (\nu^3/\epsilon)^{1/4}$	$\lambda = (15\nu/\epsilon)^{1/2}\sigma_u$
Temporal scales	$\tau_L = L/\sigma_u$	$\tau_\eta = (\nu/\epsilon)^{1/2}$
Reynolds numbers	$Re = \frac{\sigma_u L}{\nu}$	$Re_\lambda = \frac{\sigma_u \lambda}{\nu}$

Table 1.2: Relations between the triad of measured values σ_u - L - ϵ, and other important parameters.

1.5.2 Particle-turbulence coupling in the point-particle approximation

Contrarily to the motion of the fluid for which, although complex, an equation of motion is known (Navier-Stokes equation), no generic theoretical framework exists yet to write a practical equation of motion in turbulence for particles (even spherical) of arbitrary size. This is particularly due to the difficulty to define the velocity of the fluid at the scale of the particle when it has a finite size, with a typical dimension comparable to the inertial scales. Indeed, because of the multi-scale nature of turbulence, the flow can have different values of velocity all around the particle. As a consequence, only the limit idealized case of point-particles (in practice a dimension smaller than η) have a clear theoretical framework for the moment.

In the point-particle approximation, the equation of motion is given by the Maxey-Riley-Gatignol equation of motion. For a small spherical particle in a turbulent flow in the presence of gravity it allows the computation of the particle's velocity $\mathbf{v}$ from the undisturbed fluid velocity $\mathbf{u}$, at the particle position, and reads (Gatignol, 1983; Maxey and Riley, 1983a):

$$m_p \frac{d\mathbf{v}}{dt} = 3\pi\mu d_p(\mathbf{u}-\mathbf{v}) + \frac{1}{2}m_f \frac{d(\mathbf{u}-\mathbf{v})}{dt} + m_f \frac{D\mathbf{u}}{Dt} + \frac{3}{2}d_p^2\sqrt{\pi\rho_f\mu}\int_{-\infty}^{t} \frac{d(\mathbf{u}-\mathbf{v})}{dt}\frac{d\tau}{\sqrt{t-\tau}} + (m_p - m_f)\mathbf{g}, \tag{1.5}$$

with $\mu = \rho_f\nu$ the fluid dynamic viscosity, m_p the particle's mass, and $m_f = \rho_f\pi\frac{d_p^3}{6}$ the mass of fluid displaced by the particle. Note the $d\cdot/dt$ and $D\cdot/Dt$ represents respectively the Lagrangian derivatives following the inertial particles and the fluid tracer at the position of the particle. The different terms in the right hand side of Eq. 1.5, from left to right, quantify the following physics: (i) Stokes drag; (ii) added mass, the force exerted by the fluid displaced by the particle; (iii) pressure gradient, or the fluid parcel's acceleration at the particle position; (iv) history term, the interaction of the particle with its own wake; and (v) the buoyancy force. It is worth to notice that this model is valid under the assumption that the flow around the particle is an unsteady Stokes flow. This translates to a condition on the particles Reynolds number associated to the slippage velocity $|\mathbf{u}-\mathbf{v}|$ between the fluid and the particle: $Re_{\text{slip}} = \frac{d_p|\mathbf{u}-\mathbf{v}|}{\nu} \ll 1$.
Due to its complexity it is a common practice (supported by some numerical studies (Elghobashi and Truesdell, 1992)) to neglect the history term (iv), yielding:

$$\frac{d\mathbf{v}}{dt} = \frac{1}{\tau_p}(\mathbf{u}-\mathbf{v}) + \beta\frac{D\mathbf{u}}{Dt} + \frac{\Gamma-1}{\Gamma+\frac{1}{2}}\mathbf{g}, \tag{1.6}$$

where $\beta = \frac{3\rho_f}{\rho_f+2\rho_p} = \frac{3}{1+2\Gamma}$, and $\tau_p = \frac{d_p^2}{12\nu\beta}$ is the particle's viscous response time. The viscous relaxation time characterizes the inertia of the particles: the smaller it is, the faster the particles responds to the turbulent forcing. The ability of particles to respond turbulence, is given by the Stokes number $St = \tau_p/\tau_{\text{fluid}}$, where τ_{fluid} characterizes the typical time scale of the turbulence forcing the particle. For point-particles τ_{fluid} is generally taken as τ_η, which corresponds to the time-scale of turbulence at dissipative scales, yielding to the following definition of the Stokes number:

$$St = \frac{\tau_p}{\tau_\eta} = \frac{1}{36}\left(\frac{d_p}{\eta}\right)^2(1+2\Gamma) \tag{1.7}$$

Note that according to Eq. 1.6 the added mass term (ii) can also be neglected when the condition $1 \gg \beta St$ (or equivalently $1 \gg d_p/\eta$), in which case the equation of motion simply becomes

$$\frac{d\mathbf{v}}{dt} = \frac{1}{\tau_p}(\mathbf{u}-\mathbf{v}) + \frac{\Gamma-1}{\Gamma+\frac{1}{2}}\mathbf{g}, \tag{1.8}$$

Note that the approximations needed to use this Equations are not satisfied for most of the particles that will be considered in this thesis, which generally have a size comparable or larger than the dissipation scale of turbulence and cannot be considered as point-particles.

1.5.3 Beyond the point-particle model

The Maxey-Riley Gatignol equations is only supposed to be valid in the point particle approximation. This allows on one hand to be able to define $\mathbf{u}$ the velocity of the fluid at the position of the particle, and also to consider all particle Reynolds numbers as vanishing, in order to

consider linear Stokes drag. Real finite size particles can however deviate from these approximations. The coupling of finite size particles with turbulence remains an active field of research and here some of the existing strategies that allow to partially tackle this complicated problem are briefly described:

- Faxén corrections: the simplest correction to the point-particle limit is to consider the local curvature of the unperturbed flow ($\nabla^2\mathbf{u}$) at the particle position, i.e. when the particle is no longer small the flow cannot be assumed to be homogeneous over all the particle size. This idea is called Faxén corrections and can be included in the Maxey-Riley-Gatignol equation as done in the literature (Gatignol, 1983). This has been seen to improve the agreement between numerical and experimental results (Calzavarini et al., 2009) for particles such that $d_p/\eta \leq 5$ typically.

- Non-linear drag: if the slippage velocity and the size of the particle are such that the small particle Reynolds number approximation is not satisfied, the drag force (or equivalently the particle response time τ_p) in the equation of motion of the particle must be modified to account for non-linear drag effects. This is generally done by considering a finite particle Reynolds drag coefficient C_D leading to a modified particle response time $\tau_p = (24\rho_p d_p^2)/(18\mu C_D(Re_{\text{slip}})Re_{\text{slip}})$. Note that in the Stokes approximation, where $C_D(Re_p) = 24/Re_p$, the particle's response time reduces to the expression derived in the point-particle limit.

- Finite size particles at inertial scales: when particles have a finite-size particle in the range of the inertial scales of the turbulence (i.e. $d_p > \eta$) the relevant forcing time of the turbulence can be taken as the eddy turnover time at the scale of the particle: $\tau_{d_p} = (\frac{d_p^2}{\epsilon})^{1/3}$ (Xu and Bodenschatz, 2008), yielding a new definition of the Stokes number $St = \tau_p(Re_p)/\tau_{d_p}$ that compares the particle response time to the turbulent dynamic at the particle scale. Furthermore, while the Stokes number combines the influence of the particle size and density in a single parameter, studies with inertial particles larger than the dissipation scale, via both experiments and numerical simulations, have been proven this simplification to be inadequate (Fiabane et al., 2012; Homann and Bec, 2010; Lucci et al., 2011; Qureshi et al., 2008, 2007; Xu and Bodenschatz, 2008).

- Fully resolved particles simulations: in the absence of relevant models for the equation of motion of finite size particles at inertial scales, fully resolved numerical simulations are required. The first idea that comes to mind is to solve the Navier-Stokes equations of a fluid subject to the no-slip condition at the interfaces with the solid objects. The main drawback of this idea is the fact that the computational mesh needs to change with time to follow the particles (were the mesh is less coarse). To avoid this, the flow equations can be solved on a fixed grid where the presence of the solid particles is imposed by means of source terms added to the Navier-Stokes equations, this idea is called the Immersed-Boundary Method and has been pioneered in the context of particle turbulence interactions by Uhlmann (2005).
  In a similar spirit, the pseudo-penalisation method applied by Homann and Bec (2010) aims to impose the non-slip boundary condition on the particle's surface by imposing a *strong* drag to the fluid velocity at the particle location, so that it relaxes quickly to the particle solid motion.
  Finally, Naso and Prosperetti (2010) have performed Direct Numerical Simulations based on first principles to study the thickness of the particle boundary layer, that is a first step in order to define the slip velocity (i.e. the fluid velocity at the particle's position) and thus obtain an equation of motion outside the point-particle approximation.

1.5.4 Relevant dimensionless parameters: Stokes, Rouse, Reynolds number and density ratio

As discussed in Section 1.2, the problem of an inertial sphere settling in a turbulent flow, is *a priori* governed by a set of 4 dimensionless parameters: $\{\Gamma, Ga, Re, d_p/\eta\}$.

However, it is common in the literature to use a different set of parameters: $\{Ro, \Gamma, Re, St\}$, d_p/η is replaced by the Stokes number St (just introduced) and Ga is replaced by the Rouse number

$$Ro = \frac{v_s^0}{\sigma_u} \quad \text{with} \quad v_s^0 = \frac{\Gamma - 1}{\Gamma + \frac{1}{2}} \tau_p g \tag{1.9}$$

the settling terminal velocity of the considered particle in a quiescent flow (as shown by relation 1.8). Note that in the limit $\Gamma \gg 1$, the simpler relation $v_s^0 = \tau_p g$ is generally used. It is briefly show here that these substitutions are valid as Ro and St are combinations of the other dimensionless parameters.

- Stokes number
  As seen in previous subsection, the Stokes number can be written as

  $$St = \frac{\tau_p}{\tau_\eta} = \frac{1}{36}\left(\frac{d_p}{\eta}\right)^2 (1 + 2\Gamma), \tag{1.10}$$

  and is therefore a combination of Γ and d_p/η. Note that the previous relation for Stokes number only applies in the case of linear drag in the expression of τ_p. If non-linear drag corrections need to be considered a multiplicative corrective factor including the drag coefficient needs to be taken into account $f = \frac{24}{Re_{\text{slip}} C_D(Re_{\text{slip}})}$. In case where the slippage is dominated by settling, $Re_{\text{slip}} = Re_p(\Gamma, Ga)$ and $C_D(\Gamma, Ga)$ as previously discussed and in this case St becomes a combination of Γ, d_p/η and Ga. Empirical correlations for $Re_p(\Gamma, Ga)$ and $C_D(\Gamma, Ga)$ which can be used for this purpose will be further discussed when investigating the case of spheres settling in quiescent fluids in Chapter 4.

- Rouse number
  Starting from the definition $Ro = v_s^0/\sigma_u$, and plugging the relations for $v_s^0 = \frac{\Gamma-1}{\Gamma+1/2}\tau_p g$, $Ga = \sqrt{(\Gamma - 1) g d_p^3/\nu^2}$, $St = \tau_p/\tau_\eta$, $Re = \sigma_u L/nu$ and the relation $\eta^2 = \nu\tau_\eta$, the Rouse number can be rewritten in the case of linear drag expression 1.10 for the St as

  $$Ro = \frac{1}{18} Ga^2 Re^{-1} \left(\frac{L}{d_p}\right) = \frac{1}{18} Ga^2 Re^{-1/4} \left(\frac{\eta}{d_p}\right), \tag{1.11}$$

  hence, in the linear drag approximation, the Rouse number is a combination of Ga, Re. In case of non-linear drag corrections, the aforementioned additional factor $f(\Gamma, Ga)$ must be taken into account, and Ro becomes then a combination of Ga, Re and Γ.

The set of control parameters $\{Ro, \Gamma, Re, St\}$ is then indeed equivalent to the set $\{\Gamma, Ga, Re, d_p/\eta\}$ initially introduced, with the following physical meaning:

- Γ is the fluid to particle density ratio. In presence of gravity and turbulence, ought to the equivalence of gravitational and inertial mass, it quantifies simultaneously both effects, whithout however allowing to distinguish the possible relative importance of gravitational and inertial effects. This distinction is ensured by the Ro^0 and St parameters who respectively compare gravity and inertia to turbulence.

- Ro (sometimes called settling parameter) quantifies the relative importance of the typical particle's settling velocity compared to the turbulent fluctuations. In the limit of vanishing Ro particles are transported by the turbulence without a strong influence of settling while in the limit of infinite Ro they settle without being much affected by the turbulence.
- St quantifies the inertia of the particles compared to the forcing of the turbulence. In the limit of vanishing St, particles respond to turbulence as if they where fluid tracers, while in the limit of infinite St the motion of the particles is unperturbed by the presence of turbulence.
- Re quantifies the intensity of turbulence independently of any consideration associated to the particles.

It is worth to remark that the Froude number (Fr) is sometimes used instead of the Rouse number. It is defined as the ratio of rms fluid acceleration to gravitational acceleration: $Fr = \frac{\sqrt{a_0}(\frac{\epsilon^3}{\nu})^{1/4}}{g} = \sqrt{a_0}Re^{-1/4}St/Ro$, where the Heisenberg-Yaglom relation has been used ($a^2_{\text{rms}} = a_0\epsilon^{3/2}\nu^{-1/2}$) (Sumbekova, 2016). Note that Fr is a function of the other three dimensionless parameters and therefore it is equivalent to use Fr or Ro numbers to characterise this dynamics.

1.5.5 On the experimental challenges of this problem

Unveiling the global complexity of settling particles interacting with turbulence therefore implies exploring the 4D parameter space $\{Ro, \Gamma, Re, St\}$. From the experimental point of view, this turns to extremely complex as all the dimensionless control parameters are intertwined. It is then complicated to disentangle the influence on the overall dynamics from each of the physical ingredients that each number represents. Note how the following dimensionless numbers depend on the actual physical variables of the problem: $St(\epsilon, \rho_p, d_p, \nu, \Gamma...)$, $Ro(\sigma_u, \rho_p, d_p, g, \nu, \Gamma...)$, and $Re_\lambda(\sigma_u, \epsilon, \nu...)$. In a laboratory experiment one is capable of varying the following: particle's size – d_p, particle's mass density – ρ_p, turbulent energy dissipation – ϵ, turbulent velocity fluctuations – σ_u (or forcing scale), or the viscosity of the fluid – ν. If any of the particle's characteristics is changed, Rouse and Stokes numbers will vary; if one varies ϵ, Stokes and Reynolds numbers change; if one varies σ_u, Reynolds and Rouse numbers change. Finally, as all 3 parameters depend on ν modifying it does not help to vary the parameters independently.
In particular, it is interesting to disentangle the effects of particle settling (Ro effects) and particle inertia (St effects) in order to unveil their specific role and their interplay in particles/turbulence interaction. The next subsections recall some important inertial effects (associated to filtering and preferential sampling effects) and their interplay with gravitational settling. Finally the strategies considered in the present thesis to disentangle this effects are presented. They consist in changing the effective gravity to which the particle is submitted, what allows to modify the Rouse number, without modifying any of the other control parameters. Two solutions are deployed to modify effective gravity: free fall experiments in the Dryden Drop Tower (Portland, USA) and magnetic compensation.

1.5.6 Effects of particles inertia with and without gravity

Inertial effects in the absence of gravity

In order to purely study the turbulent transport of inertial particles in turbulent flows in the absence of gravity, many numerical simulations/theoretical results consider the case of 0-g, what is simply achieved by not including the buoyancy and gravity terms in the equation of motion of the particle. Two main important purely inertial effects prevail can be highlighted regarding particle/turbulence interactions:

- Filtering effects: the lag in the inertial particle response to fluid variations cause the particle velocity fluctuations to be less than those of the fluid, i.e. it yields the effect of a low-pass filter.
- Preferential Sampling: particles do not explore ergodically the flow but tend to sample preferentially certain regions with topological specificities.

Regarding filtering effects Tchen (1947) proposed to obtain the particle velocity by the application of a linear filter on the Lagrangian fluid velocity. Note that in its simplest version, the point particle equation of motion 1.8 takes the form of a simple first order linear filter where particles dynamics is simply forced by the turbulence visited by the particle. In this sense, the basic framework of Tchen-Hinze theory proposes a relation between the velocity variance of an inertial particle $\sigma^2_{\mathbf{v}}$ and that of a fluid particle $\sigma^2_{\mathbf{u}}$ and the particle response time τ_p:

$$\sigma^2_{\mathbf{v}} = \frac{T_L^2}{T_L^2 - \tau_p^2}\sigma^2_{\mathbf{u}}. \tag{1.12}$$

This basic formalism is based on approximating the Lagrangian autocorrelation function (linked to the Lagrangian spectrum) as $R(t) = \langle(\sigma_u)^2\rangle \mathrm{exp}(-\mathrm{t}/\mathrm{T_L})$ (Hinze, 1959; Mordant et al., 2001). This approach therefore does not account for finite Reynolds number effects as it does not include the small scale dissipative statistical dynamics of turbulence, where the exponential shape is lost (Mordant et al., 2004; Sawford, 1991). This has been recently tackled by Berk and Coletti (2021a), who extended the Tchen-Hinze approach to a the two-times autocorrelation model by Sawford (Sawford, 1991): $R(t) = \langle(\sigma_{\mathbf{u}})^2\rangle(T_L \mathrm{exp}(-\mathrm{t}/\mathrm{T_L}) - \mathrm{T_2 exp}(-\mathrm{t}/\mathrm{T_2}))/(\mathrm{T_L} - \mathrm{T_2})$, from which an improved relation between $\sigma^2_{\mathbf{v}}$ and $\sigma^2_{\mathbf{u}}$ can be computed:

$$\frac{\langle\sigma^2_{\mathbf{v}}\rangle}{\langle\sigma^2_{\mathbf{u}}\rangle} = 1 - \frac{St^2}{(T_L/\tau_\eta + St)(T_2/\tau_\eta + St)}. \tag{1.13}$$

As discussed below, further corrections to the previous relations are needed to account for even subtler effects such as preferential sampling (Deutsch E., 1992). Overall the prediction of the Tchen-Hinze theory for velocity fluctuations is in reasonable agreement with numerical simulations of point particle models (Deutsch E., 1992). This approach fails however to predict acceleration fluctuations, even in the case of point particle models where numerical simulations show a clear logarithmic decrease of acceleration variance with Stokes number, qualitatively consistent with a filtering effect but quantitatively disagreeing with Tchen-Hinze like descriptions. This discrepancy is very likely to be attributed to the preferential sampling effect which may have a strong impact on acceleration statistics.

Preferential sampling stands for the fact that particles tend to explore certain regions of the flow with higher probability than others. This striking phenomena, intimately related to the coupling between particles inertia and turbulence results in the somehow counter-intuitive behavior where turbulence eventually unmixes particles, promoting their spatial segregation in particle laden flows (a phenomenon called *preferential concentration* (Monchaux et al., 2012; Squires and Eaton, 1991)). Two main mechanisms are generally proposed to explain preferential sampling:

- Centrifugation (Maxey, 1987) is based on the idea that particles denser than the fluid tend to get centrifuged out of the core of turbulent eddies, while lighter particles migrate to the core of the eddies. As a consequence, dense particles would preferentially explore high-strain and low-vorticity regions of the flow while light particles would rather preferentially explore high-vorticity region.

- Sweep-stick mechanism (Coleman and Vassilicos, 2009) states that when an inertial particle encounters a flow region where the fluid acceleration is small, the particle will stick to it (with a stickiness that depends on the particle response time) and can get swept with it.

It is likely that both mechanisms play a role, with a dominant effect of centrifugation for particles with $St < 1$ and a dominant effect of sweep-stick when $St > 1$ (Coleman and Vassilicos, 2009), although the exact ranges of Stokes number where the mechanisms are relevant are not yet clear, and even their validity in some situations has been challenged (Bragg et al., 2015a,b). Beyond preferential concentration, another important effect of preferential sampling is its interplay with the aforementioned filtering effect. For instance, in the framework of original Tchen-Hinze theory, because of preferential sampling the actual Lagrangian correlation time T_L of the flow probed by the particles may differ from that of the global flow, as particles only sample part of the flow. This lead Deutsch E. (1992) to propose a revised theory, where

$$\sigma_{\mathbf{v}}^2 = \frac{(T_L^{@p})^2}{(T_L^{@p})^2 - \tau_p^2}\sigma_{\mathbf{u}}^2, \tag{1.14}$$

where $T_L^{@p}$ is the Lagrangian correlation time of the flow seen by the particle. The improved version of the theory by Berk and Coletti (2021a) accounting for finite Reynolds number effects also includes such subtleties.

While the validity of previous considerations for purely inertial effects in the absence of gravity can be tested in numerical simulations (generally in the framework of point particle models), the experimental validation is very delicate as additional effects associated to gravitational settling further impact the couplings between the particles and turbulence.

In particular, only two experimental works at very small gravity conditions have been performed. The most recent being conducted in 2006 when the identification of sweep-stick mechanism, among other recent advances, had not yet been introduced. Both 0-g experiments were conducted in a NASA's reduced gravity aircraft that provides approximately 8 sec of 0-g. In particular, Fallon and Rogers (2002) studied the clustering of inertial particles (a proxy of preferential sampling) in an air turbulent flow, although due to technical difficulties little results came from this project. They could confirm that, as it happens on Earth, the clustering seems to be maximal at $St \approx 1$; and also that the introduction of a body force (gravity) seems to decrease the clustering efficiency. On the other hand, Hwang and Eaton (2006) measured the fluid-phase to study the attenuation/enhancement of stationary homogeneous and isotropic air turbulence without mean flow, caused by a uniformly dispersed stationary array of heavy particles. They concluded, among other things, that the turbulence attenuation by the presence of turbulence is higher that what numerical simulations have predicted.
Mainly due to the limited time on the parabolic flights, both experiments focused on multiple particle dynamics and had little variation on the stokes number (i.e. particle sizes and densities). This motivates portions of this thesis, in particular to propose new strategies for systematic exploration of the parameters space in 0-g (and arbitrary values of g) experimentally deploying drop tower experiments. Particularly for the 0-g case, the high repeatability the Drop Tower approach (see Chapter 2) allows to vary the parameters of the problem in a wider way.

Interplay between inertial and gravitational effects

Gravity effects

In presence of gravity, the inertial effects just described are further complexified as particles interaction with turbulence gets strongly affected by the enhanced drift due to the gravitational

pull down of the particles. This is generally termed as a *crossing trajectories effect*, as settling inertial particles cross fluid particles trajectories (Csanady, 1963). Note that crossing trajectory already exists in gravity-less conditions; indeed inertial particles velocities $\mathbf{v}$ differ from that of the fluid, meaning that trajectories of inertial particles do cross those of fluid particles even without gravity. The effect is however strongly amplified by the mean additional slippage velocity associated to gravitational settling. Csanady (1963) rationalised the influence of crossing trajectories on particles/turbulence interaction, showing for instance that the Lagrangian correlation time $T_L^{@p}$ seen by the particles gets reduced as the particles rapidly settle across the turbulent eddies. In the point particle approximation, Csanady (1963) proposed the following relation for the modified Lagrangian correlation time (see also (Berk and Coletti, 2021a)):

$$T_L^{@p} = \frac{T_L}{\left[1 + \alpha (T_L/T_E)^2 Ro^2 (u_\eta/\sigma_u)^2\right]^2}, \tag{1.15}$$

where $\alpha = 1$ and 4 for the time scales associated to the vertical and horizontal velocity components respectively.

This effect has been introduced by Berk and Coletti (2021a) in the Tchen-Hinze approach to account for the modification of inertial filtering effects due to gravitational settling.

Gravitational settling is also expected to modify preferential sampling. A recent numerical study have shown for instance that a modified sweep-stick mechanism may drive the preferential concentration phenomenon of point particles with $St > 1$ (Falkinhoff et al., 2020).

On the other hand, not only settling modifies the inertial coupling with turbulence, but inertial effects also affect the settling itself as the consequence of the inertial interaction of the particles with turbulent eddies. The *preferential sweeping* mechanism Wang and Maxey (1993) for instance suggests that inertia may promote the trend of settling particles to fall on the downward side of the eddies as a result of centrifugation effect, leading to an enhanced turbulent settling compared to the non turbulent situation. Nielsen (1993) proposed an alternative mechanism, the *loitering effect*, where particles falling on the upward side of eddies will loiter around before eventually reaching a downward path, hence resulting in a hindered settling compared to the non-turbulent case. In spite of the relative qualitative understanding of these mechanisms, their quantitative characterization and modeling remains scarce, even in the simplified situations of point particle approximation (Gatignol, 1983; Maxey and Riley, 1983b). Settling enhancement in commonly reported in experimental studies (Aliseda et al., 2002; Berk and Coletti, 2021a), with settling velocities in turbulence is excess of up to 50% compared to the terminal velocity in quiescent fluid. The recent experiments by Berk and Coletti (2021a), where particles settling and fluid dynamics where measure simultanesously, attribute settling enhancement to a statistical over-representation of particles moving downward, rather than to a preferential sweeping effect where particles would preferentially sample downward regions of the flow. Regarding settling hindering few studies report it in homogeneous isotropic turbulence. The appearance of hindering is generally associated to Rouse number influence (Good et al., 2014; Nielsen, 1993; Sumbekova, 2016), with enhancement occurring for $Ro \lessapprox 1$ and hindering for $Ro \gtrapprox 1$, possibly as a result of the onset of non-linear drag effects (Good et al., 2014). However no consensus has emerged yet on the conditions under which turbulence would enhance or hinder settling: for instance, while simulations by Good et al. (2014) and Rosa et al. (2016) consider similar point particle situations, both studies including non-linear drag effects, the former does observe settling hinder while the latter does not. Besides, recent numerical simulations with fully resolved particles (Chouippe and Uhlmann, 2019) show only a moderate modification of turbulent settling compared to the quiescent fluid case (mostly a few percent of hindering).

1.5.7 Disentangling inertial and gravitational effects

Overall, the previous discussion shows that a deep understanding of all these mechanisms (and probably others) requires to disentangle the roles of inertia (Stokes number effects) and gravity (Rouse number effects) and to explore them at different levels of turbulence (Reynolds number). As already pointed such a program is experimentally of outmost complexity, because the relevant dimensionless parameters of the problem are strongly intertwined. A promising strategy explored in this thesis consists in performing experiments under different conditions of gravity: modifying g allows indeed to tune Ro independently of St and Re. In particular, micro-gravity experiments would allow to explore effects purely attributable to inertia, and those would then be systematically explorable by considering particles with various response time τ_p (tunable by changing the particle to fluid density ratio and/or particle size) without modifying any spurious competing effect associated to Ro. It would also become easier to explore Re effects at constant St.

Performing such micro-gravity experiments is however challenging and requires very specific facilities, such as space experiments in the ISS, parabolic flights or drop tower experiments.

Experiments in space conditions would be ideal as they allow to run experiments with unlimited amount of time of micro-gravity conditions, but opportunities are scarce and operation of experiment is complicated and hardly compatible with the ultra-high spatial and temporal resolution required to characterize particles dynamics in turbulence which require extremely controlled experiments. Parabolic flights are an interesting alternative and as a matter of fact the only two existing micro-gravity studies on the topic have been carried in parabolic flights (Fallon and Rogers, 2002; Hwang and Eaton, 2006). Parabolic-flights allow about 10-20 s of micro-gravity per parabola, and about the same of hyper-gravity. However, the limited number of flights and the limited number of parabolas per flight limit the possibility of a systematic exploration of parameter space with good statistical convergence. Drop tower experiments have a shorter micro-gravity duration (a few seconds), but it is long enough for particles with a response time of the order of $1/1O$ th of a second (what corresponds for instance to a water droplet of a few hundreds microns in air, or a millimetric metallic particle in water) to rapidly adjust to micro-gravity, while at the same time it is a light duty facility which allows to easily repeat experiments for a systematic investigation. In the present thesis a dedicated experiment has been built to be operated in the Dryden Drop Tower at Portland State University. It allows the 3D tracking of particles in a turbulent flow at a micro-gravity environment that lasts for approximately 2 seconds. This experimental setup yields $Ro \to 0$. Due to the Covid-19 pandemics, experiments could not be run yet.

Therefore, to complement the micro-gravity experiments, a different strategy based on the magnetic compensation of gravity has been developed. The advantage of magnetic compensation is that it allows to continuously tune the effective gravity $\tilde{g}$ to which particles are submitted (while micro-gravity experiments only allow to explore the 0-g situation). Magnetic compensation has been validated for the case of particles settling in a quiescent flow, showing that different settling regimes of magnetized particles can be selected by tuning the applied magnetic field. This is presented in Chapter 4. With the present facility effective gravity can be decreased down to about $0.46g$. Then a first series of experiments in turbulent conditions has been performed leading to first preliminary results on the influence of turbulence on settling terminal velocity when the Ro is continuously varied while St and Re are kept constant. Note that for a future comparison with the micro-gravity experiments to be carried, the exact same flow has been designed in both experiments. Results on turbulent magnetic compensation are presented in Chapter 5.

1.6 Thesis outline

In this thesis several aspects of the couplings between settling particles and fluids are explored among a broad range of control parameters $\{\beta, Ga, \Gamma, Re, d_p/\eta\}$. To achieve this, several experiments have been deployed. A broad outline of the experiments performed is laid out in Figure 1.9. Alongside with: particle Reynolds number Re_p; Taylor scale Reynolds number Re_λ; gravity acceleration $\tilde{g}$; particle shapes studied; and the Sections where the experimental details and results are presented for each configuration.
In particular, this thesis presents experimental studies of single inertial particles in two main water fluid configurations:

1. Quiescent Flow (first row of Fig. 1.9),
2. Turbulent Flow (second row of Fig. 1.9).

Additionally, an experimental technique to modify the local gravitational pull on magnetic particles, via the application of an external magnetic fields by six coils outside the water tanks, has been developed, validated, and applied to some cases on both fluid configurations (Figs. 1.9(b)-(c)). For the 1 mm spherical magnets here used, this method allows to reach any effective gravity value $\tilde{g}$ between 0.45g and 1g. In parallel, an experimental device that fulfils the constraints of the Dryden Drop Tower at Portland State University (USA), was designed and constructed (Fig. 1.9(d)).

In particular, the Quiescent Flow studies can be split in two subcategories:

- Creeping Flow (Fig. 1.9(a)).
  The angular and translational dynamics of single slender metallic rods settling were measured to experimentally validate the two models that include fluid inertia presented before: slender rod model and slender body theory.

- Moderate Reynolds Number Flow (Figs. 1.9(a-b))
  The settling of spherical and cubic particles in quiescent fluids were measured in wide range of the parameters space particle-to-fluid density ratio and Galileo number. In this way, numerical results predicting the different path instabilities' locations in the parameters space were contrasted with the experimental results. Additionally, the gravitational pull on the spherical particles was modified by the magnetic method presented in Section 2.4, as it was demonstrated by the possibility to modify the Galileo number (that depends on the gravitational acceleration), hence be at different regions of the parameters space and therefore have different particle trajectories.

The Turbulent Flow studies used the same turbulent flow: it consists in a cylindrical container filled with water and equipped with pumps at top and bottom whose jets collide in the tank centre to produce, to a good approximation, an homogeneous and isotropic turbulent flow with a well defined inertial range.
The turbulent experiments can be split in two categories:

- Ground Experiments
  The motion of single magnetic particles is tracked while the gravity is modified by the Magnetic Gravity Compensation method here developed. The goal is to disentangle the relative importance of Rouse and Stokes numbers in the dynamics.

- Drop Tower Experiments
  They will focus on diluted suspensions of non-magnetic inertial particles in micro-gravity conditions.

This thesis does not present experimental results from the Drop Tower configuration. It only contains the experiment's design and construction as I envisage to travel to the US facility at the end of 2021. The original plan was to travel in June 2020 but, mainly due to Covid-19, the trip was postponed a number of times. Nonetheless, I expect to have collected preliminary results by the time of my PhD thesis defence in December 2021.

The thesis is organised as follows: Chapter 2 presents the experimental devices and techniques used. The results for the settling of rods in a Quiescent Creeping Flow are presented in Chapter 3. Whereas Chapter 4 presents the results of particle settling in a Quiescent Flow, for both no magnetic field and the magnetic gravity compensation method. Finally, Chapter 5 presents the results of spherical particle settling in a Turbulent Flow.

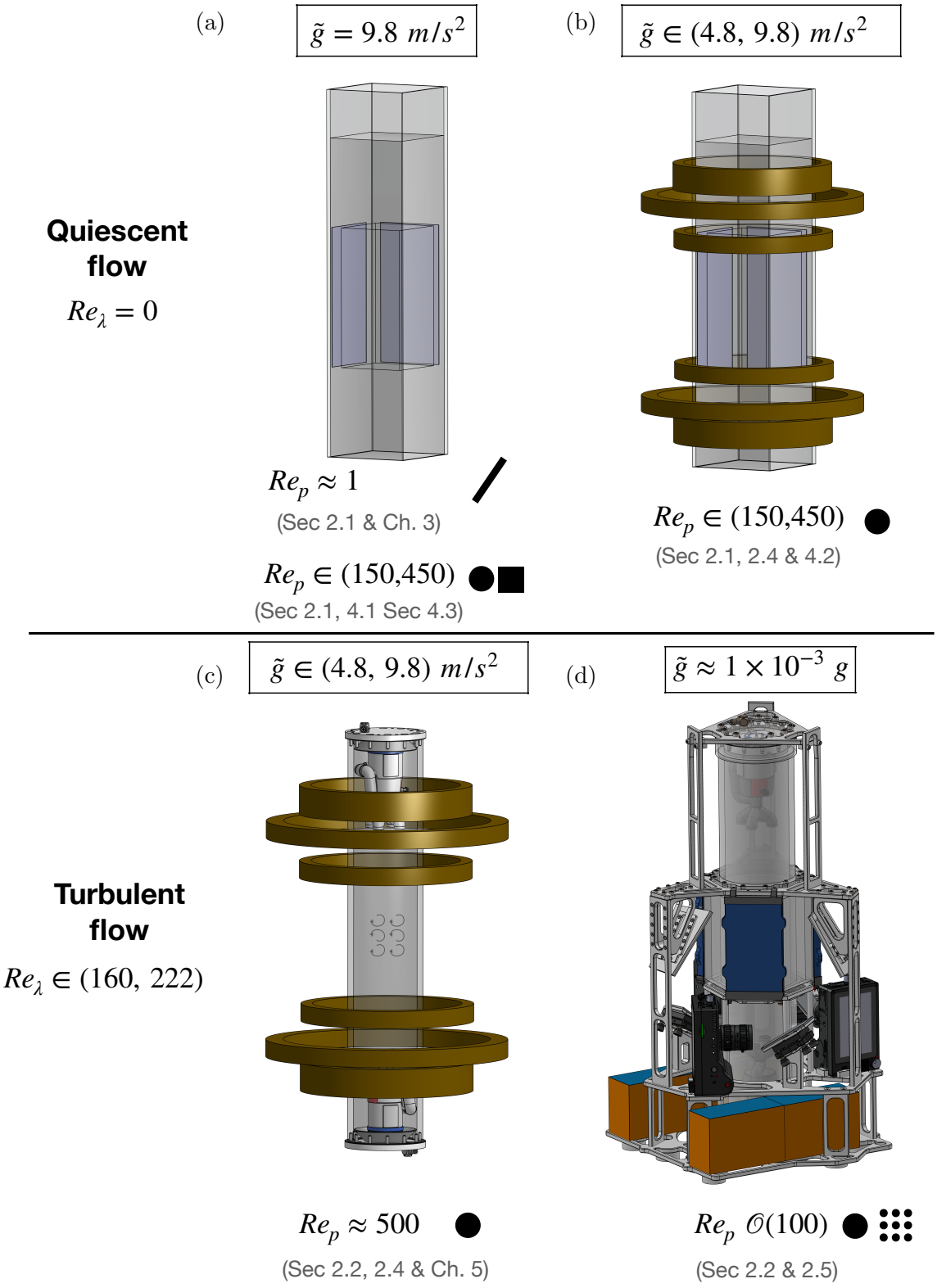

Figure 1.9: Qualitative outline of the experiments performed in this thesis. The first row represent the Quiescent Flow Experiments regarding rods at $Re_p \approx 1$ (a), spheres and cubes at moderate Re_p (a), and the magnetic gravity compensation method applied to spheres (b). The second row shows the Turbulent Flow cases ($Re_\lambda \neq 0$) here studied: single spheres at compensated gravity $\tilde{g}$ (c); single particle and suspensions at micro-g (d).

Chapter 2

Experimental Devices

As discussed in the introductory chapter, this thesis focuses on the experimental study of single particles settling in fluids. This study required the deployment of several experimental setups, measurements techniques and protocols which are described in this chapter. On one hand, we explore situations where the flow is Quiescent (see first line of Fig. 1.9) and the particle dynamics is controlled by the dimensionless parameters $\Gamma - Ga$. For the case of spherical magnetic particles in Quiescent flows at moderate particle Reynolds numbers, a Magnetic Gravity Compensation method (detailed in Section 2.4) is applied, primarily to vary the effective acceleration of gravity that the particles feel, thus modifying the effective Galileo number.
On the other hand, we consider Turbulent Flow situations with modified gravity (second line of Fig. 1.9) where the particle settling characteristics are controlled by $(\Gamma - Re_\lambda - St - Ro)$. In this case, the gravity is modified by both the Magnetic Gravity Compensation method and the use of a Drop Tower, in order to modify Ro independently from the other adimensional parameters.

2.1 Quiescent Flow Experimental Setup

The experimental details of the Quiescent Flow cases are detailed in what follows. First, Section 2.1.1 presents the devices used, whereas Section 2.1.2 details the methods and particles used, and the ways in which the control parameters of the problem were swept. Finally, Section 2.1.3 presents a summary of the experiments.

2.1.1 Experimental Setup

The water tank presented in this subsection was used to study:

1. the settling of slender particles in creeping flow (see Chapter 3);
2. the settling of spheres and cubes at moderate Reynolds number (see Chapter 4);
3. the validation and application of the method of Magnetic Gravity Compensation in the case of spheres settling in a Quiescent Flow (see Section 2.4).

These experiments are performed in a transparent PMMA tank with a square cross-section of 170×170 mm^2 and a height of 710 mm, represented in Figure 2.1. The tank is filled with different mixtures of pure glycerol (Sigma-Aldrich W252506-25KG-K) and distilled water. The glycerol concentrations range from 0% to 100%. The exact viscosity values of each mixture are measured with a rheometer, with an uncertainty of 3%, as explained in Section 2.1.2. In particular, the ranges of kinematic viscosities and fluid mass densities obtained are: $(1 \times 10^{-3}$,

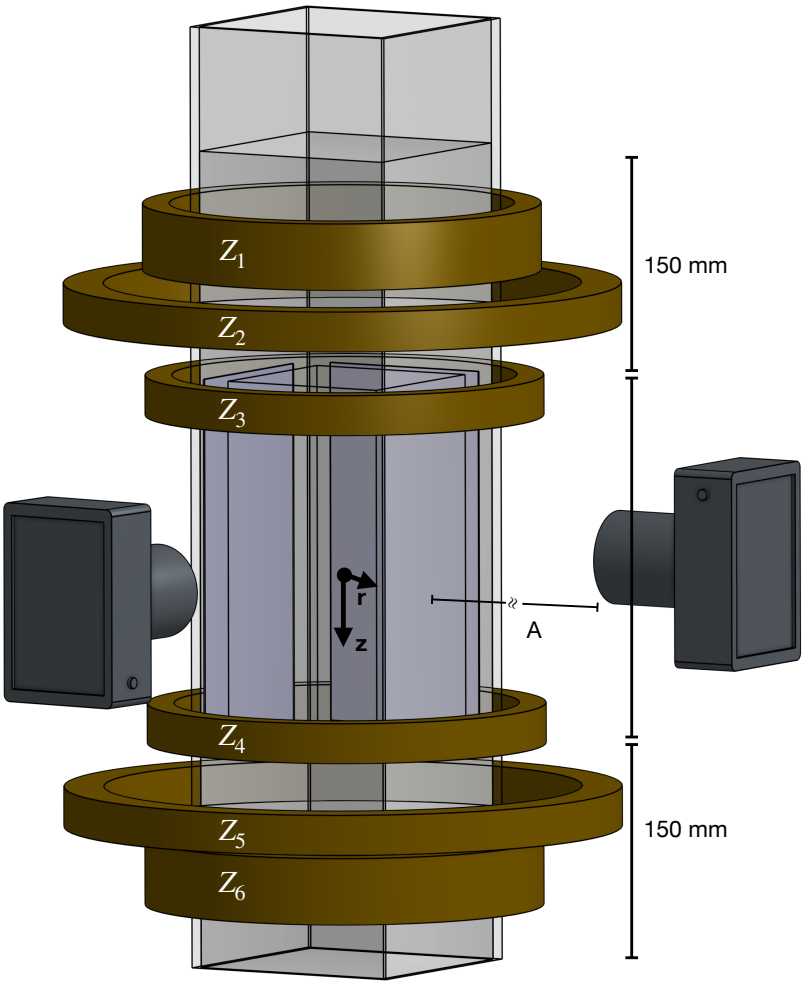

Figure 2.1: Experimental setup used to study the settling of both magnetic and non-magnetic single spheres, and slender bodies in a Quiescent Flow.

1.05) Pa.s and (1000, 1200) kg m^{-3}, respectively. Moreover, as the viscosity is dependent on the temperature, an air-conditioning system keeps a constant arbitrary room temperature around $(22 \pm 1)°C$, that yields a 5% variation in viscosity.

It is well known that the settling velocity of particles (i.e. their drag) is affected by finite size effects due to the size of the reservoir that contains them: a finite size container hinders the particle settling velocity. In a similar way to the drag (Brown and Lawler, 2003), a non-linear correlation for the wall factor $f(d_p/E, Re)$, with d_p the size of the particle and E the horizontal length of the container, is obtained using experimental data (Clift et al., 1978b). In this sense, a 150 mm region of fluid above and below the visualisation volume is set to ensure both the disappearance of any initial condition imposed on the particles and the effects of the bottom of the tank, that count also as wall effects. Furthermore, a minimum distance of 10 mm (slender bodies) and 20 mm (spherical-cubic particles) between the tank walls and the particles is maintained. In this configuration and using the correlations proposed by Chhabra et al. (2003), the settling velocity hindering is estimated to be lower than 5%, thus neglected.

To record the trajectory of the particles, two cameras model fps1000 from The Slow Motion Company point at the water tank with a resolution of 720 × 1280 px^2. These cameras allow the implementation of a 4D-LPT system that tracks the particle trajectory (see Section 2.3). These cameras have the advantage of a large internal storage capacity that allows to acquire 2 minutes recording at 2300 fps, in this way it is possible to make several realisations in a short period of time. The drawback is a triggering bug in the available camera prototypes that making the external hardware triggering nonoperational. To overcome this issue, an external optical synchronisation method detailed in the Appendix B was implemented.
To minimise perspective distortion of the projected contour of recorded objects (Huang et al., 1996; Toupoint et al., 2019), the cameras were installed *sufficiently* far from the sedimentation tank (see Section 2.3). As represented in Fig. 2.1, the cameras are set at 90° to make the 3D particle tracking more precise. The distance A to the exterior tank wall was modified in order to change the volume of the tracking region. Furthermore, to have better contrast between the particles and the background, a backlight illumination was used, with two white and homogeneous light panels are present in opposite sides of each camera. These are represented by the dark blue rectangles in the tank walls on Figure 2.1. These backlights were designed and built by the authors, as it is explained in Section 2.5.

	1	2	3	4	5	6
N	965	103	450	452	101	969
R (cm)	16.3	22.1	15.6	15.4	21.8	16.1
σ (cm^2)	15.6	3.9	3.6	3.6	3.9	15.6

Table 2.1: Characteristics of the coils used for the magnetic compensation of gravity. Columns show the following parameters for each coil used: number of turns N, radius R, and cross section σ. Each coil is represented by a number as done in Fig. 2.1

To produce the magnetic field used to modify the effective gravity feels by magnetized particles, a six-coil system has been put in place. This set of six coaxial coils is represented in Fig. 2.1, the coils are placed at distances Z_i ($i \in [1, 6]$) from the origin of coordinates, set at the middle distance between coils 1 and 6. The optimal positioning of the coils, in order to produce either a field as homogeneous as possible or a gradient of magnetic field as homogeneous as possible within the measurement volume, was estimated based on a numerical resolution of magneto-static equations with prescribed electrical currents in the coils. To simplify computations, each coil was modelled as an infinitesimal current loop. The effective number of turns and radius of the current loop that models each finite size coil is experimentally determined in the following manner: knowing the current input, the axial (r=0 in cylindrical coordinates) magnetic field

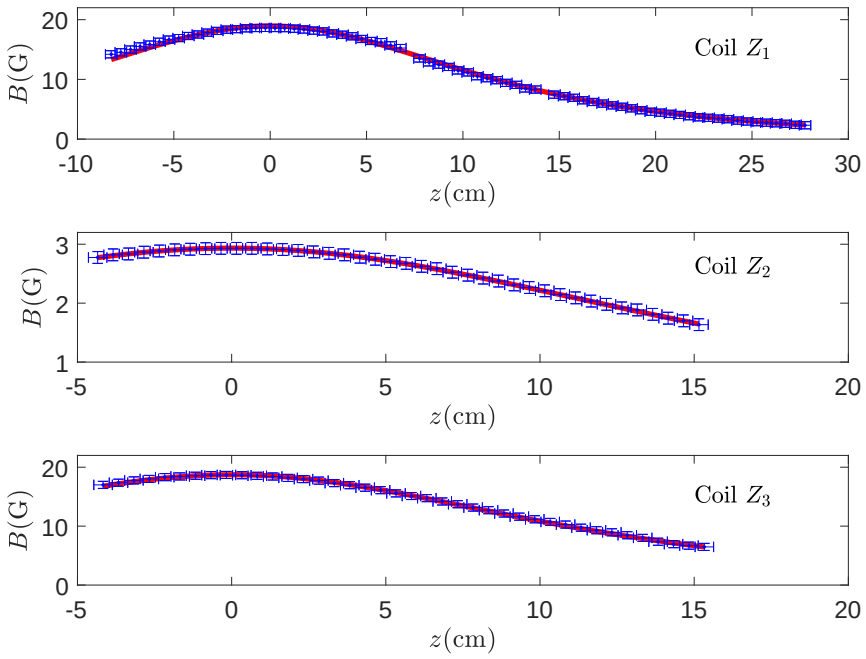

Figure 2.2: Magnetic field measurements (blue) and a non-linear fit by Equation 2.1 (red line), as a function of the distance z to the centre of each coil. Only the cases of Coils Z_1, Z_2, and Z_3 are presented, as the results for the remaining coils are analogous. Each coil was powered with $1A$ to produce this data.

as a function of the distance to the coil geometric centre was measured for each coil using a Teslameter Bell 7030. Later, the effective number of turns and radius are obtained via adjusting the measurements by the theoretical axial magnetic induction of a current loop of infinitesimal size:

$$B(z) = 2\pi 10^{-7} \frac{R^2 NI}{(z^2 + R^2)^{3/2}}, \tag{2.1}$$

with N the effective number of turns; R the coil radius; I the current (set to 1 A in the context of this validation); and z the distance from the coil geometric centre.
Figure 2.2 presents both the magnetic field measurements (blue) and the non-linear fit by Equation 2.1 (red line) as a function of the distance z to the centre of each coil, for only the case of Coils Z_1, Z_2, and Z_3 as the results for the remaining coils are analogous. Furthermore, the coils parameters are presented in Table 2.1. Moreover, the uncertainty on N and R by the aforementioned method is estimated to be 4% and 3%. Finally, the uncertainty in the coil's cross-section (each section length measured with a caliper) is 0.4 cm^2.

2.1.2 Protocol

The problems explored with this experimental setup are those of a particle settling in a Quiescent Flow. In Chapter 1, the dynamics has been seen to be controlled by two parameters: Galileo number (Ga) and particle-to-fluid density ratio (Γ). As it will be detailed in what follows, the Galileo number was swept by varying the fluid's viscosity and, when the Magnetic Gravity Compensation method is applied, the local gravity. On the other hand, Γ was modified essentially by changing the particle's material and to some extent also by the variation of fluid density between the different water-glycerol mixtures.

Fluid viscosity determination

In the Quiescent Flow experiments, the viscosity of the fluid where the particles are immersed is varied to change the Galileo number (or equivalently Reynolds number). In this context, the fluids are glycerol-water mixtures for which, although the viscosity of water and glycerol are known, the mixture viscosity can only be estimated *a priori* within an 10% error. This uncertainty comes from both the errors in the volume content of each liquid - consider that the mixtures have approximately 23 l; and the inherent uncertainty of the model (Volk and Kähler, 2018).
Measure the mixture's viscosity is then crucial to precisely know the Galileo number. There are a number of methods to measure fluid viscosity, as for instance the Capillary Viscometer that is based on the use of capillary tubes and the time it takes for a liquid to pass through the length of the tube. It is clear that the uncertainties in such a device where the time is, in general, taken by eye are considerable. The most widely used method is that of a rotational rheometer: it measures the shear stress τ (linked to the torque) required to turn an object in a fluid, for several shear rates $\dot{\gamma}$ (linked to the object's angular velocity). In this way, the functional form that relates the shear rate and stress can be measured. If the fluid is Newtonian, as it is the case here, the shear stress and shear rate are linearly related: $\tau = \mu\,\dot{\gamma}$, with μ a constant called the dynamic viscosity. The latter is a idealisation of the measurement situation: corrections due to the finite size sample size have to be made on the effective torque in order to extract the viscosity. All the necessary corrections are implemented in the software that accompanies the measurement device used, details in the PhD thesis of Ferrand (2017).
A photography of the rotational rheometer used in this thesis is shown in Figure 2.3(a). It is a Rheometer Kinexus ultra+, from Malvern industries, that allows to measure torques between $1\,\mathrm{nN}\cdot\mathrm{m}$ and $250\,\mathrm{mN}\cdot\mathrm{m}$ and angular velocities from $1\,\mathrm{rad\,s^{-1}}$ to $500\,\mathrm{rad\,s^{-1}}$, furthermore it can maintain a constant sample temperature with an error of $\pm 0.1\,^{\circ}\mathrm{C}$. In particular, the device allows to measure the entire viscosity range of the present mixtures, that is from pure water to pure glycerol: $1\,\mathrm{mPa}\cdot\mathrm{s}$ up to $1\,\mathrm{Pa}\cdot\mathrm{s}$.

There is a choice to be made regarding the geometry of the stator and rotor that will influence the presence of non-homogeneous sample behaviour. The set cone-plane configuration was chosen (see Fig. 2.3(a)) because it gives an homogeneous shear on the present viscosity range. Particularly, the cone's aperture angle is 178°, thus it seems planar. The viscosity is then obtained from a shear rate - shear stress plot, as presented in Figure 2.3(b). Although not evident in the figure, at low shear rates the fluid is not stabilised, i.e. the plot is exactly a linear function as it should be for the present newtonian fluids. Therefore, the dynamic viscosity is the slope of a linear fit to the end of the plot, as represented by the blue line in the Figure. The uncertainty on the linear fit's slope (i.e. the dynamic viscosity μ) is, for all cases, smaller than 3%. Furthermore, for all measurements, a shear rate in the range of $(0.5, 200)\ 1/s$ is imposed by the rheometer on the samples, as it was empirically seen to be a good setup for the measurement.

This device measures the dynamic viscosity μ. To know the kinematic viscosity $\nu = \frac{\mu}{\rho_f}$, it is also required to determine the fluid density ρ_f. Note that, besides, ρ_f is an important parameter here for the investigated problem (particle settling) for which $\Gamma = \rho_p/\rho_f$ is a key parameter. The density of the fluid is measured by taking a 50 ml sample and measuring its mass with a $1 \times 10^{-3}\,\mathrm{g}$ precision, yielding a density uncertainty of $2 \times 10^{-1}\,\mathrm{g\,l^{-1}}$.

The procedure to obtain a desired dynamic viscosity μ is the following:

- the volume fraction of water and glycerol required to obtain the desired viscosity are computed using a model (Volk and Kähler, 2018);
- the water tank where the experiments take place is filled, with the two liquids at the corresponding volume fraction, with a precision of 0.05 l (over a total volume of 23 l);

(a) (b)

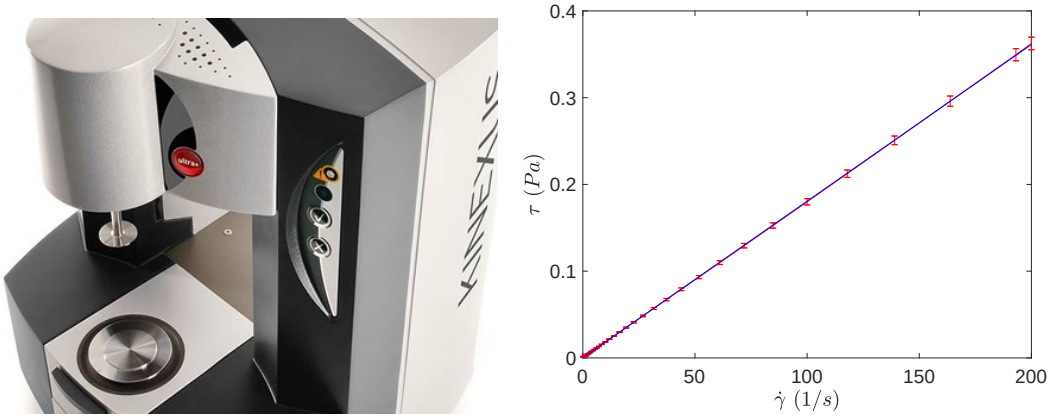

Figure 2.3: (a) Photography of the Rheometer Kinexus ultra+, from Malvern industries. It is possible to see the circular plane base where the sample is placed, and the upper spinning cone that imposes the shear rate. Note that the cone's aperture angle is 178°, thus it seems to be planar. (b) Typical Shear stress (τ) as a function of Shear rate ($\dot{\gamma}$), alongside with a linear fit whose slope is the dynamic viscosity μ.

- the mixture is stirred for approximately 120 s until the optical properties of the liquids are equal (i.e. the mixture is transparent);
- after waiting for a minimum of 5 hours for equilibrium, a 5 ml sample is removed and the viscosity is measured as it was previously laid out.

The goal in the experiments with Quiescent Flows (at moderate Reynolds number) is to explore Galileo number effects for a given class of particles. In the non-magnetic cases the viscosity is varied to modify Galileo number. In this sense, the experiments start with the higher derived viscosity (i.e. the higher glycerol concentration) which is then diluted by adding water. In particular, the procedure in the case of a mixture already present in the water tank takes the following form:

- the mixture's measured viscosity and mass density are set on the model (Volk and Kähler, 2018) to obtain the composition required to get a viscosity μ;
- the additional water is added;
- the new mixture is stirred and left to reach equilibrium;
- the new mixture viscosity is measured.

This process is repeated until the target viscosity is achieved.

Particles

- Size & Shape
  The particle's dimensions and shapes were measured using a microscope with a precision of 10 μm. In particular, no deviation from the spherical (cubic) form or the documented diameter (side length) could be measured for all the spherical (cubic) particles used here. Moreover, as the metallic rods (for the study of settling of slender bodies in creeping flow) were cut by hand there is a scatter of 0.5 mm (corresponding to less than 5% of their length) in their total length while their cylindrical shape is preserved.

- Density
  The particle's mass is measured with a precision of 1×10^{-3} g via a standard laboratory scale. By using the particle size, the volume is computed and thus the particle densities and particle-to-fluid density ratios.

- Roughness
  The surface roughness of particles have been proved to influence the boundary layer

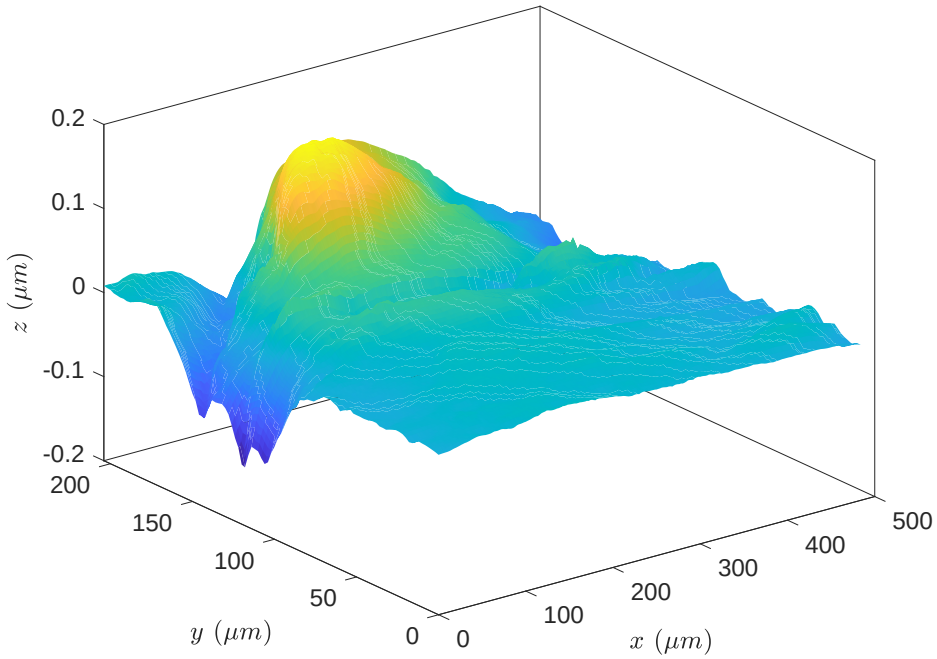

Figure 2.4: The surface of a 1 mm diameter spherical metallic particle (Particles M) over an area of $200 \times 500\mu m^2$, measured with a Scanning Electron Microscope.

around them, therefore modifying several aspects of the dynamics: for example, a particle suspension's rheology where the viscosity can be increased up to several tens percent with only a relatively small roughness (Rampall et al., 1997; Tanner and Dai, 2016; Zhao and Davis, 2003).
It is thus important to know the surface roughness of the particles here used. This is achieved using a Scanning Electron Microscope to probe a fraction of the surface (S) of a typical particle used for each experiment. With a coordinate system where z is normal to the surface, the surface roughness is quantified by the arithmetical mean height Ra, defined as:

$$Ra = \frac{1}{S} \iint_S |Z(x,y) - \bar{Z}(x,y)| \, dS,$$

where S is the fraction of the particle's surface imaged and $Z(x,y)$ the sample height profile. Ra then measures the average deviation from the mean surface value $\bar{Z}(x,y)$.
The local surface height was measured with a Scanning Electron Microscope (SEM) model ZEISS SUPRA 55 VP. This device produces an electron beam that collides with the sample, and the result of the interaction is measured to reconstruct the sample's 3D profile. Note that the measurement of non-conductive samples is problematic as the electrons are absorbed by the sample and contribute to its electrostatic charge. This problem was circumvented by using a *low* voltage difference between the plate holding the sample and

the beam.

As an example, the surface of a 1 mm spherical metallic particle (denoted Particles M in the sequel) is presented in Figure 2.4. Particularly, a positive and negative peak of height 1.5×10^{-1} µm are present on this particle surface. The arithmetical mean height in this case is Ra=50 µm. Furthermore, an area of $200 \times 500 \mu m^2$ is scanned for all cases. Values or $Ra/d_p < 5 \times 10^{-2}$ can be considered small and they are not expected to modify the dynamics in a considerable way Zhao and Davis (2003), although the literature is not extensive in this regard.

2.1.3 Summary

Table 2.2 presents the characteristics of the particles here used. In particular, it presents: particle's material, density (ρ_p), volume, arithmetical mean height (Ra), magnetic moment ($|\mathbf{M}|$), and the corresponding experimental setup where it was applied: QF and TF represent Quiescent Flow and Turbulent Flow, respectively. Whereas the magnetic spheres were only used in the application of the Magnetic Gravity Compensation Method.

With these tools, particle-to-fluid density ratios Γ between 1.1 (polyamide spheres at moderate

Material (shape)	ρ_p (kg/m^3)	Volume (mm^3)	Ra(µm)	$\lvert\mathbf{M}\rvert$ (Am^2)	Exp. Setup
Tungsten (rods)	14800	$(16\ \&\ 8)\times(\pi 0.5^2)$	15	0	QF creeping
Neodymium (spheres)	8200	$(4/3\pi) \times 0.5^3$	15	4.6×10^{-4}	QF & TF
Neodymium (cubes)	8200	$1 \times 1 \times 1$	15	0	QF
Metal (spheres)	7950	$(4/3\pi) \times \{0.5^3, 1^3, 1.5^3\}$	9	0	QF
Glass (spheres)	2500	$(4/3\pi) \times 1.5^3$	15	0	QF
Polyamide (spheres)	1150	$(4/3\pi) \times 3^3$	120	0	QF

Table 2.2: Properties of the different investigated settling particles. The rows present the different particle materials studied. Whereas the columns show: particle mass density (ρ_p); volume; average arithmetic roughness (Ra); particle's magnetic moment ($|\mathbf{M}|$); and the experiments where each particle was used. The notation for the experiments reads: QF – Quiescent flow, and TF – Turbulent flow.

Re) and 13 (rods in creeping flow) are achieved. While the Galileo number varies from 100 to 350 in the moderate Re case, and it is lower than 1 in the creeping flow case.

In the particular case of the application of the Magnetic Gravity Compensation method (detailed in the forthcoming Section 2.4) to the problem of spheres settling in a Quiescent Flow at moderated Reynolds, the parameters ($\Gamma - Ga$) were swept differently. In the other cases, Γ is varied by changing the particle material, whereas Ga by modifying the fluid's viscosity. In the Magnetic Gravity Compensation method, the particle-to-fluid density ratio Γ is constant as only the neodymium spherical particles are used. On the other hand, the fine tuning of Galileo number is not performed by changing the fluid's viscosity but by modifying the effective local gravity g^* defined as the combination of actual gravity and the vertical component of the magnetic force (one of the challenges of the technique relies on the capacity to produce a homogeneous magnetic compensation over the measurement volume, what will be detailed later on). In this case Galileo number depends on the gravity acceleration: $Ga = \sqrt{|\Gamma - 1|\tilde{d}_p \tilde{g} d_p}/\nu$. With the available coils, this method allows the gravity to be diminished to 49% of 9.8 m s^2, therefore Galileo number can be varied a ratio of in $\sqrt{0.49} \approx 0.7$ (i.e. a reduction 30%). Thus, with the available coils, it is not possible to sweep Ga in a range between 100 and 300 only by varying the gravity. It is therefore used a combination of magnetic compensation and viscosity variation, one of the goals being to explore whether it is equivalent to change Ga in one way

or the other, hence still validating the general principle of magnetic control of gravity effects on settling properties. In this sense, 9 different fluid viscosities were set (in the same fashion explained before), and for each of them the gravity was further magnetically modified to yield different Galileo numbers.

2.2 Turbulent Flow

The main goal of the turbulent experiments performed is to explore the effect of gravity on certain aspects of particle/turbulence interactions (in particular on the turbulent hindering or enhancement of settling) when all other parameters are kept constant. In terms of control parameters, the goal was therefore to be able to vary Ro while keeping Γ, St and Re constant. The turbulent water flow here presented was therefore designed and constructed to respect the constraints imposed by the Dryden Drop Tower (see Section 2.5). Furthermore, it was also designed to be compatible with the magnetic compensation experiments. It therefore needed to have the least amount of magnetic materials that would distort the Magnetic Gravity Compensation method (Section 2.4). In this sense, the only magnetic materials there present are the pump's rotors that are *far away* from the measurement region and therefore assumed to not influence the method.
The experimental details of the Turbulent Flow studies are detailed in what follows. First, Section 2.2.1 presents the devices used, whereas Section 2.2.2 details the flow characterisation techniques and particles used. Finally, Section 2.2.3 presents a summary of the regimes attained in this thesis.

2.2.1 Experimental Setup

The flow presented in this Section is the only turbulent flow that was developed or used in this thesis. It is used to study the turbulent transport of inertial particles (in the context presented in Section 1.5) in two configurations:

1. the settling of heavy magnetic spherical particles ($\Gamma = 8.2$) in environments with effective gravity $\tilde{g} \in (4.8, 9.8)$ m/s^2 (results in Chapter 5), achieved by the Magnetic Gravity Compensation method to be detailed in Section 2.4;

2. the dynamics of inertial spherical particles ($\Gamma \in [1.1, 8.2]$)) in a micro-g regime reached in the Dryden Drop Tower (see Section 2.5).

Figure 2.5 presents the cylindrical PMMA water tank of internal diameter 11 cm, height 70 cm, and thickness 5 mm, where the turbulence is generated. The tank is sealed on top and bottom by PMMA disks, tighten to the cylinder by 12 screws and a Nitrile joint. The tank is completely filled with filtered water with a measured viscosity of $\nu = (0.70 \pm 0.05) \times 10^{-6}$ m^2/s at 33 °C. Furthermore, to eliminate the air usually present in water the tank is connected to a circuit of initially hot water ($\approx$ 70 °C) by pipes connected to the nozzles top of the tank's lids (see Fig. 2.5). The hot water circulates through: the tank; one filter; a water pump; and an expansion tank (i.e. a water tank with a free surface). The water then circulates until it cools down to room temperature, and all the air bubbles in the fluid's bulk were released to the ambient in the expansion tank. Then the circuit is closed and the water inside the tank is air-free.
Note that the water temperature when performing experiments varies around (35 ± 4) °C, due to the power injection as no thermal regulation is present.
The Turbulent flow is produced at the tank's centre as a result of the interaction between two counter-facing water pumps at a distance of 40 cm powered with: 12V (nominal power input); 15V; and 18V. The input voltage variation aims to vary the turbulence intensity (i.e. Re_λ). The

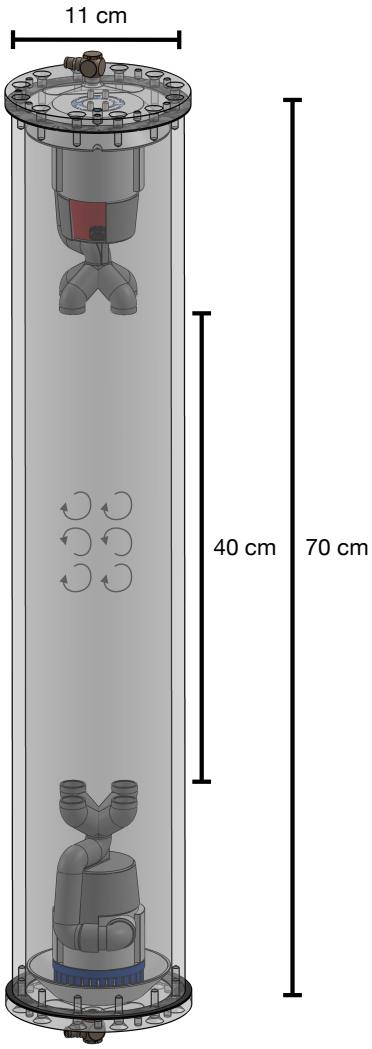

Figure 2.5: Water tank used in the Turbulent experiments. Rendered image of the cylindrical PMMA tank of internal diameter 11 cm and height 70 cm. Additionally, two pumps with 4 jets at each extreme generate a turbulent state in the centre of the tank.

pump's model is "Bilge Pumps rule – Model 25DA". The single jet produced by each pump is ramified into 4 jets thanks to a 3D printed jet divider (see Fig. 2.5), the nozzles of the two jet dividers are put in counter-phase, i.e. the nozzles on the upper pump point to the voids between those on the bottom. The latter and the optimal distance between the pumps are the result of an empirical exploration of different configurations detailed in Subsection 2.2.2.

The setup for the experiments where the gravity was compensated via the Magnetic Gravity Compensation method (see Section 2.4), consists in the cylinder in Fig. 2.5 placed inside the rectangular water tank used for the Quiescent Flow Experiments (see Fig 2.1). This was necessary to correct the distortions that a curved air-water interface produces. By inserting the cylinder inside the squared water tank, and filling it with the same liquid inside the cylinder, the air-water interface is now planar and the curved interface is an interface PMMA-water. As the PMMA's and water's index of refraction are very similar (1.4 and 1.33), and the thickness of the cylinder is 5 mm, the PMMA-water interface does not considerably distort the light rays. Furthermore, by taking further advantage of the Quiescent Flow Setup, the same 2-camera system was used to track the settling of particles, as explained in Section 2.1.

In this thesis only results from single particle settling are going to be presented. While results in the case of particle suspensions and micro-gravity are left to be obtained after the writing of this thesis. Nonetheless, the experimental device for the Drop Tower Experiments was built and tested (in ground), and it will be presented in Section 2.5. Note that the same cylinder, and therefore the same turbulence characteristics, is used to both the micro-gravity and Magnetic Gravity Compensation experiments. In this sense, direct comparisons can be made.

2.2.2 Protocol

For the optimisation of the distance between the pumps, tests with 2 pumps (with one that could be moved to change the pump-to-pump distance) in a tube, inside an already set facility equipped with 2D-PTV (in a laser plane) were performed. Later on, when the distance between pumps of 40 cm was chosen, a detailed final characterisation was performed with a Particle Imaging Velocimetry setup.

Flow optimisation – 2D Particle Tracking

The distance between the pumps and their relative orientation needed to be chosen. The proximity of the indirectly measured Eulerian second order structure function to the scaling $D_0^{2/3}$ (with D_0 the initial pair separation) was used as the criteria to decide which configuration was best (i.e. closer to an homogeneous and isotropic flow). This indirect measure was done by a 2D Particle Tracking method and the Pair Dispersion dynamics, detailed in what follows. These tests were done for distances between pumps in the range of 30 cm and 65 cm, with a step of 5 cm, for the two jet dividers nozzles configurations: phase and counter-phase. The counter-phase nozzles and a distance between pumps of 40 cm were found ideal.

The 2D Particle Tracking method consists in seeding the flow with tracer particles (200 μm polyethylene particles), illuminate the region of interest with a laser sheet and track the particles that are in the laser sheet, i.e. that reflect the light. A green laser opus 532, from Laser Quantum, with a wave length beam of 532 nm and (1.85 $\pm$0.2) mm of diameter is used. It is operated at 2.5 W (empirically found to be the optimal intensity). The beam is converted into a sheet using a light guiding arm 80X39 from Dantec Dynamics. These result on a laser sheet less than 1 mm thick. Additionally, the particles are tracked by a single camera Phantom V12 placed orthogonal to the laser sheet. In particular, the image acquisition is done at 1200 fps and 100 μs of exposure.

The particles' trajectories tracked in this configuration allow the application of the well know results for particle dispersion (in particular relating the ballistic mean square separation of

pairs to second order Eulerian structure function) in Homogeneous and Isotropic Turbulence (HIT) to obtain characteristics of the underlying turbulent flow, such as: the energy dissipation ϵ, the Kolmogorov scale η, the integral scale L, the associated time scales, and the second order structure function S_2 (Bourgoin, 2015). The method is based on the measurement of particle's pair distances $\mathbf{D}(t)$, from an initial pair separation $\mathbf{r}$. In particular, the fact that in the ballistic regime (valid at *short* times) the mean-square pair separation follows $\langle|\mathbf{D}(t)-\mathbf{r}|^2\rangle = 2\times S_2^l(r)t^2 = \frac{8}{3}C_2(\epsilon r)^{2/3}t^2$, is used to indirectly measure the longitudinal structure function S_2^l. The Pair Dispersion dynamics is detailed in the Appendix A.
The use of pair dispersion to obtain S_2 is convenient with this kind of experimental setup that yields particles' trajectories: if one would like to compute S_2 by its definition, the velocity should be computed numerically from the trajectories, adding a new layer of uncertainty and complexity. In the context of this thesis, this method was used only in this prototyping stage of the turbulent flow. Figure 2.6 presents second order longitudinal structure functions computed

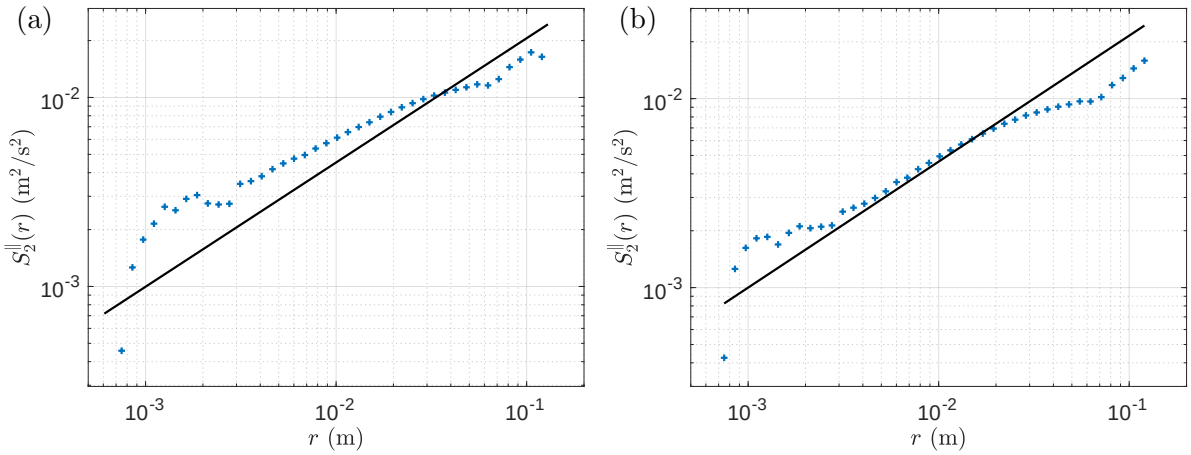

Figure 2.6: Second order longitudinal structure functions for two different distances between pumps. (a) presents the result when the pumps are separated by 35 cm, whereas in (b) the distance is 40 cm.

from the Pair Dispersion dynamics in the inertial range (Appendix A). In particular, sub-panel (b) presents the result for the optimal setup found: nozzles in counter-phase and a distance between pumps of 40 cm. While sub-panel (a) presents the case of nozzles in counter-phase and a distance between pumps of 30 cm. The second order structure function in this sub-panel does not present a $r^{2/3}$ scaling at inertial scales. This can be due to the presence of a strong mean flow structure, as observed for instance in turbulent convection (Liot et al., 2019) where large scale circulation is found to affect usual inertial scalings. Although Liot et al. (2019) show that subtracting this mean flow can effectively emphasize classical inertial law for the fluctuations, it is wise to attempt to minimize it. On the other hand, sub-panel (b) (corresponding to the flow produced when the pumps are farther away from each other) well described by the usual scaling of homogeneous and isotropic turbulence in the inertial range. Therefore the configuration of sub-panel (b) is used in all the turbulence experiments presented in this thesis. As it will be shown later, some mean recirculation still remains in this configuration, but it does not significantly affect inertial scale fluctuations.
It is worth to remark that distances up to 55 cm present a similar inertial range to that of Figure 2.6(b). Due to the experimental limitations imposed by the Dryden Drop Tower, the shorter distance between pumps was chosen.

Flow characterisation – Particle Imaging Velocimetry (PIV)

The inertial and large scales of the final facility have been fully characterised using Particle Imaging Velocimetry (PIV). Knowing the turbulence characteristics is crucial. On one hand, three of the adimensional numbers that control the problem of interest ($Ro - St - Re_\lambda$) depend on turbulence characteristics such as energy dissipation rate and integral scale. Therefore it is key to know these parameters to determine the regimes explored. On the other hand, a fine measure of the vertical mean flow $\langle u_z(\mathbf{x})\rangle$ at the position $\mathbf{x}$ (i.e. the large scale flow) is crucial to determine the actual relative particle settling velocity $W(\mathbf{x}, \mathbf{t}) = v_z(t) - \langle u_z\rangle(\mathbf{x}(t))$, where $v_z(t)$ is the instantaneous measured vertical velocity of the particle and $\langle u_z\rangle(\mathbf{x}(t))$ is the mean vertical flow at the position $(\mathbf{x}(t))$ of the particle.

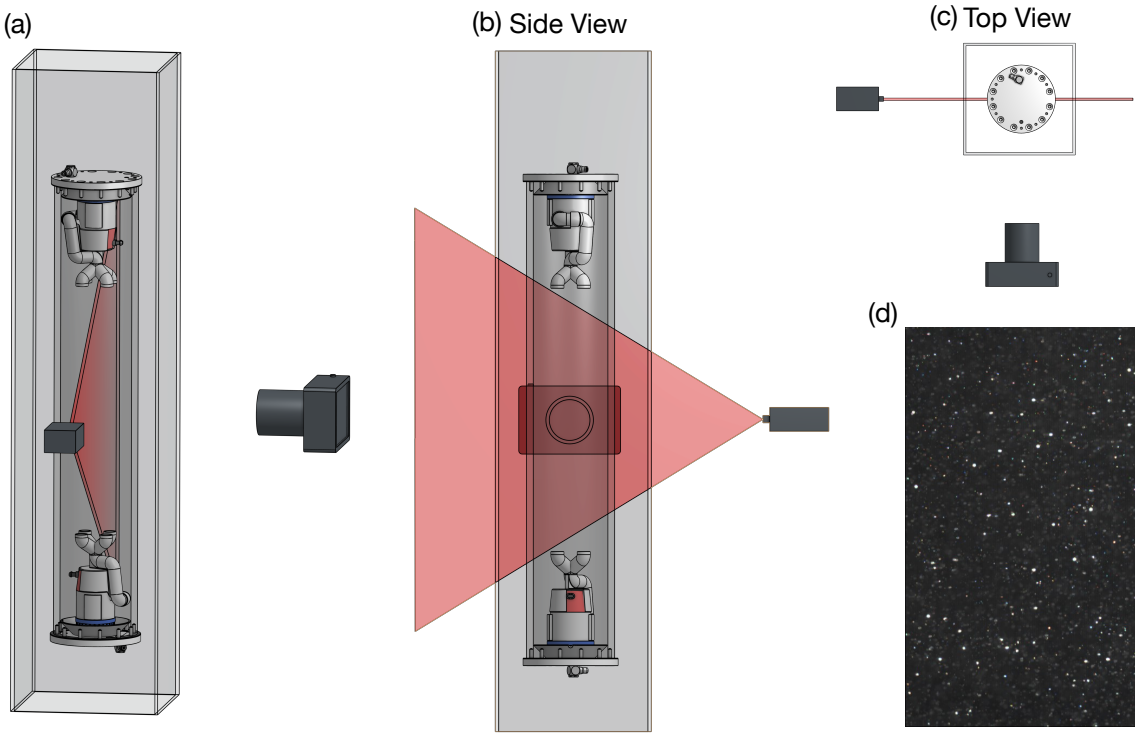

Figure 2.7: Particle Imaging Velocimetry setup. The cylinder where turbulence is generated is placed inside the square tank used for the Quiescent Flow experiments, to avoid image distortion. A laser generates a light sheet in the tank's centre and the particles in the sheet are detected by the camera. (d) presents a portion of a typical image, where the white dots are the particles in the laser sheet.

The Particle Image Velocimetry method yields the Eulerian velocity field $\mathbf{u}$. It consists in dividing the images into small portions named interrogation areas (IA); then, the IA of two successive images are cross-correlated with each other; and the correlation produces a vector that represents the particle displacement. Thus one measures the particle displacement and, dividing it by the time difference between each frame, the velocity vector is obtained at each IA. Furthermore, via interpolation, the velocity can be known with sub-pixel precision (Adrian, 1991; Discetti and Coletti, 2018).
The PIV processing was performed using an open-source MATLAB code called UVMAT (Legi Grenoble). The UVMAT algorithm first performs PIV processing of the images from a single camera using a dual-pass method where the first pass determines lower-resolution estimates of

the velocity field within an IA, whereas the second pass uses the estimates from the first pass to obtain more precise measurements of the velocity field at a higher resolution. Furthermore, the PIV data analysis is done using an open-source MATLAB code called PIVMat (PIVMat, 2015).

In particular, Figures 2.7(a-b-c) present the experimental setup for the application of PIV. The cylinder where turbulence is generated is placed inside the square tank used for the Quiescent Flow experiments in order to avoid image distortion (i.e. to have a planar air-water interface). A continuous Laser diode module, with a wave length of 450 nm (blue) and a optical power of 5W, with a Powell lens generates a light sheet with a thickness of approximately 2.5 mm in a vertical plane placed in the tank's centre. The flow is seeded with tracer particles of Polyethylene with an average diameter of 200 μm yielding a response time $\tau_p \approx 1 \times 10^{-3}$. One camera, orthogonal to the laser-sheet, model fps1000 from The Slow Motion Company is set with a resolution of 720×1280 px^2 and an acquisition frequency of 3200 fps. Sub-panel (d) presents a portion of a typical image, where the white dots are the particles in the laser sheet. The correlation was computed between two successive images separated in 1/3200 s = 0.3125 ms $= 0.0375\tau_\eta$. This time lag is estimated to be sufficiently short for the correlation to be well defined. The PIV analysis were made over 4000 pairs of images distributed over a temporal window of several minutes to ensure a good statistical convergence: it is concluded that this amount is enough as the PIV analysis over 3000 pairs of images yields the same results.

Large Scale Properties

- Mean Flow & Velocity Fluctuations

The first column of Figure 2.8 presents the PIV results for the mean flow in the centre plane, where the arrows denote the flow direction and the colour map shows the fluid velocity absolute value in meters per second. On the other hand, the second column presents the velocity standard deviation fields. Each row denotes the three different power inputs on the pumps: 12V – sub-panels (a); 15V – sub-panels (b); 18V – sub-panels (c). Note that in this reference system, gravity is horizontal and oriented to the left.
Regarding the mean flow, note how the velocity vectors in sub-panels (a.1-3) are qualitatively oriented in the same directions for all power inputs, whereas the velocity norm (see the colours) increases with it: from a maximum value of 0.22 m/s at 12V, to 0.28 m/s at 18V. This shows the presence of a robust and statistically stationary mean recirculation flow, probably resulting from the interaction between the jets of top and bottom pumps. The standard deviation on the other hand shows a mild horizontal inhomogeneity (in particular near the the right border of the measurement area) and a good vertical homogeneity. The spatially averaged mean flow is then 11.2, 12.2, and 15.8 cm/s, for 12V, 15V, and 18V, respectively. Whereas the velocity standard deviations are 8.63, 10.7, and 12.3 cm/s, for 12V, 15V, and 18V, respectively, leading to a turbulence rate $\sigma_u/\langle u \rangle$ of the order of 80%. As it will be seen later, once subtracted the presence of the mean field does not have a major impact on inertial scale fluctuations which do exhibit reasonable homogeneous and isotropic behaviors.
Figure 2.9 presents the difference between the normalised mean flow and velocity standard deviation fields when the power driving the pumps is varied. The first column presents: $\frac{\langle u^{15V \text{or} 18V} \rangle}{Max(\langle u^{15V \text{or} 18V} \rangle)} - \frac{\langle u^{12V} \rangle}{Max(\langle u^{12V} \rangle)}$. Whereas the second one shows: $\frac{\sigma_{u^{15V \text{or} 18V}}}{Max(\sigma_{u^{15V \text{or} 18V}})} - \frac{\sigma_{u^{12V}}}{Max(\sigma_{u^{12V}})}$. These are a quantification of how the mean spatial fields evolve with the power input in the pumps. For the case of the mean flows (first column), it can be seen that the mean field relative to its maximum is an 8% larger for the 15V case than the 12V case, whereas in the case of 18V the percentage grows up to 11%. In this sense, varying the power input does not significantly modify the topology of the large scale mean recirculation. An equal

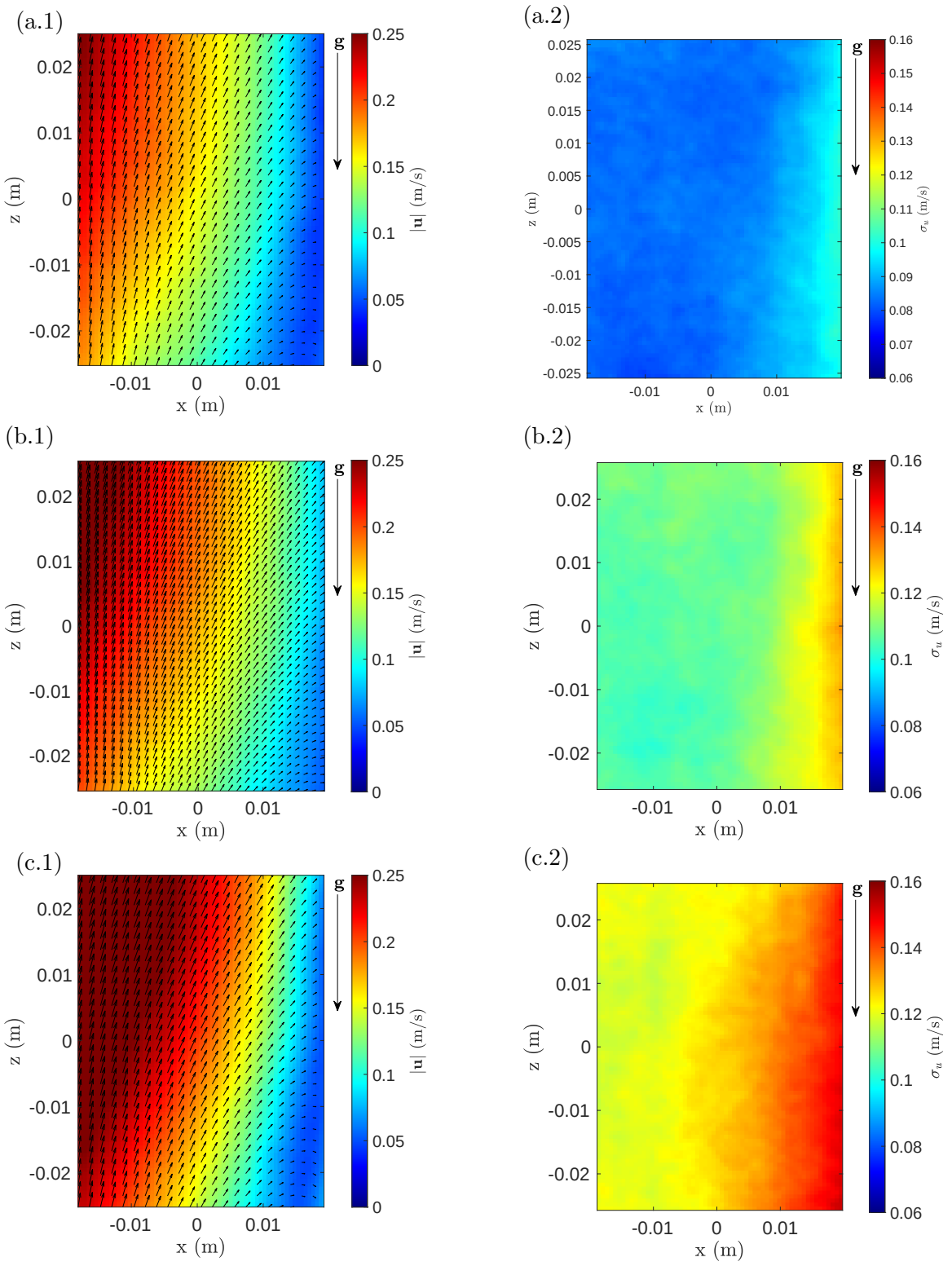

Figure 2.8: Mean velocity field (first column) and velocity standard deviation (second column) for the three different power inputs in the pumps: 12V – sub-panels (a); 15V – sub-panels (b); 18V – sub-panels (c). Note that gravity is pointing downwards.

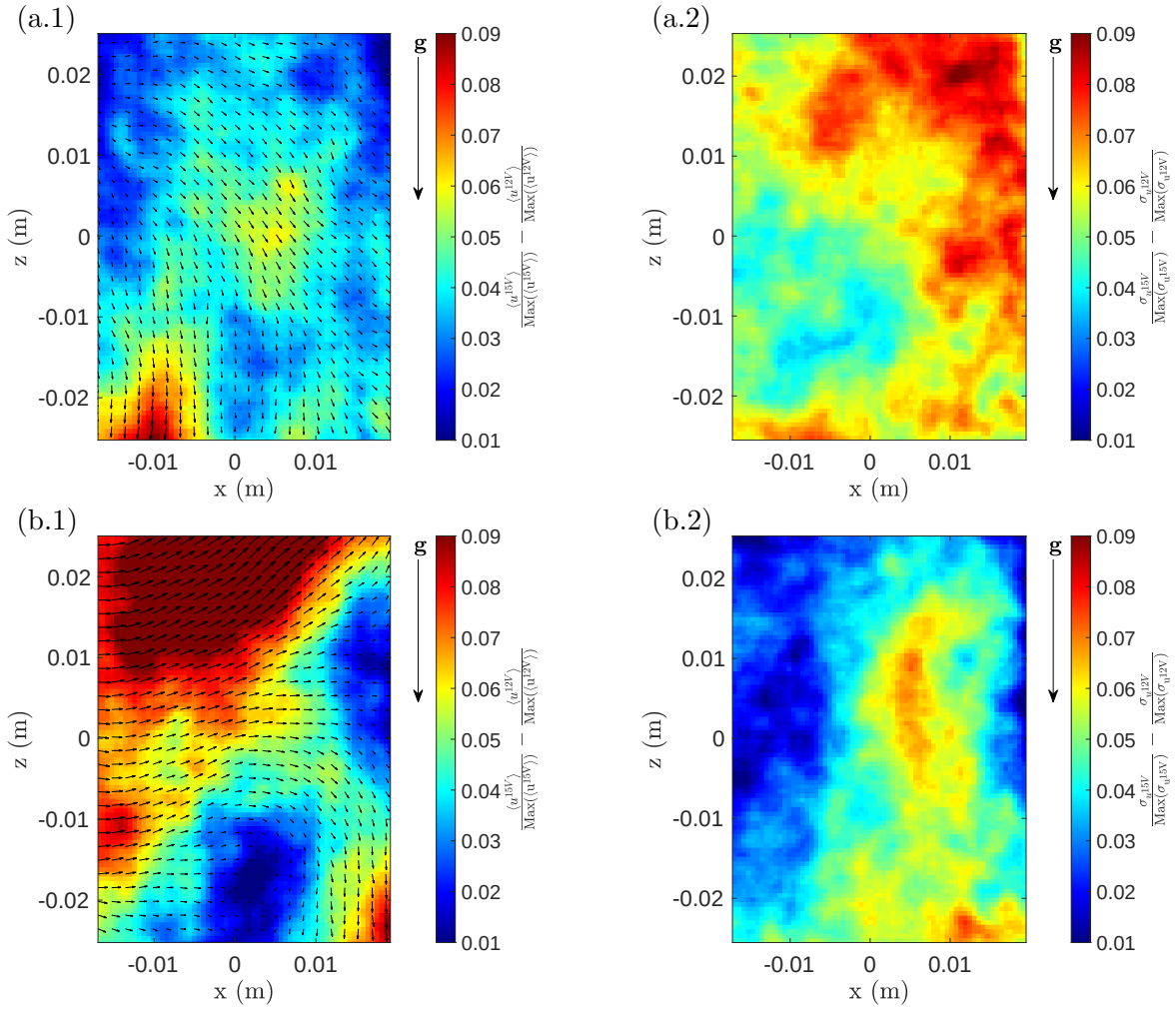

Figure 2.9: Difference between normalised fields. The first column shows the subtraction of the normalised mean flow fields: 12V-15V (sub-panel (a.1)) and 12V-18V (sub-panel (b.1)). Whereas the second column presents the same operations but over the velocity standard deviation fields: 12V-15V (sub-panel (a.2) and 12V-15V (sub-panel (b.2). Note that gravity is pointing downwards.

conclusion can be made for the relative fields of velocity standard deviation.

As it is crucial to know the vertical mean flow to obtain the particle's relative settling velocity and as the particles do not settle always in the centre plane, knowing the mean recirculation in the central plane just presented is not sufficient and the 3D mean vertical velocity field is needed in the entire domain where particles trajectories are recorded.

The previous analysis of the flow's large scales properties was done with the laser sheet in a vertical plane placed at the geometrical centre of the cylinder. In order to measure the flow's large scale inhomogeneity in space, the same measurements were performed, for the 12V case, in two additional parallel planes: 17 mm closer to the camera (i.e. away from the cylinder's axis); and 17 cm farther from the camera. That resulted in mean velocity field measurements (analogous to those presented in Fig. 2.8 for the centre plane) in three planes that span a 34 mm in the direction perpendicular to gravity. An estimation of the 3D mean vertical velocity at position of the particle $\langle u \rangle(\mathbf{x}(t))$ is then constructed by linearly interpolating the regions between the aforementioned planes. In particular the relative vertical velocity can be constructed: $W(\mathbf{x}) = v_z(\mathbf{x}) - u_z(\mathbf{x})$. Note that these 2D-2C PIV measurements only give access to 2 components of the flow velocity field, it is not possible therefore to fully correct the 2 horizontal components of particles velocity v_x and v_y. The fact that the flow in the cases of the pump's power inputs 15V and 18V do not differ greatly from that of 12V simplifies the situation. In particular, it allows to use the aforementioned mean flow interpolation for the 15V and 18V cases, scaled to match the maximum mean flow value of each case: for instance, the 15V interpolation equals that of 12V multiplied by $\frac{Max(u_z^{15V}(\mathbf{x}^{centre}))}{Max(u_z^{12V}(\mathbf{x}^{centre}))}$, with $\mathbf{x}^{centre}$ the 2D coordinates of the centre plane.

- Flow Isotropy

The large scale anisotropy of turbulent fluctuations is quantified by the ratio between the velocity standard deviation if the direction of gravity ($\hat{z}$) and the perpendicular: $\sigma_{u_z}/\sigma_{u_x}$, for the three pump's power inputs. Those fields are presented in Figure 2.10: 12V – sub-panel(a); 15V – sub-panel(b); 18V – sub-panel(c). The spatially averaged mean values of this fields are 1.30, 1.19, and 1.18, for 12V, 15V and 18V respectively. Thus the maximum anisotropy of 30% is present in the 12V case, while the other two cases stay around 20%.

Inertial Scale Properties

The inertial scale dynamics of the turbulent flow using classical structure functions analysis is quantified. In particular second order statistics are used to check inertial scale isotropy properties and estimate the energy dissipation rate ϵ.

- Second Order Structure Functions & Energy Dissipation ϵ

The energy injected to the flow per unit time and unit mass, ϵ, can be obtained by computing the Structure Functions. Firstly, the velocity increments $\delta\mathbf{u}(\mathbf{x}, r) := \mathbf{u}(\mathbf{x}+r) - \mathbf{u}(\mathbf{x})$. It is common to consider the longitudinal velocity increments which are defined as:

$$\delta_{u_\parallel}(r) := [\mathbf{u}(\mathbf{x}+r) - \mathbf{u}(\mathbf{x})] \cdot \frac{\mathbf{r}}{r}. \tag{2.2}$$

The perpendicular one is analogous but projected on a component perpendicular to $\mathbf{r}$. Note that if the turbulence is isotropic all the directions perpendicular to $\mathbf{r}$ are equivalent.

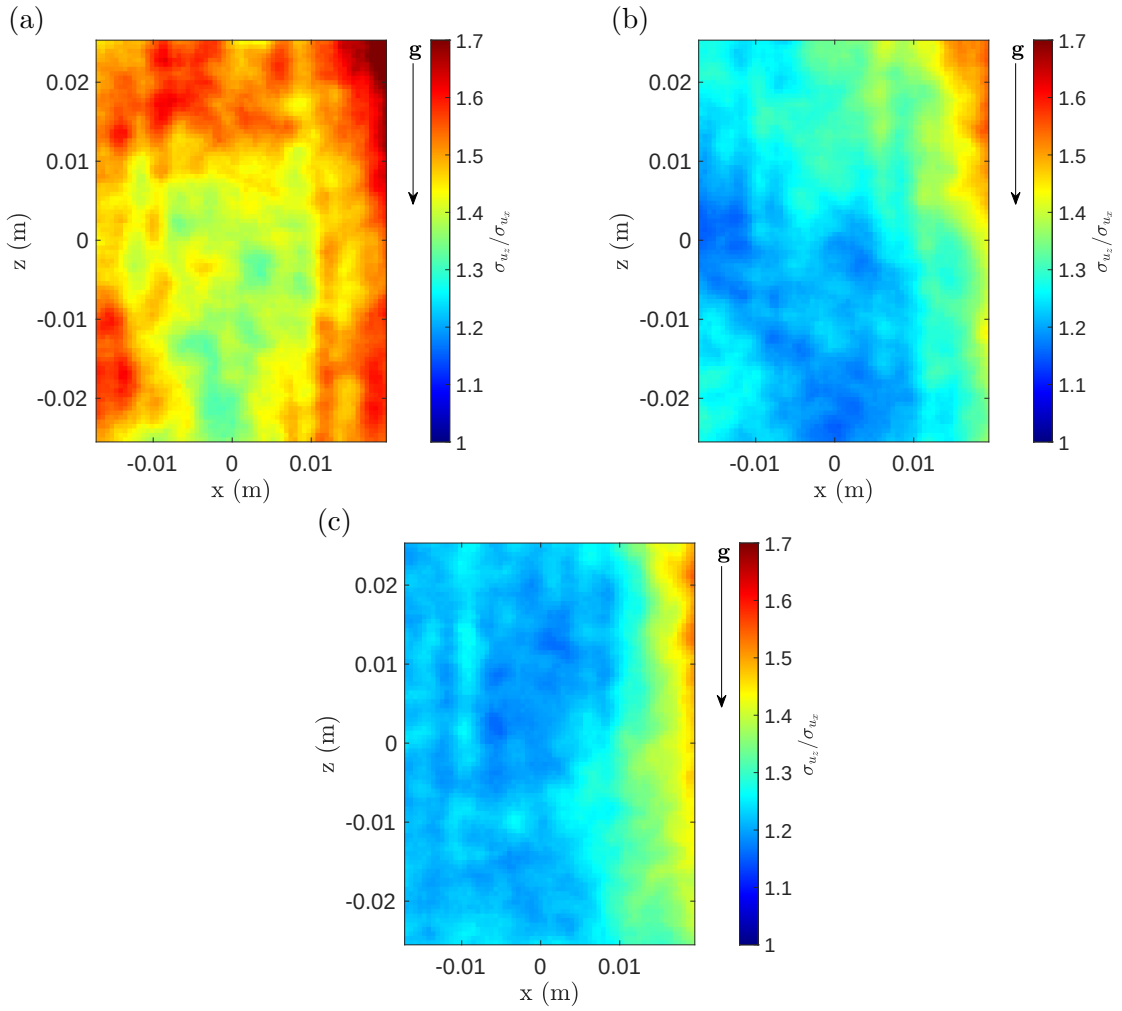

Figure 2.10: Flow's isotropy quantification: $\sigma_{u_z}/\sigma_{u_x}$ for the three pump's power inputs: 12V – sub-panel(a); 15V – sub-panel(b); 18V – sub-panel(c). The anisotropy (i.e. the mean value of these fields) is 30%, 19%, and 18%, respectively. Note that gravity is pointing downwards.

The Structure Functions of order p are then defined as the mean value of the velocity increment at the power p:

$$S_p^{\parallel} := \langle (\delta_{u_{\parallel}})^p \rangle; \tag{2.3}$$

$$S_p^{\perp} := \langle (\delta_{u_{\perp}})^p \rangle. \tag{2.4}$$

Classical Kolmogorov phenomenology for Homogeneous Isotropic turbulence predicts that $S_p^{\parallel,\perp} = C_p^{\parallel,\perp}(\epsilon r)^p$. Such scalings usually hold for low orders (up to $p \lesssim 4$) while intermittency corrections are appear at high orders (Frisch, 1995). Note that the Second Order Structure Function ($p = 2$) is the variance of the velocity increments. In that case, the constant $C_2^{\parallel}$ is empirically known to be of the order of 2.1, and $S_2^{\parallel}(r) = C_2^{\parallel}(\epsilon r)^{2/3}$ (known as the two-thirds law). Moreover, in Homogeneous and Isotropic turbulence longitudinal and transverse structure functions are related at inertial scales by (Frisch, 1995; Pope, 2011):

$$S_2^{\parallel} = \frac{3}{4} S_2^{\perp}. \tag{2.5}$$

The parallel and perpendicular Second Order Structure Functions are computed from the Eulerian velocity field $\mathbf{u}$ with an algorithm included in the package PIVMat (2015) by F. Moisy (http://www.fast.u-psud.fr/pivmat/). Figure 2.11 presents the parallel (blue) and perpendicular (red) Second Order Structure Functions for the three pump's power inputs: 12V (sub-panel (a)), 15V (sub-panel (b)), and 18V (sub-panel (c)). A reference line with slope 2/3 is placed on top of the data.
Whereas the closeness to the 2/3 scaling is identical for the three power inputs, the magnitude of the Structure Functions varies between voltages as the fluid velocity is more intense with a higher power input: the maximum value increases from 1.1×10^{-2} m^2/s^2 to 2.1×10^{-2} m^2/s^2, between 12V and 18V. This will reappear later on as ϵ will be found to increase as well: i.e. more energy is injected to the flow when the pump's power input is higher.

The energy injected can be computed by using the following relation valid in the inertial range:

$$S_2^{\parallel}(r) = C_2(\epsilon r)^{2/3}, \tag{2.6}$$

with C_2 taken as 2.1 (Pope, 2011). Figure 2.12 presents the compensated parallel second order structure function: $(S_2^{\parallel}(r)/C_2)^{3/2}1/r$ for the three pumps' power inputs: 12V (red), 15V (green), and 18V (blue). The values of ϵ are extracted from the value reached at the integral scale $L = 1$ cm (calculated in the following). The values of ϵ are represented by horizontal lines at: $\epsilon = (1.7 \pm 0.5) \times 10^{-2}$ m^2/s^3 – 12V; $\epsilon = (3.3 \pm 0.5) \times 10^{-2}$ m^2/s^3 – 15V; and $\epsilon = (4.9 \pm 0.5) \times 10^{-2}$ m^2/s^3 – 18V.

Finally, the ratio between the parallel and perpendicular Second Order Structure Functions presented in Equation 2.5 is plotted in Figure 2.13 for the three power inputs 12V (red), 15V (green), and 18V (blue). Alongside with an horizontal line at the theoretical value of 4/3 for this ratio. It can be seen that the agreement is qualitatively correct as the ratio lays near 4/3 within a 5% margin, around the inertial range.

- Spatial Correlations & Integral Scale

The longitudinal autocorrelation of velocity fluctuations can be estimated from $S_2^{\parallel}$ as:

$$R^{\parallel}(r) = 1 - \frac{S_2^{\parallel}}{\sigma_{u_x}^2 + \sigma_{u_z}^2}, \tag{2.7}$$

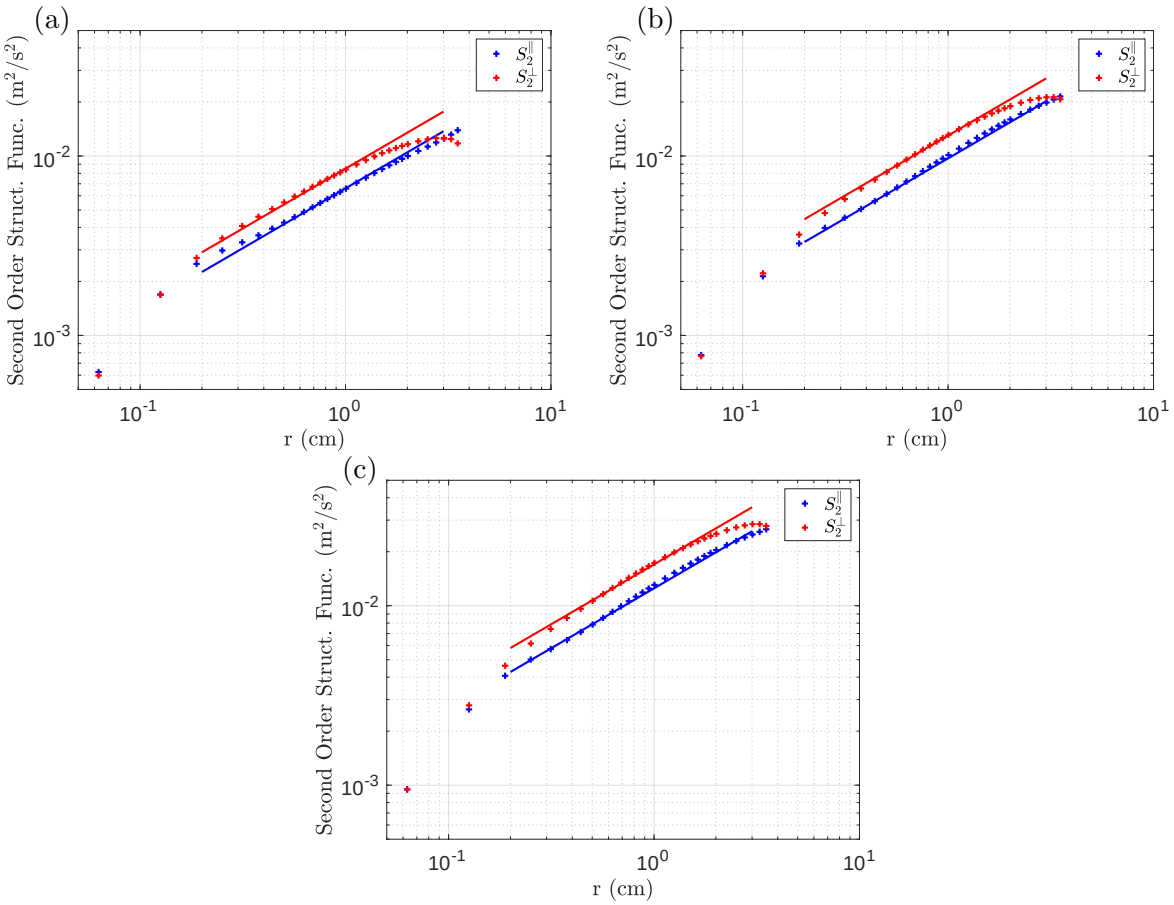

Figure 2.11: Parallel (blue) and perpendicular (red) Second Order Structure Functions for the three pump's power inputs: 12V (sub-panel (a)), 15V (sub-panel (b)), and 18V (sub-panel (c)). A reference line with slope 2/3 is placed on top of the data

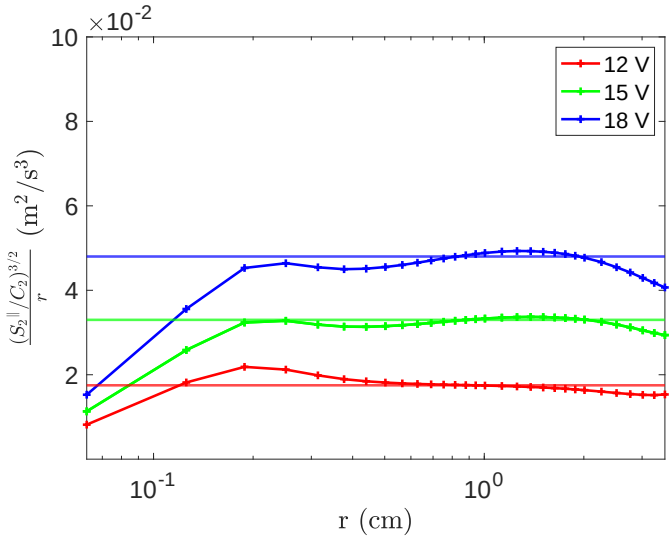

Figure 2.12: Compensated second order parallel structure functions. $(S_2^{\parallel}(r)/C_2)^{3/2}1/r$ for the three pumps' power inputs: 12V (red), 15V (green), and 18V (blue). The values of ϵ are extracted from each value reached in the integral scale $L = 1.06$ cm.

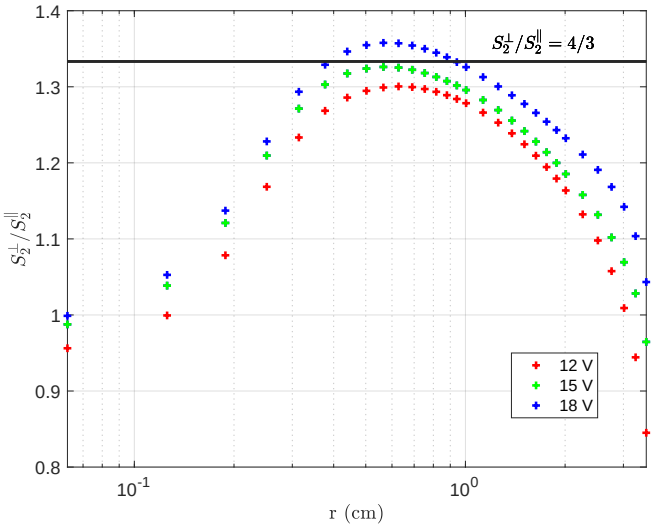

Figure 2.13: Ratio between the parallel and perpendicular Second Order Structure Functions. For the three power inputs 12V (red), 15V (green), and 18V (blue). Alongside with an horizontal line with the theoretical value of 4/3 for this ratio.

where instead of the usual $2\sigma_u^2$ denominator in the second term of the r.h.s., the vertical and horizontal contributions due to the large scale anisotropy in previous subsection have been separated.

The longitudinal integral scale L is then defined as the integral of $R^{\parallel}(r)$ (Pope, 2011):

$$L = \int_0^{\infty} R^{\parallel}(r)dr. \tag{2.8}$$

The latter Equation is used to obtain the integral scale. Figure 2.14 presents the cumulative integral of the longitudinal autocorrelation, for the three power inputs: 12V (red); 15V (green); and 18V (blue). The integral scale L corresponds to the asymptotic value, when the plot reaches a plateau at large separations. The value of L is represented by horizontal lines. It can be seen that for the case of 12V, the integral seems to have converged as the plot reaches a plateau in the last three points. On the other hand, the convergence is not completely reached in the cases 15V and 18V. However, overall the integral scale does not significantly vary between realisations. Hence the same value of integral scale will be considered for all cases: (1.06 ± 0.1) cm (taken as the average of the value determined for the three power inputs).

- Estimation of C_ϵ

As discussed in Chapter 1, it exists a relation between the three main parameters of turbulent fluctuations measured so far: ϵ, σ_u, and L (Pearson et al., 2002; Sreenivasan, 1998):

$$L = C_\epsilon \sigma_u^3/\epsilon, \tag{2.9}$$

with C_ϵ a constant of order one. Figure 2.15 presents the cube of the standard deviation of the Eulerian velocity field (σ_u^3) versus the energy injected (ϵ) for the three power input cases. In order to have a single scalar relation σ_u is defined as $\sigma_u = \sqrt{\frac{1}{2}\left(\sigma_{u_x}^2 + \sigma_{u_z}^2\right)}$. The linear relation between ϵ and σ_u^3 is confirmed. A linear fit to the data yields a slope

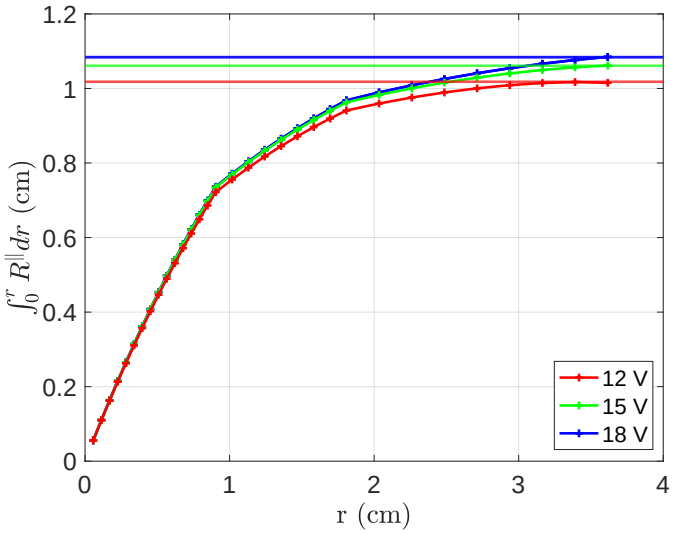

Figure 2.14: Integral of the autocorrelation. For the three power inputs: 12V (red); 15V (green); and 18V (blue). Horizontal lines represent the values of the integral scale L estimated from this results.

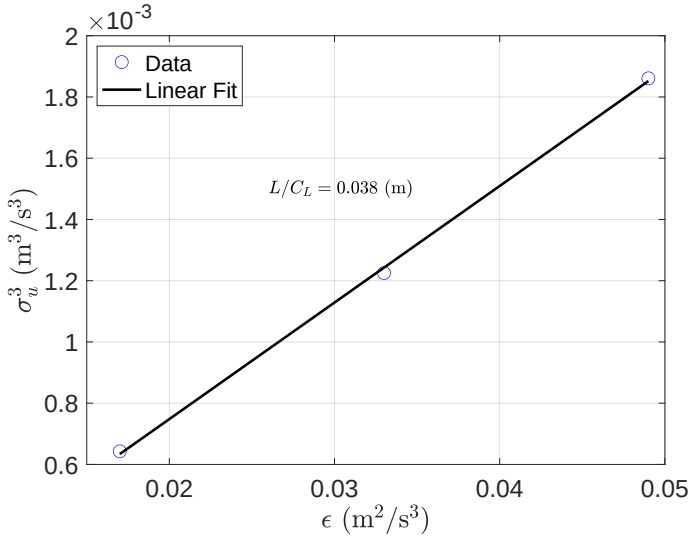

Figure 2.15: Determination of C_ϵ. The cube of the standard deviation of the Eulerian velocity field (σ_u^3) versus the energy injected (ϵ) for the three power input cases. The relation must be linear and its slope equals L/C_ϵ, the integral scale divided by a constant C_ϵ.

$L/C_\epsilon = 3.8$ cm. Considering the values for the integral scale obtained before, $C_\epsilon \approx 0.27$. This value is qualitatively correct given the $\mathcal{O}(1)$ value obtained in the literature Pearson et al. (2002); Sreenivasan (1998).

2.2.3 Summary

A summary of the regimens of particle and turbulent flow that can be achieved are presented in this subsection.

Turbulence characteristics

The regimens that this turbulent flow can achieve are presented in Table 2.3: energy dissipation ϵ; the Reynolds number based on Taylor's scale Re_λ; the velocity standard deviation $\sigma_u = \sqrt{\frac{1}{2}\left(\sigma_{u_x}^2 + \sigma_{u_z}^2\right)}$; the Kolmogorov scale η; and the Kolmogorov time scale τ_η; integral scale L; and integral time scale τ_L. These values were computed from the three measured parameters $\epsilon - \sigma_u - L$ and the relations presented in Table 1.2. In particular, $Re_\lambda = \sqrt{15Re} = \sqrt{15\sigma_u L/\nu}$.

Input Voltage	ϵ (m^2/s^3)	Re_λ	σ_u (cm/s)	$\sigma_{u_z}/\sigma_{u_x}$	$\langle \mathbf{u}\cdot\hat{z}\rangle$ (cm/s)	η (μm)	τ_η (ms)	L (cm)	τ_L (ms)
12 V	1.7 $\times 10^{-2}$	125	8.6	1.30	11.2	78	7.2	1.06	123
15 V	3.3 $\times 10^{-2}$	142	11.1	1.19	12.2	67	5.1	1.06	95
18 V	4.9 $\times 10^{-2}$	152	12.8	1.18	15.8	60	4.2	1.06	83

Table 2.3: Flow ranges attained by this experimental device. The columns present the ranges of: energy dissipation ϵ; Reynolds number based on Taylor's scale $Re_\lambda = \sqrt{15Re}$; velocity standard deviation σ_u; fluctuations isotropy $\sigma_{u_z}/\sigma_{u_x}$; Kolmogorov scale $\eta = (\nu^3/\epsilon)^{1/4}$; Kolmogorov time scale $\tau_\eta = (\nu/\epsilon)^{1/2}$; integral scale L; and integral time scale $\tau_L = L/\sigma_u$ that this device can achieve.

Particles

The settling experiments in the turbulent flow (results presented in Chapter 5) were carried using neodymium magnetized spheres (with a density ratio with water of 8.2) of diameter 1 mm. While the experiments to be made in the Dryden Drop Tower will involve different kind of particles, from negatively to positively buoyant.
Table 2.4 presents the regimes reached with this flow and the particles in use, for both the Magnetic Gravity Compensation method (whose results are discussed in Chapter 5) and the micro-gravity experiments to be made in the Dryden Drop Tower, for the three voltage inputs on the water pumps. The rows present the different parameters, with the control parameters $\{Re, \Gamma, Ro, St\}$ in red. In particular, the rows show: $Re = \sigma_u L/\nu$; $Re_\lambda = \sqrt{(15Re)}$; $Fr = \sqrt{a_0}(\epsilon^3/\nu)^{1/4}/g$, with $a_0 = 0.13(Re_\lambda)^{0.6}$ (Sawford, 1991); $\sigma_u^{@P} = \sqrt{1/2(\langle\sigma_{u_x}\rangle^2 + \langle\sigma_{u_z}\rangle^2)}$ the flow velocity standard deviation at the positions of the particles; $\langle \mathbf{u}\cdot\hat{z}\rangle^{@P}$ the mean vertical flow at the position of the particles; $\Gamma = \rho_p/\rho_f$; d_p/η; d_p/L; $Ga = u_g d_p/\nu$; $\tau_p^0 = d_p^2/(12\nu\beta)$; $\tau_p = \tau_p^0 f(\Gamma, Ga) = \tau_p^0 24/(Re_p C_D(Re_p))$; $St = \tau_p/\tau_\eta$; $St_{d_p} = \tau_p/(d_p^2/\epsilon)^{1/3}$; $St_L = \tau_p/\tau_L$; and $Ro = (\Gamma - 1)/(\Gamma + 1/2)\tau_p g/(\sigma_u^{@P})$.

$g^* = \tilde{g}/g$	1.0 ± 0.02	0.90 ± 0.02	0.78 ± 0.02	0.71 ± 0.02	0.63 ± 0.02	0.57 ± 0.02	0.49 ± 0.02			micro-g
Voltage (V)	12	12	12	12	12	12	12	15	18	12-15-18
Re	1047	1047	1047	1047	1047	1047	1047	1352	1559	$\mathcal{O}(10^3)$
Re_λ	125	125	125	125	125	125	125	142	152	$\mathcal{O}(10^2)$
Fr	0.26	0.29	0.34	0.37	0.42	0.46	0.54	0.89	1.2	∞
$\langle\sigma_u\rangle^{@P}$	0.105	0.105	0.104	0.104	0.104	0.105	0.103	0.134	0.153	$\mathcal{O}(10^{-1})$
$\langle\mathbf{u}\cdot\hat{z}\rangle^{@P}$	0.146	0.139	0.143	0.144	0.141	0.144	0.141	0.158	0.205	$\mathcal{O}(10^{-1})$
Γ	8.2	8.2	8.2	8.2	8.2	8.2	8.2	8.2	8.2	$\mathcal{O}(1)$
d_p/η	12.8	12.8	12.8	12.8	12.8	12.8	12.8	14.9	16.6	$\mathcal{O}(1)$
d_p/L	0.1	0.1	0.1	0.1	0.1	0.1	0.1	0.1	0.1	$\mathcal{O}(10^{-2})$
Ga	303	288	268	255	240	230	212	212	212	$\mathcal{O}(10^2)$
τ_p^0 (ms)	550	550	550	550	550	550	550	550	550	$\mathcal{O}(10^{-3})$
τ_p (ms)	48	51	54	56	59	61	64	64	64	$\mathcal{O}(1)$
St	6.8	7.1	7.5	7.8	8.1	8.5	9.0	12.7	15.4	$\mathcal{O}(10^{-1})$
St_{d_p}	1.2	1.3	1.4	1.4	1.5	1.5	1.6	2.1	2.3	$\mathcal{O}(10^{-2})$
St_L	0.4	0.4	0.4	0.4	0.4	0.5	0.5	0.7	0.8	$\mathcal{O}(10^{-3})$
Ro	3.7	3.5	3.2	3.0	2.8	2.6	2.4	1.9	1.7	0

Table 2.4: Parameters achievable by this water turbulence device. The columns present the different parameters for each adimensional gravity $g^* = \tilde{g}/(9.8\ \mathrm{m/s^2})$ (with $\tilde{g}$ the effective gravity, see Section 2.4) and the micro-gravity environment, for each voltage on the pumps. While the rows present the different parameters, with the control parameters $\{Re, \Gamma, Ro, St\}$ in red. In particular, the rows show: $Re = \sigma_u L/\nu$; $Re_\lambda = \sqrt{15Re}$; $Fr = \sqrt{a_0}(\epsilon^3/\nu)^{1/4}/g$, with $a_0 = 0.13(Re_\lambda)^{0.6}$ (Sawford, 1991); $\sigma_u^{@P} = \sqrt{1/2(\langle\sigma_{u_x}\rangle^2 + \langle\sigma_{u_z}\rangle^2)}$ the flow velocity standard deviation at the positions of the particles; $\langle\mathbf{u}\cdot\hat{z}\rangle^{@P}$ the mean vertical flow at the position of the particles; $\Gamma = \rho_p/\rho_f$; d_p/η; d_p/L; $Ga = u_g d_p/\nu$; $\tau_p^0 = d_p^2/(12\nu\beta)$; $\tau_p = \tau_p^0 f(\Gamma, Ga) = 24\tau_p^0/(Re_p C_D(Re_p))$; $St = \tau_p/\tau_\eta$; $St_{d_p} = \tau_p/(d_p^2/\epsilon)^{1/3}$; $St_L = \tau_p/\tau_L$; and $Ro = (\Gamma - 1)/(\Gamma + 1/2)\tau_p g/\sigma_u^{@P}$.

2.3 4D-LPT

The settling regimes and dynamics of the particles, whether in the quiescent or the turbulent flow cases, is characterized using timer resolved Lagrangian Particle Tracking (4D-LPT. This allows to track the particle's position in space via the use of a 2 or 3-cameras system. Its principle and execution are detailed in this Section.

2.3.1 Principle

The 3D trajectories of the particles studied in this thesis are obtained from the 4D-Lagrangian Particle Tracking method (sometimes called Particle Tracking Velocimetry), where 4D represents the three spatial coordinates plus time. For information about general methods to detect particles in flows read Discetti and Coletti (2018).

Figure 2.16 presents a top view of the optical arrangement set of the two experimental setups presented in this thesis: Quiescent Flow and Turbulent Flow with magnetic gravity compensation. The grey rectangle represents the water tank whose centre is being recorded with two cameras (C1 and C2). To have a good contrast between the objects and the background, two homogeneous white light panels are set to fill the images from each camera. In this way, the objects that appear between the backlight and the camera appear black on a white surface (see Fig. 2.17(a)). Note that, while the optics in the micro-gravity experiment designed for the Dryden Drop Tower has some differences (detailed in Section 2.5), the main idea of backlight imaging is kept.

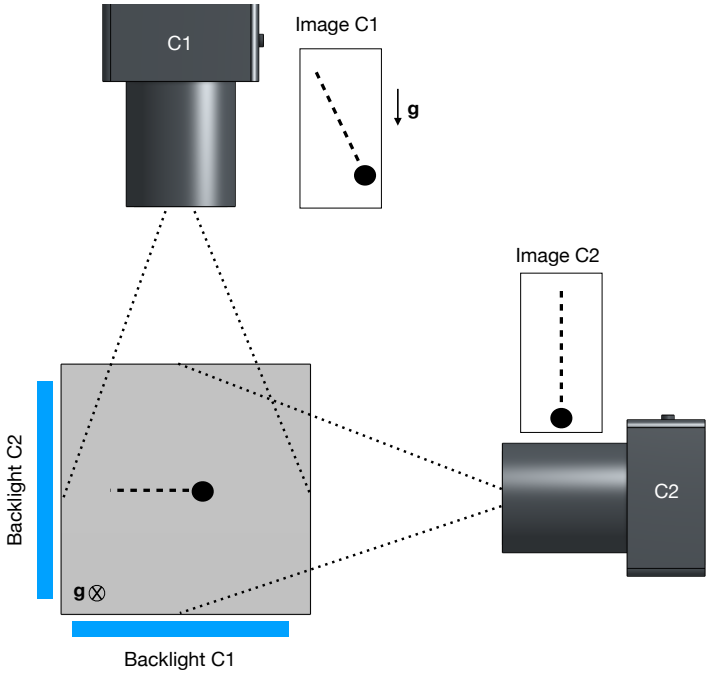

Figure 2.16: Schematic of 4D-LPT setup. Top view of the optical arrangement set in two of the experimental setups presented in this thesis: Quiescent Flow and Turbulent Flow (with magnetic gravity compensation). The grey rectangle represents the water tank whose centre is being recorded with two cameras (C1 and C2), and the light blue rectangles represent the backlights.

In general, the LPT method consists in using two or more cameras that simultaneously image a region in 3D space: note that the exact distance between one camera and the object imaged cannot be quantified if one had only one camera, hence the method requires $n \geq 2$ cameras. The relation between the object position on the cameras (pixel units) and its 3D position (meters) is obtained via a calibration of the optical arrangement, that is accomplished by placing a target of known dimensions in the 3D space that the cameras simultaneously image (Hartley and Zisserman, 2004). Furthermore, the calibration has to absorb the non-linear distortions and reflection effects that come from the interfaces (not always planar nor optically homogeneous) that a light ray traverses. These includes aberrations due to the optics and due to interfaces. For example, in a PMMA square tank filled with water (as it will be the situation in the Quiescent Flow Experiments), there are two interfaces (air-PMMA and PMMA-water).
Calibration the allows to retrieve the 3D position of an object from the intersection of virtual light rays that link each camera to the object detected in each image. Obtain these rays is one of the more subtle aspects of 4D-LPT. A guide to the implementation of the 4D-LPT system herein utilised can be found in (PTV), that is based on Bourgoin and Huisman (2020)'s paper. The method consists then on the following steps:

1. Calibration of the optical system;
2. Particle's centroid detection in each image;
3. 3D particle's position determination;
4. Particle tracking in time.

Details about these steps are presented in what follows.

2.3.2 Mise en œuvre

The cameras setup and its parameters change throughout the different experiments performed in this thesis. For instance, the Drop Tower Experiment uses a 3-camera Chronos 2.1-HD setup (at approximately 1000 fps at full resolution of 2.1Mpx), whereas the ground experiments have a 2-camera system made of fps1000 cameras (up to 3200 fps at full resolution of 1MPx) from The Slow Motion Company (as sketched in Fig. 2.16. This difference relates to the fact that ground experiments aimed at tracking single particles, while drop tower experiments will also investigate multi-particle dynamics and preferential concentration effects for which a larger number of cameras improves the resolution of possible ambiguities in the matching step. Furthermore, the effective visualization area is varied by changing the distance between the cameras and the particles, and/or the lenses characteristics. All these variations mostly influence the particle detection step of the 4D-LPT method, as a different particle size threshold has to be set. Apart from the latter, the core of the method explained in what follows, is common to all these experimental setup variations. The particularities of each experiment are discussed in the "Experimental Setup" Subsection present in each corresponding Chapter.
In what follows the main steps of the 4D-LPT method will be presented for the simpler spherical particle case, whereas the particularities of the anisotropic particles' case are discussed in Subsection 2.3.3.

Particle detection in each camera

The first step of the 4D-LPT method is to detect the particles positions $\mathbf{X}_{\text{pixels}}$ in the image of each camera. Figure 2.17 presents three steps of the particle detection process that will be explained in what follows, using as example the case of a single spherical magnet of diameter 1 mm settling in the Turbulent Flow presented before. In particular, Fig. 2.17(a) shows the raw

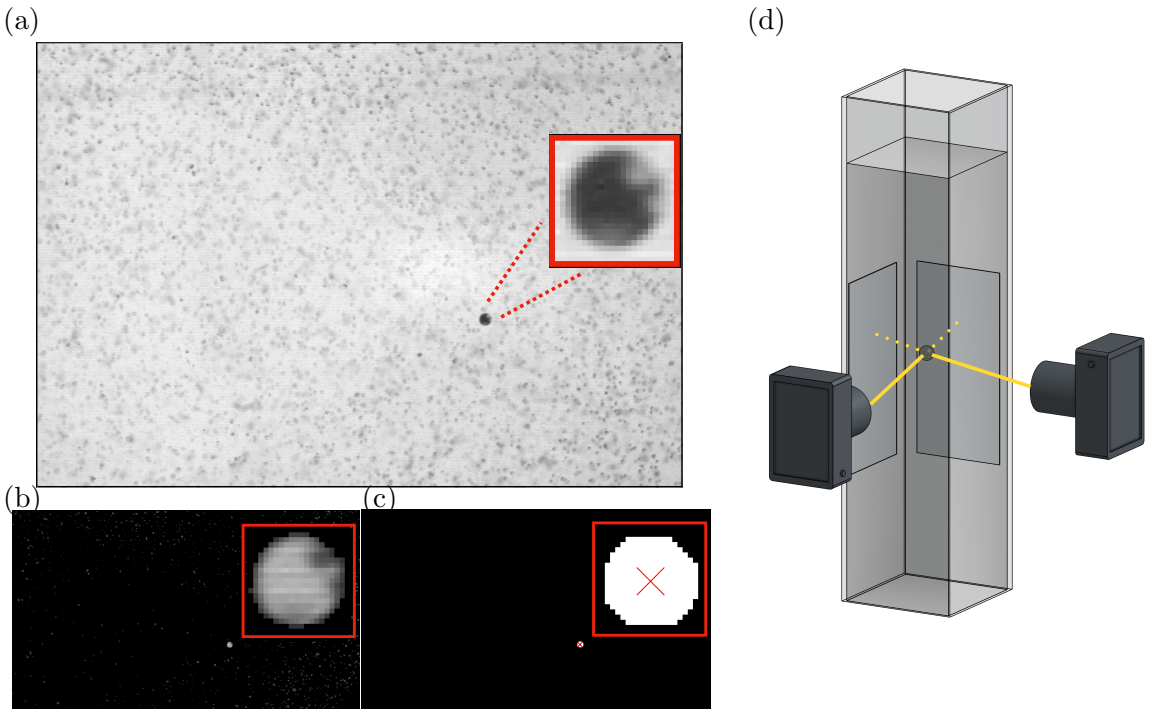

Figure 2.17: Particle detection stages. Three steps of the particle centroid detection process explained in the body, for a single spherical magnet of diameter 1 mm settling in the Turbulent Flow presented before. The panel (a) presents a raw image with the 1 mm particle and small tracer particles. The panel (b) show the resulting image after the application of the Steps 1-2-3 explained in the body, whereas panel (c) presents the final image alongside with the particle centre detection. Furthermore, the 3D particle position measurement method is qualitatively presented in the panel (d): rays (yellow) that join each camera to the particle centroid are intersected to obtain the particle 3D position.

Unsigned Integers of 8 bits (uint8) image and the inset presents a zoom on the particle. In this camera configuration the particle has a diameter of approximately 16 pixels.Finally, the small particles in the image are tracer particles that remained on the flow from the PIV characterisation. Although there is a lower concentration that the one used in the PIV experiments. In most experiments those particles are not present, the method is nevertheless illustrated in this situation to show the robustness of the settling particle detection even in the presence of such background "noise".

The image analysis was done with MATLAB and the steps from the raw image to the particles' positions can be summarised as:

1. A background image, i.e. an image of the setup without any particles, is removed from the image.
2. The complement of the image is taken.
3. All image pixels with an intensity below a threshold are set to zero.
4. The image is binarised.
5. Morphological operations are applied to remove undesired pixels and/or fill gaps.
6. The particle centroid $\mathbf{X}_{\text{pixels}}$, in units of pixels, is detected via the *regionprops* function of MATLAB.

Details of each step follow:

Step 1. cleans the image from fixed defects such as scratches in the water tank or backlight inhomogeneities, leaving only the particles.

Step 2. The complement of the image is taken as the used algorithms of particle detection are set by default to detect light objects in a dark background. The result of the application of the Steps 1 and 2 is presented in Fig. 2.17(b), alongside with a zoom on the particle (red box).

Step 3. Note on Fig. 2.17(a) how the smaller particles, that in this context have to be deleted, have a lower intensity that the particle. This effect can be used as a method to filter them out by setting an intensity threshold, that in this case was set to 50 (recall that the image is in units of uint8). This threshold erases all the faint points that are present in Fig. 2.17(b).

Step 4. The binarisation of the image provides better defined particle edges that make more accurate the particle detection by *regionprops*.

Step 5. The two most widely morphological operators that one can apply to an image are image Opening and Closing. Both consists in combinations of Erosion and Dilatation fundamental operators using a given structural element (Kernel) with some prescribed 2D shape, such as circular, applied to all the pixels of a binary image. For the case of the Closing operator, when the Kernel is centred on a black pixel (i.e. value equal to zero) and there are more than n pixels with value one that overlap with the Kernel, the black pixel is set to one. In other words, the Closing operator closes gaps between pixels. This operator is particularly useful in the following case: note that the insets in Figs. 2.17(a-b) show light (subpanel (a)) and dark (subpanel (b)) spots on the particle surface. These are caused by light from the complementary backlight that is being reflected on the particle. If these spots happen to have an intensity comparable to the threshold set in Step 3., the particle will stop being circular and that may affect the accuracy of the centroid detection. In this sense, the Closing operator with a circular Kernel of the same diameter than the particle was applied to close the gap.
On the other hand, the Opening operator can be used to eliminate sets of pixels that are smaller than the Kernel size. This operator is an alternative to the Step 3 that discriminated the small particles by its intensity, Opening the image allows to discriminate the particles by size.

Step 6. The final image that only has an intensity non-zero in the particle image is presented in Fig. 2.17(c), alongside with a zoom on the particle and a red cross that represents the detection of the centroid (in practice this is done by means of the *regionprops* algorithm in Matlab©). It performs a fit of the object by a 2D ellipsoid, and from it centroid, object area, and other parameters are obtained. This approach yields continuous parameters, i.e. the centroid's position precision is sub-pixel.
Note that it is not strictly necessary for the detection algorithm that the image has only one particle. If one applied *regionprops* to a binarised image that still contained some undesired objects, the centroid of the particle of interest will still be detected, alongside with the other dozens objects detected. The particle is isolated before the application of the algorithm so it will not be necessary to identify it from the other dozens detected. Although not ideal, that could be done simply by filtering for instance by area of the centroids found.
There are more subtleties to this process that have to be tacked for each particular situation. For instance, when the particles are smaller and get closer to the empirical limit of 3 pixels, a Gaussian filter can be used to smooth the particle image and achieve sub-pixel definition, or a prescribed particle profile (often Gaussian) can be fitted around intensity peaks in the image

considered as particles.

In this way, the particle position in pixel units $\mathbf{X}_{\text{pixels}}$ is obtained for each camera. The next step is to convert these positions into rays in 3D (joining each camera detector to the particle centroid) that can be intersected to find the particle position in the 3D space of the laboratory.

3D particle position

Although the particle's position $\mathbf{X}_{\text{pixels}}$ at each camera is known, the 3D position of the particle cannot be quantified if one had only one camera (camera sensors are 2D, so at least 2 are needed to access 3D data), hence the method requires $n \geq 2$ cameras. In this sense, Figure 2.17(d) presents a sketch of the 2 cameras experimental setup that was used in this thesis (besides the micro-gravity experiment), 3D yellow lines that join the camera sensors and the particle' centroid are drawn. The particle position in 3D is then obtained as the point where all the rays coming from different cameras intersect.

A way to take into account each camera's optical system (camera, lenses and interfaces) is needed to construct the rays, i.e. a calibration. The calibration procedure is, in general, simple: a target of known dimensions, in the present thesis a white plaque with equidistantly printed black dots, is placed in the region imaged by all the cameras, and pictures of it are taken at different positions. Later on, a process similar to that presented in the previous Subsection is applied to obtain the centre of the black dots, whose position in 3D is known. The calibration method varies in the step that follows, that is how one goes from the points' positions at each camera to a 3D ray that links them to the cameras.

To that end, it exists a simple model, widely used, where each camera is modelled as purely projective system (pinhole model) (Tsai, 1987). Generally, it works well if there are not optical interfaces nor major optical distortions between the cameras and the objects to be detected (see, for example, its application in the context of free-surface wave-turbulence (Cabrera and Cobelli, 2021)).

As several interfaces are present in the situations that interest this thesis, a more elaborated method is used (Machicoane et al., 2019). This calibration only assumes that the light rays travel in a straight line within the measurement area (a reasonable assumption in the absence of stratification or any source of optical index inhomogeneity) uses a series of plane-by-plane non-linear (generally cubic) transformations between the sensor coordinates and the spatial coordinates of the calibration plate at different locations. This can be done regardless of the actual path and eventual aberrations outside the volume of interest, which can be very complex as interfaces and lenses are traversed. This transformation then allows to back project the center of a detected particle on the camera sensor to real space at each of the calibration plane position, what gives a series of possible positions aligned along the corresponding light ray, whose equation is simply retrieved by a linear 3D fit.

Note the differences between the approaches: whereas the pinhole approach builds on a physical camera model, there is no physical input to the Machicoane et al. (2019) approach. The calibration, then, automatically absorbs optical imperfections or complex lens arrangements.

As said before, once the 3D rays are corresponding to a particle detected on each camera are found, the particle position is obtained from the intersection between them. It is clear that due to slight errors (both in the center detection and in the calibration) the rays will not exactly intersect. The middle point, closer to all the rays, is then taken as the particle position in 3D. In particular, this distance between rays sets the uncertainty in particle position, which further impacts velocity and acceleration estimates (obtained by numerical differentiation of particle trajectories).

It is worth to remark that when a single particle is being tracked, it is trivial to match the

corresponding centers detected on the sensors of each camera and hence the corresponding intersecting rays. When several particles are being tracked simultaneously, an additional matching step is required Bourgoin and Huisman (2020). This was not necessary for the results presented in this manuscript, but will be for the upcoming drop tower experiments where multiple particles will be simultaneously tracked.

Particle tracking

The particle tracking consists in the construction of a 3D trajectory from successive particles' 3D positions. In the results presented in this thesis, the particle tracking is trivial as the experiments involve a single particle. In the near future (after the submission of this thesis), when particle suspensions are studied in the context of micro-gravity, some thought has to be put in the particle tracking problem. For instance, if two particles become close in space and then drift apart how can the individual trajectories be differentiated? In very dilute case, one can assume that this will not happen and the particle can be identified at consecutive frames by the *closest neighbour method*, that identifies a particle i at the frame $fr + 1$ as the particle that is closer to the i's particle position at the frame fr. When the suspensions are not diluted, more sophisticated methods need to be applied. In this spirit Bourgoin and Huisman (2020) use *predictive tracking* that estimates the particle i's position at the frame $fr + 1$ by a non-linear fit of the preceding frames, and then takes the closest particle to the predicted position as the particle i. Even more sophisticated methods such as *shake the box* exist in the literature (see, for example, Discetti and Coletti (2018)).

A further aspect is that of Trajectory Stitching, that attempt to fill gaps on the trajectories caused by particle detection issues, i.e. the particle is not tracked on several frames. In this case, one has pieces of trajectories and the idea is to reconstruct the complete trajectory. In other words, one interpolates the gaps in the trajectories: a possible method to do so can be found in PTV.

The particle tracking step necessitates the images to be finely synchronized in time. This is usually implemented in the software of the cameras, or externally by a trigger. That is the case of the cameras Chronos 2.1HD from Krontech. On the other hand, the cameras fps1000 from the Slow Motion Company have a software bug that inhibits that function. Details about the fps1000 cameras' synchronisation procedure is presented in the Appendix B.

2.3.3 Subtleties in the anisotropic particle case

Whereas the particle tracking, 3D matching, and system calibration do not vary in the case of an anisotropic particle, with respect to the spherical particle case, the particle detection requires to be rethought in order to get the particle's absolute orientation in 3D.
As an example, figures 2.18 presents two images of a 1 mm diameter and 16 mm length cylindrical rod, settling in a Quiescent Creeping Flow. The sub-panel (a) presents the rod image in the case when the rod is perpendicular to the image, while the red line represents its symmetry axis and the white points are the reference points to be matched in 3D space, as it will be discussed in what follows. (b) presents the same rod with its axis non-contained in the image plane, what can lead to perspective issues, as commented at the end of this Subsection.

The particle's centroid can be obtained in the same fashion as for the sphere: it can be computed by the algorithm *regionprops* of MATLAB (2019), as it detects the particle's centroid regardless of its shape. On the other hand, to measure the particle angle in 3D, it is chosen to do the 3D matching not only on the particle's centroid but as well on its two extrema (*large* white dots on Fig. 2.18(a)) and, to have more precision, as well on two artificially added points that equidist from each extrema and the centroid (*small* white dots on Fig. 2.18(a)). To analyse the data obtained in this thesis, it was found that the more precise way to obtain the position

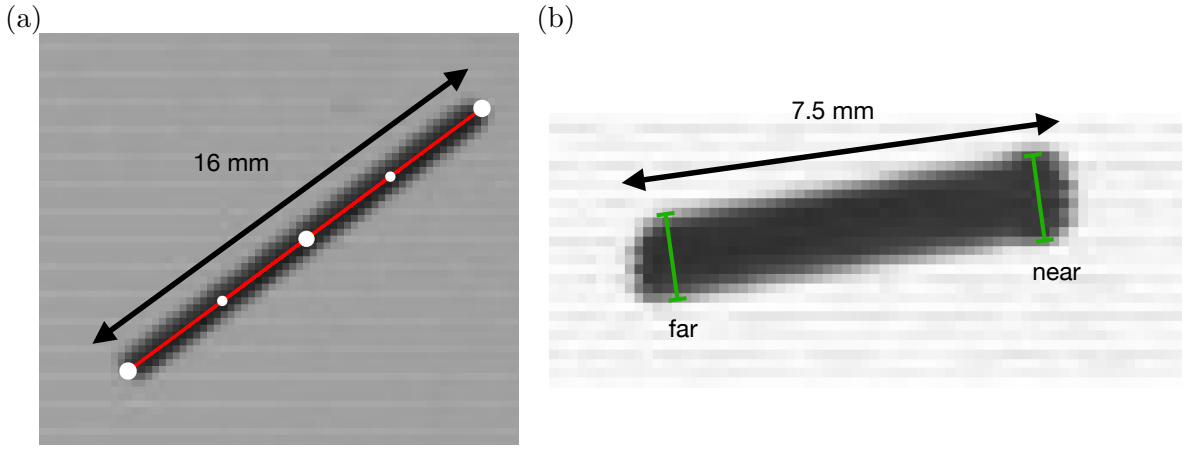

Figure 2.18: Two images of a 1 mm diameter and 16 mm length rod, settling in a Quiescent Creeping Flow. (a) presents a rod with its axis (red line) contained in the image plane (i.e. no perspective), alongside with three *large* white dots that represent the centroid and the extrema while the two *small* dots are points that equidist from the extrema and the centroid. (b) shows a zoom of the same rod with its axis outside the image plane, what makes the rod's extrema to be at different distances from the camera ("near" and "far"), the rod then appears to be shorter. Two identical green lines measure the particle diameter as seen by the camera: it can be seen that there is little perspective.

of the extrema on each image was to detect the contour of the object (via the MATLAB (2019) function *bwskel*) and apply *regionprops*, along with its *extrema* and *centroid* properties, to obtain the positions of the extrema and centroid in pixel units. Then two additional equidistant points are added and the process that follows the "Particle Detection in each camera" subsection is applied for all five points represented in Fig. 2.18(a). Later on, it is straightforward to take the five points' positions in 3D and join them by a line to have a 3D representation of the rod's position in space, and compute its angle with the vertical for each frame.

This method (in particular the justification to use additional equidistant points between the center and the extrema) requires the images to have negligible perspective effects. In other words, the rod needs to preserve its shape in the image, regardless of its orientation. This perspective effect is useful in every day life as it makes images seem tridimensional: for instance, in the picture of a long straight road one can tell that it continues for a long distance because its apparent width decreases as it is further away. Moreover the length of this road also seems to vary, i.e. the distance between the dashes in the dividing line becomes shorter.
If this would happen in the case of a rod, the aforementioned method will give an incorrect rod angle and position. The perspective effect is not present in the present optical configuration, as the distance between the cameras and the rod is much larger than the rod length. This can be checked from two simple observations: firstly, if there were perspective effects, the 3D matching step would not work as rays coming from each camera will not be close enough. Secondly, the particle diameter is measured at each rod extrema when its symmetry axis is not contained in the plane of the image. In this configuration, one extrema of the rod is *closer* whereas the other is *nearer* to the camera; hence the perspective would make the diameter smaller in the farther extrema. Figure 2.18(b) presents a rod in such a configuration, alongside with two identical green bars to be used as a reference to measure the rod's apparent diameter. Perspective effect is almost imperceptible, as the near extrema apparent diameter is only about 1 pixel larger than

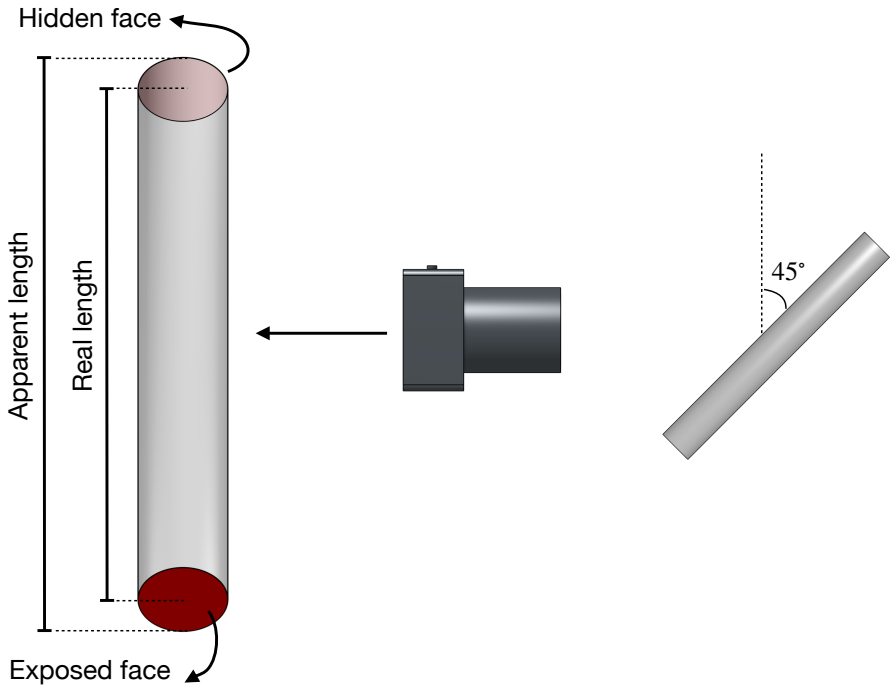

Figure 2.19: Sketch representing the edges effect that yields to a larger apparent rod's length. A camera images a rod with a 45° orientation with the vertical (right hand side), and its image (left hand side) shows how the faces contribute to the total length seen by the camera.

the far one, over a 11 pixels diameter. Nonetheless, this proportion is in reality smaller as all the realisations of rods settling in Quiescent Creeping Flow with an angle between the rod's axis and the image plane larger than 50° were discarded (see Figure 2.20). Note that, for a rod 16 mm long, a 45° angle between the rod axis and the image plane yields an apparent rod length of $\cos(45°)16 = 11.3$ mm. Therefore to get an apparent length of 7.5 mm, as presented in Fig. 2.18(b), the angle between the image plane and the rod's axis was $\cos^{-1}(7.5/16) = 62°$. Furthermore, perspective manifest itself more strongly near the borders of an image, as compared to the centre region. This is taken into account in the previous as the settling rod on Fig. 2.18(b) is at the lower border of the image.

Finally, the effect of the edges has to be considered: when an a finite sized anisotropic object is viewed from different angles, its apparent length can be modified. This phenomena is sketched in Figure 2.19 where a camera images a rod with a 45° inclination with the vertical. Its image is represented at the camera's left hand side: both circular faces of the rod's image (red) contribute to the apparent rod's length (recall that black and white cameras are utilised). The error induced by this effect in a rod at 45° yields to an apparent length = (real length) + (rod's diameter)/$\sqrt{2}$. This is an upper bound for the error as the edges effect is maximum at 45°.

Note that the rod's centroid detection is not influenced by this effect, while the 3D angle is: the extrema points, that come from the ellipsoidal fit, are at different positions on both cameras. Figure 2.20 sketches this effect. It presents a top view of the experimental setup in the case of the Quiescent creeping flow. The grey rectangle represents the water tank whose centre is being recorded with two cameras (C1 and C2). A rod (not in scale) is in the tank's centre, and a zoom of it is show in the upper right. The coloured circles in the rod's corners represent the rod's extrema positions that each camera see (camera 1 and 2 are represented by red and blue,

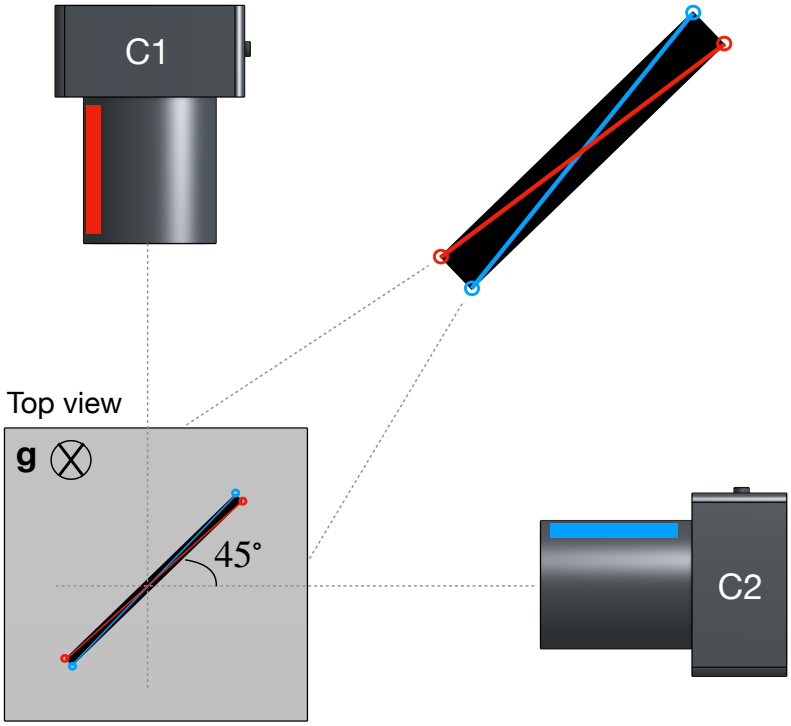

Figure 2.20: Top view of the experimental setup in the case of the Quiescent creeping flow. The grey rectangle represents the water tank whose centre is being recorded with two cameras (C1 and C2). A rod (not in scale) is in the tank's centre, and a zoom of it is show in the upper right. The coloured circles in the rod's corners represent the rod's extrema positions that each camera see (camera 1 and 2 are represented by red and blue, respectively), while the lines represent the apparent rod's axis at each camera.

respectively), while the lines represent the apparent rod's axis at each camera. It can be seen that the rod's centroid, defined by the intersection of the blue and red lines, is detected well. On the other hand, the rod's axis is different for each camera. In particular, the upper bound of the error in the 3D matching of the rod's extrema is estimated as half the rod's radius, in the present cases of rods with 1 mm diameter and lengths of 8 and 16 mm, the uncertainty in the angle can be estimated as 1.8° and 0.9°, for the 8 and 16 mm particles, respectively. Although these uncertainties are not negligible, they are smaller than the measurements scatter caused by physical effects, as it will be discussed in the Chapter 3.
These effects become important as the cylinders are less elongated and algorithms that correct them have to be applied, as detailed in Toupoint (2018).

2.4 Magnetic Field Gravity Modification

The implementation of magnetic fields to control aspects of diamagnetic/paramagnetic fluids in the Fluid Dynamics community is not new. The focus in the literature is mostly related to diamagnetic objects (e.g. DNA, water, proteins). When ways to circumvent Earnshaw's theorem came to light (Beaugnon and Tournier, 1991; Earnshaw, 1842), it was possible to levitate living diamagnetic objects such as frogs (Simon and Geim, 2000). These studies were central for the technique of high-gradient magnetic separation that allows the sorting of a sample's components that have different magnetic susceptibilities (He et al., 2014; Okada et al., 2006; Zhao et al.,

2018). In parallel, the Magnetic Resonance Imaging community developed the technical aspects to achieve an arbitrary magnetic field profile in a laboratory (or an hospital), with the use of coils (Hidalgo-Tobon, 2010; Turner, 1993). These are apart from the study of particles in conductive fluids under the influence of external magnetic inductions, that are central to a number of industrial situations: for example, in the context of clean metal production (Pan et al., 2019). On the other hand, the profiles of the external magnetic induction needed to obtain a constant vertical force that can counteract gravity in a number of scenarios like, for example, liquid helium or oxygen were also studied (Chatain et al., 2006; Lorin et al., 2013; Mailfert, Alain et al., 2015; Nikolayev et al., 2011).
With all these tools in hand, progress has also been made in the particular context that interests the present work: paramagnetic/ferromagnetic or permanently magnetised particles in a weak diamagnetic liquid (water), in a low external magnetic induction environment (thus no water magnetisation occurs). Some studies explored the effects of an homogeneous magnetic induction on one or more particles in non-magnetic fluids (Box et al., 2017; De La Rosa Zambrano et al., 2018; Keaveny and Maxey, 2008; Kumaran, 2019; Vessaire et al., 2020). On the other hand, we could not find studies in the context of Fluid Mechanics about the utilisation of particles with a permanent magnetisation and an inhomogeneous external magnetic field that can compensate gravity in a non-magnetic fluid. In this context, as it will be presented in the next Sections, the presence of an external magnetic field is manifested in two ways: the application of a torque that orients the particle's magnetic moment with the external induction; and the application of a force acting on the particle's centre of mass. The former appears when there is a magnetic induction and the latter in the case of an inhomogeneous induction (i.e. $\nabla B \neq 0$).

2.4.1 Interaction of a permanent dipolar magnetic moment with an external field

The first person to unravel the force between two current-carrying wires was André-Marie Ampère who incidentally lived in a village 20 km north from Lyon called Poleymieux-au-Mont-d'Or. From the equation modelling this force (called Ampere's law) the unit of current "Ampere" is defined and the vacuum permeability can be measured. Without going into details, the force $\mathbf{F}^M$ and torque $\mathbf{T}^M$ felt by a particle with a dipolar magnetisation $\mathbf{M}$ (that can be thought as a current loop) and mass m, expressed in cylindrical coordinates (recall the cylindrical symmetry of the experimental setup Fig. 2.1) read (Jackson, 1999):

$$\mathbf{F}^M = \nabla(\mathbf{M} \cdot \mathbf{B}), \tag{2.10}$$

$$\mathbf{T}^M = -\mathbf{M} \times \mathbf{B}. \tag{2.11}$$

Although the derivation of these expressions from first principles is not presented here, it is worth to mention that these expressions are the lowest order force and torque and they are only valid when the external magnetic induction varies *slowly* over the region of the dipole. In other words, when the magnetic induction can be well approximated by only the two first terms of its expansion around the dipole source – see Section 5, Equation 5.65 of Jackson (1999). Additionally, beware that here $|\mathbf{M}|$ is the total particle magnetisation and not the particle magnetisation per unit of volume.
The magnitude of the force and torque are linearly dependant on the magnetisation value $|\mathbf{M}|$. The particle magnetisation depends on the particle material that can be ferromagnetic, diamagnetic or paramagnetic. The three types of material can be separated into two categories: a previously magnetised ferromagnetic particle (permanent magnet) that has a constant dipolar moment $|\mathbf{M}|$; and a diamagnetic, paramagnetic or not previously magnetised ferromagnetic particle that has a magnetisation proportional to the external magnetic induction: $\mathbf{M} = \frac{\chi_v \mathrm{V}}{\mu_0(1+\chi_v)}\mathbf{B}$, with χ_v the volumetric magnetic susceptibility and V the particle's volume (O'Handley, 2000).

Typical values of χ_v for diamagnetic (e.g. graphite), paramagnetic (e.g. aluminium) and ferromagnetic (e.g. iron) materials are: $-1 \times 10^{-6}, 1 \times 10^{-5}$ and 1×10^{5}, respectively. Given a magnetic field and its gradient, the force generated on a particle will increase by 10 orders of magnitude if it is made of a ferromagnetic material instead of a diamagnetic or paramagnetic material. With the goal of imposing a force with a magnitude comparable to the gravitational pull using the lowest possible power input and coil size to generate the external magnetic induction, it is chosen to use ferromagnetic particles. In this material category there are still two options: previously magnetised particles, a.k.a. permanent magnets that have a remanent field $|\mathbf{B}_{\text{rem}}|$; or a ferromagnetic particle with no remanent magnetic field, that will be magnetised only in the presence of $|\mathbf{B}|$. Permanent magnets are chosen for two reasons:

- the value of $|\mathbf{M}|$ is constant and approximately 2 orders of magnitude larger for the permanent magnet case than for ferromagnetic particles (calculation done in next Subsection).
- It is necessary to demagnetise the ferromagnetic particles, this is to set $|\mathbf{B}_{\text{rem}}|$, before each experimental realisation. As the particles tend to keep some remanent magnetic field, $|\mathbf{M}|$ will not be a constant value throughout all realisations. That will lead to different magnetic force and torque magnitudes, and ultimately to a variable gravity compensation. As a remark, the demagnetisation process could be done by applying an oscillating magnetic field with a time decreasing amplitude; or heating up the particles above their Curie's temperature.

In particular, the magnetic moment $|\mathbf{M}|$ of a permanent magnet can be computed, if one assumes that the magnetic dipolar moment is dominant, in the following manner:

$$|\mathbf{M}| = \frac{|\mathbf{B}_{\text{rem}}|V}{\mu_0}, \tag{2.12}$$

where V is the volume of the magnet, μ_0 the vacuum magnetic permeability (note that $\mu_0 \approx \mu_{\text{water}}$) and $|\mathbf{B}_{\text{rem}}|$ is the residual magnetic flux density, in other words, the magnet's flux density when the external coercive field strength is zero that is given in the magnet's data sheet.
In this way, the magnetic terms in Equations 2.10-2.11 can be rewritten as:

$$\mathbf{F}^{\mathbf{M}} = \nabla\big(|\mathbf{M}||\mathbf{B}|\cos(\psi)\big) = |\mathbf{M}|\nabla|\mathbf{B}|\cos(\psi), \tag{2.13}$$

$$T^M = -|\mathbf{M}||\mathbf{B}|\sin(\psi). \tag{2.14}$$

With ψ the angle between $|\mathbf{M}|$ and $|\mathbf{B}|$, i.e. the angle such that $\mathbf{M} \cdot \mathbf{B} = |\mathbf{M}||\mathbf{B}|\cos(\psi)$ (see Fig. 2.21). Note that the magnetic torque T^M is restitutive, i.e. $\mathbf{M}$ parallel to $\mathbf{B}$ (i.e. $\psi = 0$) is the stable orientation. Therefore, if the external magnetic induction orientation is fixed in $\hat{z}$, the particle can only freely rotate around the latter. This rotation-blocking effect happens regardless of the force applied on the particle, as T^M is independent of $\nabla|\mathbf{B}|$.
Equation 2.13 is only valid if one assumes that the angle ψ does not vary: $\nabla\cos(\psi) \approx 0$.

2.4.2 Magnetic gravity compensation

The goal is to use the properties of the magnetic force just described to compensate (at least partially) the gravity felt by a particle with a permanent magnetic moment $\mathbf{M}$. Figure 2.21 presents a sketch of the situation: a magnetic particle is in the bulk of a fluid in the presence of both the gravitational field and an external magnetic field with a linear profile in gravity's direction. Furthermore, the angle ψ between the magnetic moment $\mathbf{M}$ and the vertical magnetic induction $\mathbf{B}$ (introduced in Eq.2.13-2.14). Recall that this angle is assumed to be approximately zero as the magnetic torque in this thesis' overweights any other torque present in the system – this claim will be corroborated in Section 2.4.4.

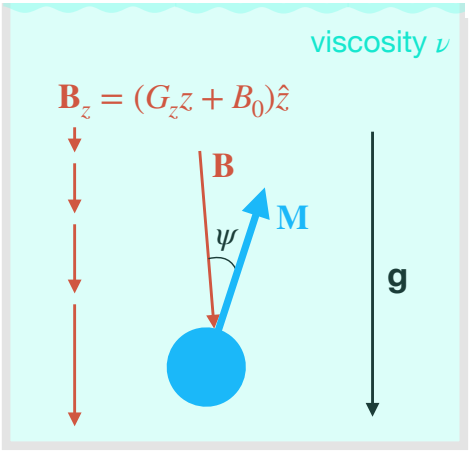

Figure 2.21: Sketch of the experimental configuration. A magnetic particle is in the bulk of a fluid in the presence of both the gravitational field and an external magnetic field with a linear profile in gravity's direction. Furthermore, the angle ψ between the magnetic moment $\mathbf{M}$ and the vertical magnetic induction $\mathbf{B}$ is showed.

The fluid forces are left to be introduced in Section 2.4.4. The equations of motion Eq. 2.10-2.11 are now rewritten with the gravitational field: with the addition of the weight force mg, an effective gravity $\tilde{g}$ can be defined and the equation of motion, projected on gravity's direction $\hat{z}$, reads:

$$\mathbf{F} \cdot \hat{z} = m\tilde{g} = m\big[g - |\mathbf{M}|\nabla_z|\mathbf{B}|\cos(\psi)/m\big]. \tag{2.15}$$

To be able to homogeneously compensate the gravity, the magnetic force on gravity's direction ($\mathbf{F}^M \cdot \hat{z}$), hence the vertical magnetic gradient $\nabla_z\ |\mathbf{B}|$ needs to be a constant ($\mathrm{G_z}$) independent of z. Alongside with that, the external magnetic induction $|\mathbf{B}|$ has to be a solution of Maxwell's equations, leading to the following set of equations:

$$\nabla_z\ |\mathbf{B}| = G_z, \tag{2.16}$$
$$\nabla \cdot \mathbf{B} = 0, \tag{2.17}$$
$$\nabla \times \mathbf{B} = 0. \tag{2.18}$$

Recall that, as presented in Section 2.1, the experimental coils system has rotational symmetry around the z-axis, therefore the magnetic field does not depend on the cylindrical coordinates' polar angle. The following solution is then proposed for equations 2.16-2.18: $\mathbf{B}(r,z) = B_r(r)\ \hat{r} + (G_z\ z + B_0)\ \hat{z}$, in cylindrical coordinates. B_r can be obtained by solving Eq. 2.17, leading to the following magnetic field induction:

$$\mathbf{B}(r,z) = (-\mathrm{G_z}/2\ r)\ \hat{r} + (\mathrm{G_z}\ z + B_0)\ \hat{z}. \tag{2.19}$$

Additionally, this magnetic induction respects the irrotational condition (Eq. 2.18). On the other hand, Equation 2.16 is only exactly satisfied at $r = 0$. The latter is an unavoidable consequence of the solenoidal nature of magnetic fields: it is not physically possible to have a non-constant magnetic induction (in this case a linear profile vertical profile with $\nabla_z|\mathbf{B}|$ =constant) only directed in the vertical, over a region in space. Note that it is possible to have:

1. a vertical homogeneous magnetic induction (e.g. at the centre of a very long solenoid);
2. a vertical non-constant magnetic induction over a line (e.g. $r = 0$ in the present case).

Case 1. does not fulfil the goal of this thesis as, on one hand, there is no $\nabla|\mathbf{B}|$ and the particles would only be subjected to a magnetic torque, thus no magnetic force and no gravity compensation. On the other hand, a long solenoid surrounding the water tank would inhibit the cameras to image the particles.
Case 2. is the best solution given the solenoidal nature of magnetism and technical constraints such as the need to have optical access to the water tank. The major drawback is that the magnetic field has a radial component, that makes the magnetic force to have a radial component. This may be a problem as the particles might experience a horizontal drift that does not come from the hydrodynamics. As it will be detailed in Section 2.4.4, to avoid said drifts the magnetic induction strength can be chosen to yield a radial magnetic force inferior to the hydrodynamical drag. The latter will then set the maximum gravity compensation level that can be reached without having particle drift.

With Eq. 2.19 for the desired magnetic field, the radial and vertical magnetic forces then read:

$$\begin{aligned} F_z^M(r,z) &= |\mathbf{M}|\,\frac{\partial|\mathbf{B}|}{\partial z} = |\mathbf{M}|\,\frac{(\mathrm{G_z}z+B_0)\mathrm{G_z}}{\sqrt{(\mathrm{G_z})^2/4r^2+(\mathrm{G_z}z+B_0)^2}}, \\ F_r^M(r,z) &= |\mathbf{M}|\,\frac{\partial|\mathbf{B}|}{\partial r} = |\mathbf{M}|\,\frac{r\ (\mathrm{G_z})^2/4}{\sqrt{(\mathrm{G_z})^2/4r^2+(\mathrm{G_z}z+B_0)^2}}. \end{aligned} \tag{2.20}$$

Note that $F_r^M(r\to 0)=0$ and $F_z^M(r\to 0)=|\mathbf{M}|G_z$. Therefore, as discussed before, the gravity can be compensated at r=0, without any radial force present.

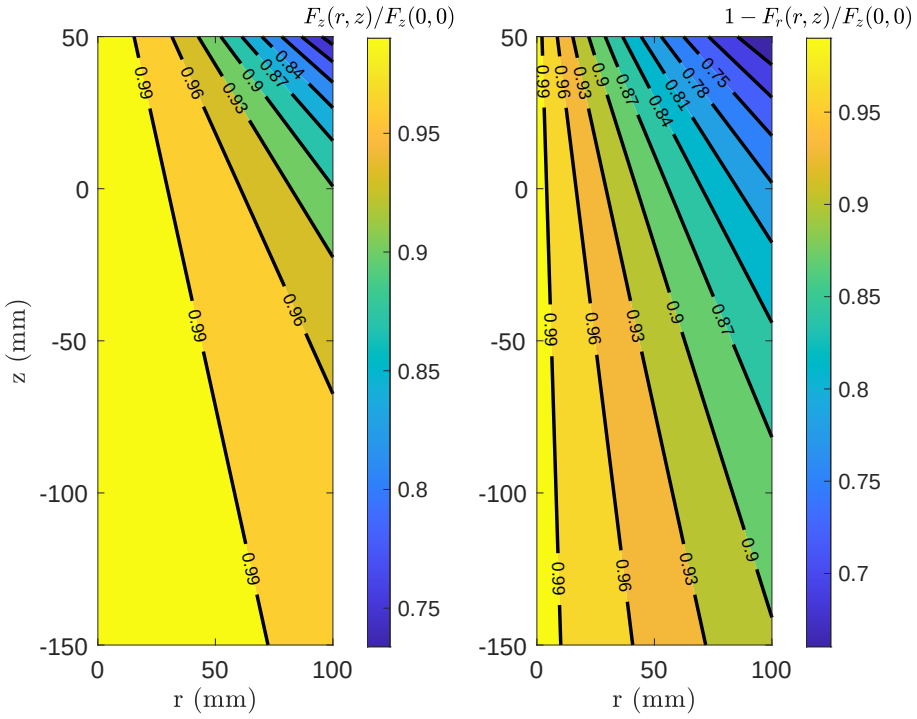

Figure 2.22: Countour plot of the axial (left) and radial (right) component of the theoretical magnetic force, normalised by the axial force at z=0: $F_z^M(r,z)/F_z^M(0,0)$ and 1-$F_r^M(r,z)/F_z^M(0,0)$, respectively.

Figures 2.22a-b present contour plots of $F_z^M(r,z)/F_z^M(0,0)$ and 1-$F_r^M(r,z)/F_z^M(0,0)$, respectively. Note that the normalisation chosen is: $F_z^M(0,0)=|\mathbf{M}|G_z$. Values of $G_z=-270$ G/m, $B_0=26$ G and $z\in(-150,50)$ mm were used to compute the forces from Equations 2.20, as

these are typical magnitudes for the present experimental setups.
The axial component of the force F_z^M has a weak dependence on z and r, as it is quantified by Figure 2.22a: a maximum axial force variation of 20% is achieved at $z \approx 50$ mm and $r \approx 100$ mm. Whereas, at $z \in (-150, 0)$ mm and $r \in (0, 50)$ mm, typical values in this thesis, the axial magnetic force has fluctuations below 2%. On the other hand, the radial force F_r^M has a stronger dependence on r and z (see Figure 2.22(b)). At 100 mm away from the axis and z=50 mm, the radial force becomes as high as 30% of the reference axial force at the center $F_z^M(0, 0)$. While, at the ranges $z \in (-150, 0)$ mm and $r \in (0, 50)$ mm the maximum value of radial force is reduced to less than 10% of its axial counterpart.

Finally, the relative magnitude of the axial and radial forces can be calculated:

$$\frac{F_r(r, z)}{F_z(r, z)} = 1/4 \frac{\mathrm{G_z}\ r}{\mathrm{G_z}\ z + B_0}. \tag{2.21}$$

As the objective is to solely counteract gravity, a radial force is not desired and the latter ratio needs to be minimised. There are two ways to achieve it: keep r small compared to $(z + B_z(0)/\mathrm{G_z})$; and/or have the biggest possible value for B_0. The latter approach is ideal because it allows to have a bigger volume (r-z) where the axial force is homogeneous and the radial forces are small. Albeit it translates to more current on the coils (recall that $|\mathbf{B}| \propto I$) and, therefore, thicker coils' winding and the subsequent need of external cooling.

Although it is not necessarily of interest here to fully compensating the gravitational pull, a.k.a. levitation, it is relevant to comment that these results are in agreement with Earnshaw's theorem (Earnshaw, 1842), which proves that the dynamics of a magnetic dipole $\mathbf{M}$ in an external magnetic induction $\mathbf{B}$ cannot have a stable equilibrium point ($\nabla^2 U_M > 0$, with U_M the magnetic energy). In this case there is a non-restitutive radial force that will drift an object away from the axis and prevent any stable levitation.

2.4.3 Magnetic Particles

The permanent magnets of spherical shape used here are made of neodymium (NdFeB / N35) with a Nickel coating that protects it from corrosion. These are bought from the company HKCM Engineering. When choosing a material for a magnet there are a number of properties to take into account, they usually come encoded in a B-H curve. These curves represent in the magnet's magnetic flux density (in the magnet's surface) versus the external magnetic field applied. In this context, the principal 3 properties to look at are:

1. remanent magnetic field ($|\mathbf{B}_{\mathrm{rem}}|$), which measures the strength of the magnetic field produced by the magnet when no external magnetic field is applied.

2. Coercivity, the material's resistance to becoming demagnetized when an external magnetic field is applied.

3. Curie temperature (T_c), the temperature at which the material loses its magnetisation.

It is needed to revise the temperatures of operation and compare them with the curie temperature, in this case around $300°C$. It is worth to note that the demagnetisation process is not sudden but gradual, and even at temperatures lower than Curie's it can be some demagnetisation. Also, the operation temperature limit can be often set by the coating resistance. For all the particles the maximum operation temperature is $80°C$. In the context of this thesis where the experiments are performed in liquid water, the temperature is always below $80°C$.
On the other hand, if the external magnetic field is strong enough, demagnetisation may occur even at room temperature. The magnetic induction needed to completely demagnetise the particles is approximately 1.4 T, that is far bigger than the approximately 10 mT magnetic fields

here set. Furthermore, no measurable demagnetisation was measured for these magnets when subjected to a 10 mT magnetic induction, at room temperature.
Having analysed the previous aspects of the magnets and the setup it is possible to affirm that the magnet's magnetisation $|\mathbf{M}|$ will be constant along all measurements. The magnetisation can be calculated from the remanent magnetic field data given by the manufacturer ($|\mathbf{B}_{\text{rem}}| = 1192\ mT$) and the particle radius (in this case $r = 0.5$ mm), as mentioned in Eq 2.12:

$$|\mathbf{M}| = |\mathbf{B}_{\text{rem}}|V/\mu_0 = 4.96 \times 10^{-8}\ G^{-1}\ m^2\ s^{-2}. \tag{2.22}$$

Although the companies selling magnets have some public information about their products, they do not give explanations from first principles about the properties of magnetic materials, the interested reader can refer to the book from Miyazaki and Jin (2012).

2.4.4 Equations of motion in a fluid media

This report applies the previously described gravity modification method in the context of a particle settling in a flow. Hence, Equations 2.10-2.11 have to include the hydrodynamical effect on the particles. Neglecting added mass and history forces the fluid adds a drag (Brown and Lawler, 2003) and a torque (Lukerchenko et al., 2008) to the particles yielding the following equations of motion:

$$\mathbf{F} = (m_p - m_f)g\ \hat{z} - \mathbf{M}\cdot\nabla B - \frac{1}{8}C_D\pi d_p^2\rho_f\mathbf{v}|\mathbf{v}|, \tag{2.23}$$

$$\mathbf{T} = -1/64 C_\omega\rho_f\omega|\omega|d_p^5 - \mathbf{M}\times\mathbf{B}, \tag{2.24}$$

with particle density ρ_f, kinematic viscosity ν, the angular velocity ω and the translational C_D and rotational C_ω drag coefficients.
The relative magnitude of the magnetic to hydrodynamical perpendicular force $F_r^* = F_r^M/F^{\text{fluid}}$, and torque $T^* = T^M/T^{\text{fluid}}$ can be bounded:

$$F_r^* = F_r^M/F^{\text{fluid}} = \frac{|\mathbf{M}|\ \frac{r\ (\mathrm{G_z})^2/4}{\sqrt{(\mathrm{G_z})^2/4r^2+(\mathrm{G_z}z+B_0)^2}}}{1/8 C_D d_p^2\pi\rho_f v^2} \approx \frac{10^{-6}\ \text{N m}}{10^{-3}\ \text{N m}} = 10^{-3}, \tag{2.25}$$

$$T^* = T^M/T^{\text{fluid}} = \frac{|\mathbf{M}||\mathbf{B}|}{1/64 C_\omega d_p^5\pi\rho_f\omega^2} \approx \frac{10^{-3}\ \text{N m}}{10^{-13}\ \text{N m}} \approx 10^{11}. \tag{2.26}$$

This bounds were obtained using the following values: $r = 10$ cm; $z = 10$ cm; $G_z = \nabla_z B = 290$ G/m; $B_0 = 20$ G; $C_D = 1$; $d_p = 1$ mm; $\rho_f = 10^3$ kg/m^3; $v = 1$ m/s; $\omega = 2$ rad/s; $C_\omega = 1$.
The ratio F_r^* is small but it will grow when different values of $\nabla_z|\mathbf{B}|$ are used. Furthermore, when studying the settling of spheres in a Quiescent Moderate Reynolds number flow, these two forces will become comparable and a drift (i.e. the magnetic force has the ability to push particles perpendicularly to gravity) will be measured. This will set the smaller effective gravity that can be achieved in this configuration without getting particle drift, that results in $\tilde{g} = 0.43$ m/s^2.
On the other hand, as $T^* \gg 1$, the claim that the angle ψ between the particle magnetic moment $\mathbf{M}$ and $\mathbf{B}$ can be taken as approximately zero is now justified: the magnetic torque is much bigger than that from the hydrodynamics, hence the particle can only rotate about the gravitational vertical axis (see Eq. 2.14).

Finally, note that the fluid drag and torque are simpler under the Stokes regime (Brown and Lawler, 2003; Gatignol, 1983):

$$\mathbf{F} = (m_p - m_f)g\ \hat{z} - \nabla(\mathbf{M}\cdot\mathbf{B}) - 3\pi d_p\eta\mathbf{v}, \tag{2.27}$$

$$\mathbf{T} = \pi\eta d_p^3\omega - \mathbf{M}\times\mathbf{B}. \tag{2.28}$$

2.4.5 Magnetic Field at the laboratory

The six circular coaxial coils used to generate the magnetic induction deduced in Equation 2.19 were sketched in Figure 2.1, and their characteristics were shown in Table 2.1. As previously mentioned in Section 2.1, the coils are modelled as infinitesimal current loops, therefore the theoretical axial magnetic field at the 6-coil system axis reads:

$$\mathbf{B} = B_z\hat{z} = 2\pi 10^{-7} \sum_{i=1}^{6} \frac{R_i^2\ N_i\ I_i}{((z+Z_i)^2 + R_i^2)^{1.5}}\hat{z}. \tag{2.29}$$

In order to set the magnetic field presented in Equation 2.19 at the laboratory, a nonlinear least squares fit of Equation 2.29 to the axial component of Equation 2.19: $B_z = \mathrm{G_z\ z + B_0}$, is performed. The fit's fixed parameters are: N_i (number of turns); R_i (coil's radius); G_z; B_0; and Z_{fit} the range at which the fit is performed. The output parameters are then: I_i the current in each coil; and Z_i the distance between the coils geometrical centre and origin of coordinates z=0.
Note that there is no radial dependence on Eq. 2.29, i.e. the equation is that of the magnetic induction at the axis of a system of 6 infinitesimal current loops. The condition of linear axial magnetic field $B_z = \mathrm{G_z\ z + B_0}$ is then imposed by the fit at the axis of the coil system. The magnetic field outside the axis is estimated by the Maxwells' equations, i.e. the inhomogeneity deduced theoretically and presented in Figure 2.22 is used to estimate the magnetic field out of the axis. Although, the magnetic induction homogeneity outside the axis was qualitatively measured and it was found to be well represented by Figure 2.22.

Two sets of values for G_z, $\mathrm{B}_z(0)$ and Z_{fit} were chosen:

1. **Case** CstB**: homogeneous vertical magnetic induction.**
   In this case $\nabla_z|\mathbf{B}| = 0$ & $|\mathbf{B}| \neq 0$, yielding no magnetic force and the rotation-blocking effect previously discussed, respectively.

2. **Case** Cst∇_zB**: constant gradient vertical magnetic induction.**
   In this case $\nabla_z|\mathbf{B}| \neq 0$ & $|\mathbf{B}| \neq 0$, yielding a magnetic force (that will compensate gravity) and the rotation-blocking effect, respectively.

The two cases differ on the magnetic force magnitude (proportional to $\nabla_z|\mathbf{B}|$) that they impose on the particles: whereas the Case Cst∇_zB blocks the rotation and applies a force, Case CstB blocks the rotation and the applied force is approximately zero. In particular, the size of the fit window Z_{fit} needed to be shortened for Case Cst∇_zB, to minimise inhomogeneities in $\nabla_z|\mathbf{B}|$.

The specific values of these two sets of input parameters in the non-linear fit to Eq. 2.29 are presented in Table 2.5. Alongside with the corresponding magnetic induction measurements discussed in what follows.

	Non-linear fits		Measurements	
	Case CstB	Case Cst∇_zB	Case CstB	Case Cst∇_zB
G_z (G/m)	0	-270	0 ± 20	-286±25
B_0 (G)	20	26	20±1	22±1
Z_{fit} (mm)	(-150, 50)	(-100, 0)	✗	✗

Table 2.5: Details of the two external magnetic induction of interest: Case CstB and Cst∇_zB.

On the other hand, the specific coil's positions (Z) and currents (I) given by the fit, for the Cases CstB and Cst∇_zB are presented in Table 2.6. Note that for the Case CstB only four coils are used as the two extra ones have arrived to the laboratory later.

	Case CstB		Case Cst∇_zB	
	Z (cm)	I (A)	Z (cm)	I (A)
Coil 1	✗	✗	26.5	2.28
Coil 2	14.2	4.24	24.5	-1.77
Coil 3	12	0.20	12	1.70
Coil 4	-12	0.16	0	0.52
Coil 5	-14.2	4.46	-24.5	-3.06
Coil 6	✗	✗	-26.5	-1.16

Table 2.6: Coil's positions and currents given by the fit to obtain the two cases of magnetic induction profile: Cases CstB and Cst∇_zB. The coils' names follow the definition presented in Figure. 2.1.

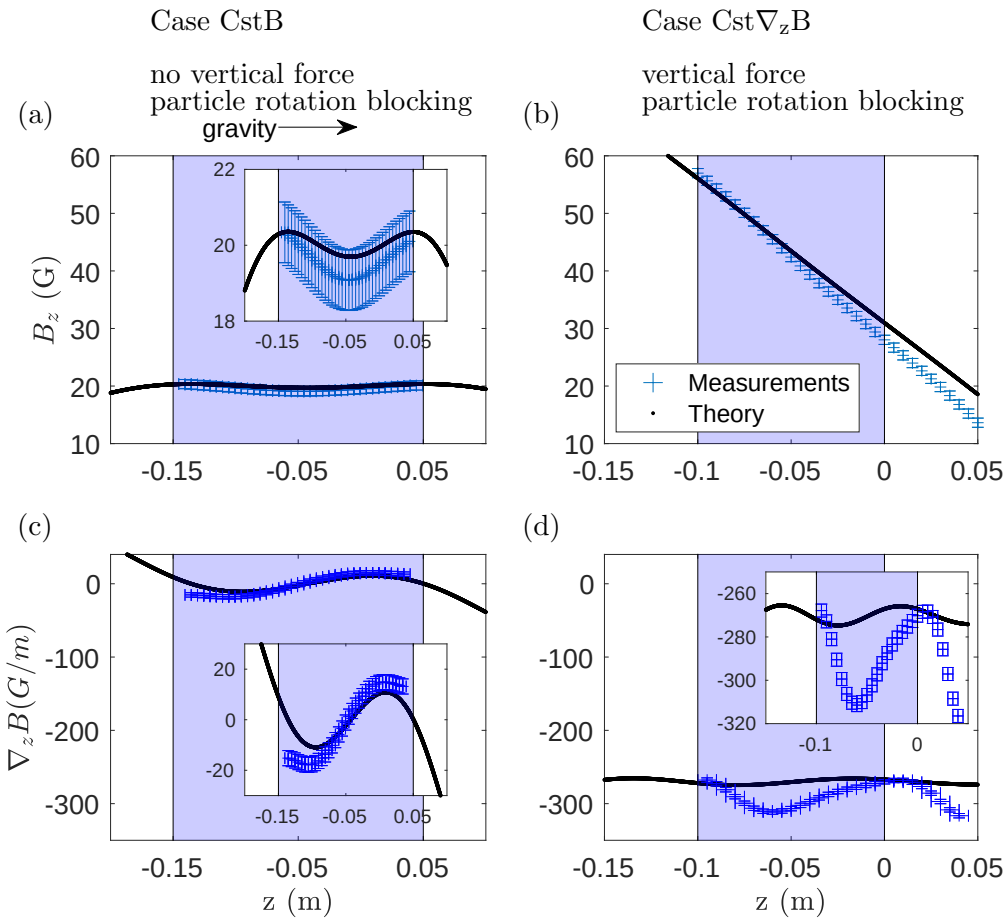

Figure 2.23: Gradient of B_z computed from the axial magnetic induction measurements (blue points) and simulations (black line). Whereas the insets present the measurements and simulations results of the axial magnetic induction as a function of the distance to the origin z=0. Finally, a horizontal arrow denotes the rightwards gravity direction.

Figure 2.23 presents the profiles of axial magnetic induction B_z (first row) and its gradient $\nabla_z B$ (second row) obtained by the non-linear fit (black lines), and from measurements performed with a Teslameter Bell 7030 (blue crosses), against the distance to the origin. Finally, the blue shade represents the region where the fit was performed (i.e. Z_{fit}). Note that because the magnetic field is measured at the axis, and the Equation fitted represents the centre of a current loop (where the magnetic field in purely vertical): $\mathbf{B} = B_z \hat{z}$.

It can be seen that, for the case CstB, the magnetic field measurements (Fig. 2.23(a)) overlap with the simulation, whereas the magnetic induction gradient (Fig. 2.23(c)) presents an average difference of 10%, with maximum values of 30% that occur near the extremes of Z_{fit} (blue shaded region). On the other hand, the Case Cst∇_zB has a 10% discrepancy on the magnetic induction gradient $\nabla_z B$ (Fig. 2.23(d)). Whereas the magnetic field overlaps with the measurements in the range $Z_{fit} \in (-0.1, 0)$ m (Fig. 2.23(b)). Additionally, note that the radial-to-axial force ratio (Equation 2.21) takes the following maximum values for the cases CstB and Cst∇_zB: 1×10^{-2} and 1.5×10^{-1}, respectively.
In the case of the 1 mm spherical permanent magnets that are here studied, these inhomogeneities in the magnetic induction gradient produce a 5% variability in the effective gravity value for the Case Cst∇_zB, and an effective gravity between $\tilde{g} = 9.5$ m s^{-2} and 9.8 m s^{-2} for Case CstB.

The presence of oscillations in the magnetic field can be explained as the interference between the higher harmonics that compose the total magnetic induction of each coil, these phenomena has been observed (Mailfert, Alain et al., 2015). The interaction between these higher harmonics can be modified considerably by small errors in the coil positioning. In this sense, Figure 2.24 shows the theoretical magnetic field (a) and gradient (b) for Case Cst∇_zB, evaluated at different coil Z_1 positions: its original position (black); 5 mm downwards (red); and 5 mm upwards (magenta). While in the subplot (a) the three magnetic fields are almost indistinguishable, the differences are clear in subplot (b): within the measurement region (grey area) a difference of up to 3% is present. Note that the coil positioning error in this thesis is estimated to be 5 mm, this value includes the approximation of the coils by an infinitesimal loop at its geometrical centre, and the 2 mm precision in positioning given by the tools used. These factors explain the difference between the experimental measurements and the simulated values encountered in Figure 2.23.

2.4.6 Phenomena Validation at Re ≈1

The settling of an axially magnetised NdFeB/N35 permanent magnet shaped as a parallelepiped of $10 \times 2 \times 2$ mm^3 (see Figure 2.25(a)) in the Stokes regime was measured to qualitatively check the validity of Equations 2.28-2.27. These equations imply that the magnetic force should change its sign (i.e. switch between enhanced/diminished gravity) if the external magnetic induction inverts its direction: a permanent magnet with magnetisation $\mathbf{M}$ aligns with the external magnetic induction $\mathbf{B}$. The axial magnetic induction chosen to test this has a constant gradient equal to -250 G/m, and it is set such that its sign changes at z=0 (see Figure 2.25(b)). The magnetic induction gradient variability of this magnetic field is analogous to that of the Case Cst$\nabla_z B$, although for the sake of simplicity it is not presented here. In this manner, the parallelepiped dynamics can be measured for $\mathbf{B} > 0$, $\mathbf{B} < 0$, and the sign transition. Finally, to have the magnetic field dominating the particle dynamics, i.e. to avoid wake instabilities, the rectangular container presented in Section 2.1 is filled with pure glycerol (Sigma-Aldrich W252506-25KG-K) with a kinematic viscosity of 1 Pa s, that leads to $Re_p = 2$ (based on the full cuboid length).
Figure 2.25(a) presents a raw image of the cuboid as it rotates following the external magnetic induction direction. In particular, Figure 2.25(c) presents the cuboid angle with the vertical as

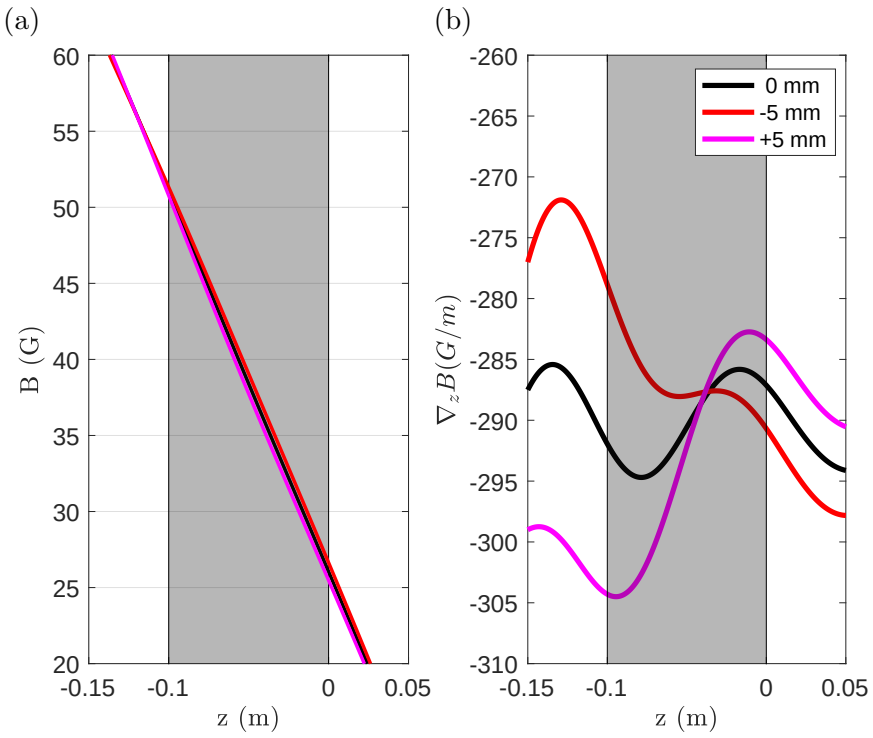

Figure 2.24: Theoretical magnetic field (a) and gradient (b) for Case Cst∇_zB, evaluated at different coil Z_1 positions. It shows the original coil position (black); 5 mm downwards (red); and 5 mm upwards (magenta).

a function of the distance to the center of the coil system (where the magnetic field changes its sign). It can be seen that at the beginning $\psi \approx 0$ (magnetisation anti-parallel to gravity); when approaching z=0 the cuboid starts going to its stable horizontal position ($\psi = 90$ °) citepSB ours; finally, when the magnetic field starts pointing downwards, the cuboid rotates to align with the new magnetic induction direction, yielding $\psi = 180°$. This behaviour was expected from Equation 2.11. On the other hand, Figure 2.25(d) presents the cuboid axial position (z) as a function of time. Two different settling velocities (i.e. two different slopes) can be seen for $z < 0$ ($\nabla B < 0$ and $B < 0$) and $z > 0$ ($\nabla B < 0$ and $B > 0$). Finally, note that in Figure 2.25(c) the time to go from $\psi = 0°$ to 90° is shorter than the time to go from $\psi = 90°$ to 180°. The later is caused by the settling velocity increase that occurs when the magnetic field changes of sign: an angle versus position plot does not present such asymmetry.
Two things were then verified in the laboratory: 1) a constant gradient magnetic field can modify the settling velocity; 2) the magnetic field direction (and the consequent particle orientation) define the direction of the force, as stated in Equation 2.10. It is worth to remark that the magnetic torque (proportional to $|\mathbf{B}|$) needs to be much bigger than any fluid-related torques to keep $\mathbf{M}$ parallel to $\mathbf{B}$ and so to have a constant magnetic force.

2.5 Dryden Drop Tower Experiment – Zero-g

The micro-gravity experiments will be performed in the Dryden Drop Tower facility, located at the Center for Engineering, Science and Technology at Portland State University (see Fig. 2.26). The tower has a height of 31.1 m with a free fall distance of 22.2 m, where gravity values of $10^{-3}g_0$ ($g_0 = 9.8$ m/s^2) are achieved for approximately 2 s. The experiment, mounted on a rig,

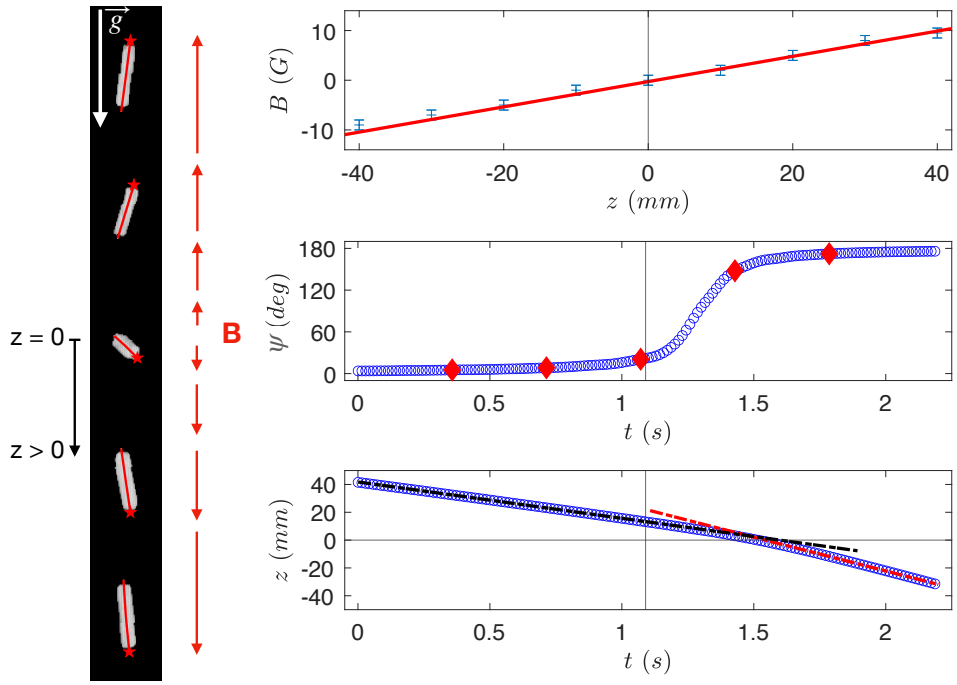

Figure 2.25: (a) Four snapshots of a permanent magnet shaped as a parallelepiped settling at $Re_p = 2$, in a magnetic field with constant gradient such that $B(z = 0) = 0$ (Panel (b)). (c) Parallelepiped's angle with the vertical as a function of time, alongside with red diamonds that identify the five states represented in Panel (a). (d) Parallelepiped's vertical position as a function of time, alongside with two linear fits (dashed lines), in the $B \neq 0$ regions , that show the difference in settling velocity on both sides, i.e. diminished and enhanced effective gravitational pull.

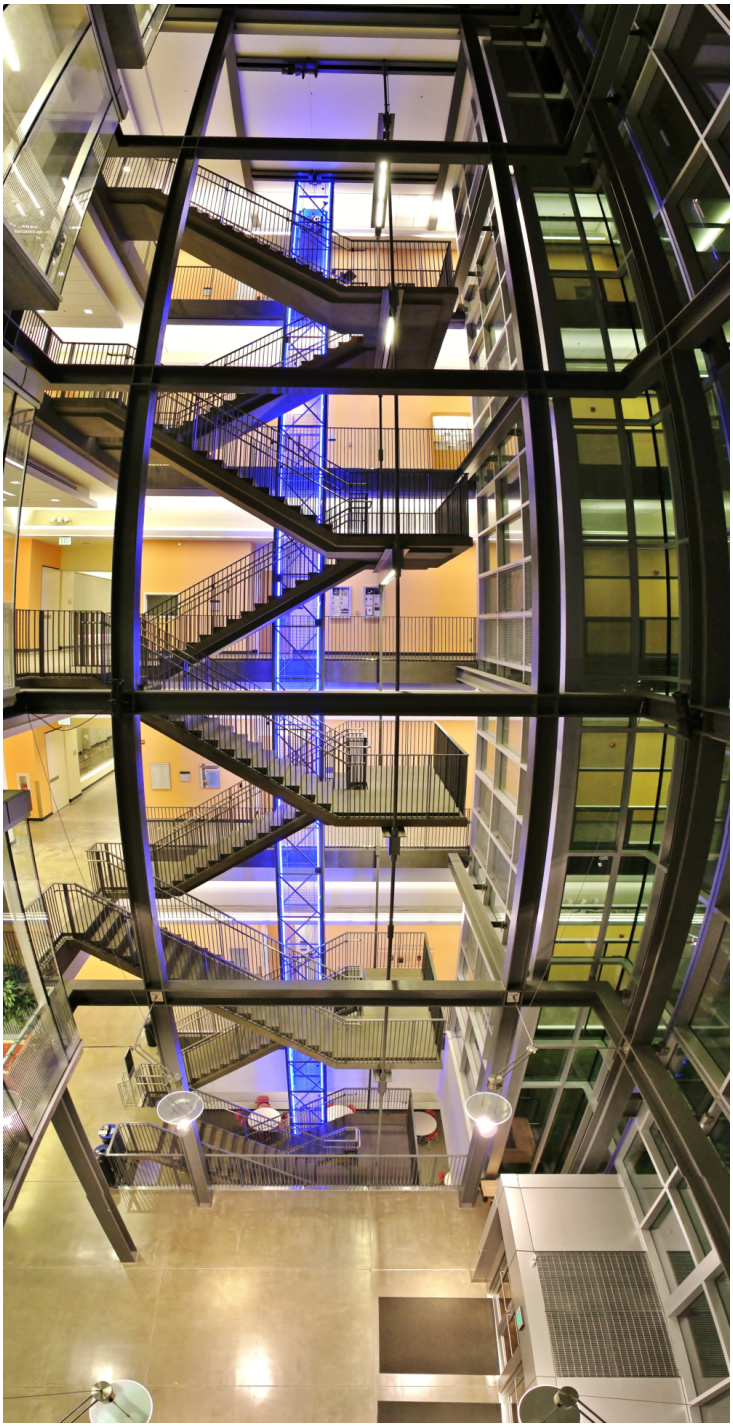

Figure 2.26: Photography of the Dryden drop tower.

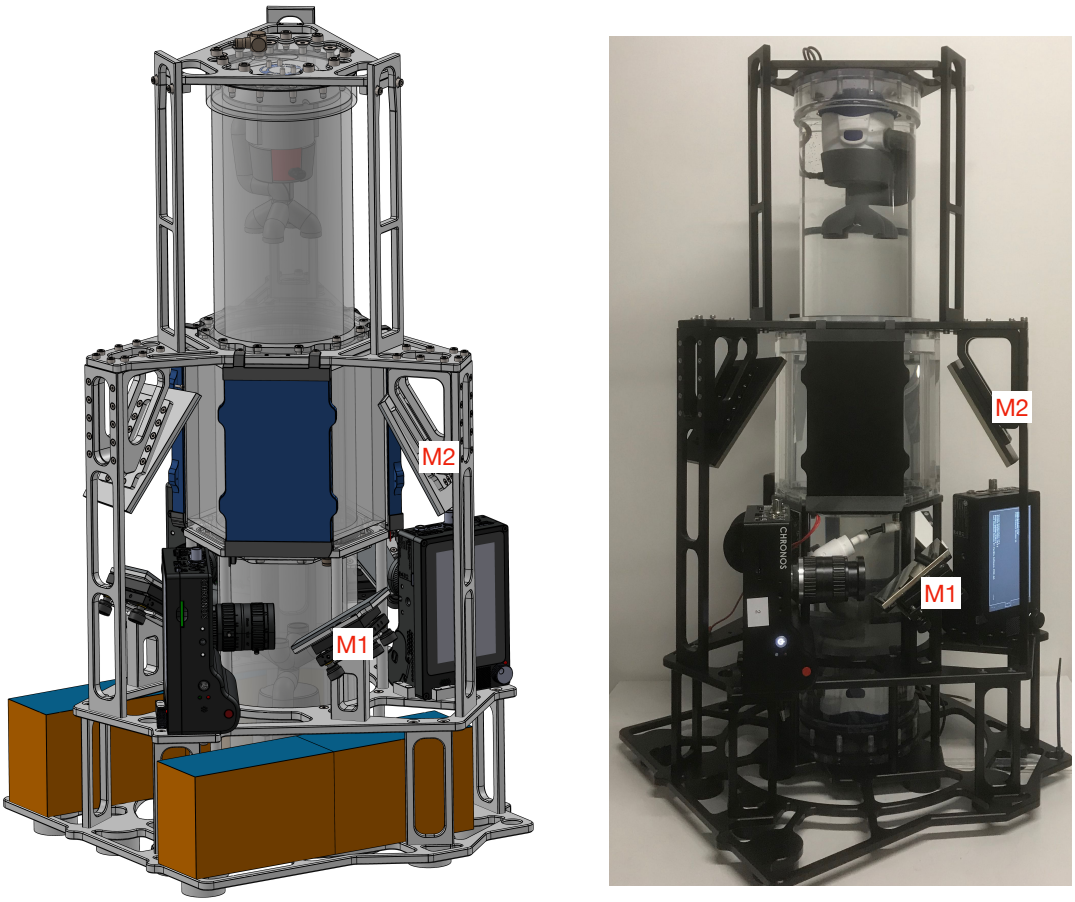

Figure 2.27: Digital render (a) and photography (b) of the zero-g experiment.

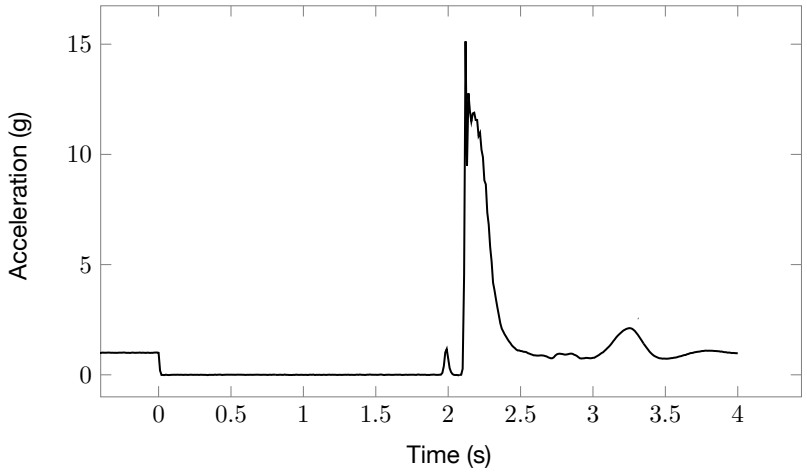

Figure 2.28: Rig's acceleration as a function of time, with $t = 0$ the beginning of the free fall. Particularly, there is a peak deceleration of $15g$ at $t \approx 2.3$ s.

falls freely inside a drag shield that takes the form of a $56 \times 40 \times 81$ cm^3 rectangular prism, guided by two 'non-contact' stainless steel cables that run the length of the tower. Two aluminium fins rigidly mounted to the drag shield pass through two 1.1 m long permanent magnets at the lower level of the tower. The relative motion between the fins and parallel magnetic fields generate eddy currents in the fins that resist motion and decelerate the drag shield before it comes to rest on foam pads (i.e. eddy current braking). Limited by the latter, the maximum weight of the experiment is 100 lbs ($\approx$ 45 kg). Figure 2.28 shows the rig's acceleration as a function of time, with $t = 0$ the beginning of the free fall. Particularly, this deceleration mechanism leads to a peak and average decelerations of 15 g_0 and 8.5 g_0, respectively. Furthermore, a touch-screen computer permits safe, single-operator control of the primarily automated tower functions which allows for a short automated retrieval time of 5 min that permits repetitive realisations in the same day. The latter is one of the great advantage of this facility as it allows to get big amounts of data, in several different configurations. That was a problem with the only 2 experiments regarding inertial particles in turbulence, in zero-g, (Fallon and Rogers, 2002; Hwang and Eaton, 2006) presented in Section 1.5: because they were performed in parabolic flights, the zero-g time (linked to data statistic convergence) and the repeatability were limited.

The experiment built to fit the drop tower's rig is presented in Figures 2.27(a)-(b), in particular, Fig. 2.27(a) presents a 3D render of the complete device, whereas Fig. 2.27(b) shows a photography of it. The only differences between these two Figures are: the batteries are only present in the render – orange-blue boxes at the base of Fig. 2.27(a); cables and water pipes are only present in the photography. The setup consists on: three cameras Chronos 2.1HD from Krontech; a set of six mirrors – see optical system presented below; the water-tank presented in Section 2.2; a set of batteries; three backlights of those presented in Section 2.5 – see blue (Fig.2.27(a)) or black (Fig.2.27(b)) rectangles in the tank's center; and a 3D printed box containing the power management system.
The development of this experiment was a challenge in a number of ways, mostly linked to the weight and size constraints: as previously mentioned, this experiment needs to fit in a rig of $56 \times 40 \times 81$ cm^3 and it has to be much lighter than $\approx$ 45 kg. Note that 45 kg is the absolute maximum weight, one would like to be well below it. For example, the weight constraints forced the elimination of unnecessary material from the aluminium experiment's skeleton (see empty spaces in black aluminium pieces in Fig. 2.27(b)), while keeping a rigidity good enough to stand the $15g_0$ peaks that occur in the deceleration. Not only the deceleration is to be taken into account, there are also low frequency vibrations (of the order of 0.5 Hz) called g-jitter, that are well documented for experiments at low gravity (Kamotani and Ostrach, 1992; Thomson et al., 1996). In the case of a drop tower they are mainly caused by the atmospheric drag. To measure these, a 3D accelerometer is mounted in the experiment, in this way the spectra of the g-jitter can be quantified and thus removed from the measurements via temporal filters on the data. Note that the specifics of the g-jitter can not be known before hand because they depend on the particularities of each experiment dropped, such as total mass, inertia tensor, etc.
In particular, the device is composed of three main pieces:

1. the cylinder where the turbulent flow is produced (already described in Section 2.2.2);

2. the power and control system;

3. the optical system that allows particle tracking.

2. The setup is powered by a pack composed of three Lithium Iron Phosphate batteries LiFePO4 of 12.8 V and 10 Ah connected in series (Expert Power, 2021). The total voltage of this the ensemble ranges then from 39 V to 36 V as they discharge. While the choice of a series connection imply the handling of a larger voltage, it also provides an balanced discharge of the batteries which, with a parallel connection, would otherwise have required a dedicated

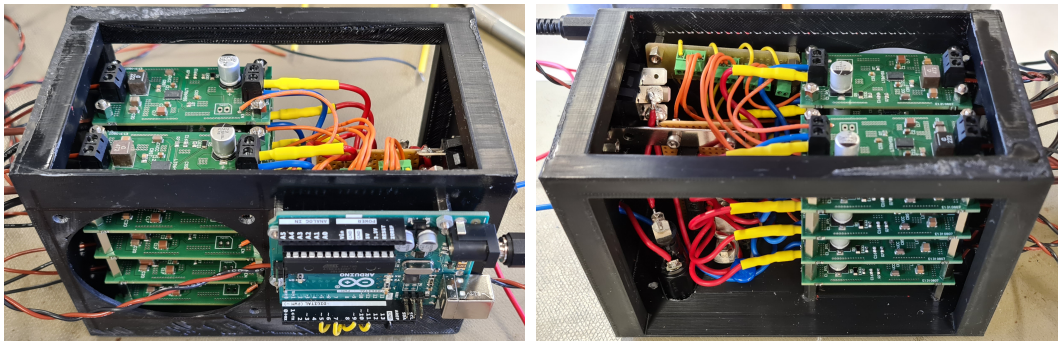

Figure 2.29: Photography of the electronics box. It contains the power managing system that gives power autonomy to the experiment.

circuit. The battery pack voltage is regulated by a set of custom DC-DC converter boards (see red circles in Fig. 2.29) made by the staff of our laboratory's Electronic Engineering Service. Each electrical component in the setup is powered by a single DC-DC board that delivers the correct voltage. The boards are based on the LT8645S synchronous step-down (buck) regulator IC (Analog Devices, 2021b). Using such a switched-mode converter ensures a higher DC-DC conversion efficiency and a compact design. Furthermore, each board has an "enable" pin that, when receives a voltage (lower) higher than 0.1 V, (disables) enables the board's output. These pins then allow a subset of the converter boards to be switched ON or OFF to save energy. In this way, it is possible for the pumps and backlights to be turned off during the retrieval time, which is much longer that the free fall time (4 minutes versus 30 seconds). By doing so, the autonomy time of the experiment is increased by approximately 6 times: yielding an approximate autonomy of 4 hours. In particular, when all the components are turned on the current rises up to $7.2A$, although that only happens for approximately 3 seconds. The control of the enable pins is done as follows: the enable pin of each converter board is connected to a digital output (DO) of an Arduino microcontroller (Arduino, 2021) mounted in the experiment. As such, the enable pin is used as a digital switch, activating the converters only when the Arduino's DO is set to high. The switching of each element is controlled depending on the experiment's acceleration, that is measured by an accelerometer (Analog Devices, 2021a) connected to the Arduino board. The Arduino is then programmed with instructions to turn on the elements, with certain time delays, after a threshold on its acceleration is reached.
The power from the batteries is directed to a 3D printed ABS plastic box that contains the 10 DC-DC converters: 3 for the cameras; 3 for the backlights; 1 for the Arduino UNO; 2 for the pumps; and 1 for the network switcher (see item 3. in this Section). It also contains a 7.5 A fusible and a manual switch to power all the DC-DC boards. Additionally, a schottky diode is placed at the input of each card to avoid inverse currents: in some conditions, for instance when the batteries are disconnected, the voltage on the DC-DC converters outputs can be bigger than their inputs and produce a current from output to input that burns the converters. Finally, the box contains a fan to cool down the DC-DC converters that is powered by the same board as the Arduino board. Photography's of this box are presented in Figure 2.29.

3. A set of three black and white high speed cameras model Chronos 2.1 HD (Krontech) is set to track the dynamics inside the water-tank via a 4D-LPT system (see Section 2.3). Furthermore, the lenses were the model CK10M5020S43 from the company Lensagon: 10 Megapixel C-Mount for 4/3" sensors (the sensor size of these cameras), with a focal length of 50mm (Lensagon). Due to the very limited horizontal space on the rig, the cameras can not point directly to the tank. To circumvent this limitation, 2 surface mirrors, that allows the cameras to be nearly in contact

with the water tank, were placed to redirect the light rays to each camera. These mirrors can be identified in Figure 2.27(a)-(b), as they are labeled by the red letters M1 and M2, and a light ray path is sketched in red. The mirror M2 is fixed to the aluminium structure, whereas M1 is fixed to a Kinematic Mount from Thorlabs (Thorlabs) with additional holes to hold the mirrors. In particular, these are custom made synthetic fused silica mirrors made by the French branch of the company OptoSigma.
Note that in the deceleration process the static water pressure is increased up to a maximum of 15 times the value at g_0. In a rectangular water tank, the glue in each sharp edge is necessarily a weak spot that could experience fatigue after a number of drops. For that reason, the water tank was chosen to be cylindrical. Although the curved shape presents another challenge that is image distortion – see, for example, the distortion on the image of the upper pump in Fig. 2.27(b). As it was commented for the ground experiments using this turbulent flow (Section 2.2.1), a planar boundary is needed between the air and water phases to avoid image distortion. In the ground experiments with the magnetic fields, that was accomplished by inserting the cylinder on the rectangular water tank utilised in the Quiescent Flow Experiments. In the case of the Drop Tower a similar approach is taken: a PMMA irregular hexagon is built around the cylinder, as presented in Fig. 2.5. This hexagon has 3 "big" and 3 "small" planar faces: the backlights are located in the big ones; and the light rays going to the cameras pass through the small ones. This imbalance in size is to maximise the acquisition volume: consider that with a fixed lens angular aperture, the image in real world units grows with the distance to the lens. Finally, this hexagon is filled with water and sealed, at top and bottom, by toric joints that are closed by a plastic ring (see Fig. 2.5).
The three cameras are synchronised by one of the Arduino's Digital Outputs: the cameras take images continuously, overwriting the old ones, and when the acceleration measured by the sensor mounted in the Arduino board is bigger than g_0, the Arduino's DO goes high and all the images in the cameras' internal memories are saved. Later, the cameras are connected to a local network, via a network switcher mounter in the experiment, that allows to control them remotely. This is important as the rig can only be accessed from one side, leaving two cameras out of reach. In this way, after each drop, when the experiment is towed to the control center at the top of the drop tower one can connect a computer (a Raspberry pi, for example) to the local network and download the images to the external SD hard drives connected to each camera.

This experimental device is the result of the work of a number of people:

- The 3D mechanical conception, including the optical arrangement, and some aspects of the electronic control were done by Richard Pedurand, a postdoc working in our group at the time.
- The electronic control and powering of the device was mostly handled by the Electronic Engineering Service of the ENS de Lyon, in particular by Pascal Metz and his student Mathurin Picoul.
- The rest of things were done by me, such as all the tests and the service unit.
- Myself, Dr. Plihon and Dr. Bourgoin managed the project as a whole.

Illumination

Custom backlights to implement the 4D-LPT system presented in Section 2.3 are needed to be designed and constructed to fit the technical constraints of both the experiments with magnetic fields and those performed in the Dryden Drop Tower. In the magnetic case, as the backlights needed to be inside the coils that generate the external magnetic field (see Fig. 2.1), it has to be

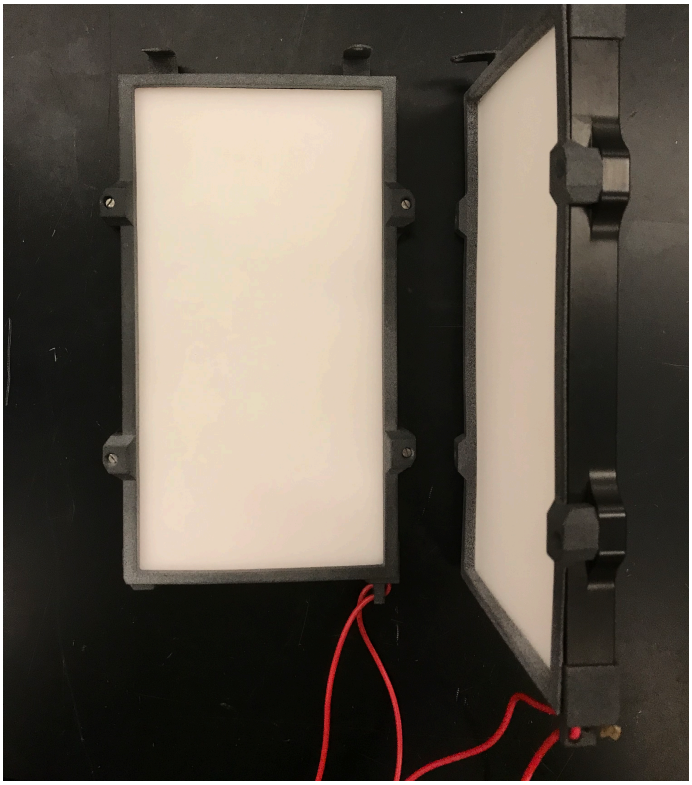

Figure 2.30: Two backlights assembled.

non-magnetic. On the other hand, the size constraints in the Dryden Drop Tower experiment need a particularly compact backlight.

In backlight illumination, there is a good contrast between particles and background: the image is white (although saturation must be avoided) and the particles black (see Figure 2.17). An homogeneous light panel is needed as inhomogeneities may make difficult the application of thresholds to resolve the particles' edges and to distinguish them from dust or other undesired points in the image. Additionally, one would like the biggest possible backlight intensity for two reasons: (1) smaller lens aperture, yielding a deeper depth of field; (2) higher acquisition frequency, i.e. faster shutter speed.
For many purposes affordable commercial solutions are available. However, the geometrical constraints of the Dryden Drop Tower required to design and build dedicated light panels.

The light panels are usually made of led stripes because of their efficiency. The panel performance is directly related to both the led stripe density and intensity, i.e. the intensity per unit of surface requires to be maximised. Additionally, there are two main types of led layouts to build a light panel: (a) led array on the panel surface (i.e. leds facing the camera), plus a diffuser to homogenise the light; or (b) led stripe on the border of the panel (facing inwards), plus a wave guide and a diffuser. Although option (a) has a higher led density and therefore higher light intensity, to achieve homogeneity, a thick diffuser has to be set and the light intensity is highly diminished. Furthermore, the diffuser needs to be placed at a minimum distance l from the led array to allow the light beams to overlap before reaching the diffuser, and so to achieve a good degree of homogeneity: $l >$ led separation$/(2 \times \tan(\text{beam angle}/2))$. With a beam angle of 120° and a led separation of 3.3 mm: l = 0.34 mm, that is too small and therefore difficult to set experimentally. It is then chosen to build option (b).

The led stripe chosen is composed by SMD 2216 leds and it has the following properties: distance between leds of 3.3 mm, 6000 K, 6.92 lumens/led, beam angle of 120°, 24 VDC, 24 W/m,

and a width of 10 mm. A transparent acrylic plaque 5 mm thick is used as wave guide, whereas a sand-blasted acrylic plaque 3 mm thick acts as diffuser. The wave guide-leds and diffuser-wave guide separations are set to virtually zero: the plaques are in contact with each other, and the wave guide position coincides with the position of the leds so all the light enters the wave guide. Moreover, it was empirically found, as one might expect, that the wave guide thickness must match that of the leds to have maximum light transmission.
Two sizes of led panels are build: a *big one* for the Quiescent Flow Experiments and a *small one* for the Turbulent Flow Experiments. Their dimensions are: 150×250 mm^2 and 110×180 mm^2; whereas their consumption is 24 W and 20 W, respectively. Figure 2.30 presents a picture of the led panel that is utilised in the Dryden Drop Tower experiment (the *small one*).
Furthermore, all the materials that compose the backlights are non-magnetic: the diffuser and wave guide are made of plastic; the leds are non-magnetic (at the magnetic fields here utilised); the back cover and supports are made of aluminium and ABS plastic, respectively. This is crucial as these panels are also used in the Quiescent Flow configurations where the Magnetic Gravity Compensation method is applied: if the light panels were magnetic, the external magnetic field inside the water tank would be distorted.
The led panel presented in Fig. 2.30 is powered with 30 V for more than 10 hours (not continuously) without any sign of damage.

Note that considerable improvements on the measurements might be achieved if the spectral response of the cameras is taken into account to choose the wavelength of the light panel. In the present case, the spectra response is maximal at approximately 500 nm, that matches the characteristics of the chosen leds. In particular, the sensitivity of a colour camera can be higher for a particular colour and the led wavelength should be chosen to match it.

Chapter 3

Slender bodies

3.1 Theoretical background

The experiments were performed with cylindrical rods of density ρ_p, half-length l and radius a. The particle aspect ratio is $\beta = l/a$. The motion of the particles is characterized by the center of mass, $\mathbf{x}$, and the unit vector, $\hat{\mathbf{n}}$, characterizing the orientation, as illustrated in Fig. 3.1. The orientation of $\hat{\mathbf{n}}$ is defined by the angles ψ and θ. The vector $\hat{\mathbf{p}}$ is orthogonal to the projection of $\hat{\mathbf{n}}$ onto the horizontal $(\hat{\mathbf{e}}_x, \hat{\mathbf{e}}_y)$ plane, $\hat{\mathbf{p}} = \sin(\psi)\hat{\mathbf{e}}_x - \cos(\psi)\hat{\mathbf{e}}_y$, and $\hat{\mathbf{e}}_z$ is the vertical. In the experiments, the initial angular velocity was orthogonal to the plane spanned by $\mathbf{g}$ and $\hat{\mathbf{n}}$ (See Section 3.3). In other words, the angle ψ remains constant, so the angular dynamics is described by θ only.

The particle Reynolds number is defined as

$$\mathrm{Re}_p = \frac{l|\mathbf{w}|}{\nu}, \tag{3.1}$$

where $\mathbf{w}$ is the velocity of the center of mass. The particle Reynolds number allows to quantify the respective role of the inertial and viscous effects in the problem. In this experiments, Re_p does not exceed 1. As a consequence, the force and the torque acting on the particle originate from the viscous term (the Stokes forces and torques, $\mathbf{f}_S$ and $\mathbf{T}_S$), plus contributions due to fluid inertia, which are derived in a systematic perturbation expansion in the parameter Re_p, denoted here as $\mathbf{f}_I$ and $\mathbf{T}_I$.

The equations of motion for the translational degrees of freedom read as

$$\frac{d\mathbf{x}}{dt} = \mathbf{w} \quad \text{and} \quad \frac{d\mathbf{w}}{dt} = \mathbf{g} + \frac{\mathbf{f}_H}{m_p}, \tag{3.2}$$

where $\mathbf{f}_H \equiv \mathbf{f}_S + \mathbf{f}_I$ is the total hydrodynamic force acting on the particle, and m_p is its mass. The general expression for the Stokes force is: $\mathbf{f}_S = 6\pi a\mu\mathbb{A}(\hat{\mathbf{n}})(\mathbf{u} - \mathbf{w})$, where μ is the dynamic viscosity of the fluid, $\mathbf{u}$ is the undisturbed velocity of the fluid at the particle position (equal to zero in a quiescent flow), and $\mathbb{A}(\hat{\mathbf{n}})$ is the resistance tensor Kim and Karrila (1991). The tensor $\mathbb{A}$ can be expressed in terms of two coefficients, $A_\perp$ and $A_\parallel$: $A_{ij} = A_\perp(\delta_{ij} - n_i n_j) + A_\parallel n_i n_j$. The expressions of $A_\perp$ and $A_\parallel$ depend on the shape of the particle (rod or spheroid), and in particular on its aspect ratio β, and are given in Appendix 3.4.1. In the limit $\beta \gg 1$, the expressions reduce, for the two shapes considered, to $A_\perp = 2A_\parallel = (4/3)[\beta/\log(\beta)]$. Equation (3.2), together with the specific form of $\mathbf{f}_S$, imply that if $|\mathbf{f}_I| \ll |\mathbf{f}_S|$ the particle velocity $\mathbf{w}$ relaxes with a characteristic (Stokes) time $\tau_p = a^2\log(\beta)(\rho_p/\rho_f)/(3\nu)$. In the experiments, it is observed that the characteristic time scales of the particles (of the order of seconds) are much longer than τ_p (of the order of a milliseconds). This implies that the dynamics is overdamped, and that the center-of-mass velocity can be obtained by solving $\mathbf{g} + \mathbf{f}_H/m_p = 0$ at any time.

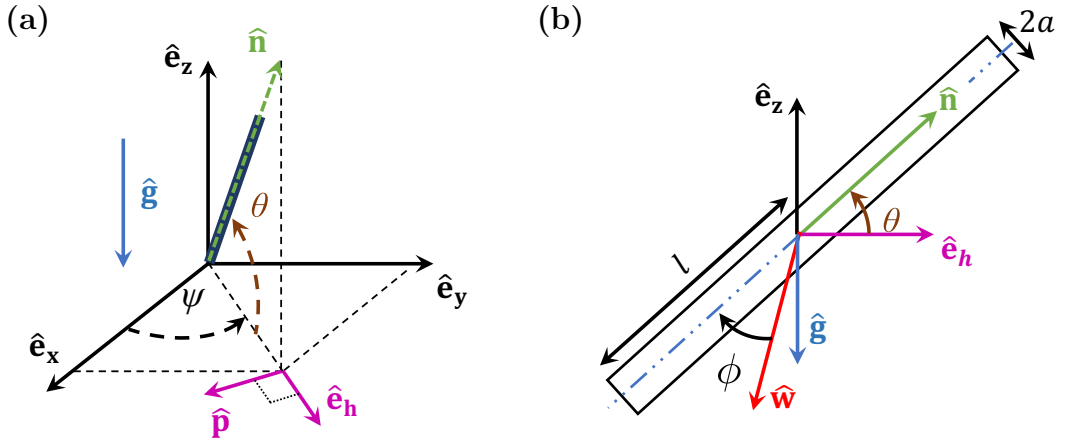

Figure 3.1: Representation of the settling cylindrical particle (a) in 3D and (b) in the vertical plane $(\hat{\mathbf{n}}, \mathbf{g})$. See text for details.

The effect of finite fluid-inertia leads to a correction to the Stokes force. In the case of a spheroid, this correction to the resistance tensor can be expressed as: $\mathbb{A}^s \rightarrow \mathbb{A}^s + \mathbb{A}^s_I$. Similarly, the expressions for the corrections to the force for a slender rod, $\mathbf{f}^r_I$, can be found in Khayat and Cox (1989), and are given in the Appendix 3.4.1.

As stated before, in the experiments the change in the orientation of a particle is due to variations of the angle θ only. The equation of motion for this angle is obtained by projecting the equation for the angular momentum along the $\hat{\mathbf{p}}$-direction:

$$I_p \ddot{\theta} = (\mathbf{T}_S + \mathbf{T}_I) \cdot \hat{\mathbf{p}}, \tag{3.3}$$

where I_p is the moment of inertia of the particle with respect to its center of mass, perpendicular to its axis ($I_p = \frac{1}{12} m l^2$). As it was the case for the force, the torque can be written as the sum of a contribution due to viscous forces (Stokes), $\mathbf{T}_S$, and a contribution due to inertia, $\mathbf{T}_I$. The general expression for the Stokes torque is Jeffery (1922): $\mathbf{T}_S = 6\pi a \mu [\mathbb{C}(\boldsymbol{\Omega} - \boldsymbol{\omega}) + \mathbb{H} : \mathbb{S}]$, where $\boldsymbol{\omega}$ is the angular velocity of the solid, $\boldsymbol{\Omega} = 1/2(\nabla \wedge \mathbf{u})$ the vorticity, and $\mathbb{C}$ is the resistance tensor. The last term, $\mathbb{H} : \mathbb{S}$, involves the strain in the fluid, which vanishes in a fluid at rest, as considered here. In a quiescent fluid, the torque is therefore proportional to the particle angular velocity ω which equals $\dot{\theta}$ since the ψ angle is constant:

$$T_S \equiv \mathbf{T}_S \cdot \hat{\mathbf{p}} = -C_S \dot{\theta}, \tag{3.4}$$

where C_S is a resistance coefficient proportional to μa^3. The dimensionless constant of proportionality depends on the details of the particle. In the very large β limit, the expression for C_S reduces to

$$C_S = \frac{8\pi}{3} \frac{\mu l^3}{\log \beta}. \tag{3.5}$$

As it was the case for the dynamics of the center of mass, the resistance term $-C_S \dot{\theta}$ provides a characteristic relaxation time scale for the particle orientation which is, up to a numerical factor of order 1, equal to the characteristic time τ_p already introduced Anand et al. (2020). The time scale over which the angle θ evolves is also found to be very long compared to τ_p, which ensures that, to a very good approximation, the left-hand side of Eq. (3.3) can be set to 0. This allows to relate directly, via Eq. (3.4), the projection of the torque due to the inertial forces, $\mathbf{T}_I$, perpendicularly to $\hat{\mathbf{n}}$, $T_I \equiv \mathbf{T}_I \cdot \hat{\mathbf{p}}$:

$$T_I = C_S \dot{\theta}. \tag{3.6}$$

Determining the torque $\mathbf{T}_I$ is a very challenging problem, even in the small-Re_p limit.

The results from this experiments carried out with rods are compared to the results of the slender-rod theory of Khayat and Cox (1989) , valid asymptotically when $\beta^{-1}\mathrm{Re}_p \ll 1$ and $\beta \gg 1$. The first criterion is very well satisfied in the experiments. The second one is not, since $\beta = 8$ or 16 in the experiments, and since the small parameter in the slender-rod theory is $1/\log\beta$. It is therefore compared also with a second perturbative theory for the torque, valid when the particle has a spheroidal shape Dabade et al. (2015). This theory is valid for any arbitrary aspect ratio, β, but only to leading order in Re_p. Furthermore, it was found numerically to describe the torque acting on spheroidal particles quite well, with an accuracy of $\sim 20\%$ for $\beta = 6$ over the range of Re_p in the experiment Jiang et al. (2021). Note that the theory was derived for spheroidal particles, but it is expected that it nevertheless works qualitatively for rod-like particles of the same aspect ratio and the same particle mass.

At small Reynolds numbers, symmetry considerations Jiang et al. (2021); Subramanian and Koch (2005) indicate that the torque takes the form

$$\mathbf{T}_I = F(\beta)\rho_f l^3(\mathbf{w}\times\hat{\mathbf{n}})(\mathbf{w}\cdot\hat{\mathbf{n}}). \tag{3.7}$$

The expression (3.7) shows that $\mathbf{T}_I$ is along $\hat{\mathbf{p}}$, and that its norm reads

$$T_I = F(\beta)\rho_f l^3|\mathbf{w}|^2\sin\phi\cos\phi = C_I|\mathbf{w}|^2\sin 2\phi. \tag{3.8}$$

The shape factor $F(\beta)$ depends only on the particle aspect ratio. As a result, the factor C_I is known for spheroids Dabade et al. (2015) and in the slender-rod limit Khayat and Cox (1989); Lopez and Guazzelli (2017); its values are denoted as C_I^s and C_I^r. The corresponding formulae are summarized in Appendix 3.4.2. Note that the expressions for the two theories coincide in the limits $\mathrm{Re}_p \to 0$ and $\beta \to \infty$, where: $C_I(\beta) \approx -5\pi/[3(\log\beta)^2] \times (\rho_f l^3/2)$. Combining Eqs. (3.6) and (3.8) leads to the prediction of the model that

$$\dot{\theta} = \frac{C_I}{C_S}|\mathbf{w}|^2\sin 2\phi. \tag{3.9}$$

This overdamped torque model for rods was found to qualitatively reproduce experimental results of rods settling in a cellular flow Lopez and Guazzelli (2017), and allowed to investigate the settling of anisotropic particles in turbulent flows Kramel (2017). The expressions of the torque for spheroids have been validated numerically Jiang et al. (2021), and used to study theoretically and numerically the settling of spheroids in turbulence Anand et al. (2020); Gustavsson et al. (2019, 2021); Sheikh et al. (2020). Note that when the fluid is in motion, the local velocity gradients may contribute to the torque expression Einarsson et al. (2015). In this experimental setup, with $\rho_p/\rho_f \gg 1$, the corresponding contributions are negligible.

3.2 Experimental setup

The experiments were performed in the PMMA tank described in Section 2.1. The tank was filled with pure glycerol (Sigma-Aldrich W252506-25KG-K), with a density $\rho_f = 1216$ kg m^{-3} and dynamic viscosity $\mu = 1.05$ Pa.s at 22°C in which the settling of heavy cylindrical particles was measured. The cylindrical particles were made of Tungsten-Carbide (WC with 5% Cobalt), manufactured by Comac Europe, with a density $\rho_p = 14800$ kg/m^3, resulting in a fluid-to-particle density ratio of $\rho_p/\rho_f = 12.1$. Cylindrical rods were milled and filed at lengths $2l = (16.0 \pm 0.5)$ mm and (8.0 ± 0.5) mm, from long cylinders of diameter $2a = 1$ mm, resulting in cylindrical particles with aspect ratios β of 16 and 8. The surface roughness was measured using a Scanning Electron Microscope, leading to an average arithmetic roughness value of 15 μm.

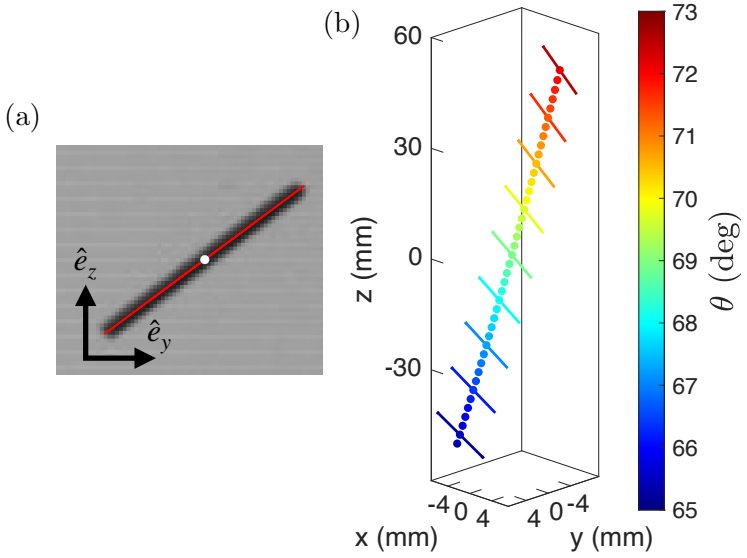

Figure 3.2: (a) Typical raw image obtained from one camera showing the particle of aspect ratio $\beta = 16$, the detected particle center line (in red) and center of mass (white dot). (b) Successive positions of a rod's center line and center of mass during one experiment (for $\beta = 16$), color coded by the value of the angle θ. For the sake of clarity, only one center of mass data-point out of 80, and one center line each 5 center of mass data-points are shown.

The particle Reynolds number Re_p was measured to lie between 0.255-0.390 for $\beta = 16$, and 0.105-0.150 for $\beta = 8$. The particles trajectories were reconstructed from images acquired using two cameras (fps1000 model from The Slow Motion Company). The cameras acquire images at a frame rate of 1400 fps with a resolution of 720×1280 px^2. The volume over which the trajectories of the particles are reconstructed is $130 \times 130 \times 200$ mm^3.

The particles are backlight-illuminated by using two white and homogeneous light panels (presented in Section 2.5). A typical image captured from one camera shows the projection of the cylindrical particle in the (y, z) plane in Fig. 3.2(a). For each image, and on both cameras, the detection of the particle is computed using the MATLAB function *regionprops*, which detects the particle's major axis and minor axis, center of mass and orientation (see Fig. 3.2(a)). The 3D orientation of the particle is then obtained from a 4D-LPT algorithm (see Section 2.3): a set of five points on the major axis are matched in 3D from the projections in the (y, z) and (x, z) planes (the five points are equally spaced between the two extrema). The particle position and orientation is thus reconstructed in 3D, as shown in Fig. 3.2(b), and all parameters related to the dynamics of the particles can be subsequently computed. The evolution of a typical sedimentation experiment is displayed in Fig. 3.2(b), from top to bottom as time increases, clearly demonstrating that the angle θ decreases in time. The tracking error of the 4D-LPT system was shown to be inferior to 130 μm, or equivalently 50% of the pixel size. Additionally, the raw data was filtered via the convolution with a Gaussian kernel of variance $\sigma = 1.2 \times 10^3$ and $\sigma = 8 \times 10^2$, for $\beta = 8$ and 16 respectively.

The particles were released in the fluid with chemical tweezers: the particle is completely submerged, and released only when the glycerol's free surface was at rest (approximately after 15 s). A minimum time of 90 s is taken between two successive realisations to assure that the fluid has no motion left from the previous drop. For both $\beta = 8$ and $\beta = 16$, 25 independent realisations have been acquired.

With the values of the physical parameters in the experiment, the characteristic time scale of the

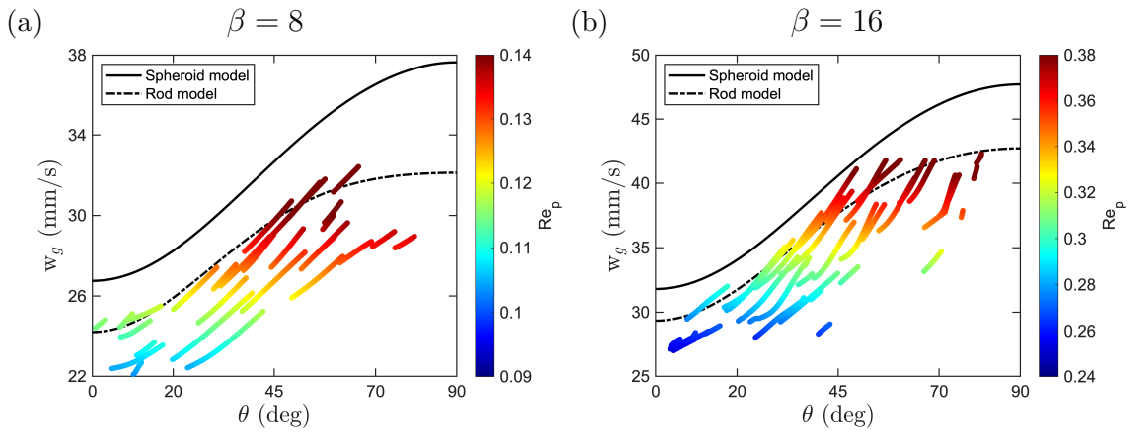

Figure 3.3: Evolution of the vertical component of the velocity w_g as a function of the angle θ for (a) $\beta = 8$ and (b) $\beta = 16$. Each line represents one realisation, color-coded by the value of Re_p. Prediction for the spheroid model (solid black line) and for the slender-rod theory Khayat and Cox (1989) (dashed-dotted black line).

particles, τ_p, introduced in Section 3.1, does not exceed 10^{-3} s, which is very short compared to the characteristic time of the evolution. Note that, additionally, there is 150 mm of fluid above and below the visualization volume. A particle then travels for approximately $1000\tau_p$ before and after it enters the detection volume: the fluid above makes the particle lose memory of any transient produced in the release; whereas the fluid below keeps the particle away from the bottom-wall at all times.

3.3 Experimental Results

Recall that the motion of the rods was found to be, to a very good approximation, planar. Namely, the variations of the angle ψ between the projection of the $\mathbf{n}$ vector on a horizontal plane and an arbitrary fixed horizontal vector, as illustrated in Fig. 3.1 (a), are less than 5° during a given experiment, with a typical value of 2° over all realisations. Therefore, the values of the torques valid in the case of a planar motion, where the orientation is parametrised solely by the angle θ are used.

3.3.1 Translational motion

For all experimental realisations, the ratio between the particle inertial term $m_p \mathrm{d}\mathbf{w}/\mathrm{d}t$ and the Stokes force term $\mathbf{f_S}$ in Eq. (3.2) was computed to be of order 10^{-3}. In other words, the particle inertia contribution in the translational dynamics can be neglected and the particle dynamics is overdamped, as anticipated from the ratio between τ_p and the characteristic time for the evolution of θ.

Figure 3.3 shows the settling velocity of the rod w_g, defined as the projection of $\mathbf{w}$ on the vertical vector $\mathbf{g}/|\mathbf{g}|$, as a function of its orientation θ, for the two values of β considered. As for all the figures in this Chapter, each trajectory is color-coded with its instantaneous particle Reynolds number Re_p based on the particle half-length l. The time series of the evolution of θ are displayed in Fig. 3.4, and, as anticipated, it is observed that the position of the particle, hence its velocity, evolve over a time scale which is much longer than τ_p. It can also be observed in Fig. 3.3 that the settling velocity is an increasing function of θ: in other words, the settling velocity increases when particles become vertical. This can be readily understood, since the drag

decreases when θ increases from 0 to 90°. Therefore, the particle Reynolds number increases linearly with the settling velocity. The measured settling velocity is compared with the settling velocity calculated by integrating the equation of motion, Eq. (3.2), using for the hydrodynamic force the expressions for the spheroids model or for the slender-rod model, and including the particle inertia, despite its weak contribution in the overdamped regime. Recall that, in the framework of the spheroid model, the values of β and the mass m_p of the cylindrical particles used in the experiments are used, and not the values for a spheroid with exactly the same geometrical dimensions as that of the particles used in the experiments, for the computation of the resistance tensors $\mathbb{A}_S$ and $\mathbb{A}_I$ respectively due to the Stokes and to the fluid inertia corrections. The velocity predicted by the spheroid model is shown as a full black line in Fig. 3.3, and the prediction from the slender-rod model is displayed as a dash-dotted line.

For the two values of β considered, the predicted velocities overestimate the measured values, or equivalently, the predicted values of the hydrodynamic forces underestimate the actual force. However, the qualitative agreement is satisfactory: the relative difference is always smaller than 16% (for the spheroid model) and 6% (for the slender-rod model) for $\beta = 16$, and respectively 20% and 10% for $\beta = 8$. As expected, the agreement with the predictions is better for the slender-rod model than for the spheroid model, as the particles used in the experiment have a cylindrical shape. Nonetheless, as the aspect ratio increases, the agreement improves from $\beta = 8$ to $\beta = 16$, even with the spheroid model. These observations can be rationalized by noticing that the sharp ends at the extrema of the cylinder play a less important role when β increases.

The horizontal component of the measured velocity remains smaller than 20% of the vertical one, see Figure 3.7 in Appendix 3.4.3. The figure also shows the ratio of the horizontal and the vertical velocities predicted by the two models discussed in Section 1.3 for spheroids and slender-rods. It can be seen from Figure 3.7 that the ratio of the experimentally measured horizontal and vertical velocities is qualitatively consistent with the predictions of the two models.

3.3.2 Angular motion

Figure 3.4 shows the time dependence of the angle θ for the two aspect ratios considered, for a number of different initial rod orientations. The experimental data is color-coded with the instantaneous particle Reynolds number as indicated by the colorbar. The different realizations correspond to different initial orientations covering the range $\theta(t = 0) \in (0, \pi/2)$. For all realizations, θ decreases with time, meaning that particles tend to orient their broadside facing down, resulting in a maximal drag, as previously illustrated in Fig. 3.2(c). This trend, which has already been reported Bragg et al. (1974); Gustavsson et al. (2019); Jayaweera and Mason (1965); Lopez and Guazzelli (2017); Roy et al. (2019); Sheikh et al. (2020), is a consequence of the action of the inertial torque T_I. Equation (3.8) shows (for spheroids), in the case of a fluid at rest, that under the effect of this torque, the particle orientation has two fixed points, a vertical one ($\theta = \pi/2$), and an horizontal one ($\theta = 0$), but only the latter is stable. This is consistent with the observation that in Fig. 3.4 the magnitude of the angular velocity reduces as the particle approaches horizontal orientation, i.e. as θ tends to 0.

Finally, it is worth mentioning that the particle Reynolds number, Re_p, is smaller when the particle settles horizontally ($\theta = 0°$) as compared to vertically ($\theta = 90°$). This is a consequence of the fact that the drag exerted on a fiber settling broadside down is higher than that on a fiber settling with its narrow edge first. The later results in a velocity increase with θ, as seen in Figure 3.3.

The importance of the particle inertia term in the rotational dynamics, Eq. (3.3), from the ratio $I_p\ddot{\theta}/C_S\dot{\theta}$ is quantified. This ratio is very small, well below 10^{-3}, for the two β values. As a consequence, the left-hand side term of Eq. (3.3) is negligible with respect to either of the two terms on the right-hand side. In other words, the particle inertia contribution in the rotational

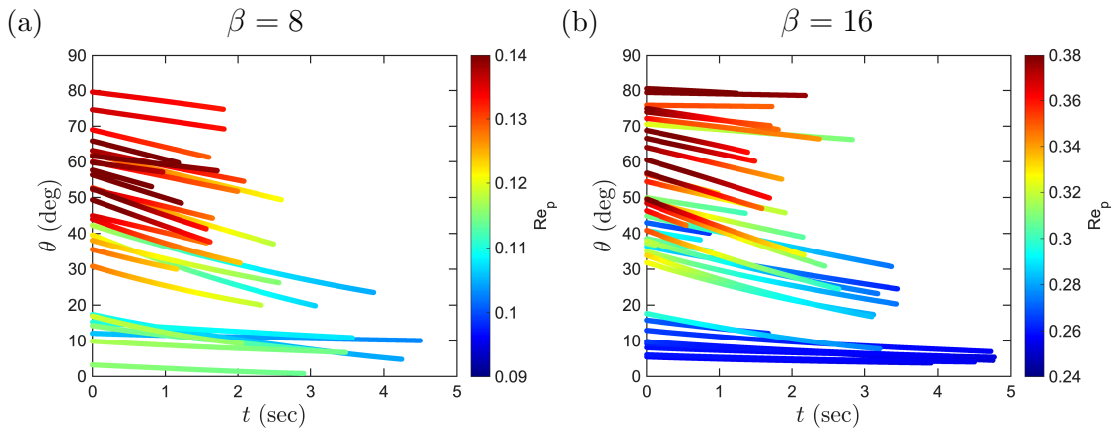

Figure 3.4: Time evolution of the orientation angle θ for a) $\beta = 8$ and b) $\beta = 16$ for all realizations, color-coded by the value of Re_p.

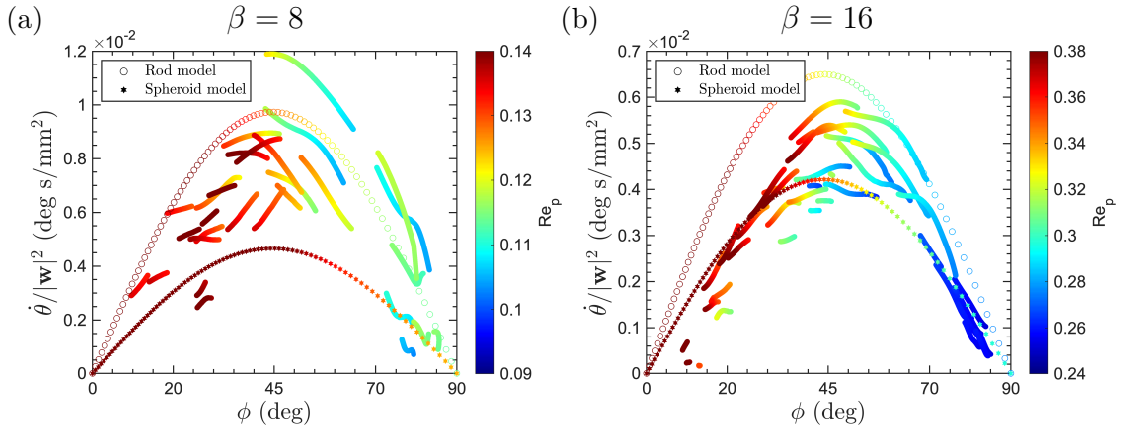

Figure 3.5: The measured angular velocity, $\dot{\theta}$, divided by $|\mathbf{w}|^2$, color coded by the local value of Re_p. The predictions of Eq. (3.9) are shown for the spheroid model and for the slender-rod model, as indicated by the legend. Panel (a) corresponds to $\beta = 8$, and (b) to $\beta = 16$.

dynamics can be neglected: the fluid-inertia torque (T_I) and the Stokes torque (T_S) essentially balance each other, so the particle angular dynamics is overdamped. Neglecting the second order derivative in Eq. (3.3) allows to simply relate the torque T_I to the instantaneous rotation rate, $\dot{\theta}$, which therefore provides an elementary way to determine T_I. To compare the results of the experiments with the prediction of Eq. (3.9), Fig. 3.5 shows, for $\beta = 8$ (panel a) and for $\beta = 16$ (panel b), the measured ratio $\dot{\theta}/|\mathbf{w}|^2$ as a function of the pitch angle, ϕ. The trajectories are color coded by the recorded value of the particle Reynolds number, Re_p, as indicated by the color bars. Equation (3.9) predicts that the points should be along a curve $\dot{\theta}/|\mathbf{w}|^2 = (C_I/C_S)\sin 2\phi$. The expected values for rods (empty circles) and for spheroids (stars) are indicated in the figure. It is also tested the torque expression proposed by Kharrouba et al. (2021): it leads in the regime of the experiments ($Re_p < 0.4$) to curves virtually indistinguishable from those plotted by using the slender-rod model from Khayat and Cox (1989) (empty circles). As shown in Fig. 3.5, the constants C_I/C_S for rods and spheroids differ by a factor ≈ 2 for $\beta = 8$, and ≈ 1.5 for $\beta = 16$.

The dependence of $\dot{\theta}/|\mathbf{w}|^2$ qualitatively follows the $\sin 2\phi$ prediction, although with a very large dispersion, particularly for $\beta = 8$. Interestingly, for both $\beta = 8$ and $\beta = 16$, the slender-rod theory overpredicts the value of $\dot{\theta}/|\mathbf{w}|^2$. On the other hand, the spheroid theory underpredicts the observed dependence, although the agreement becomes better when $\beta = 16$.

In view of the limitations of the theory, it is reassuring to see that the theoretical predictions provide the right order of magnitude for the experimental results. To discuss further, recall that the two theories used here for comparison have different shortcomings. Namely, the slender-rod theory (open circles) is valid over a larger range of Reynolds numbers (it only requires that, with this notation, $\mathrm{Re}_p \ll 1$); but the theory is valid only when $\log \beta \gg 1$, which is not particularly well satisfied. On the other hand, the theory for spheroids works for any aspect ratio (β does not need to be very large); but the predictions of the torque deviate by $\sim 30\%$ for values of $\mathrm{Re}_p = 0.3$, and deviations grow when Re_p increases Jiang et al. (2021). In this context, these observations fall in the delicate regime where both theories have shortcomings.

The relatively good agreement between the predictions of the slender-rod theory Khayat and Cox (1989) when $\beta = 8$ is surprising, as the value $\beta = 8$ is not particularly large. In fact, the agreement when β increases to $\beta = 16$ tends to deteriorate, which indicates that the slender-rod approximations does not provide a satisfactory description of the results. In a similar spirit, the relatively better agreement between these measurements for $\beta = 16$ and the prediction for spheroids is very likely to be coincidental: it is not expected to indicate a definite trend, valid at larger values of β.

It is interesting to compare the trends in these experiments with previous experimental investigations Roy et al. (2019). As already noticed, the expression for the torque obtained in the slender-rod approximation provides a very good description of the results at $\beta = 8$ ($\mathrm{Re}_p \lesssim 0.15$). At the comparable, higher values $\beta = 16$ in this case, and $\beta = 20$ in Roy et al. (2019), the prediction of the slender-rod theory Khayat and Cox (1989) overpredicts the torque. Notice that the Reynolds number in Roy et al. (2019) is significantly larger: $\mathrm{Re}_p \approx 1.6$, although the values of $\mathrm{Re_p}/\mathrm{rmlog}(\beta)$ are both small. At the larger value of $\beta = 100$ in Roy et al. (2019), the theoretical prediction of Khayat and Cox (1989) underestimates the experimentally measured torque. The Reynolds number, however, is even larger: $\mathrm{Re}_p \approx 8.6$, which adds some extra uncertainties when comparing the measurements with the theoretical expressions, obtained by assuming $\mathrm{Re}_p \ll 1$. Note, however, that the value of $\mathrm{Re}_p/rmlog(\beta)$ remains small: $\mathrm{Re}_p//rmlog(\beta) \approx 0.09$. For this reason, it would be extremely interesting to obtain results at the large aspect ratios considered in Roy et al. (2019), but at a lower Reynolds number, as could be obtained by using a more viscous fluid, as done here.

3.4 Appendix

3.4.1 Expression for the force acting on anisotropic particles

Recall the general expression for the Stokes force:

$$\mathbf{f}_S = 6\pi\mu a \mathbb{A}(\hat{\mathbf{n}})(\mathbf{u}-\mathbf{w}), \tag{3.10}$$

where the components of the tensor $\mathbb{A}$ are given by $A_{ij} = A_{\parallel} n_i n_j + A_{\perp}(\delta_{ij} - n_i n_j)$. The expression for $A_{\parallel}$ and $A_{\perp}$ are, in the case of a spheroid:

$$A^s_{\parallel} = \frac{8}{3}\frac{\beta}{\chi_0 + \beta^2\gamma_0} \quad \text{and} \quad A^s_{\perp} = \frac{8}{3}\frac{\beta}{\chi_0 + \alpha_0}, \tag{3.11}$$

with

$$\alpha_o = \frac{\beta^2}{\beta^2-1} - \beta\frac{\cosh^{-1}\beta}{(\beta^2-1)^{3/2}} \;,\; \gamma_o = \frac{-2}{\beta^2-1} + 2\beta\frac{\cosh^{-1}\beta}{(\beta^2-1)^{3/2}} \text{ and } \chi_0 = 2\beta\frac{\cosh^{-1}\beta}{(\beta^2-1)^{1/2}}. \tag{3.12}$$

In the case of a rod, the expression of the coefficients $A^r_{\perp}$ and $A^r_{\parallel}$ are:

$$A^r_{\parallel} = \frac{2}{3}\frac{\beta}{\log\beta} \quad \text{and} \quad A^r_{\perp} = \frac{4}{3}\frac{\beta}{\log\beta}. \tag{3.13}$$

The correction to the force due to inertial effects has been derived for spheroids in Oberbeck (1876). The expression for the coefficients $A^s_{I,\perp}$ and $A^s_{I,\parallel}$ are:

$$A^s_{I,\parallel} = [3A_{\parallel} - (A_{\parallel}\cos^2\phi + A_{\perp}\sin^2\phi)]A_{\parallel} \quad \text{and} \quad A^s_{I,\perp} = [3A_{\perp} - (A_{\parallel}\cos^2\phi + A_{\perp}\sin^2\phi)]A_{\perp}, \tag{3.14}$$

where $\phi = \cos^{-1}(\hat{\mathbf{w}}\cdot\hat{\mathbf{n}})$.

In the case of a rod, the fluid-inertia correction to the force, $\mathbf{f}^r_I$, is given by:

$$\frac{\mathbf{f}^r_I}{2\pi\mu|\mathbf{w}|l} = \left(\frac{1}{\log\beta}\right)^2 \Bigg[\tag{3.15}$$

$$\frac{2\cos\phi\hat{\mathbf{w}} - (2-\cos\phi+\cos^2\phi)\mathbf{n}}{2\mathrm{Re}_p(1-\cos\phi)}\Big\{E_1[\mathrm{Re}_p(1-\cos\phi)] + \log[\mathrm{Re}_p(1-\cos\phi)] + \gamma - \mathrm{Re}_p(1-\cos\phi)\Big\}$$

$$-\frac{2\cos\phi\hat{\mathbf{w}} - (2+\cos\phi+\cos^2\phi)\mathbf{n}}{2\mathrm{Re}_p(1+\cos\phi)}\Big\{E_1[\mathrm{Re}_p(1+\cos\phi)] + \log[\mathrm{Re}_p(1+\cos\phi)] + \gamma - \mathrm{Re}_p(1+\cos\phi)\Big\}$$

$$-[\cos\phi\mathbf{n} - 2\hat{\mathbf{w}}]\Big\{E_1[\mathrm{Re}_p(1-\cos\phi)] + \log(1-\cos\phi) + E_1[\mathrm{Re}_p(1+\cos\phi)] + \log(1+\cos\phi)$$

$$+\frac{1-e^{-\mathrm{Re}_p(1-\cos\phi)}}{\mathrm{Re}_p(1-\cos\phi)} + \frac{1-e^{-\mathrm{Re}_p(1+\cos\phi)}}{\mathrm{Re}_p(1+\cos\phi)} + 2(\gamma + \log(\mathrm{Re}_p/4))\Big\} + 3\cos\phi\mathbf{n} - 2\hat{\mathbf{w}}\Bigg],$$

where $\hat{\mathbf{w}}$ is the unit vector along fiber velocity $\mathbf{w}$, and γ is Euler constant.

3.4.2 Expression for the torque acting on anisotropic particles

The crucial parameter for this work is the ratio C_I/C_S in Eq. (3.9), where C_S and C_I are defined by Eq. (3.4) and (3.8) respectively.

Spheroids In the case of spheroids, the shape factor, $F(\beta)$, has been determined in Dabade et al. (2015) (see in particular Eq. 4.1). The function $F(\beta)$ is represented e.g. in Fig.1 of Jiang et al. (2021). In the limit of very large aspect ratio, $\beta \gg 1$, $F(\beta) \approx -5\pi/[3(\log\beta)^2]$.

The ratio between the two coefficients C_I and C_S^s, appearing in Eq. (3.9), is independent of particle size and only depends on β and ν; it is given as

$$\frac{C_I^s}{C_S^s} = \frac{\rho_f l^3 F(\beta)}{2}\frac{3}{16}\frac{1}{\pi\mu a^3\beta}\left(\frac{\alpha_o+\beta^2\gamma_o}{1+\beta^2}\right) = \frac{3}{32}\frac{\beta^2 F(\beta)}{\pi\nu}\left(\frac{\alpha_o+\beta^2\gamma_o}{1+\beta^2}\right) \tag{3.16}$$

The ratio in Eq. (3.16) is plotted in figure 3.6.

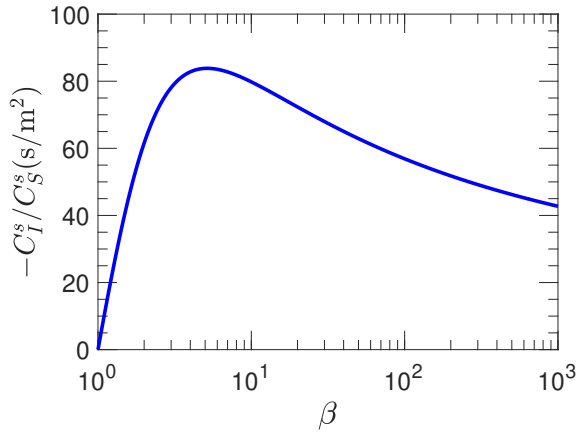

Figure 3.6: The ratio $-C_I^s/C_S^s$ in the case of spheroids, plotted as a function of β at $\nu = 1.05/1216\mathrm{m^2s^{-1}}$.

Slender-Rods In the case of rods, the expression for the torque T_I^r is given by Khayat and Cox (1989):

$$T_I^r = H(\mathrm{Re}_p,\phi)|\mathbf{w}|\sin 2\phi = C_I^r|\mathbf{w}|^2\sin 2\phi, \tag{3.17}$$

where $C_I^r = H(\mathrm{Re_p},\phi)/|\mathbf{w}|$ with the following expression for H:

$$\begin{aligned}\frac{(\log\beta)^2}{2\pi\mu l^2}H(\mathrm{Re_p},\phi) = {}& \frac{1}{2\mathrm{Re}_p(1-\cos\phi)}\left\{2+2\frac{e^{-\mathrm{Re}_p(1-\cos\phi)}-1}{\mathrm{Re}_p(1-\cos\phi)} - E_1[\mathrm{Re}_p(1-\cos\phi)] - \log[\mathrm{Re}_p(1-\cos\phi)] - \gamma\right\}\\ &+\frac{1}{2\mathrm{Re}_p(1+\cos\phi)}\left\{2+2\frac{e^{-\mathrm{Re}_p(1+\cos\phi)}-1}{\mathrm{Re}_p(1+\cos\phi)} - E_1[\mathrm{Re}_p(1+\cos\phi)] - \log[\mathrm{Re}_p(1+\cos\phi)] - \gamma\right\}\\ &-\frac{1}{\mathrm{Re}_p(1-\cos\phi)\cos\phi}\left\{1-\frac{1-e^{-\mathrm{Re}_p(1-\cos\phi)}}{\mathrm{Re}_p(1-\cos\phi)}\right\}+\frac{1}{\mathrm{Re}_p(1+\cos\phi)\cos\phi}\left\{1-\frac{1-e^{-\mathrm{Re}_p(1+\cos\phi)}}{\mathrm{Re}_p(1+\cos\phi)}\right\}.\end{aligned} \tag{3.18}$$

In the limit $\mathrm{Re}_p \to 0$, appropriate in the case of this study, and for $\beta \gg 1$, it is found that:

$$T_I^r \approx -\frac{5\pi}{6(\log\beta)^2}\rho_f|\mathbf{w}|^2 l^3\sin 2\phi, \tag{3.19}$$

which coincides with the expression derived in Dabade et al. (2015). The ratio C_I^r/C_S^r for rods reads

$$\frac{C_I^r}{C_S^r} = \frac{H(\mathrm{Re}_p,\phi)}{|\mathbf{w}|}\frac{3}{8\pi}\frac{\log\beta}{\mu l^3} = \frac{3}{8\pi}\frac{H(\mathrm{Re}_p,\phi)\log\beta}{|\mathbf{w}|\mu l^3}. \tag{3.20}$$

For a particle settling in a viscous fluid, the ratio in Eq. (3.20) is a function of particle orientation through the particle Reynolds number, Re_p, the settling velocity, $\mathbf{w}$, and the pitch angle, ϕ. The averaged values (over all orientations) of C_I^r/C_S^r for the cylindrical particles under consideration are -170 and -115 for $\beta = 8$ and $\beta = 16$, respectively. The corresponding values in case of spheroids are -82 and -75, see Fig. 3.6.

3.4.3 Horizontal translational dynamics

Figure 3.7 shows the ratio between the horizontal, w_h, and the vertical, w_g, components of velocity. As it was the case in Fig. 3.5, the expected ratios from the spheroid model (full line) and from the slender-rod model (dashed-dotted lines), for $\beta = 8$ (panel a) and for $\beta = 16$ (panel b) are shown. The ratios are all found to be small, less than $\sim 20\%$, in agreement with the predictions from the two models, which differ by no more than $\sim 20\%$ from each other.

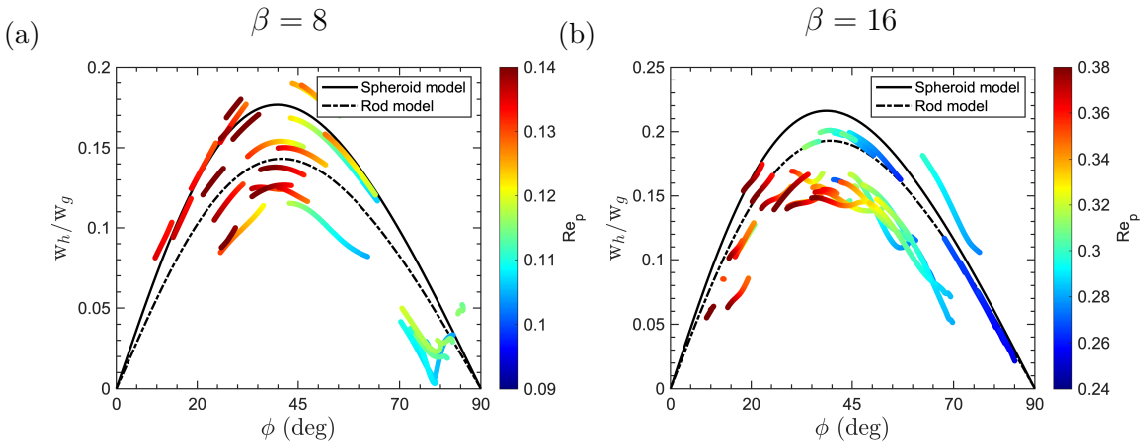

Figure 3.7: Ratio between horizontal (w_h) and vertical (w_g) velocity components, as a function of ϕ.

Chapter 4

Path instabilities

4.1 Spheres

The settling of spheres in a Quiescent Flow over a wide range of Galileo numbers and particle-to-fluid density ratios is studied in this Section. The results are compared with the predictions of numerical simulations presented in Section 1.4. These experiments are performed with the experimental device presented in Section 2.1.

4.1.1 Definition of the problem

The problem consists in a sphere of diameter d_p and density ρ_p settling in a quiescent fluid of density ρ_f and kinematic viscosity ν under the effect of gravity g. Recall that this problem is controlled by two dimensionless parameters (see Section 1.2): $\Gamma = \frac{\rho_p}{\rho_f}$ and $Ga = \sqrt{|\Gamma - 1| g d_p^3 / \nu^2}$. Depending on these, the settling sphere undergoes different trajectory types which are investigated in this Chapter with the following focusing on the following characteristics:

- Trajectory geometry
  - obliquity (mean angle with the vertical);
  - rectilinear or oscillating nature of the path;
  - planarity.
- Particle dynamics
  - frequency of path oscillations (when present);
  - terminal velocity (and drag).

All measured quantities are made dimensionless by the reference scales presented in Table 4.1. Recall that $u_g = \sqrt{|\Gamma - 1| d_p g}$ is the buoyancy velocity. The dimensionless quantities are denoted by an upper-script asterisk, for example, the particle velocity: $\mathbf{v}^* = \mathbf{v}/V_{\text{ref}}$.

$L_{\text{ref}} = d_p$	$V_{\text{ref}} = u_g$
$T_{\text{ref}} = u_g/d_p$	$f_{\text{ref}} = d_p/u_g$

Table 4.1: Reference length (L_{ref}), time (T_{ref}), velocity (V_{ref}) and frequency (f_{ref}) used to make dimensionless the measured quantities.

The square root of the ratio between the two eigenvalues λ_1 and λ_2 of this matrix, $0 \geq \sqrt{\lambda_2/\lambda_1} \leq 1$, is a measure of planarity (Zhou, 2016). This ratio depicts intermediate cases, whereas exactly planar and non-planar trajectories yield to $\sqrt{\lambda_2/\lambda_1} = 0$ and 1, respectively.

4.1.2 Experimental Protocol

The experiments are performed in the setup presented in Section 2.1. The trajectory of a single settling sphere is tracked in 3D at 2300 fps with a matching error smaller than 90 μm, that represents less than 35% of the pixel size.

To vary Ga:
The water tank is filled with different mixtures of glycerol (Sigma-Aldrich W252506-25KG-K) and distilled water. The glycerol concentrations range from 10% to 60%, leading to a kinematic viscosity and mass density ranges for the mixture of [1, 10^{-3}] Pa.s and [1020, 1200] kg m^{-3}, respectively.

To vary Γ:
Three kind of spheres with different mass densities are used:

- Metal (Particle M);
- Glass (Particle G);
- Polyamide (Particle P).

Their characteristics are listed in Table 4.2: average arithmetic roughness (Ra); particle density; diameter; particle-to-fluid density ratio ($\Gamma = \rho_p/\rho_f$) range; and Galileo number ($Ga = u_g d_p/\nu$) range.

Material	*Label*	*Ra* (μm)	ρ_p (kg/m^3)	d_p (mm)	Γ	Ga
Metal	M	9	7950	1 - 3	6.6-7.8	142-265
Glass	G	15	2500	3	2.1-2.5	112-270
Polyacetal	P	120	1150	6	1-1.1	100-300

Table 4.2: Properties of the investigates settling spheres. The rows present the three different particle materials studied: Metallic (M), Glass (G), and Polyamide (P). Whereas the columns show: average arithmetic roughness (Ra); particle mass density (ρ_p); particle-to-fluid density ratios explored (Γ); and the Galileo number ranges studied (Ga).

Three classes of data sets are taken with different optical magnification: "Short", "Large" and "Extended" field of view. They result in different measurement volume heights h, and hence different maximum particle's dimensionless trajectory lengths h/d_p: this was accomplished by changing the particle's diameter d_p and the height of the measurement volume h. The measured volume has a 150×150 mm^2 transverse section in all three cases. The details of these data sets are presented in Table 4.3. It has 3 rows representing the three data sets and 4 columns showing: h, the tracking volume height; d_M, d_G and d_P, the metallic, glass and polyamide particle diameters used.
All the above mentioned geometrical (obliquity, linearity and planarity) and dynamical characteristics (spectral content and terminal velocity) of particle trajectories cannot be equally addressed depending on the effective height of the measurement volume. Regarding inclination, it is empirically found that to measure it, trajectories of at least $h/d_p = 10$ are enough to have a converged trajectory angle. In other words, the standard deviation of the angle's distribution (composed of at least 15 different trajectories) is less than 0.5°. The trajectory inclination with the vertical is quantified by both the mean value of the dimensionless perpendicular (to gravity) velocity, and by the angle with the vertical of a 3D linear fit to the entire trajectory, yielding the same results.
To quantify the planarity via the method explained presented in Section 4.1.1, it is empirically found that longer realisations are needed: $h/d_p \gtrsim 80$.

Finally, to obtain the spectral content of the trajectories via a Power Spectral Density, it is found that the trajectories have to be even longer to yield acceptable results: $h/d_p \gtrsim 150$ (this mostly results from the Heinsenberg's uncertainty principle which requires long enough trajectories to achieve a good spectral resolution).
Note that these three different data sets are the product of a progressive experimental approach: the first set of measures was done in the "Short" configuration (i.e. measurement volume height $h = 70$ mm), that has the higher magnification, thus better spatial resolution. However, the preliminary data analysis made clear that the trajectories were too short to extract well defined spectra and trajectory planarity studies. Thus, at the expense of losing resolution, a lower magnification was set (i.e. $h = 200$ mm). This allowed to increase the trajectory length that still was found to be too short for a spectral analysis. Hence the particle diameter of the Particles M was decreased to 1 mm to yield the "Extended" configuration, that was empirically found to be long enough to quantify all the trajectory's characteristics.
In this sense, the data set "Short" is utilised only to quantify the trajectory inclination; "Long" is used for the inclination and the planarity; and "Extended" is used to quantify inclination, planarity and spectral content.

Additionally, the raw trajectories are filtered via the convolution with a Gaussian kernel of width $\sigma = 12$ frames that behaves as a low-pass filter with a cut-off frequency $f_c = \text{fps}/\sigma = 2300$ Hz$/\sigma = 191$ Hz. The higher dimensionless frequency detected in this study will be $f^* \approx 0.27$, these yield a frequency in real units of $f = f^*/(1/300\ s) = 81\ Hz$. Note that the relation between the cut-off frequency and the frequency to measure respects the Nyquist-Shannon sampling theorem.

Label	h(mm)	d_M(mm)	d_G(mm)	d_P(mm)	h/d_p range
Short	70	3	3	6	(11.6, 23.3)
Long	200	2	3	6	(33.3, 100)
Extended	200	1	✗	✗	200

Table 4.3: Rows present the three classes of data sets taken: Short, Long and Extended. Whereas the columns present the visualisation volume height h, the particle's diameters utilised for each particle material: d_M; d_G; and d_P, and the ranges of the ratio h/d_p achieved.

The experimental procedure is the following: the tank is filled with a water-glycerol mixture and, after thermal equilibrium is reached after approximately 24 hours (the temperature at different positions in the fluid's bulk differs in less than $0.5°C$), a standard calibration of the 4D-LPT system is performed. The spheres are released at the axis of the tank with chemical tweezers: they are completely submerged and released after approximately 20 s, when the fluid free surface is at rest. A minimum time of 120 s is taken between drops to assure that the fluid has no perturbations left from the previous drop.

In this Section the sedimentation of the non-magnetic Particles M, G and P is presented. The coils are turned off and there is no magnetic interaction.

4.1.3 Parameters space

As discussed in the first Chapter (Section 1.4.2), Figure 4.1 presents the parameters space particle-fluid density ratio - Galileo number for the trajectory dynamics of a single sphere settling in an otherwise quiescent flow, alongside with all 63 data-points measured in this work. Each of the 63 data-points is composed of between 5 and 25 realisations. The three data sets "Short", "Long" and "Extended" are represented by squares, triangles and diamonds, respectively. Note that a maximum value of $Ga = 240$ could be reached in the "Extended" configuration as that

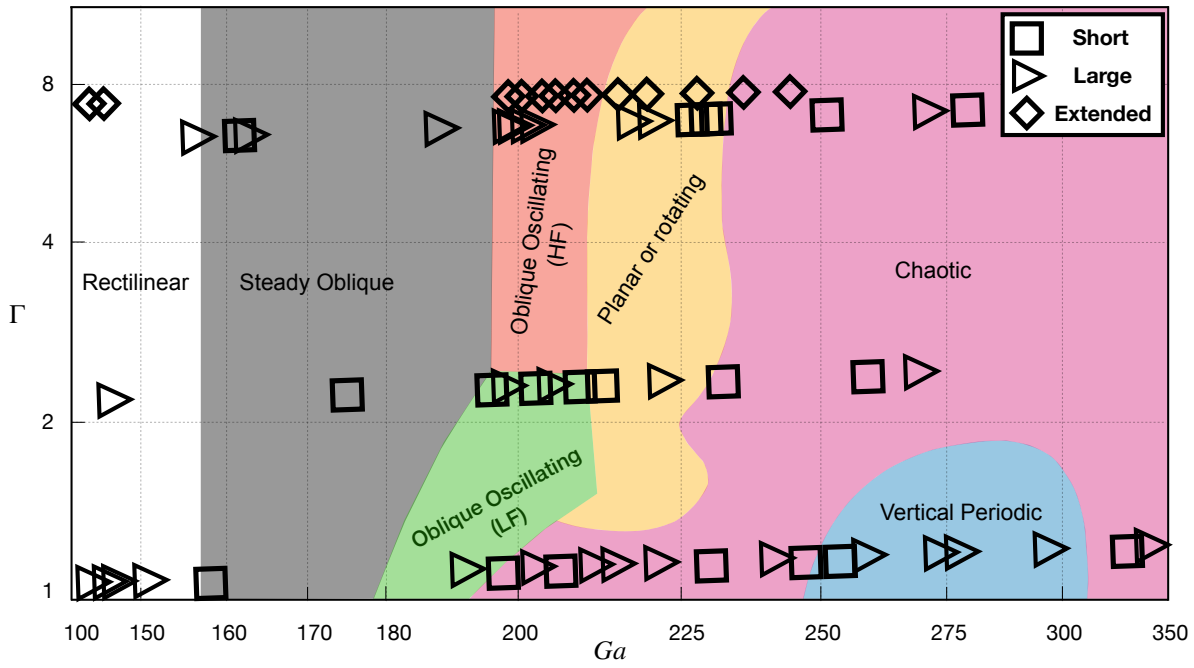

Figure 4.1: Particle-to-fluid density ratio - Galileo number space of parameters built from numerical data (Zhou and Dusek, 2015), alongside with the points measured in this work.

is the Ga obtained when using pure water (i.e. the lowest viscosity case).
This graph was built from numerical results (Jenny et al., 2004, 2003; Zhou and Dusek, 2015). They have identified numerically seven regimes, that differ in the trajectory inclination, planarity and the presence or absence of periodic oscillations. These are:

- the Rectilinear Regime, with planar trajectories and no inclination or oscillations (Stokes regime);
- the Steady Oblique Regime, with planar and oblique trajectories and no oscillation (see Fig. 4.2(a));
- the Oblique Oscillating Regime, with planar and oblique trajectories, and the presence of oscillations at a principal frequency that depends on the particle-fluid density ratio: High Frequency (HF, $f^* = 0.18$) and Low Frequency (LF, $f^* = 0.068$);
- the Planar or Rotating Regime, a tri-stable regime composed of trajectories that are oblique and oscillate at the High or Low Frequency, and have a slowly rotating symmetry plane (hence generating helicoid-like trajectories) or planar trajectories, coexisting with Chaotic regimes. The tri-stability is then composed of High Frequency regime, Low Frequency regime, and Chaotic regime (see Fig. 4.2(b));
- the Vertical Periodic Regime, where the trajectories are planar, rectilinear, and at oscillate at the high frequency f^*=0.18;
- and finally, the Chaotic Regime, where there is no periodic oscillations nor planarity and the trajectories are oblique (see Fig. 4.2(c)).

Recall that in numerical simulations the regime Planar or Rotating is composed of very slim (in Ga range) sub-regimes which are hardly distinguishable from each other in experiments as the

uncertainties in Ga here are comparable to the width in Ga range of the zone of existence of the sub-regimes. The planar and rotating regime is then drawn as a single tri-stable regime composed of Low Frequency, High Frequency, and Chaotic regimes. While in numerical simulations it is bi-stable (Chaotic plus High Frequency) followed by another slim bi-stable region (Chaotic plus Low Frequency), before settling on the Chaotic regime (Zhou and Dusek, 2015). Apart from the tri-stability, trajectories in this regime are predicted to be helicoidal.

Finally, as already discussed in Section 1.4.2, only two experimental studies have explored the predictions made by simulations (Horowitz and Williamson, 2010; Veldhuis and Biesheuvel, 2007).
The work of Veldhuis and Biesheuvel (2007) (2007), although with some discrepancies, has been able to qualitatively validate part of the parameters space for the dynamics described in the numerical simulations: $\Gamma < 2.3$ and $Ga < 212$. Those experiments were targeted to identify the Oblique Oscillating regimes and their onsets, up to a particle-fluid density ratio of 2.3.
On the other hand, Horowitz and Williamson (2010) (2010) were mostly interested in rising spheres and Galileo numbers smaller than 1×10^4 whereas the aforementioned numerical simulations explore the dynamics up to $Ga = 350$.

A number of important regions in the parameters space and trajectory characteristics observed in numerical simulations by Zhou and Dusek (2015) have to be still corroborated, for instance: systematic study of trajectory angle as a function of Galileo number; dynamics at particle-to-fluid density ratio higher than 2.3; the new Vertical Periodic Regime identified they identified; planarity lose threshold (Chaotic Regime onset); among others.

4.1.4 Experimental Results

In what follows the results obtained in the context of this thesis for settling spheres in quiescent fluid are presented.

Trajectories geometry

Figures 4.2(a), (b) and (c) present some representative Particles M's 3D trajectories, centred in the horizontal axis, alongside with their top and side view. The black vertical line in the center axis represents the downwards gravity vector.
Fig. 4.2(a) represents the planar and oblique type of trajectories found after the first bifurcation and up to the trajectories measured at Ga = 205. Note that the approximately constant angle but different trajectory directions form a cone in the 3D space. Note that the same trajectories are seen up to $Ga \approx 217$, i.e. Fig. 4.2(a)'s trajectories are representative to both the Steady Oblique and Oblique Oscillating regime, indeed, oscillations are hardly visible by simple visual inspection of the trajectories and become recognizable only when looking and the particle velocity.
Figure 4.2(b) presents some trajectories that seem to be a portion of an helicoid (for instance the blue dark curve) co-existing with non-planar trajectories that do not have a circular shape in top view, recalling what might be chaotic trajectories.
Finally, Fig. 4.2(c) presents two trajectories that fall in the Chaotic Regime: where all trajectories are different and no pattern of planarity or oscillations is present. Note that the trajectory oscillations detected via the PSDs presented in what follows are not visible at these scales.

After these brief qualitative description of some observed trajectory regimes, the next Subsections present a systematic quantitative analysis of the different properties used to characterise trajectories geometry and dynamics : angle with the vertical, planarity, oscillations and spectral content and finally terminal velocity and drag.

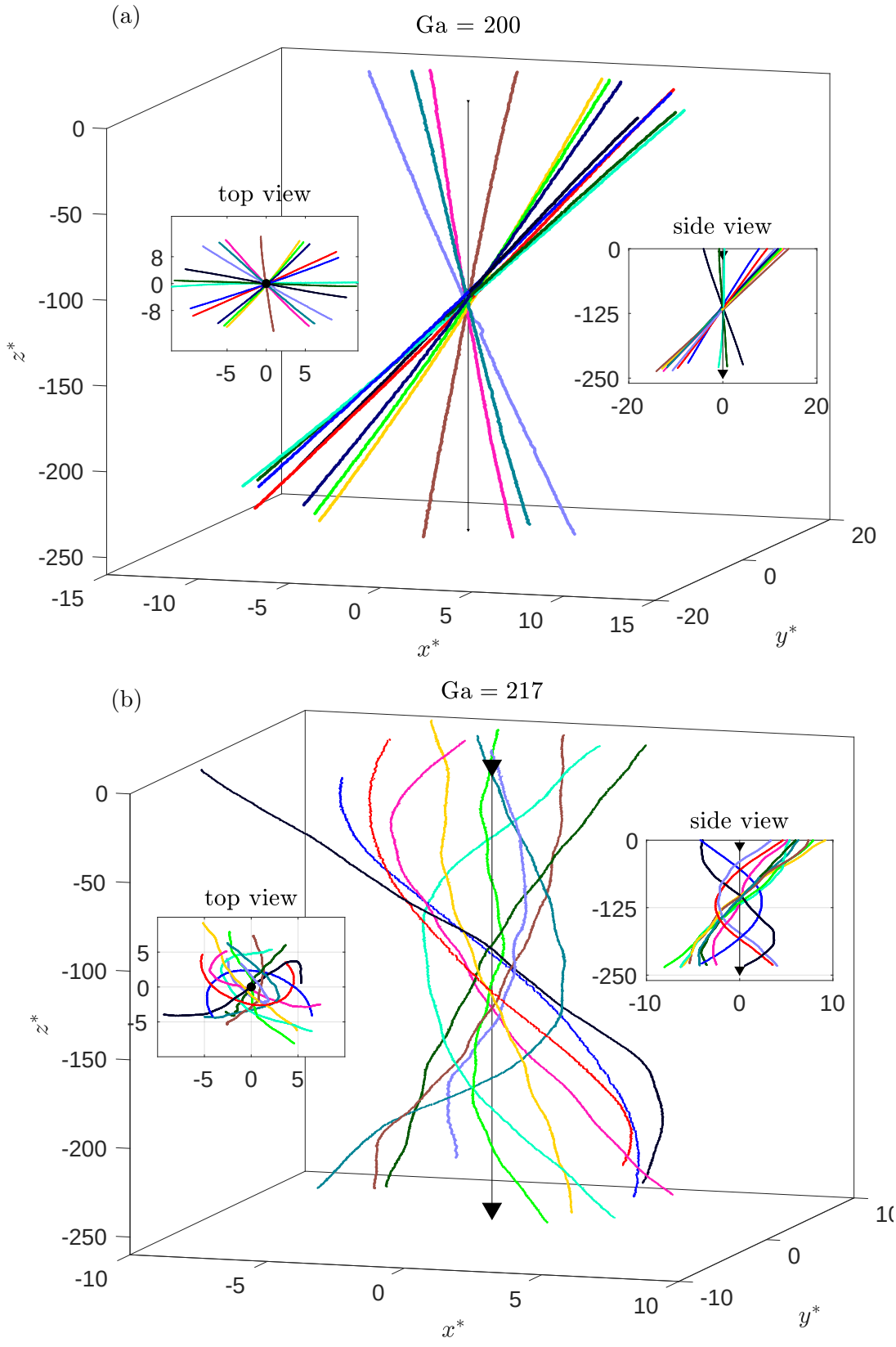
(a)
Ga = 200
top view
side view
z^*
x^*
y^*
(b)
Ga = 217
top view
side view
z^*
x^*
y^*

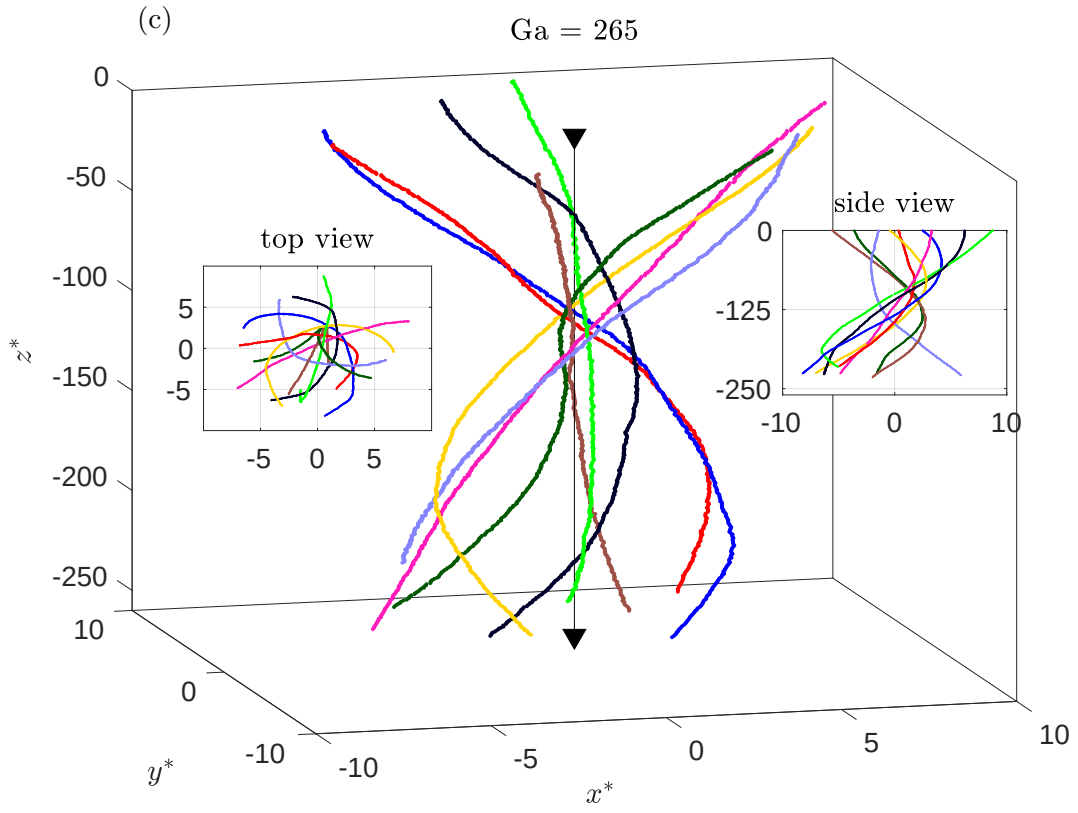

Figure 4.2: Typical trajectories of the three main regimes: Steady Oblique (a), Planar or Rotating (b) and Chaotic (c).

Trajectories Angle

The trajectory angle dependence on Ga computed from the 3D linear fit method, for the three particle materials studied, is presented in Figure 4.3. The figure is composed of 3 rows (a)-(b)-(c) that show the results for Particles M, G and P, respectively. Furthermore, the different regimes for each particle-to-fluid density ratio are delimited by the dashed vertical lines and identified by coloured rectangles that respect the colour code in Fig. 4.1. Furthermore, the symbols follow the nomenclature of Fig. 4.1: diamonds, triangles, and squares represent the "Extended", "Large", and "Short" regimens, respectively. As Fig. 4.1, the regimes delimitations are taken from the results of Zhou and Dusek (2015).
A smooth transition from rectilinear to oblique (primary regular bifurcation) is seen for Particles P and M. Furthermore, if the threshold between this regimes is defined as the Galileo number value at which the trajectory has a non-zero angle, Particles P and M present threshold values of (125 ± 10) and (115 ± 10), respectively, leading to a joint threshold at $Ga \approx (120 \pm 15)$. The trajectory angle depends on Galileo number, see, for example, Particles M: the angle varies monotonously from 3 to 6 degrees in the Ga range 140-190. Additionally, the maximum observed angles are $(5.7° \pm 0.2°)$, $(5.1° \pm 0.2°)$ and $(5.1° \pm 0.2°)$ degrees for Particles M, G and P, respectively. Consistently, the maximum angle is reached in all cases in what have been identified as the Oblique regimes (both Steady or Oscillating). Considering that the maximum angle seems to be reached at $Ga \approx 200$ for all cases, the (incidental) lack of Particles P measurement points in that region leaves open the possibility of a maximum angle bigger than the one at disposal.
Furthermore, a common qualitative trend that starts growing, then reaches a maxima and a local minima can be seen, for Particles G and P. Whereas for Particles M the trend can also be identified but the presumed minima is defined only by one point. The value of Ga where the local minima occurs is Γ dependent, being at $Ga = (240 \pm 20)$ and $Ga = (280 \pm 20)$, for Particles G and P, respectively. Finally, the angle is not well defined after the Oblique Oscillating Regime for Particles M, and in the Chaotic Regime for particles P. In those areas, the same values of Ga yield angles that do not overlap, and in particular differ in up to 3°. This is consistent with the fact that at large Ga settling occurs in the Chaotic regime.

The angle in $Ga \in [190, 230]$ is not very well defined for any of the particles. This range of Ga corresponds to the Planar or Rotating tri-stable regime qualitatively seen in the 3D trajectories presented in Fig. 4.2(b).

Note that predictions for the angle variation with Ga are not available in the literature. There is only a qualitative numerical prediction for an angle "of about 4 to 6 degrees" in the Steady Oblique and Oblique Oscillating regimes.

Trajectories Planarity

The trajectory planarity is quantified by the eigenvalues of the perpendicular velocity correlation matrix, defined as:

$$\langle \mathbf{v}_\perp^* \ \mathbf{v}_\perp^{*\mathrm{T}} \rangle = \begin{bmatrix} < v_x^{*2} > & < v_x^* v_y^* > \\ < v_y^* v_x^* > & < v_y^{*2} > \end{bmatrix}, \tag{4.1}$$

The aforementioned eigenvalue planarity analysis could only be made for Particles M in the Long and Extended data-sets as the results for the other particle-fluid density ratios and data-sets are not conclusive, presumably because of their short trajectory length. Note that any trajectory would be planar if a short enough portion is considered.

Figure 4.4 shows the ratio $\sqrt{\lambda_2/\lambda_1}$ versus Ga number, for Particles M, in the Long (Triangles) and Extended (Diamonds) data-sets. As in previous figures, the different regimes are delimited by dashed vertical lines and identified by coloured rectangles, information that comes from the literature (Zhou and Dusek, 2015).
It can be seen that the planarity is lost at Ga $= (220 \pm 15)$, where the ratio between the

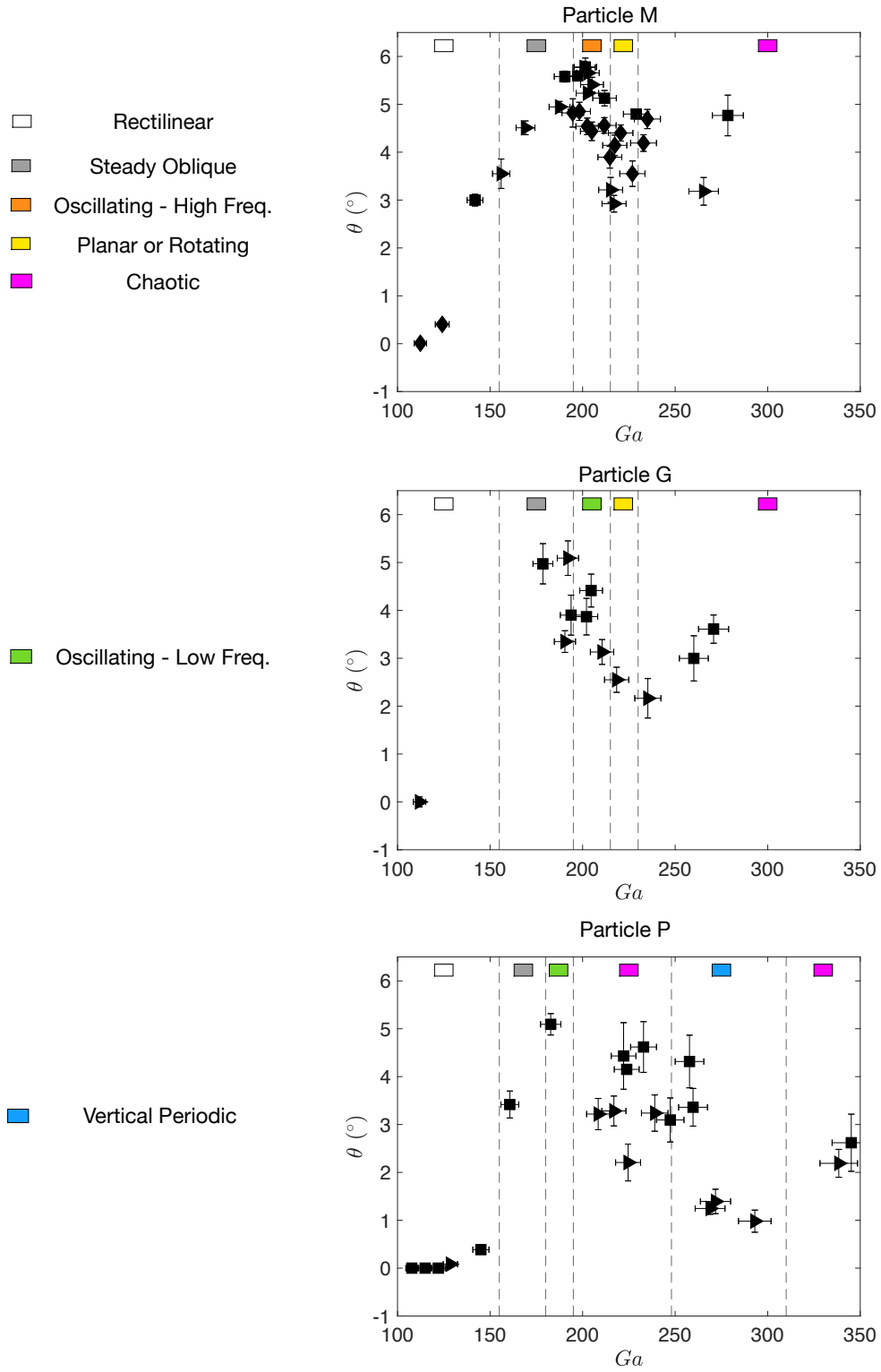

Figure 4.3: Trajectory angle versus Galileo number for the three particle materials M (metal), G (glass) and P (polyamide). Additionally, the different regimes, as expected from numerical simulations in Fig. 4.1, are delimited by the dashed vertical lines and identified by the coloured rectangles whose colour match that of Fig. 4.1.

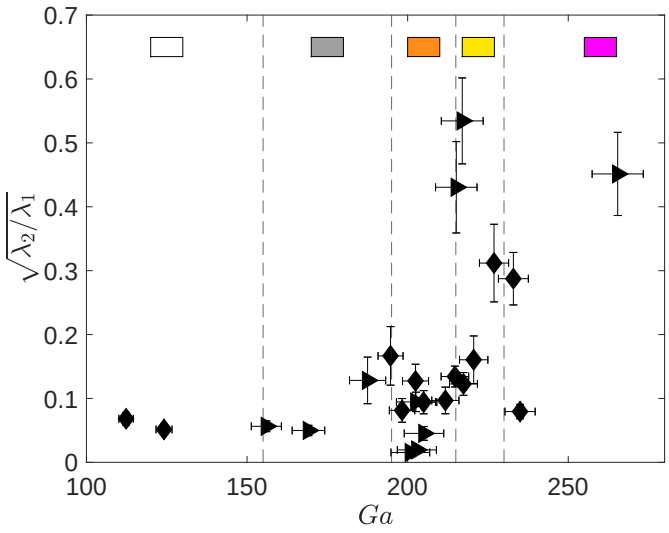

Figure 4.4: Planarity versus Galileo number for the M particles in the Long and Extended data-sets. The parameter $\sqrt{\lambda_2/\lambda_1}$ measured planarity: a perfectly planar or non planar trajectory yields 0 and 1, respectively. Additionally, the different regimes presented in Fig. 4.1 are delimited by the dashed vertical lines and identified by the coloured rectangles. Furthermore, the symbols follow the nomenclature of Fig. 4.1: diamonds, triangles, and squares represent the "Extended", "Large", and "Short" regimens, respectively.

eigenvectors of the velocity correlation matrix $\sqrt{\lambda_2/\lambda_1}$ goes from approximately 0.15 to 0.4. The range of Galileo number where planarity is found to be lost is consistent with the transition towards the Planar or Rotating regime reported in numerical simulations. Some difference can be noted between the 2 mm diameter particles that compose the data-set "Long" and the 1 mm particles from the measurements-set "Extended": the planarity lost for "Long" is well defined at Ga $\approx$ 215 whereas "Extended" loses its planarity at Ga $\approx$ 225. Considering that the points' scatter in Galileo number is taken as 10, the onset for the planarity lost overlaps for both particles diameters and it is taken as $Ga = (220 \pm 15)$.

The loss of planarity seems to be associated to the emergence of helicoidal trajectories. Figure 4.2(b) presents indeed a sample trajectory, representative of the ensemble of trajectories, that seems to be a half-helicoid. They are found at Ga = {215, 217, 221} and Ga = {228,233}, in the "Long" and "Extended" data-set, respectively. The aforementioned loose of planarity for data with Galileo numbers bigger than (220 ± 15) (see Figure 4.4) can then be related to the appearance of these helicoid-like trajectories. Limitations of the measurement volume (even in the "Extended" configuration) do not allow to be fully conclusive as only a portion of the helicoid's period is recognisable. However, assuming that these trajectories are helicoids, the radius of their horizontal projection R (Figure 4.2(b) top view) would be roughly 7 diameters. Furthermore, the pitch would be approximately 500 diameters.
Similar helicoid-like trajectories have also been seen experimentally by (Veldhuis and Biesheuvel, 2007), for the equivalent of the present Particles G. In this sense, the results of this work seem to confirm the existence of such a regime for Ga $\in$ [215, 233] and larger particle-to-fluid density ratios in the range of Particles M ($\Gamma \approx 7.5$). Nevertheless further experiments with a taller visualisation volume are needed to definitely confirm both the existence of helicoids and their properties. Particularly because, as it will be presented in the next paragraph, those trajectories also appear (albeit with less probability) in the Chaotic Regime.

At larger values of Ga, the loss of planarity arises from the chaoticity of the trajectories as

illustrated in Fig 4.2(c). All the trajectories in the Chaotic Regime are different from each other and, as it will be presented in the next Section, they have no common dominant frequency.

Nonetheless, although not presented here, the trajectory planarity for Particles P and G can be roughly identified by looking at the trajectories in 3D, from where one can qualitatively see similar behaviours and onsets to those exposed in the literature.

Trajectories Oscillations

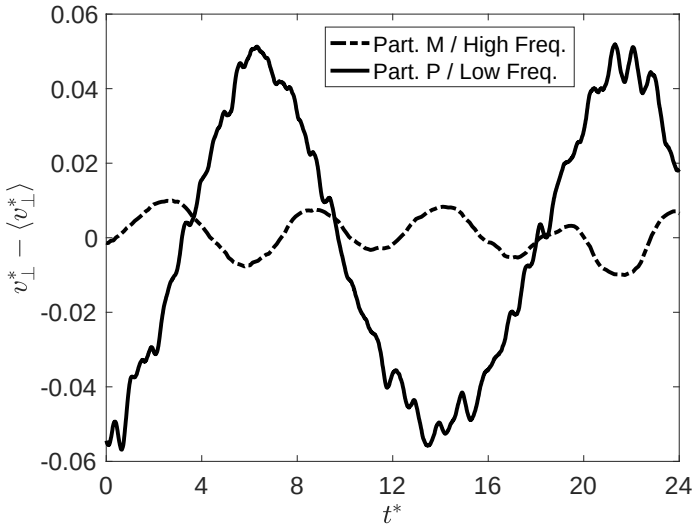

Figure 4.5: Typical perpendicular (to gravity) velocity fluctuations for trajectories in the Low (continuous line) and High (dashed line) Frequency regimes.

The analysis of the emergence of oscillatory dynamics has been performed by studying the dimensionless fluctuations of the perpendicular velocity (component perpendicular to gravity): $v'^*_\perp := v^*_\perp - \langle v^*_\perp \rangle$.
One of the questions to address is the frequency dependency on density ratio Γ in the Oblique Oscillating regime. Indeed, while numerical simulations predict a transition from Low Frequency ($f^* = 0.068$) to High Frequency ($f^* = 0.18$) as $\Gamma \gtrapprox 2.3$, no thorough experimental evidence has yet been given. Furthermore, the simulations predict the exclusive presence of High Frequency oscillations for Γ between 2.3 and 10 (the highest value in numerical results), in the Oblique Oscillating regime. The dynamics of particles close to the high Γ has yet to be corroborated experimentally.

A sample of perpendicular velocity fluctuations versus time is presented in Figure 4.5, for Particles M (Ga=200, "Extended") and P (Ga=192, "Long"), respectively. The observed regimes exhibit clean oscillations characteristic of the Oblique Oscillating regime (remember that $\theta \approx 5°$ for particles at these Ga) with marked frequency and amplitude differences. Particles M (denser) show higher frequency and smaller amplitude than Particles P (lighter), in agreement with numerical simulations. It is possible to qualitatively extract the principal dimensionless frequencies for both regimes: f* $\approx \{0.07, 0.2\}$, for Low and High Frequency respectively. These values are close to the numerical prediction of f* $\approx \{0.068, 0.18\}$.
An amplitude difference between the High and Low Frequency perpendicular dimensionless velocity oscillations of approximately 5 times is measured. What is in disagreement with numerical simulations that predict a ratio of ≈ 12.

A deeper analysis of the oscillatory dynamics of the particles in the different regimes can be performed by computing the Power Spectral Density (PSD) of the velocity fluctuations. This

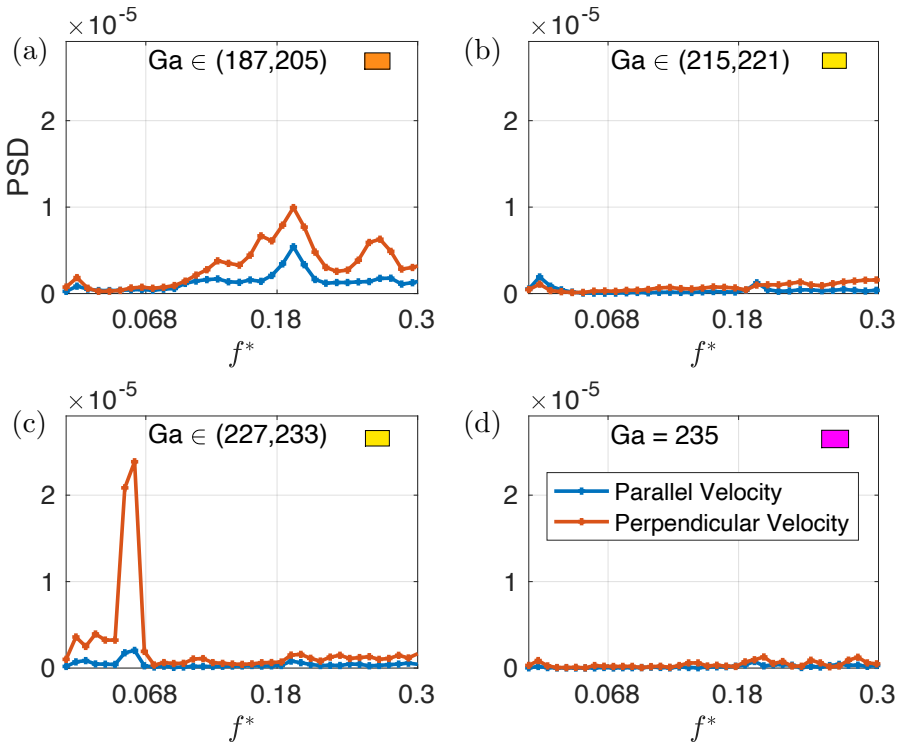

Figure 4.6: Spectral content of the Particle M's parallel and perpendicular velocity fluctuations ($v'^{*}_{\parallel}$ and $v'^{*}_{\perp}$, respectively) in the Extended data-set. The Galileo number ranges are noted in each sub-panel and belong to the regimes represented by the colored rectangles as done in Fig. 4.1.

analysis is performed on the "Extended" measurements only. Indeed Low Frequency oscillations with a typical dimensionless frequency of $f^* \approx 0.07$ are marginally captured in the "Long" data-set (only roughly more than one period is visible in Fig. 4.5). Only the denser, Particles M, will therefore be addressed in this part.
Figure 4.6 presents the "Extended" data-set M Particles' velocity fluctuations PSDs, for both parallel and perpendicular components. Each sub-figure presents the ensemble average of all PSDs in the Ga regions where the spectral content was observed not to significantly change: Ga = {187, 195, 198, 202, 205} for Figure 4.6(a), Ga = {215, 217, 221} for Figure 4.6(b), Ga = {227, 233} for Figure 4.6(c), and Ga = 235 for Figure 4.6(d). All measurements with Ga smaller than 187 have no spectral content (settling is then stationary, either vertical or oblique), therefore not shown.

The perpendicular velocity fluctuations PSD present in Figure 4.6(a) shows that for $Ga \in [185, 205]$ oscillations have a broad frequency peak centred around a dominant frequency $f^* = (0.19 \pm 0.01)$, and a secondary frequency around $f^* = (0.27 \pm 0.01)$. The spectral resolution, limited by the accessible trajectory length is of the order of 0.010, taken as half the difference between two consecutive points in the PSDs. The dominant frequency is consistent with the oscillations reported for Particles M at $Ga = 200$ in Fig. 4.5. It is also consistent with the value predicted by simulations which was reported by (Zhou and Dusek, 2015) to be $f^* = 0.18$.
The main difference between these experiments and the simulations is the non-negligible intensity of the $f^* \approx 0.27$ peak (and possibly a sub-harmonic of $f^* \approx 0.13$). The existence of the frequency peak at f* = 0.27 has been seen experimentally by (Veldhuis and Biesheuvel, 2007) with a particle-fluid density ratio of approximately 2.3 that, nevertheless, falls in the High Frequency Regime predicted by simulations. It is worth noting that the spectra of parallel (to gravity) velocity does not present harmonics, only the High Frequency component f* = (0.19 ± 0.01).

When Ga is increased to the range $[215, 221]$ trajectories seem to lose any significant spectral signature. The parallel velocity PSD in Figure 4.6(b) has indeed only one mild peak at f* = (0.19 ± 0.01), with an intensity 6 times smaller than in the previous Ga range identified as the High Frequency Regime. Furthermore, the perpendicular velocity PSD does not have any frequency with a significant amplitude.
The angular and planarity analysis in the previous Section suggest that trajectories of Particles M in this range of Ga might fall in the helicoidal category. However, the estimated pitch of the helicoids ($\approx 500 d_p$) would correspond to a frequency of oscillation of $f^* = v_{\parallel}^*/(500) \approx 2 \times 10^{-3}$, out of reach of the 0.01 resolution of the present spectral analysis.

At higher Ga, in the range $[225, 235]$, the perpendicular velocity fluctuations PSD presented in Fig. 4.6(c) has a marked peak at the Frequency $f^* = (0.055 \pm 0.010)$ which could correspond to a Low Frequency situation according to he previous classification. A 10 times lower peak with a High Frequency component at $f^* \approx 0.19$ is present as well. Whereas the parallel velocity fluctuations globally share the spectral content with a smaller intensity. Note that a planarity lose was measured in this range of Galileo numbers.

At the largest Ga explored, Figure 4.6(d) presents the PSDs for the case Ga = 235. It does not present any dominant frequency, as would be expected for a Chaotic dynamics.

Settling Velocity & Drag

In this Subsection, the particle terminal velocity as a function of Γ and Ga is studied.
The dimensionless particle terminal velocity v_s^* can be rewritten in terms of Ga and Re_p:

$$v_s^* = \frac{v_s}{V_{\text{ref}}} = \frac{Re_p(Ga, \Gamma)}{Ga}. \tag{4.2}$$

Knowing $Re_p(Ga, \Gamma)$ is therefore equivalent to knowing $v_s(Ga, \Gamma)$.
Brown and Lawler (2003) propose an empirical correlation in the form of a relation Re_p = f(Ga)

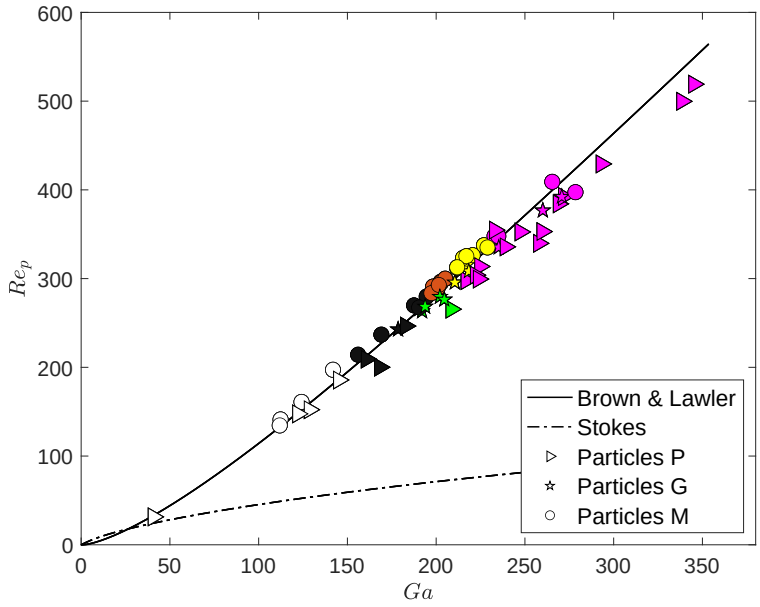

Figure 4.7: Galileo number versus Reynolds number. Alongside with the empirical correlation in Eq. 4.3. The symbols represent the different density ratios (i.e. particle type): triangles – Particles P ($\Gamma \approx 1.2$); stars – Particles G ($\Gamma \approx 2.5$); circles – Particles M ($\Gamma \approx 7.5$). Whereas the colors represent the different trajectory regimes, as done in Fig. 4.1.

for dense settling particles (hence ignoring any Γ dependency) :

$$Re_p = \frac{Ga^2(22.5 + Ga^{2.7126})}{0.0258Ga^{4.7126} + 2.81Ga^{3.7126} + 18Ga^{2.7126} + 405}. \tag{4.3}$$

This correlation, and all previous versions in the literature as well as the related correlation for the drag coefficient C_D, neglect the eventual influence of Γ in $Re_p = \mathrm{f}(\Gamma, \mathrm{Ga})$, thus in v_s. This assumption has been proven to be wrong (only) for light particles, i.e. $\Gamma < 1$ (Auguste and Magnaudet, 2018; Karamanev and Nikolov, 1992). We will address its relevance for the cases of heavy settling spheres investigated in this thesis.

Figure 4.7 presents the Galileo number versus particle Reynolds number for the three particle cases, alongside with the empirical correlation Eq. 4.3 and the Stokes model. The symbols represent the different density ratios (i.e. particle type): triangles – Particles P ($\Gamma \approx 1.2$); stars – Particles G ($\Gamma \approx 2.5$); circles – Particles M ($\Gamma \approx 7.5$). Whereas the colors represent the different trajectory regimes, as in Fig. 4.1.
The correlation by Brown and Lawler (2003) matches reasonably the experimental data for all three Γ values within a 30% margin. A slight systematic trend of the scatter of the points in fig. 4.7 with Γ can however be seen: note how the triangles (less dense particles) are systematically below the correlation by Brown and Lawler (2003) while the circles (denser particles) are above it. This becomes clearer in Figure 4.8 where the particle Reynolds number is compensated by the empirical correlation.

It is conventional to study the relation between Ga and Re through the drag coefficient that allows to compute the force due to hydrodynamical drag. A general relation between Ga and Re that depends on the drag coefficient C_D can be extracted from Newton's equation of motion

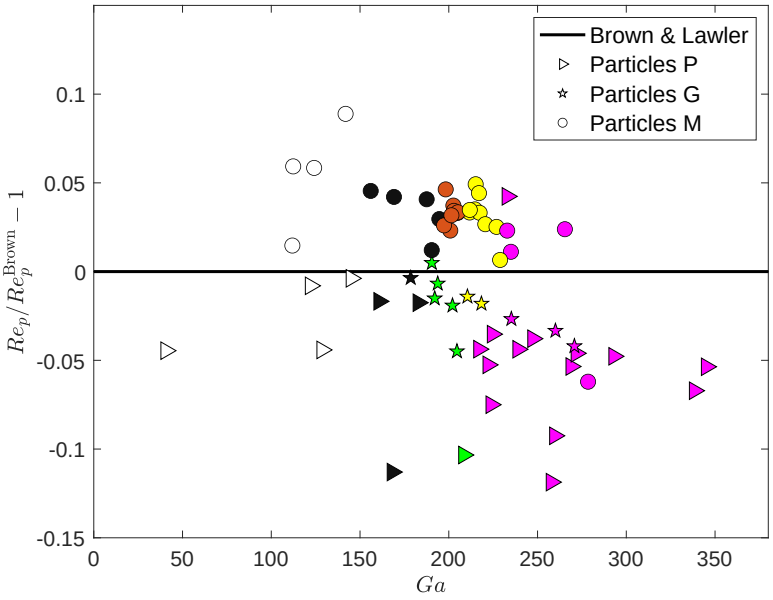

Figure 4.8: Galileo number versus Reynolds number compensated by the empirical correlation from Eq. 4.3. The symbols represent the different density ratios (i.e. particle type): triangles – Particles P ($\Gamma \approx 1.2$); stars – Particles G ($\Gamma \approx 2.5$); circles – Particles M ($\Gamma \approx 7.5$). Whereas the colors represent the different trajectory regimes, as done in Fig. 4.1.

(see Section 1.4.1):

$$C_D(Re_p, \Gamma) = \frac{4}{3}\left(\frac{Ga}{Re_p(\Gamma, Ga)}\right)^2. \tag{4.4}$$

In a similar way as before, C_D is usually considered to be independent on Γ and an empirical correlation has been obtained (Brown and Lawler, 2003):

$$C_D(Re_p) = \frac{24}{Re_p}(1 + 0.150Re_p^{0.681}) + \frac{0.407}{1 + \frac{8.710}{Re_p}}. \tag{4.5}$$

Apart from the question of the Γ dependency, it could be noted that this relation gives C_D as a function of Re_p, which, for the case of settling particles is actually a response parameter and not a control one. This makes this relation unpractical as, for instance a simple estimation of the terminal settling velocity based on such a relation requires an iterative approach, or to solve the full particle equation of motion. A relation $C_D(Ga)$ would actually be more convenient, as it would directly give the drag coefficient from the actual control parameter Ga. Such a relation can be given combining the correlation 4.5 with Eq. 4.3 which permits the variable change $Re_p \rightarrow Ga$ that yields $C_D(Ga)$.

Figures 4.9 presents the drag coefficient versus Galileo and Reynolds numbers for the three particle cases, alongside with the empirical correlation Eq. 4.5 and its Ga dependent version. The symbols represent the different density ratios (i.e. particle type): triangles – Particles P ($\Gamma \approx 1.2$); stars – Particles G ($\Gamma \approx 2.5$); circles – Particles M ($\Gamma \approx 7.5$). Whereas the colors represent the different trajectory regimes, as in Fig. 4.1. In a similar manner, Figure 4.10 presents an equivalent plot but with the drag coefficient compensated by the empirical correlation.
The same behaviour seen in Fig. 4.8 is present here. The correlation (Brown and Lawler, 2003) works reasonably well over the full range, although with a margin of the order of 30% where a systematic trend with Γ can be seen: the drag coefficient for the less dense particles (triangles)

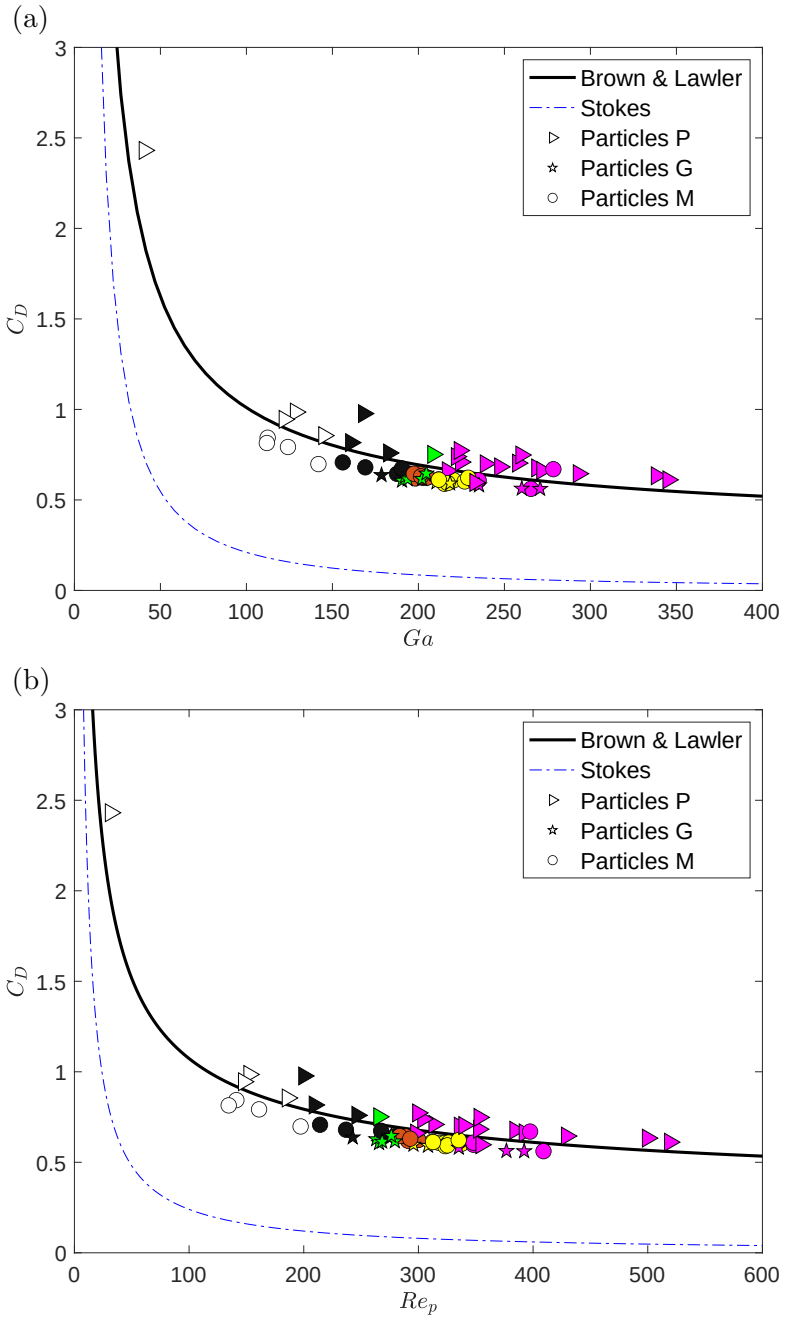

Figure 4.9: Drag coefficient versus Galileo (a) and Reynolds (b) numbers. The symbols represent the different density ratios (i.e. particle type): triangles – Particles P ($\Gamma \approx 1.2$); stars – Particles G ($\Gamma \approx 2.5$); circles – Particles M ($\Gamma \approx 7.5$). Whereas the colors represent the different trajectory regimes, as in Fig. 4.1.

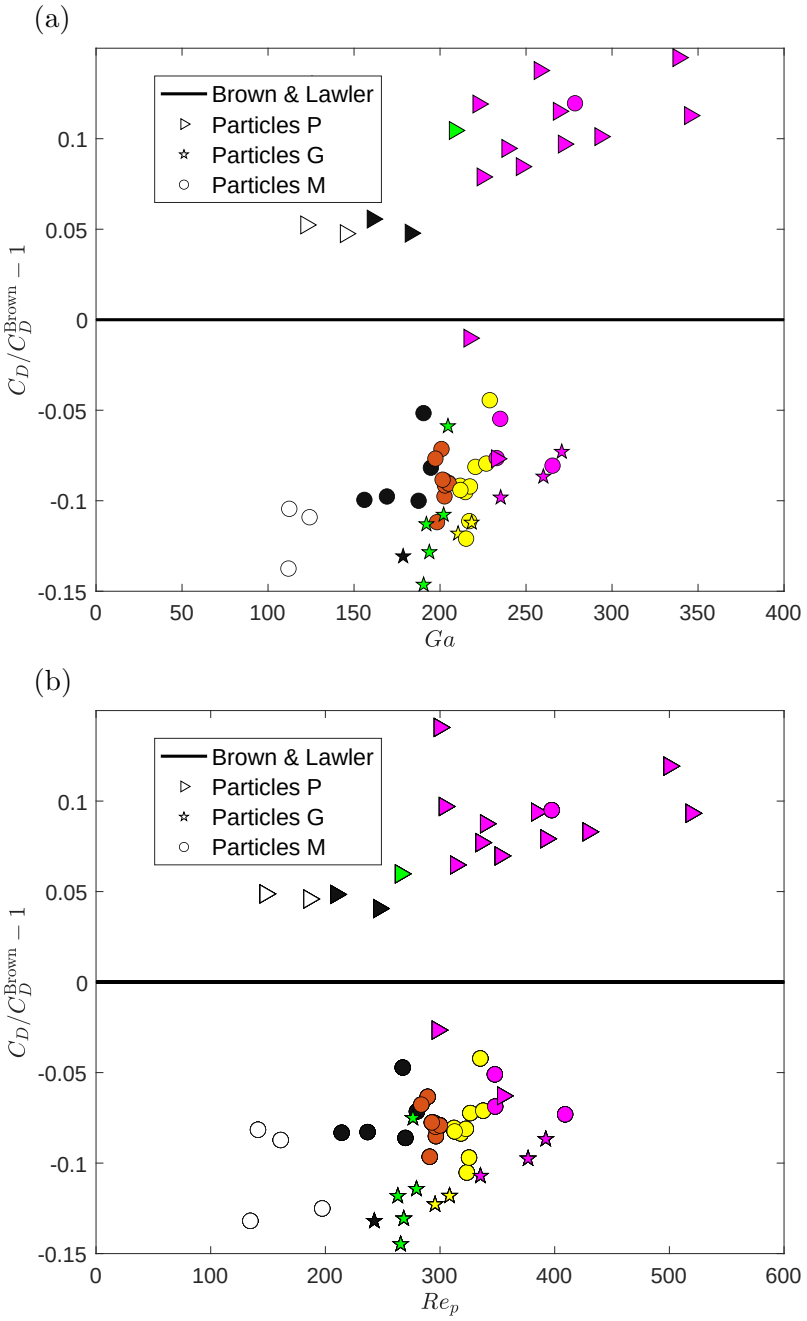

Figure 4.10: Drag coefficient compensated by the empirical correlation from Eq. 4.3, versus Galileo (a) and Reynolds (b) numbers. The symbols represent the different density ratios (i.e. particle type): triangles – Particles P ($\Gamma \approx 1.2$); stars – Particles G ($\Gamma \approx 2.5$); circles – Particles M ($\Gamma \approx 7.5$). Whereas the colors represent the different trajectory regimes, as in Fig. 4.1.

is generally under-predicted by Brown and Lawler (2003) correlation while that of the other denser particles is slightly over-predicted.

These results challenge the widespread approximation that the drag coefficient and the particle Reynolds number of dense settling spheres do not depend on Γ for heavy particles. A dependence on Γ is found as C_D and Re_p vary of about 20 to 30% between the less dense particles ($\Gamma \approx 1.2$) and the denser particles ($\Gamma \approx 7.5$).
It is worth to remark that the results from the denser particles and the intermediate density ratio ones ($\Gamma \approx 2.5$) are hardly distinguishable. This suggest that the Γ dependence found is only relevant at Γ values close to one, i.e. closer to the rising particle case where a strong Γ dependence is found (Auguste and Magnaudet, 2018; Karamanev and Nikolov, 1992).

4.1.5 Conclusions

The results presented in this section can be qualitatively summarised as:

- Trajectory geometry
  - the qualitative geometry of trajectories was analysed;
  - the mean angle with the vertical was found to present a rich dynamics as Ga number and particle-to-fluid density ratio are varied;
  - for Particles M, a clear transition between planar and non-planar trajectories was quantified.
- Particle dynamics
  - the spectra of path oscillations was quantified for Particles M as a function of Ga, and the existence of two regimes "Low and High Frequency" was qualitatively confirmed;
  - the terminal velocity and drag were found to depend on the particle-to-fluid density ratio.

4.2 Spheres at modified gravity

In this Section the local gravitational pull is modified via the magnetic gravity compensation method presented in Section 2.4. The goal here is to test whether the effective Galileo number (and hence the settling regime) of magnetic particles can be magnetically tuned rather by changing the fluid viscosity (as done in the previous Section). Furthermore, these results confirm the validity of the magnetic gravity compensation method. This is the first step towards the deployment of a global strategy to explore the influence of gravity in particle/fluid interactions.

4.2.1 Parameters explored

The same experimental setup used to study the settling of non-magnetic spheres presented in the previous Section is used here, with the only difference of the magnetic field presence and the use of magnetic particles. These are 1 mm diameter particles (Particles MAG from now on) with a density of 8200 kg/m^3 comparable to the Particle M density. Therefore, they occupy the same regions in the parameters space presented in Figure 4.1(d), thus their trajectory dynamics are expected to be similar. Besides, Particles MAG's magnetic moments $|\mathbf{M}|$ can be computed using Equation 2.12, as it was done in Section 2.4.3 – Eq. 2.22 where a magnetic dipolar moment of $|\mathbf{M}| = 4.96 \times 10^{-8}$ G^{-1} m^2 s^{-2} was found.

The particles are affected in two ways due to the presence of the external magnetic inductions here produced: firstly, as the applied magnetic field is mostly vertical on the region of interest, particle rotation is partially blocked and only allowed around the vertical axis. Secondly, the spatial profile of the imposed field is specifically tailored to be as close as possible to an homogeneous vertical gradient field in the region of interest, hence particles experience an almost constant magnetic force which counteracts the gravitational force yielding different effective gravity values $\tilde{g}$.

To disentangle the specific role of rotation blockage, an additional dedicated set f=of experiments was conceived with an imposed uniform magnetic field (with no gradient in order to modify the gravity). In the sequel, the following nomenclature will be used to refer to the different experiments:

- $\emptyset B$
  Reference case with no magnetic field (detailed in the previous section).
- Case CstB
  Uniform applied field (effect of rotation blocking). The magnetic induction profile was presented in Fig. 2.23(b)-(d).
- Case Cst∇_zB
  Uniform applied magnetic gradient (effect of rotation blocking and modified gravity). The magnetic induction profile was presented in Fig. 2.23(a)-(c).

Additionally, the visualisation area in Case Cst∇_zB has a height $h/d_p \approx 100$ that coincides with the conditions of the data set "Large" presented in the study of spheres, whereas Case CstB has a height $h/d_p \approx 200$ that matches that of the data set "Extended". This difference is due to the finite size of the coils that can produce an homogeneous magnetic induction in a larger region of space compared to the generation of an homogeneous magnetic induction gradient (see Section 2.4.5). As discussed previously, trajectories with a length of $l/d_p \gtrapprox 150$ are needed to extract in a precise way the spectral content via a PSD. Therefore, PSDs only for Case CstB will be presented.

For the Case Cst∇_zB, Table 4.4 summarises the different regimes of effective gravity $\tilde{g}$ explored (details of $\tilde{g}$ estimation are given in next Subsection). Note that effective gravity will be given from now on in dimensionless form $g^* = \tilde{g}/g$. In practice, changing the effective gravity is achieved by simply multiplying the currents in all the coils from the reference configuration for which the spatial uniformity of magnetic gradient has been optimised (detailed in Section 2.4.5). The exploration of settling regimes is then performed by changing independently the effective

	Cst∇_zB $\times$ 5/3	Cst∇_zB $\times$ 1	Cst∇_zB $\times$ 2/3	Cst∇_zB $\times$ 3/5	Cst∇_zB $\times$ 1/3
$g^* = \tilde{g}/g$	0.43 ± 0.02	0.65 ± 0.02	0.77 ± 0.02	0.80 ± 0.02	0.90 ± 0.02
G_z (G/m)	-476 ± 42	-286 ± 25	-191 ± 16	-171 ± 15	-95 ± 8

Table 4.4: Different magnetic induction gradients applied and regimes of effective gravity $\tilde{g}$ explored. The columns present the five different variants of the magnetic field Case Cst∇_zB. While the rows show the dimensionless gravities g^* defined as the ratio between the effective gravity $\tilde{g}$ and the usual gravity acceleration $g = 9.8$ m/s^2, and the values of $\nabla_z B$ evaluated at $r = 0$ (i.e. the coils' axis) previously denoted G_z.

gravity and the fluid viscosity according to the following protocol. For a given value of fluid viscosity, all the different values of $\tilde{g}$ are applied to sweep Galileo number. In this way, with a fixed viscosity, the Galileo number can be swept by varying the effective gravity in between 65% and 100% of its value at $g = 9.8$ m/s^2. Overall, the range of Ga values explored ranges from $\mathcal{O}(100)$ to $\mathcal{O}(200)$.

Terminal Velocity & Homogeneity of $\tilde{g}$

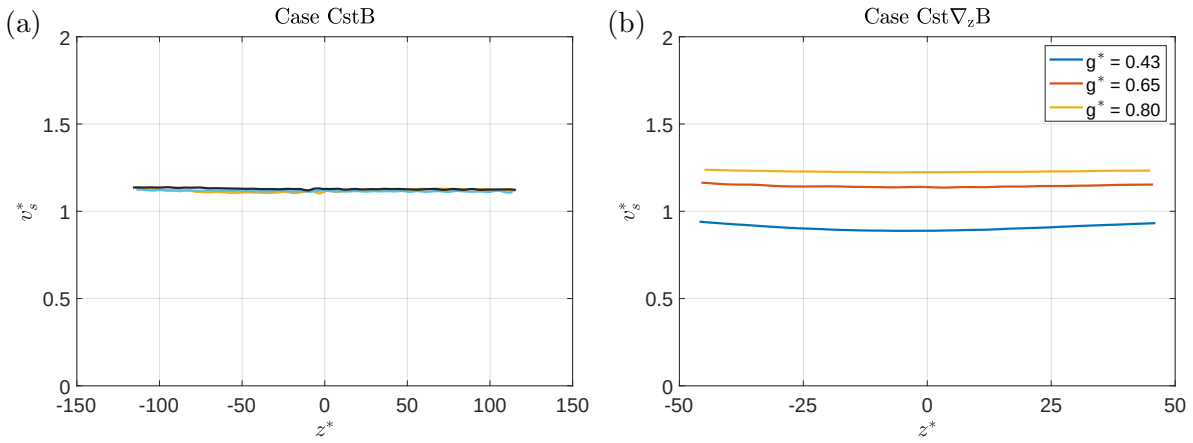

Figure 4.11: Representative settling velocities (i.e. component parallel to gravity) velocities of spheres settling, versus dimensionless distance to origin, under the two external magnetic field Cases studied: CstB and Cst∇_zB. (a) Three settling velocities for Case CstB at low Ga. (b) One settling velocity at low Ga for each of the following three dimensionless gravity values of Case Cst∇_zB: $g^* = 0.43,\ 0.65$, and 0.80.

It is important to verify that the particles do reach a constant terminal velocity, and that there is no global deviation caused by the magnetic field gradient inhomogeneities presented in Section 2.4. In this sense, Figure 4.12 presents some examples of the evolution of vertical velocities versus distance to the origin (set at the geometrical center of the coils, see Section 2.1) for three different amplitudes of magnetic induction in the Rectilinear regime ($Ga < 150$).
Figure 4.11(a) explores the effect of rotation blockage (Case CstB). A terminal regime with constant settling velocity, independent of the intensity of the applied field, is observed, with typical variations between realisations of less than 3%. Fluctuations of this order of magnitude match those present in the non-magnetic spheres previously studied. Hence the fluctuations seen in the curves are attributed to the usual variability of particles settling, printing no major effect of rotation blockage on the terminal velocity.
On the other hand, Fig. 4.11(b) shows one representative settling velocity at $Ga = (103 \pm 5)$, (125 ± 5), and (126 ± 5) for three dimensionless gravity values of Case Cst∇_zB: $g^* = 0.43,\ 0.65$, and 0.80. As it will be reflected in the trajectory angle discussion in the next Subsection, the magnetic field to produce the lowest dimensionless gravity $g^* = 0.43$ is too strong and produces an horizontal drift, i.e. the perpendicular magnetic force becomes stronger than the fluid drag. In this sense, this sub-panel shows that the settling velocity in that case (blue curve) is affected much more than in the other g^* cases: the settling velocity is not constant, at $|z^*| = 46$ the velocity value increases by 8% for $g^* = 0.43$, whereas less than 2% for the other cases.
It is then concluded that measurements up to $g^* = 0.65$ can be expected to behave analogously to the non-magnetic spheres previously studied. This claim will be confirmed in what follows.

The fact that the particles reach a terminal velocity allows the definition of a constant effective gravity, and determining its precise values is crucial. Recall the equation linking $\tilde{g}$ with the experimental parameters (see Section 2.4.1):

$$\tilde{g} = g - |\mathbf{M}|\nabla_z|\mathbf{B}|/m. \tag{4.6}$$

As discussed in Subsection 2.4.3, the value of $|\mathbf{M}|$ can be computed from the manufacturer's data and $\nabla_z|\mathbf{B}|$ was measured (see Subsection 2.4.5). The values of $\tilde{g}$ can then be computed.

The effective gravity can as well be obtained by measuring the terminal settling velocity with no external magnetic induction applied $v_{s,0}$ and comparing it to that of magnetic particles $v_{s,M}$ settling in the same flow but with its gravity being modified. Recall that the particle settling velocity can be calculated as:

$$v_s = \sqrt{\frac{m_p g}{\frac{\pi}{8} C_D(Re) d_p^2 \rho_f}}, \tag{4.7}$$

where the Γ correction for the drag correlation in Brown and Lawler (2003) classical formula is neglected. The ratio $m_p/\frac{\pi}{8} d_p^2 \rho_f$ being identical in both (magnetic and non magnetic) cases (i.e. Particles MAG):

$$g^* = \frac{\tilde{g}}{9.8\ m/s^2} = \frac{v_{s,M} 2 C_D(Re_M)}{v_{s,0}^2 C_D(Re_0)}, \tag{4.8}$$

with $Re_0 = v_{s,0} d_p/\nu$, and $Re_M = v_{s,M} d_p/\nu$. Then, using the drag correlation (Brown and Lawler, 2003) presented in Section 1.4.1, it is possible to extract $\tilde{g}$ for all the multiples of Case Cst∇_zB studied.

Values of $\tilde{g}$ that overlap with the computed ones are independently obtained from particle terminal settling velocities of Particles MAG. The values of g^* reached in this work where presented in Table 4.4.

4.2.2 Experimental Results

The results of single spherical magnetic particles settling in a Quiescent Flow are presented in an analogous format to that of the previous Section. Firstly the trajectory angle and planarity are compared to the non-magnetic case presented in the previous Section, and later on the same is done for trajectory oscillations.
The same qualitative regimes found in the Case $\emptyset B$ (previous Section) are found here.

Trajectories Angle & Planarity

Figure 4.12 presents the trajectory angles versus Ga number, alongside with the measurements from Particles M (black dots) presented in Section 4.1 that serve as reference. Additionally, the vertical dashed lines show the onsets for the different regimes explained in the previous Section. In the same configuration, Figure 4.13 presents the estimator of trajectory planarity $\sqrt{\lambda_2/\lambda_1}$. In particular, Fig. 4.12(b) and Fig. 4.13(b) present the measurements against a Galileo number that was calculated with the effective gravity value $\tilde{g}$, whereas Fig. 4.12(a) and Fig. 4.13(a) show the measurements as a function of Ga number computed assuming that the gravity did not change with the application of the external magnetic induction, i.e. $\tilde{g} = 9.8$ m/s^2. Finally, different markers and colors are used to distinguish the data points. Specifically, the red crosses denote the measurements from Case CstB, and the small black dots are the data from Particles M, whereas the rest of the markers are the different configurations of Case Cst∇_zB previously mentioned.
Note that in the case of Particles M and Case CstB, the points keep the same abscissa between the sub-panels (a) and (b) because in the Case CstB, $\tilde{g} = g = 9.8$ m/s^2.

For both the trajectory planarity and angle, the data points collapse into a single trend when the corrected $Ga(\tilde{g})$ is used. While for Case CstB no correction in Ga is needed and an identical behaviour is observed compared to the Case $\emptyset B$ (Particles M). The latter implies that there is no measurable effect of the rotation blockage on the trajectory angle or planarity as predicted by Zhou and Dusek (2015).

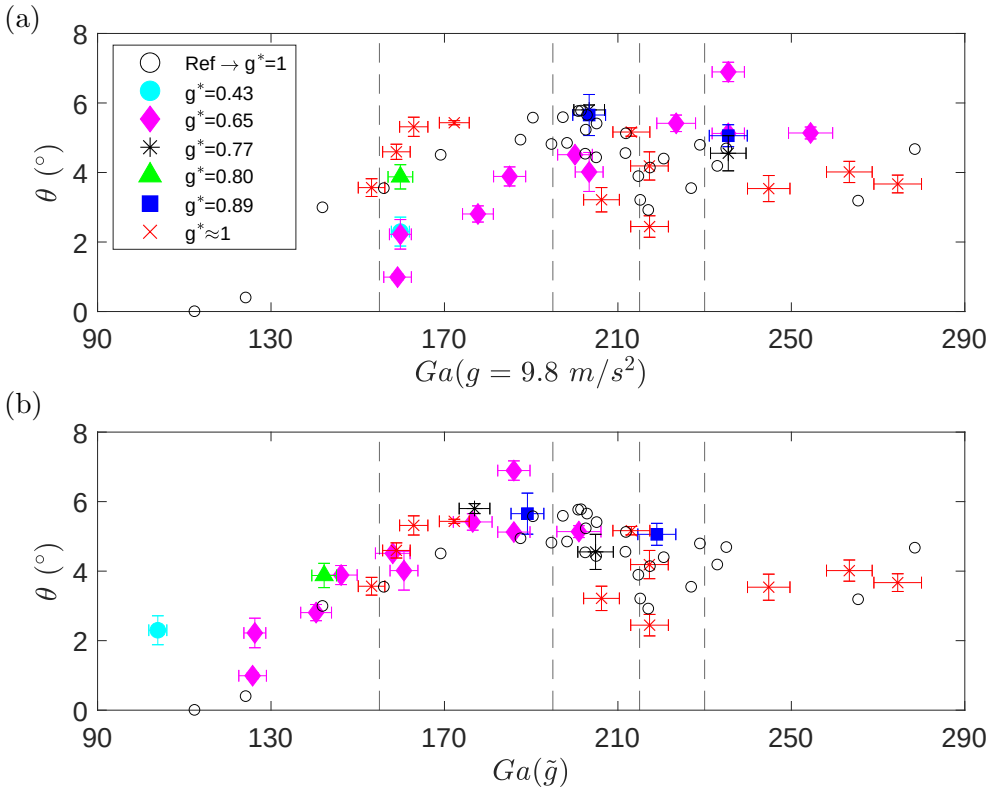

Figure 4.12: Trajectory angles with the vertical versus Ga number, alongside with the measurements from Particles M (black dots) presented in Section 4.1 that serve as reference. Additionally, vertical dashed lines show the onsets for the different regimes explained in the previous Section. In particular, (a) shows the measurements as a function of a Ga number computed assuming that the gravity did not change with the application of the external magnetic induction, i.e. $\tilde{g} = 9.8$ m/s^2, whereas (b) presents the measurements against a Galileo number that was calculated with the corrected gravity value $\tilde{g}$. Finally, different markers and colors are used to distinguish the data points as denoted in the legend.

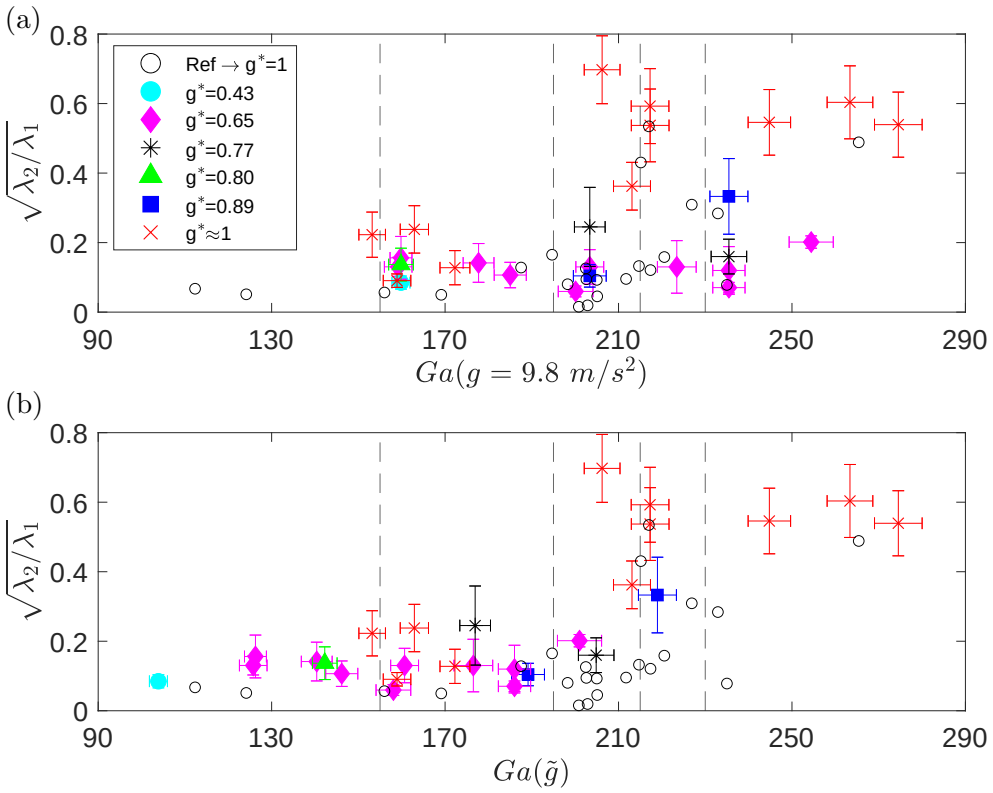

Figure 4.13: Trajectory planarity $\sqrt{\lambda_2/\lambda_1}$ with the vertical versus Ga number, alongside with the measurements from Particles M (black dots) presented in Section 4.1 that serve as reference. Additionally, vertical dashed lines show the onsets for the different regimes explained in the previous Section. In particular, (a) shows the measurements as a function of a Ga number computed assuming that the gravity did not change with the application of the external magnetic induction, i.e. $\tilde{g} = 9.8$ m/s^2, whereas (b) presents the measurements against a Galileo number that was calculated with the corrected gravity value $\tilde{g}$. Finally, different markers and colors are used to distinguish the data points as denoted in the legend.

Hence the uniform magnetic gradient strategy indeed allows to explore Galileo number effects and settling regimes as if viscosity were varied.

Note the single point (light blue circle) with $\tilde{g} = (4.2 \pm 0.2)\ m/s^2$ and $Ga = 103$, that corresponds to the strongest magnetic gradient applied (Case Cst∇_zB $\times$ 5/3). It is off the trend in Fig. 4.12(b). Furthermore, note how the same point in Fig. 4.13(b) is not off trend. This can be attributed to the radial magnetic force becoming closer in magnitude to the fluid drag, hence influencing the trajectory angle and not its planarity.

Trajectories Geometry

In the previous Subsection it was shown that magnetic particles follow the same angle and planarity trends as the non-magnetic case. The qualitative geometry of the trajectories matches as well that of $\emptyset B$ (see Subsection 4.1.4).

Figure 4.14 presents some representative 3D trajectories (first column) alongside with a top view (second column). All these trajectories belong to Case CstB, as those of Case Cst∇_zBhave the same dynamics but with shorter trajectories. Each sub-panel presents results with Ga in the main four regimes previously identified:

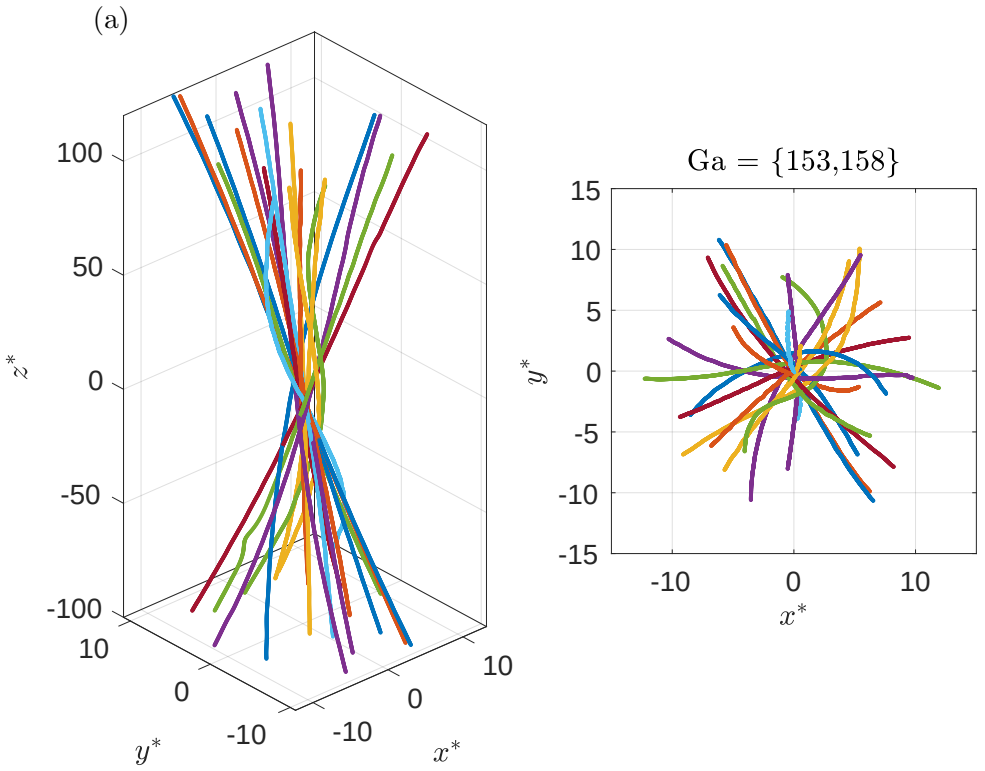
(a)
100
50
0
-50
-100
z^*
10
0
-10
y^*
10
0
-10
x^*
Ga = {153,158}
15
10
5
0
-5
-10
-15
y^*
-10
0
10
x^*

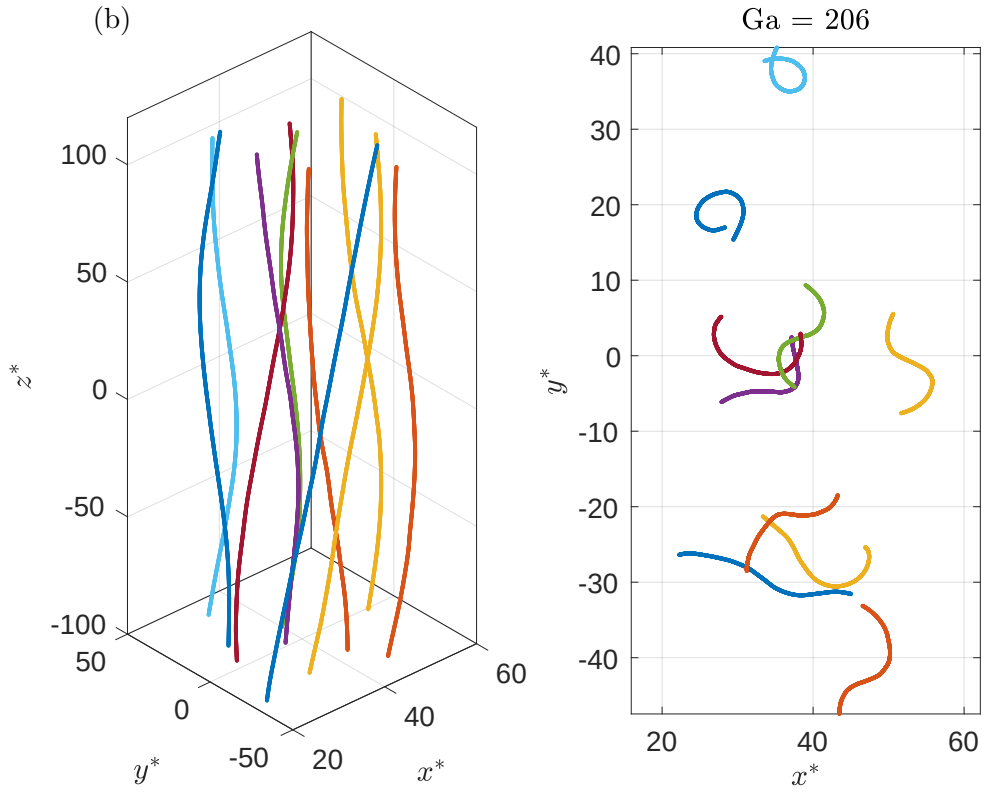
(b)
100
50
0
-50
-100
z^*
50
0
-50
y^*
20
40
60
x^*
Ga = 206
40
30
20
10
0
-10
-20
-30
-40
y^*
20
40
60
x^*

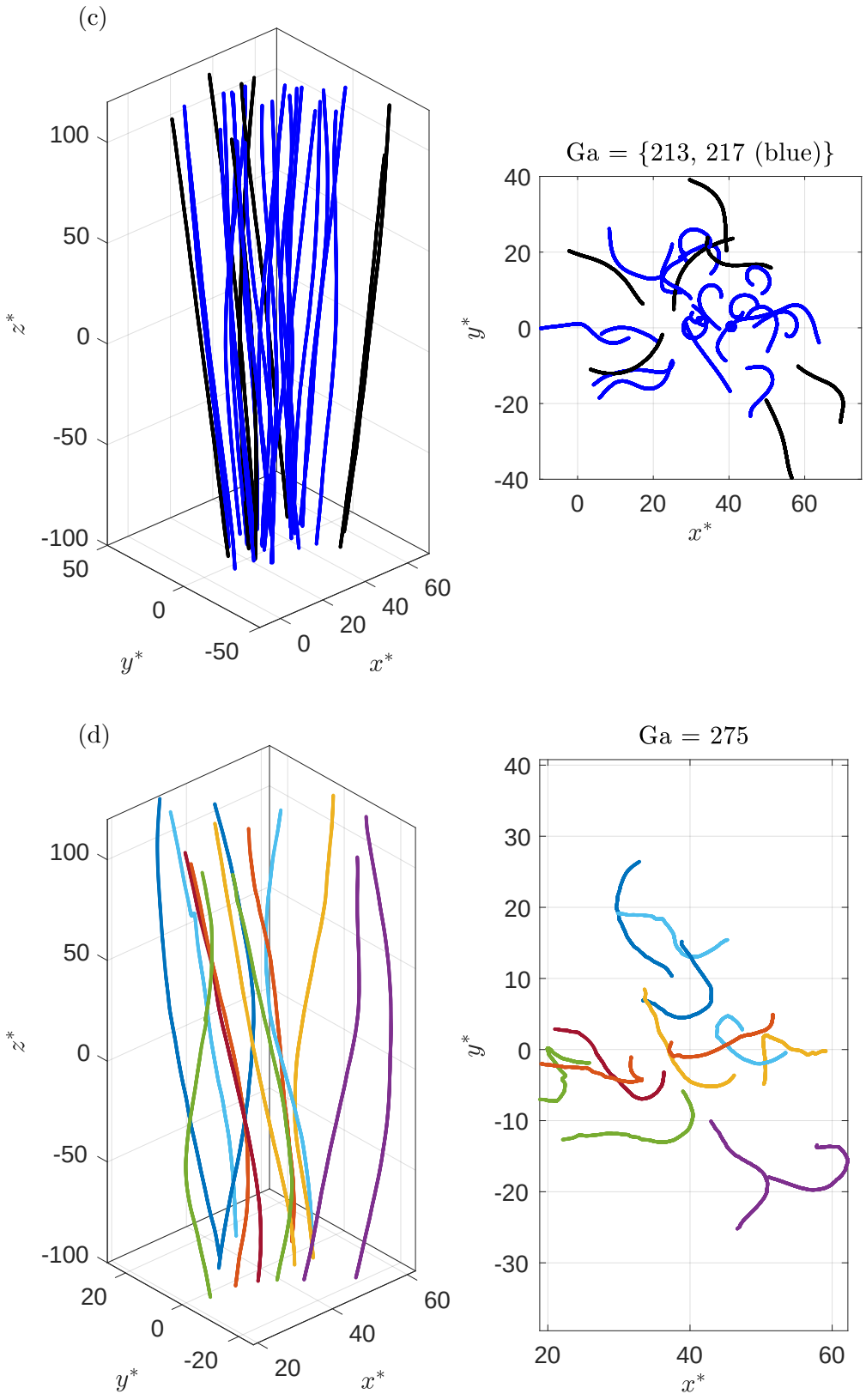

Figure 4.14: Representative 3D trajectories (first column) alongside with a top view (second column), for results with Ga in the main four regimes previously identified. Sub-panel (a) – $Ga = \{153, 158\}$, Steady Oblique regime. Sub-panel (b) – $Ga = 206$, Oblique Oscillating regime. Sub-panel (c) – $Ga = \{213, 217\}$, Planar or Rotating regime. Sub-panel (d) – $Ga = 275$, Chaotic regime.All these trajectories belong to Case CstB. Those from Case Cst∇_zBhave the same dynamics but with shorter trajectories.

- Steady Oblique – $Ga = \{153, 158\}$
  Figure 4.14(a) presents some trajectories in this regime. The trajectories are planar and have a well defined angle with the vertical that, after removing the mean values, form a cone in 3D space. These trajectories are less planar (although still overall planar) than those of Case $\emptyset B$. Note that this difference can be observed from the planarity quantification done before (Fig. 4.13) where the magnetic particles have a value of $\lambda_2/\lambda_1 \approx 0.2$ versus 0.05 for Case $\emptyset B$.

- Oblique Oscillating – $Ga = 206$ (Fig. 4.14(b));
  While trajectories at $Ga = 206$ would be expected to be in the Oblique Oscillating regime according to numerical simulations, non planar (probably helicoidal) trajectories are observed, as represented in Figure 4.14(b). Besides, although not visually evident, spectral analysis in next subsection will reveal an oscillating dynamics at the Low Frequency rather than the High Frequency expected for the Oblique Oscillating regime and seen for particles $\emptyset B$. On the other hand, the trajectories here are not planar as identified in the previous planarity analysis where the red cross at $Ga = 206$ has a planarity of $\lambda_2/\lambda_1 \approx 0.7$.
  Overall these properties are similar with the trajectories belonging to the Planar or Rotating regime (Fig. 4.14). It is likely that considering the uncertainty in Ga and the vicinity with the frontier with this zone of the parameter space, this measurements shall be attributed to the Planar or Rotating regime: this will be confirmed in the sequel as the PSDs in particular are very much alike.

- Planar or Rotating – $Ga = \{213, 217\}$ (Fig. 4.14(c));
  Figure 4.14(c) presents some trajectories in this regime. They are composed of weakly non-planar trajectories (black) and some helicoids with diameter $D \approx 10$, and pitch $P \approx 500$ (equivalent to those of Case $\emptyset B$).
  Recall that a tri-stable region is predicted by numerical simulations for these ranges of Ga. Apart from the effects on angle and planarity (discussed in the Case $\emptyset B$), this sub-panel makes explicit the presence of two regimes at these Ga numbers: helicoid-like trajectories coexist with oblique non-planar ones.

- Chaotic – $Ga = 275$ (Fig. 4.14(d)).
  Finally, the Chaotic regime matches correctly the characteristics found for the Case $\emptyset B$: all trajectories are different, non-planar and oblique.

The trajectories found while the particle rotation is blocked and an effective gravity is set are indistinguishable from those found in the case of non-magnetic particles. This supports the conclusion that rotation blockage and the addition of a magnetic force do not affect the regimes that a settling particle undergoes.

Trajectories Oscillations

As it was the case in the measurements without magnetic field, regimes with periodic oscillations are found in both CstB and Cst∇_zB cases. Recall that the quantitative PSD study is only possible for Case CstB, as the visualisation height is too short for Fourier analysis in the other case. The Case CstB is interesting to study the possible impact of rotation blockage on the trajectory oscillation frequency. In particular in the Oblique Oscillating and the tri-stable regimes that follow it.

Figure 4.15 presents the power spectral density of the trajectories with $Ga = 206$ (sub-panel (a)), and $Ga = 213$ and 217 (sub-panel (b)). While sub-panels (c) and (d) recall the data in Case $\emptyset B$ at $Ga \in [187, 205]$ and $Ga \in [215, 221]$, respectively.

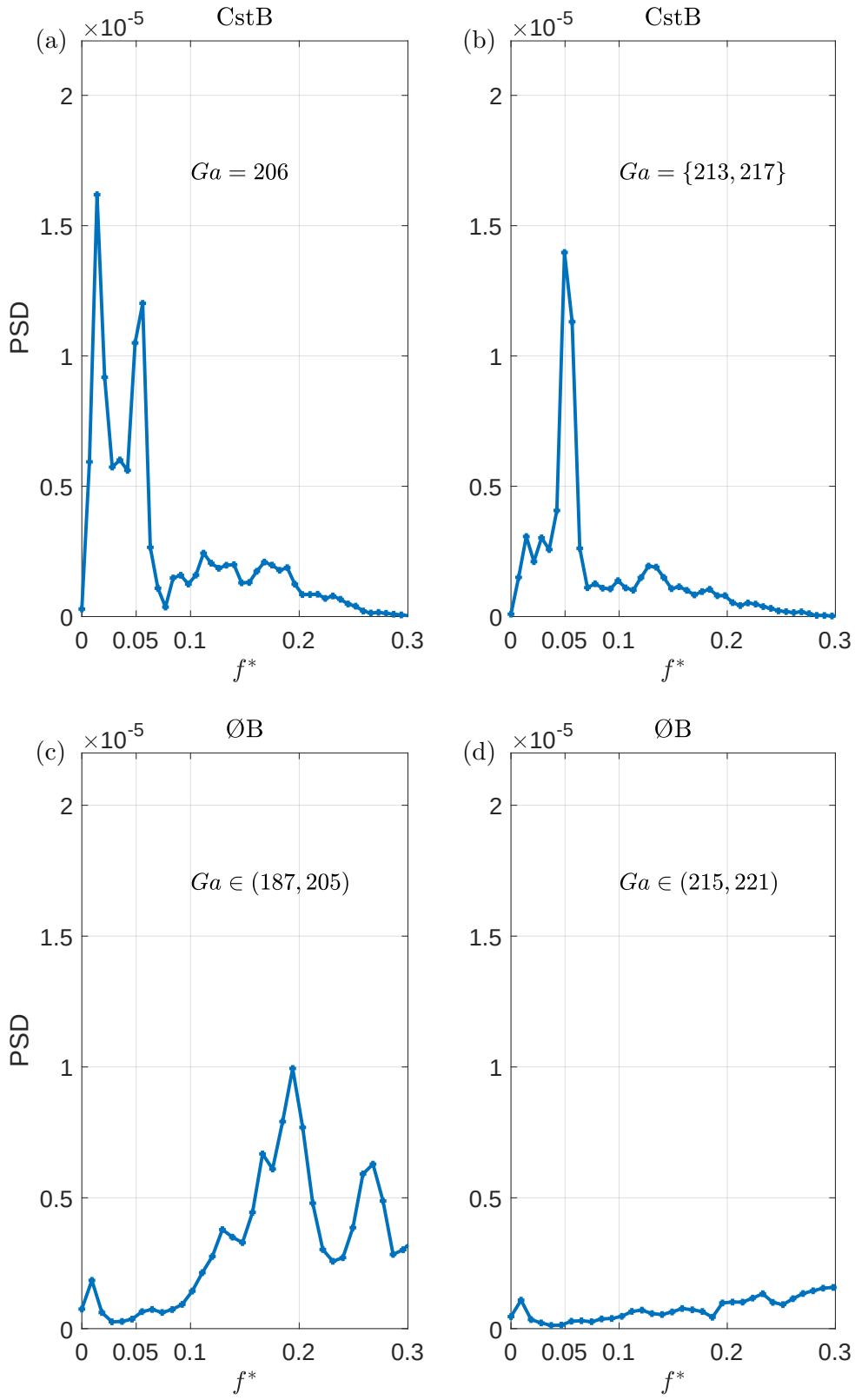

Figure 4.15: Averaged over all trajectories power spectral density for different realisations in the Planar or Rotating tri-stable region. The first row presents data from magnetic particles in the Case CstB, while the second row recalls the PSDs obtained for the Case $\emptyset B$ (see Subsection 4.1.4). In particular, sub-panel (a) shows data with $Ga = 206$, whereas sub-panel (b) presents $Ga = \{213, 217\}$ measurements. Sub-panels (c) and (d) show data at $Ga \in (187, 205)$ and $Ga \in (215, 221)$, respectively.

Differences between this data and that of the Case $\emptyset B$ are found. Firstly, Fig. 4.15(a) should resemble the spectra shown in Fig. 4.15(c), i.e. it shall fall in the High Frequency Regime, with planar trajectories and oscillations at the High Frequency $f^* = (0.19 \pm 0.01)$. As discussed before, the trajectories at this Ga are not planar.
In this sense, the measurements might indicate that the rotation blockage does have an effect in the oscillation frequency. Although, the uncertainty in Ga, the resemblance between Fig. 4.15(a) and Fig. 4.15(b), and the fact that the transition between the Oblique Oscillating and Planar or Rotating regime is around these Ga point to the measurements at $Ga = 206$ being part of the Planar or Rotating regime.

On the other hand, Fig. 4.15(b) presents the average PSD of all the trajectories with $Ga = \{213, 217\}$, as their spectral content is identical. They are in the delimitation between the Oblique Oscillating and the Planar or Rotating regimes and, as it was previously seen, they fulfil the conditions for the Planar or Rotating regime. Furthermore, their spectra presents oscillations exclusively at a frequency $f^* = (0.05 \pm 0.01)$ that qualitatively coincides with the Low Frequency $f^* \approx 0.068$.
Although this behaviour was not observed in this range of Ga for the Case $\emptyset B$ it is not inconsistent with the existence of the tri-stable regime Planar or Rotating (composed of Low and High Frequency, and Chaotic regimes) at $Ga \in [215, 230] \pm 10$. Recall that this tri-stable regime was predicted by numerical simulations to be at $Ga \in [219, 240]$ (Zhou and Dusek, 2015).

4.2.3 Conclusions

Regarding trajectory angle and planarity, only minimal differences have been found between the magnetic and no magnetic cases. Recall that in the magnetic case, apart from having an effective gravity, there is also a particle rotation blockage.
The regime Planar or Rotating is numerically predicted to be tri-stable (Chaotic - High Frequency - Low Frequency) over a slim region of $Ga \in (220, 230) \pm 10$ that can not be distinguished with the present uncertainties. and The present measurements do not allow to conclude whether there is a rotation blockage effect or not in the region Planar or Rotating.

4.3 Cubes

The settling of cubes in a Quiescent Flow follows a somewhat similar dynamics to that of spheres. In particular, an identical Experimental Setup to that utilised for non-magnetic spheres is used here. In this sense, see Section 2.1 and Section 4.1.3 for experimental details.
The addition of particle anisotropy and sharp edges make even harder the development of theoretical models that are not even available for spheres. Furthermore, this problem has an additional degree of freedom, crucial to the dynamics, that is particle orientation. The following experiments of single cubes settling in quiescent flows unraveled a rich dynamics that was contrasted with recent numerical results from the literature (Seyed-Ahmadi and Wachs, 2019), yielding a good quantitative agreement.

4.3.1 Definitions

The problem consists in a cube of side $d_p = 1$ mm and density $\rho_p = 8.2$ kg/m^3 settling in a quiescent flow with kinematic viscosity ν. As for the spheres, this problem is controlled by two dimensionless parameters (see Section 1.2): Ga and Γ. Note that the cube orientation is an output parameter as the settling velocity.
Depending on Ga and Γ, the settling cube undergoes different trajectory types that will be

characterize as for the spheres by their geometrical (angle, linearity and planarity) and dynamical (oscillations, terminal velocity) properties.

$L_{\text{ref}} = 1$ mm	$V_{\text{ref}} = \sqrt{4/3\lvert\Gamma - 1\rvert d_p g}$
$T_{\text{ref}} = V_{\text{ref}}/L_{\text{ref}}$	$f_{\text{ref}} = L_{\text{ref}}/V_{\text{ref}}$

Table 4.5: Reference length (L_{ref}), time (T_{ref}), velocity (V_{ref}) and frequency (f_{ref}) used to make dimensionless the measured quantities.

All measured quantities are made dimensionless by the reference scales presented in Table 4.5. The dimensionless quantities are denoted by an upper-script asterisk, for example, the particle velocity: $\mathbf{v}^* = \mathbf{v}/V_{\text{ref}}$.

The trajectory planarity will be quantified in the same way detailed in Section 4.1.

4.3.2 Parameters space & experimental setup

Parameters \ Regimes	Vertical	Helicoidal	Chaotic
$Ga^{\text{num. simuls.}}$	100-125	125-175	175-250
$Ga^{\text{experiments}}$	103	{138, 161}	{176, 201}

Table 4.6: Settling regimes explored in this work for the settling of cubes according to the value of the Galileo number. The columns present the three different regimens explored here, while the rows show Galileo number. In particular, the first row presents the onset predictions from numerical simulations (Seyed-Ahmadi and Wachs, 2019) – $Ga^{\text{num. simuls.}}$, in the case of cubes with a particle-to-fluid density ratio Γ equal to 7. Whereas the second row presents the experimental Galileo numbers – $Ga^{\text{experiments}}$ measured here for cubes with $\Gamma \in [8, 8.2]$.

Table 4.6 presents the range of Galileo numbers studied in this Section for the settling of cubes in a quiescent flow, recalling the corresponding regimes according to numerical simulations by Seyed-Ahmadi and Wachs (2019). While the first row presents each regime's onset as predicted by simulations (Seyed-Ahmadi and Wachs, 2019), the second row shows the 5 data points taken in this thesis. All the points are taken in the data-set category "Extended" introduced in the study of spheres, i.e. the dimensionless maximum trajectory length is $h/d \approx 200$.

Additionally, the raw trajectories are filtered via the convolution with a Gaussian kernel of width $\sigma = 12$ frames, as done in the case of spheres. As it was the case before, the relation between the cut-off frequency and the frequency to measure respects the Nyquist-Shannon sampling theorem according to the typical expected oscillation frequencies.

Four regimes, that differ in the particle's angular velocity, trajectory inclination, planarity, and periodic oscillations are identified numerically. These are:

- ($Ga \approx 85$) the Oblique Regime, with no angular rotation (incidence angle of $\approx 2°$), planar and oblique trajectories, and no oscillations (not studied here).
- ($70 \lesssim Ga \lesssim 120$) The Unsteady Vertical Regime, with angular rotation around the perpendicular (to gravity) axis, planar and vertical trajectories, and non-periodic oscillations.
- ($130 \lesssim Ga \lesssim 170$) The Helical Regime, with constant angular rotation around the perpendicular axis, non-planar and oblique trajectories, and no oscillations.
- ($180 \lesssim Ga \lesssim 250$) The Chaotic Regime, with a variable angular rotation around the perpendicular axis, non-planar and oblique trajectories, and non-periodic oscillations.

These experiments have a particle-to-fluid density ratio in the range $\Gamma \in [8, 8.2]$, whereas the numerical literature goes to a maximum of $\Gamma = 7$. Nevertheless, comparisons are going to be made as the dynamics in the literature simulations does not change considerably for particles above $\Gamma \approx 6$. In this sense, the experimental results here presented allow to validate the following claims made in numerical works (Seyed-Ahmadi and Wachs, 2019):

1. At $Ga = 103$, the dynamics fall in the Vertical Regime.
2. At $Ga = 138,$ and 161, the dynamics are in the Helical Regime.
3. At $Ga = 176,$ and 201, the dynamics are in the Chaotic Regime.
4. The amplitude of the non-periodic perpendicular (to gravity) velocity fluctuations in the Unsteady Vertical Regime have an dimensionless amplitude of 0.1.
5. The trajectory angle at the Unsteady Vertical Regime is close to zero.
6. The trajectory angle, in the Helical Regime, is $\theta = (2° \pm 1°)$ at $Ga = 161$, and $\theta = (8° \pm 1°)$ at $Ga = 160 - 170$. Note that these are specified for cubes with $\Gamma = 4$.
7. The drag suddenly increases when the trajectories become helicoidal.

4.3.3 Experimental Results

In what follows the results obtained in the context of this thesis are presented. The analysis is focused on the trajectory angle, planarity, and spectral content. Additionally, the cube terminal velocity and its drag are discussed.

Trajectory Geometry

Figures 4.16 exposes some trajectories for each Galileo number studied. The first column presents the 3D trajectories whereas the second one shows an upper view. In particular, each row has the results for the following Galileo numbers 103 (a.1-a.2); 138 (b.1-b.2); 161 (c.1-c.2); 176 (d.1-d.2); 201 (e.1-e.2). Moreover, the colour code is maintained within rows.

The trajectories in Figs. 4.16(a) – $Ga = 103$ do not deviate from the initial plane that the cube randomly choses, i.e. the trajectories are planar. Furthermore, it is clear that the trajectory angle with the vertical is not constant: compare the trajectories in the upper-right corner of Fig. 4.16(a.2) to the other ones. One might note that the settling of all those outlier trajectories start in the same region of space. It is not expected that this dual dynamics was caused by the initial position: at higher Ga, there are trajectories starting in that region of space and they are not outliers (see, for example, Fig. 4.16(d.2)). This dual behaviour will be quantified in other ways in what follows.

It is clear from Figs. 4.16(b) – $Ga = 138$ that the trajectories are not planar, in particular they are helicoidal. Moreover, they are not vertical and, as it will be quantified in what follows, their angle with the vertical is around $\theta \approx 4°$. Although the fact that the cube's path is not vertical makes difficult a quantitative observation of the helicoid diameter from Figs. 4.16(b), it can be qualitatively seen that the helicoid diameter D^* does not vary much. In particular it is found to be $D^* = (0.8 \pm 0.2)$. Finally, as it will be later quantified by a Power Spectral Density, the helicoids pitch P^* (in units of cube side length) is $P^* \approx 25$.

(a.1)

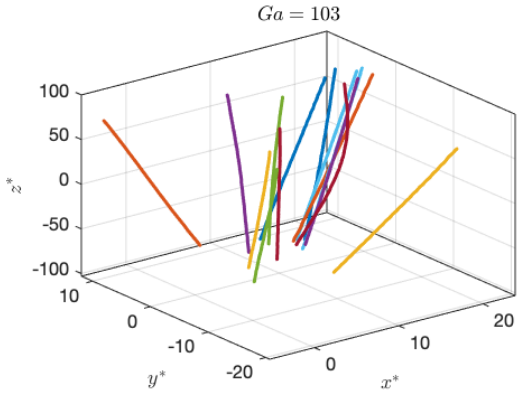

(a.2)

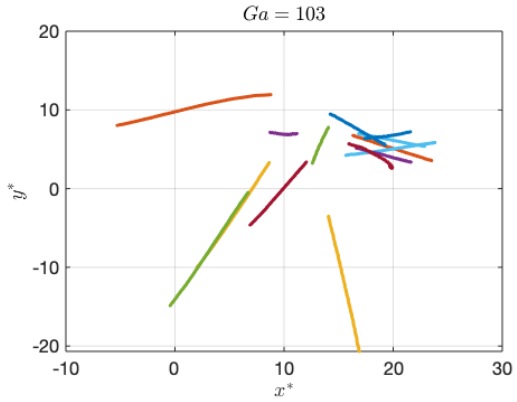

(b.1)

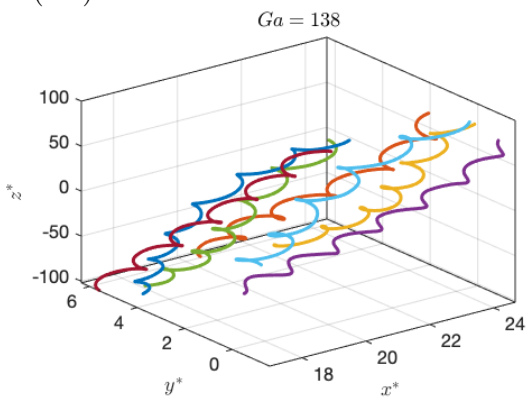

(b.2)

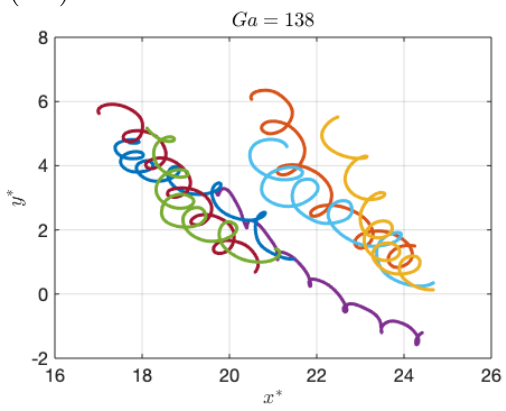

(c.1)

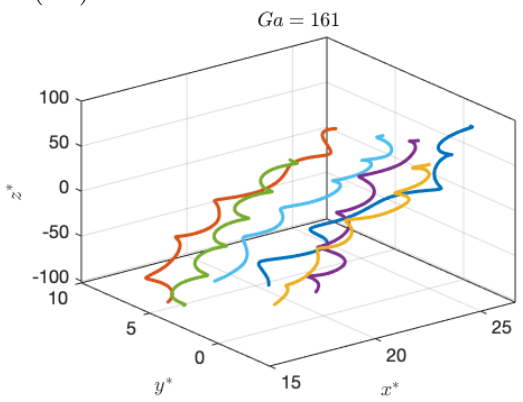

(c.2)

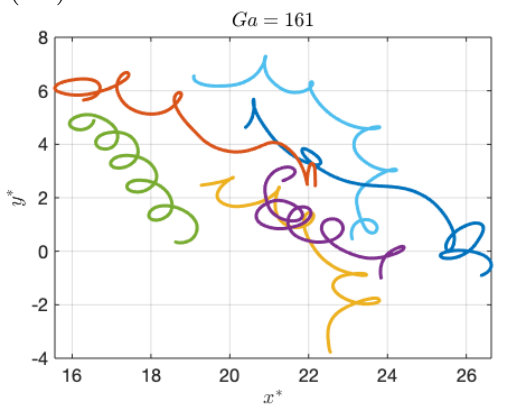

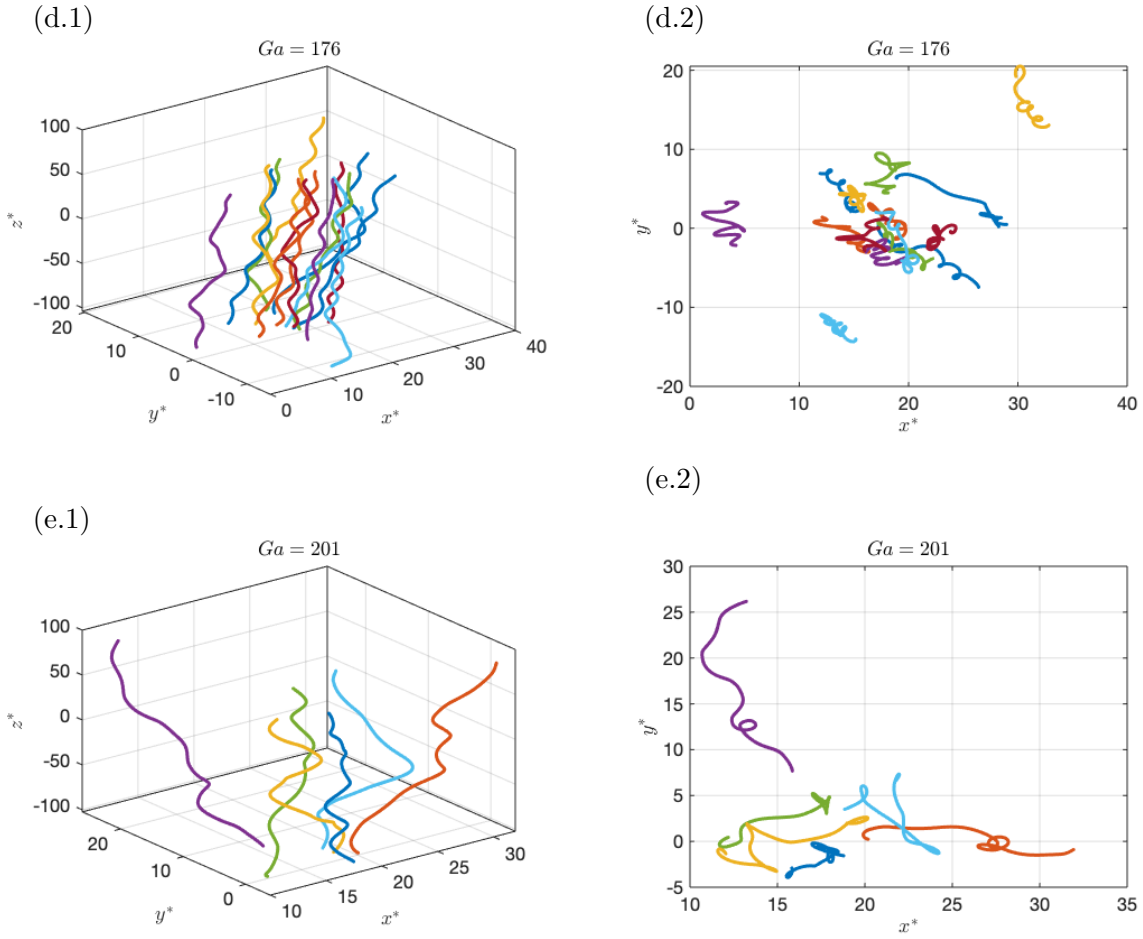

Figure 4.16: Some representative 3D (first column) and upper view (second column) plots of dimensionless trajectories of a single cube settling in an otherwise quiescent flow. Each row presents the results for the five Galileo numbers here studied: 103 (a.1-a.2); 138 (b.1-b.2); 161 (c.1-c.2); 176 (d.1-d.2); 201 (e.1-e.2).

In the case at $Ga = 161$ presented in Figs. 4.16(c) the helicoidal state seems to start fading and the cubes take helicoidal paths that are not stable: the Chaotic Regime starts to appear at this Ga. See, for example, the dark blue curve: it does one entire step of an helicoid before the trajectory drifts. Nonetheless, the trajectory angle is well defined around $\theta \approx 4.7°$.
The helicoidal shapes are further lost in the paths at $Ga = 176$ shown in Figs. 4.16(d). Still some trajectories similar to those encountered at $Ga = 161$ exist: see for example, any of the two yellow curves. But, the majority of the paths do not seem to follow a pattern. The angle is well defined at $\theta \approx 4.9°$.
In the case $Ga = 201$ presented in Figs. 4.16(e), the trajectories settle to the Chaotic Regime. This is characterised by its non-planarity, the absence of periodic oscillations, and a *big* dispersion in trajectory angle. In other words, each trajectory is different.
Finally, the trajectories at $Ga = 138, 161,$ and 176 are oriented in the same sense, i.e. the initial direction at which they settle is going towards negative values of x^*. This might be caused by a small push, in a fixed direction, on the particles when they are released. This is not expected to change the dynamics, as the initial trajectory direction does not affect the characteristics of the trajectories.

Trajectory angle & planarity

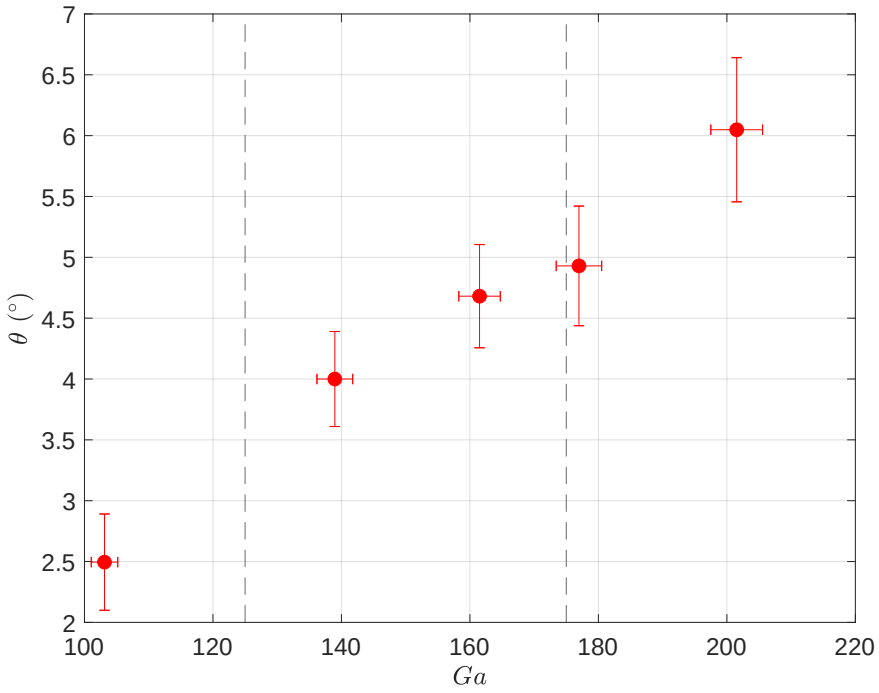

Figure 4.17: Trajectories mean angle versus Galileo number. Alongside with vertical dashed lines that delimit the three different regimes identified by the numerical results in the literature.

Figure 4.17 presents the trajectory angle θ as a function of Galileo number. The angle is quantified, as it was done for spheres, via a 3D line fit of the trajectory and the perpendicular velocity value $v_{\perp}^{*}$ (see Subsection 4.3.3), yielding the same results. Furthermore, the two dashed vertical lines present the division between regimes as predicted by numerical simulations in the literature. The uncertainty on the angle is taken as half the standard deviation of the angle distribution, whereas the error in Galileo number, reflects the 4% uncertainty in the viscosity measurement (see Section 2.1.2).
The average trajectory angle is far from zero for all the experiments. The smaller angle being close to 2.5, for the case with $Ga = 103$. Furthermore, the angle follows a growing trend with Ga, which is well approximated by a linear trend $\theta \approx 3.5 \times 10^{-2} Ga - 1$ (with θ in degrees).

On the other hand, Figure 4.18 presents the trajectory planarity $\sqrt{\lambda_2/\lambda_1}$ (see Section 4.1) as a function of Galileo number. Recall that $\sqrt{\lambda_2/\lambda_1} = 0$ represents a completely planar trajectory, whereas a value of 1 is obtained when the trajectory is not planar. Furthermore, as it was done for Fig. 4.17, two vertical lines present the proposed division between regimes predicted by numerical simulations in (Seyed-Ahmadi and Wachs, 2019).

It is clear that the planarity is suddenly lost between the measurements at $Ga = 103$ and 138, where $\sqrt{\lambda_2/\lambda_1}$ goes from 0.04 to 0.24. This coincides with what was concluded from the qualitative visual inspection of the 3D trajectories: the lost of planarity coincides with the apparition of helicoidal trajectories, and it is never recovered after. In general, the trajectories are less planar when Ga grows, reaching a maximum $\sqrt{\lambda_2/\lambda_1}$ value of 0.43 at $Ga = 201$.

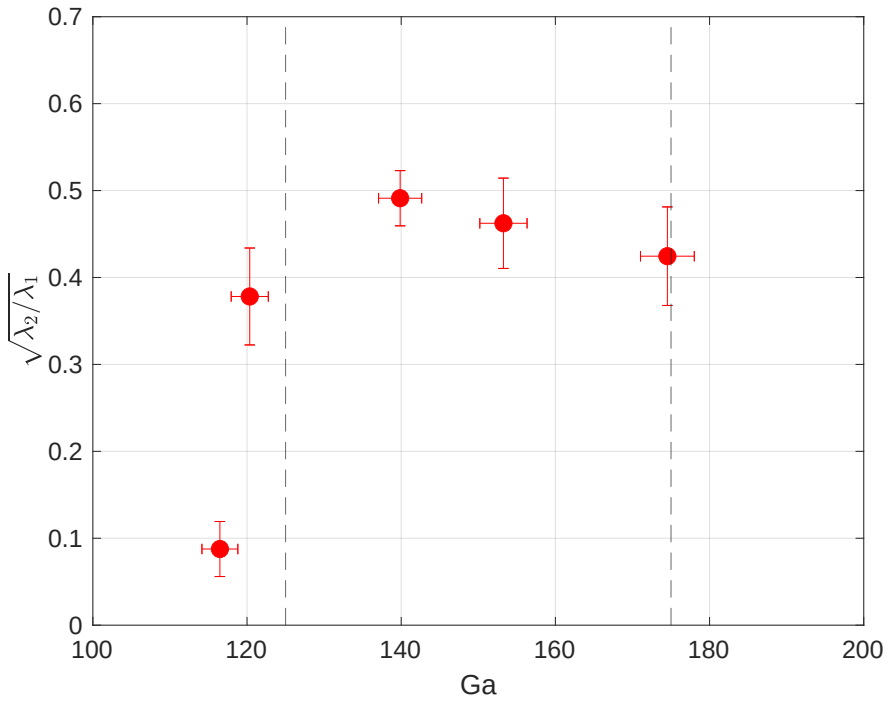

Figure 4.18: Trajectories planarity (quantified as in Section 4.1) versus Galileo number. Alongside with vertical dashed lines that delimit the three different regimes identified by the numerical results in the literature.

Trajectories Oscillations

Figures 4.19 present the Power Spectral Density (PSD) of the dimensionless perpendicular (to gravity) cube velocity $v_{\perp}^{*}$, averaged over all realisations with the same given Galileo number Ga. In particular, each panel shows the results for the following Ga: 103 (a); 138 (b); 161 (c); 176 (d); 201 (e). Finally, note that, analogously to the sphere's analysis in Section 4.1.4, the PSD frequency resolution correspond to the distance between two consecutive points and is limited by the length of the recorded trajectories.
No significant spectral content is observed in panel (a) for the smallest Ga explored (103) while the spectral content has small variations between the different other values of Ga explored. More precisely, Whereas at $Ga = 103$ the cubes do not present substantial oscillations at any band, the measurements with $Ga = 138$ start to show significant spectral content in a frequency band centered at $f^{*} = (0.34 \pm 0.06) \times 10^{-1}$. Note that this Ga is where the pure helicoidal trajectories were measured, therefore $f^{*} = 0.34 \times 10^{-1}$ is the main helicoid's frequency. Furthermore, at $Ga = 161$ the peak at $f^{*} = (0.34 \pm 0.06) \times 10^{-1}$ is intensified, and a 10 times smaller peak appears at $f^{*} = (0.66 \pm 0.06) \times 10^{-1}$, which is very likely an harmonic of the dominant first peak.

At $Ga = 176$ the peak around 0.34×10^{-1} is maintained, and a new one appears at $f^{*} = (0.49 \pm 0.06) \times 10^{-1}$. Finally, the dynamics at $Ga = 201$ intensifies and narrows the band at $f^{*} = (0.49 \pm 0.06) \times 10^{-1}$ present in the previous sub-panel, while the low frequency peak shifts to a lower value of $f^{*} = (0.12 \pm 0.06) \times 10^{-1}$.

Note how the width of the frequency peaks consistently increases with Galileo number: going from a *relatively well* defined dominant frequency of 0.34×10^{-1} at $Ga = 138$ to a broader spectral content at larger values of Ga. In this sense, the loss of helicoidal trajectories is manifested by the broadening of the spectral content.

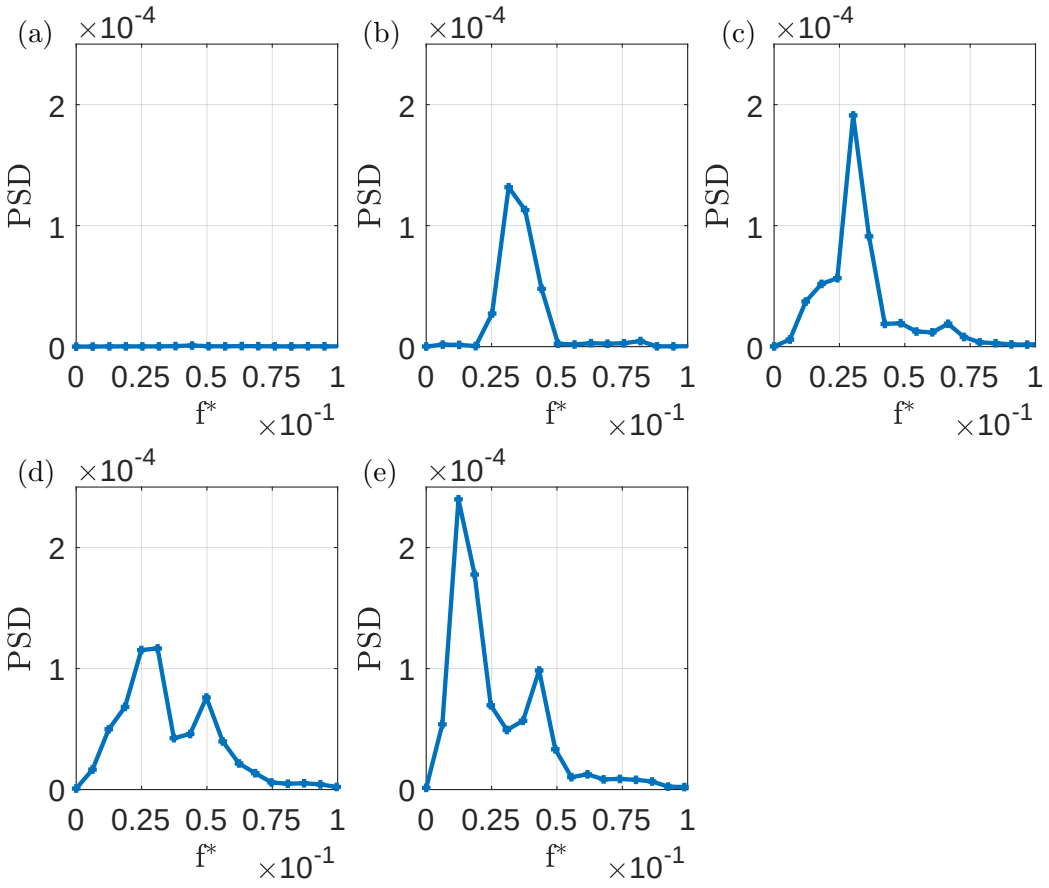

Figure 4.19: Average of the spectra over all trajectories with the same Galileo numbers, in terms of the dimensionless frequency f^*. Each sub-panel shows the result for each Galileo number: 103 (a); 138 (b); 161 (c); 176 (d); 201 (e).

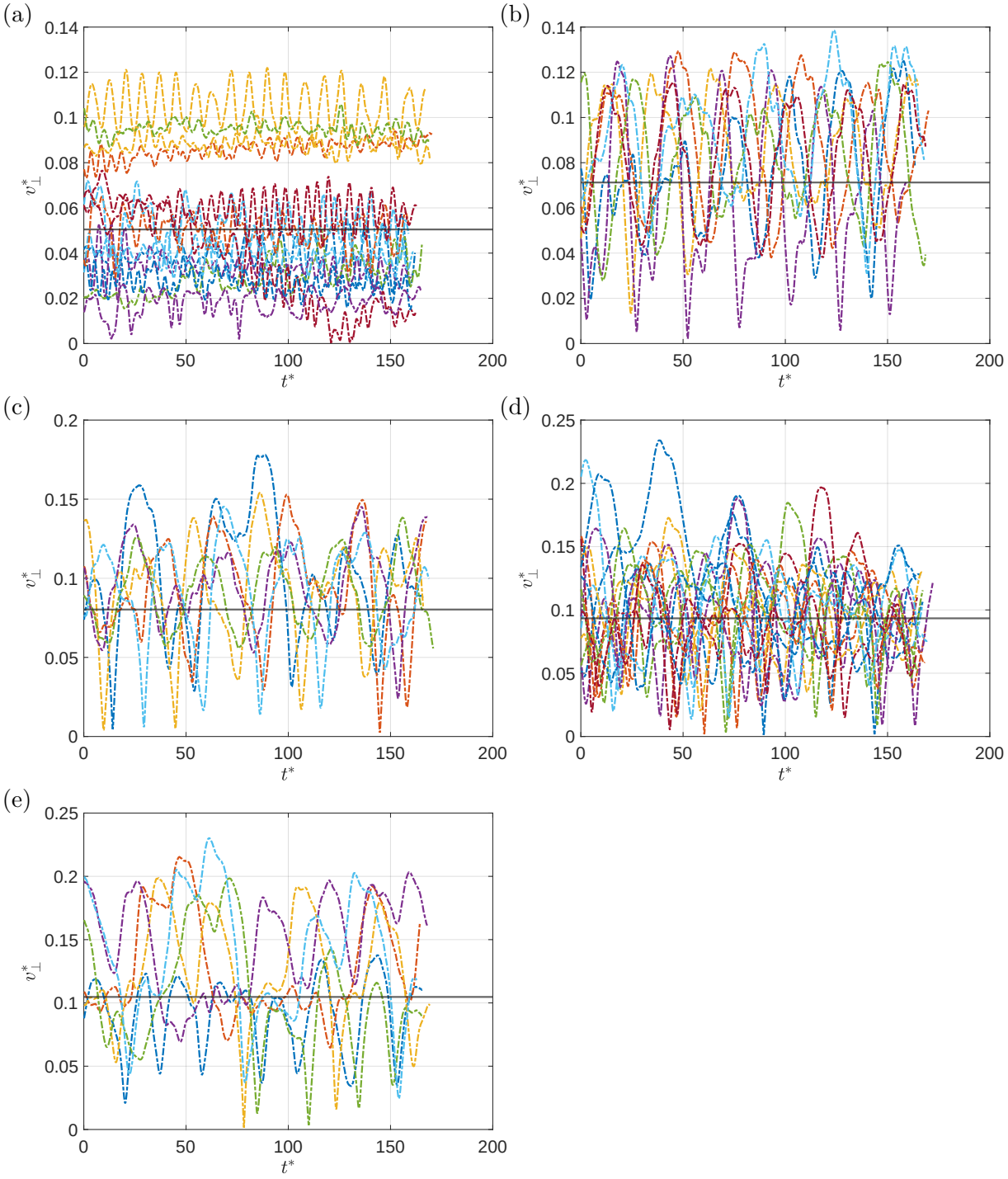

Figure 4.20: Dimensionless perpendicular (to gravity) cube settling velocity $v_\perp^*$, as a function of the dimensionless time t^*. The sub-figures present some characteristic velocities for the 5 Galileo numbers here studied: 103 (a); 138 (b); 161 (c); 176 (d); 201 (e). Moreover, the horizontal black line represents the mean value of $v_\perp^*$. Finally, the case $Ga = 103$, presented in the sub-panel (a), shows all the realisations and not only a representative subset.

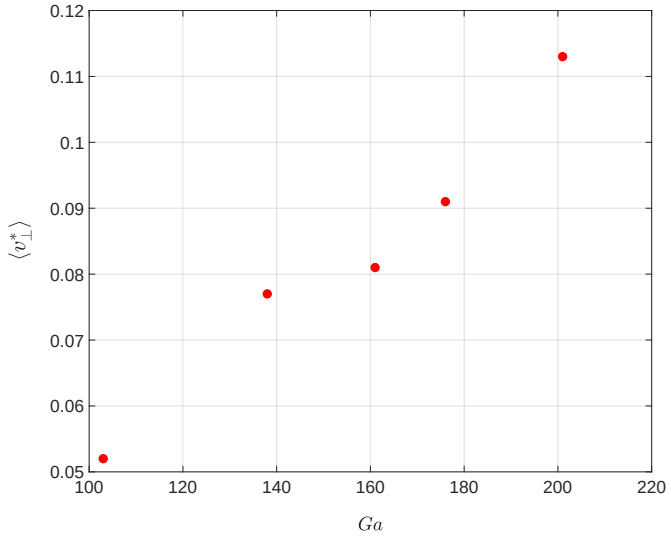

Figure 4.21: Dimensionless perpendicular velocity of settling cubes as a function of Galileo number.

Figures 4.20 present some representative dimensionless perpendicular (to gravity) cube velocities $v_\perp^*$, as a function of the dimensionless time t^*. Each sub-figure presents the velocities for each Galileo number explored: 103 (a); 138 (b); 161 (c); 176 (d); 201 (e). Moreover, the horizontal black line represents the mean value of $v_\perp^*$.
Exceptionally, sub-panel (a) contains all the experimental curves obtained. The latter is to expose the intriguing dual behaviour that the cubes have at $Ga = 103$: the definition of a perpendicular velocity mean value has to be done carefully as it is not representative of the dynamics. Furthermore, some velocity signals do show oscillations, although the frequency is very different between realisations. Besides, the amplitude of oscillations is more than 7 times smaller than for the other Ga cases. This is the reason that their averaged PSD did not present spectral content in the scale of Fig. 4.19(a). On the other four sub-panels, common frequencies that coincide with those presented in their respective PSDs can be seen.
On the other hand, the mean value of the velocity $\langle v_\perp^* \rangle$, shown as the horizontal black lines in figure 4.20 reflects the obliquity of the trajectories and follows a similar trend as the trajectory angles (figure 4.21).

Drag

Following (Seyed-Ahmadi and Wachs, 2019; Tran-Cong et al., 2004a), the drag coefficient is defined in terms of the parallel (to gravity) dimensionless velocity: $\langle C_D \rangle = 1/\langle v_\parallel^* \rangle^2$. Note that because the projected surface of a non-isotropic particle depends on its orientation, it is better to study the drag with a definition non dependant on the angle. Specially when the particle orientation is not resolved, as it is the case in these experiments.
There are not many experiments that explored the drag on cubic particles, the better correlation between Re_p and $\langle C_D \rangle$ was done in 1989 (Haider and Levenspiel, 1989). In this correlation the particle orientation is not taken into account, and it is a good approximation for a number of non-spherical objects. The drag coefficient depends on only two parameters: Re_p, and the sphericity ϕ. The latter accounts for the particle shape and it is defined as $\phi = s/S$, with s the surface of a sphere having the same volume as the particle, and S the actual surface area of the particle. Note that $\phi = 1$ if the particle is a sphere, and $\phi = 0.805$ for the case of the 1 mm

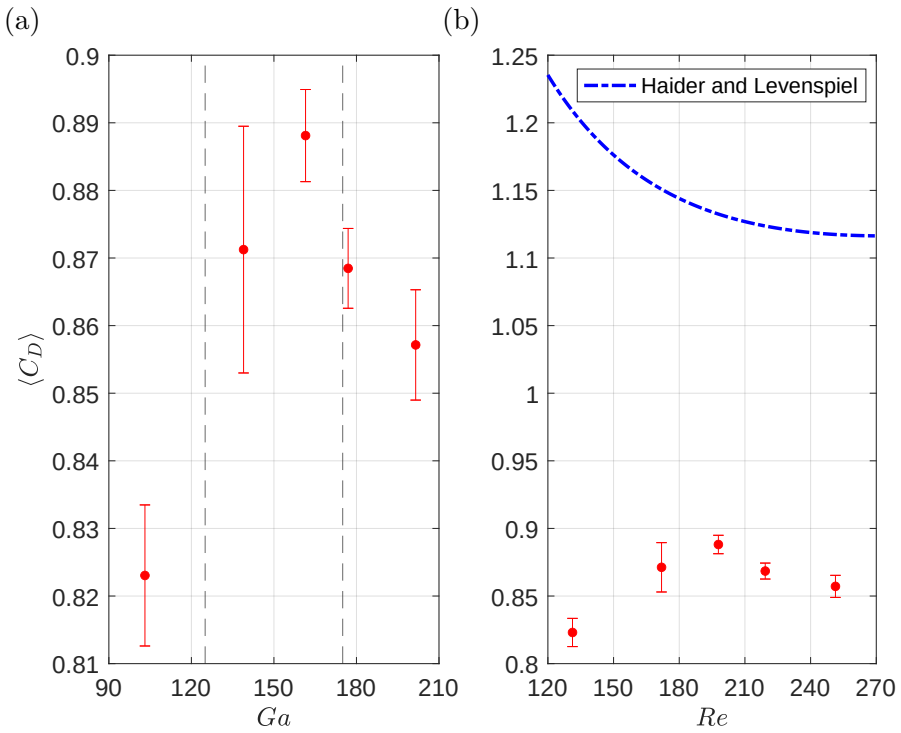

Figure 4.22: Mean drag coefficient versus Galileo (a) and Reynolds (b) numbers, computed as $\langle C_D \rangle = 1/\langle v_{\parallel}^* \rangle^2$, with $v_{\parallel}^*$ the parallel to gravity dimensionless velocity. Furthermore, the blue dashed line presents a commonly used drag correlation (Haider and Levenspiel, 1989).

cubic particles here utilised. In particular, the drag coefficient can be approximated as:

$$\langle C_D \rangle = \frac{24}{Re_p}\left(1 + (8.1716\,\exp(-4.0655\phi) Re_p^{0.0964+0.5565}\right) + \frac{73.69 Re_p\,\exp(-5.0748\phi)}{Re_p + 5.378\,\exp(6.2122\phi)}. \quad (4.9)$$

The drag coefficients calculated from the measurements are presented in Figures 4.22. In particular, the panel (a) shows the drag coefficient $\langle C_D \rangle$ as a function of Ga, whereas panel (b) presents it as a function of particle Reynolds number. Additionally, panel (b) presents in a dashed blue line the correlation from Equation 4.9. The error bars are taken as the standard deviation of the C_D distribution.
A sudden increase in drag, from 0.823 to 0.887, can be seen between the measurements at $Ga = 103$ and 138, that is where the helicoidal regimes appear. Although the drag is maximum at $Ga = 161$, where the trajectories were found to be unstable helicoids. On the other hand, from panel (b), it can be seen that while the agreement the correlation form (Haider and Levenspiel, 1989) with the drag measurement is far from accurate, this correlation still resolves reasonably the order of magnitude of the drag coefficient.

4.3.4 Comparison with literature's numerical predictions

With the results presented here, the literature numerical (Seyed-Ahmadi and Wachs, 2019) claims mentioned in Section 4.3.2 can be validated.
Firstly, the onsets proposed by numerical simulations are quantitatively correct. The measurements at $Ga = 103$ present characteristics close to those of a Vertical Regime, although not perfectly: the trajectory angle with the vertical is $\theta = (2.5° \pm 0.4°)$ rather than zero, although this angle is the smaller measured. Assuming the linear trend of the angle trajectory angle θ

with Ga can be extrapolated to smaller valued of Ga, the present results predict a vanishing angle for $Ga \approx 30$. It would be interesting to perform measurements at such smaller values of Ga, what would require smaller cubes, and/or less dense, and/or higher fluid viscosity than what was available at the time this work was done. Furthermore, the measurements at $Ga = 138$ and 161 are found to be in the Helicoidal Regime: the trajectories are found to be perfect helicoids at $Ga = 138$ and unstable ones at $Ga = 161$, in the same way that was predicted by the numerical literature. Moreover, the trajectories at $Ga = 176$ and 201 share the characteristics predicted for a Chaotic Regime: relatively wide spectral content, large trajectory angle dispersion, and non helicoidal trajectories. Furthermore, it was seen that the *chaos* seems to completely settle at $Ga = 201$, whereas at $Ga = 176$ some patterns still emerge.
Secondly, the amplitude of the fluctuations of $v_\perp^*$, for $Ga = 103$ in the Vertical Regime is found to be around 0.02, instead of approximately 0.1. Although, amplitudes closer to 0.1 are obtained in the other cases.
Thirdly, the trajectory angle predictions in the Helical Regime are qualitatively correct: at $Ga = 161$ $\theta = (4.7° \pm 0.4°)$, when the angle predicted by the simulations is $(2° \pm 1°)$; and at $Ga = 176$ $\theta = (4.9° \pm 0.5°)$, when the predicted angle is $(8° \pm 1°)$. Recall that these angle predictions were made for particles with particle-to-fluid density ratio equal to 4, and here the value is ≈ 8. A possible dependency on Γ cannot be ruled out.
Finally, a the sudden drag increase that coincides with the apparition of helicoidal trajectories was measured, in very good agreement with numerical simulations where a similar drag increase is reported around $Re_p = 150$.

Chapter 5

Particles settling in Turbulent Flows

This chapter presents an investigation on the settling of inertial particles in turbulent conditions, with the particular goal to explore the eventual enhancement and/or hindering of settling due to turbulence. As detailed in the introductory section, this problem is primarily controlled by a set of 4 dimensionless parameters which can be chosen as $\{Re, \Gamma, St, Ro\}$, where Re is the turbulence Reynolds number, Γ the particle-to-fluid density ratio, St the Stokes number (which quantifies the inertia of the particle compared to the turbulent forcing) and Ro the Rouse number (which compares the settling velocity in the absence of turbulence to the fluctuating velocity of turbulence). One of the goals in this chapter is to explore the influence of turbulence on settling when Ro is varied independently of St. This can be stated as an attempt to disentangle the effects of inertial mass and gravitational mass on particle/turbulence interactions. As pointed in the introductory chapter, this is not trivial to achieve on ground experiments, as Ro and St are interwinded and changing the nature of the particles, of the fluid, or the turbulence results in a combined modification of both parameters. The solution envisioned here to explore Ro effects independently of St effects is therefore to perform experiments at different effective gravities. This is achieved by means of the magnetic compensation of gravity, which was successfully tested in a previous chapter for the case of spheres settling in quiescent flows. Note that the results presented in this chapter where obtained in the last months of the thesis and shall therefore be considered as preliminary and as a path opening for future systematic studies, which will be carried in parallel with micro-gravity experiments in the Dryden Drop Tower at Portland State University.

5.1 Parameters space & experimental setup

The flow is generated in a cylindrical container, placed inside the experimental setup previously used for the magnetic experiments in a Quiescent Flow (see Section 2.1), where the turbulent flow is generated by jets created at the top and the bottom of the vessel that collide at the tank's center (see Section 2.2). Having the cylinder placed inside the square vessel, also full of water, eliminates optical distortions due to the cylindrical interface.
The 4D-LPT method discussed in Section 2.3 is used with two cameras (in the same fashion as the previous Chapter) to track the dynamics of single 1 mm diameter magnetic particles (Particles MAG in Section 4.2) at 3200 fps.
The main experiments have been performed with the pumps operating at their nominal electrical supply of 12 V. While a limited set of experiments have been carried at non-nominal supplies of 15 V and 18 V in order to carry a preliminary exploration of the effect of varying some turbulent properties of the flow such as σ_u, ϵ, and therefore Re_λ.

Finally, the effective gravity pulling the particles is modified via the magnetic field method

detailed in Section 2.4, validated in the quiescent flow case (Section 4.2). The coils are set up in the configuration of Case Cst∇_zB, that allows to homogeneously compensate the gravitational pull over a region of 10 cm in the vertical located at the center of the water tank, with the current in the coils as the main control parameter of the adimensional gravity $g^* = \tilde{g}/9.8\ \mathrm{m\ s^{-2}}$.

Table 5.1 presents the parameters explored in this Chapter. In particular, for each value of adimensional gravity g^* and voltage on the pumps. While the rows present the different parameters, with the control parameters $\{Re, \Gamma, Ro, St\}$ in red. In particular, the rows show:

- Turbulent integral Reynolds number $Re = \sigma_u L/\nu$, and Reynolds number based on Taylor microscale $Re_\lambda = \sqrt{15Re}$;
- The flow Froude number $Fr = \sqrt{a_0}(\epsilon^3/\nu)^{1/4}/g$, with $a_0 = 0.13(Re_\lambda)^{0.6}$ (Sawford, 1991);
- Average velocity standard deviation of the background flow explored by the particles $\sigma_u^{@P}$, estimated from the mean standard deviation Eulerian field given by the PIV characterization of the flow (see section 2.2) interpolated along the particles path;
- Average vertical velocity of the background flow explored by the particles $\langle \mathbf{u} \cdot \hat{z} \rangle^{@P}$, estimated from the mean Eulerian velocity field given by the PIV characterization of the flow (see section 2.2) interpolated along the particles path;
- Particle-to-fluid density ratio $\Gamma = \rho_p/\rho_f$;
- Particle diameter to turbulent dissipation scale ratio d_p/η;
- Particle diameter to turbulent integral scale ratio d_p/L;
- Particle Galileo number $Ga = u_g d_p/\nu$;
- Particle response time in the linear drag approximation $\tau_p^0 = d_p^2/(12\nu\beta)$;
- Particle response time with non-linear drag correction $\tau_p = \tau_p^0 f(\Gamma, Ga) = 24\tau_p^0/(Re_p C_D(Re_p))$, where the particle Reynolds number is taken as the terminal Reynolds number $Re_p(\Gamma, Ga)$ estimated *a priori* (neglecting density corrections) based on the correlations relation 4.3 discussed in section 4.1.4. The corresponding drag coefficient $C_D(Re_p)$ is then estimated using the correlation relation by Brown and Lawler (2003) (Eq. 4.5);
- Particle Stokes number based on the turbulent dissipation time scale $St = \tau_p/\tau_\eta$;
- Particle Stokes number based on turbulent time at the scale of the particle size $St_{d_p} = \tau_p/(d_p^2/\epsilon)^{1/3}$;
- Particle Stokes number based on the turbulent Eulerian integral time scale $St_L = \tau_p/\tau_L^E$;
- The particle Rouse number $Ro = (\Gamma - 1)/(\Gamma + 1/2)\tau_p g/\sigma_u^{@P}$;

For each dataset (i.e. for each column in Table 5.1) about 100 independent drops of particles where achieved, leading to 100 trajectories per dataset which enable to characterize settling statistics.

$g^* = \tilde{g}/g$	1.0 ± 0.02	0.90 ± 0.02	0.78 ± 0.02	0.71 ± 0.02	0.63 ± 0.02	0.57 ± 0.02	0.49 ± 0.02			micro-g
Voltage (V)	12	12	12	12	12	12	12	15	18	12-15-18
Re	1047	1047	1047	1047	1047	1047	1047	1352	1559	$\mathcal{O}(10^3)$
Re_λ	125	125	125	125	125	125	125	142	152	$\mathcal{O}(10^2)$
Fr	0.26	0.29	0.34	0.37	0.42	0.46	0.54	0.89	1.2	∞
$\langle\sigma_u\rangle^{@P}$	0.105	0.105	0.104	0.104	0.104	0.105	0.103	0.134	0.153	$\mathcal{O}(10^{-1})$
$\langle\mathbf{u}\cdot\hat{z}\rangle^{@P}$	0.146	0.139	0.143	0.144	0.141	0.144	0.141	0.158	0.205	$\mathcal{O}(10^{-1})$
Γ	8.2	8.2	8.2	8.2	8.2	8.2	8.2	8.2	8.2	$\mathcal{O}(1)$
d_p/η	12.8	12.8	12.8	12.8	12.8	12.8	12.8	14.9	16.6	$\mathcal{O}(1)$
d_p/L	0.1	0.1	0.1	0.1	0.1	0.1	0.1	0.1	0.1	$\mathcal{O}(10^{-2})$
Ga	303	288	268	255	240	230	212	212	212	$\mathcal{O}(10^2)$
τ_p^0 (ms)	550	550	550	550	550	550	550	550	550	$\mathcal{O}(10^{-3})$
τ_p (ms)	48	51	54	56	59	61	64	64	64	$\mathcal{O}(1)$
St	6.8	7.1	7.5	7.8	8.1	8.5	9.0	12.7	15.4	$\mathcal{O}(10^{-1})$
St_{d_p}	1.2	1.3	1.4	1.4	1.5	1.5	1.6	2.1	2.3	$\mathcal{O}(10^{-2})$
St_L	0.4	0.4	0.4	0.4	0.4	0.5	0.5	0.7	0.8	$\mathcal{O}(10^{-3})$
Ro	3.7	3.5	3.2	3.0	2.8	2.6	2.4	1.9	1.7	0

Table 5.1: Parameters achievable by this water turbulence device. The columns present the different parameters for each adimensional gravity $g^* = \tilde{g}/(9.8\ \mathrm{m/s^2})$ (with $\tilde{g}$ the effective gravity, see Section 2.4) and the micro-gravity environment, for each voltage on the pumps. While the rows present the different parameters, with the control parameters $\{Re, \Gamma, Ro, St\}$ in red. In particular, the rows show: $Re = \sigma_u L/\nu$; $Re_\lambda = \sqrt{15Re}$; $Fr = \sqrt{a_0}(\epsilon^3/\nu)^{1/4}/g$, with $a_0 = 0.13(Re_\lambda)^{0.6}$ (Sawford, 1991); $\sigma_u^{@P} = \sqrt{1/2(\langle\sigma_{u_x}\rangle^2 + \langle\sigma_{u_z}\rangle^2)}$ the flow velocity standard deviation at the positions of the particles; $\langle\mathbf{u}\cdot\hat{z}\rangle^{@P}$ the mean vertical flow at the position of the particles; $\Gamma = \rho_p/\rho_f$; d_p/η; d_p/L; $Ga = u_g d_p/\nu$; $\tau_p^0 = d_p^2/(12\nu\beta)$; $\tau_p = \tau_p^0 f(\Gamma, Ga) = 24\tau_p^0/(Re_p C_D(Re_p))$; $St = \tau_p/\tau_\eta$; $St_{d_p} = \tau_p/(d_p^2/\epsilon)^{1/3}$; $St_L = \tau_p/\tau_L$; and $Ro = (\Gamma - 1)/(\Gamma + 1/2)\tau_p g/\sigma_u^{@P}$.

5.2 Filtering of the trajectories and their derivatives

When it comes to analyse Lagrangian trajectories retrieved from 4D-LPT in turbulence, it is important to appropriately chose the filtering parameters used to smooth the trajectories and estimate their derivatives (to access velocity and acceleration statistics) in order to optimize the hindering of noise while keeping most of the small-scale turbulent dynamics. This is particularly important when derivatives are considered as differentiation is a high pass operation which tends to amplify the effect of noise. As an example, the blue plots in Figure 5.1 represent the temporal evolution of the vertical (z) component of a sample recorded trajectory, and the corresponding velocity and acceleration estimated from a simple finite difference scheme. While the presence of noise is imperceptible for the position signal, it becomes visible for the velocity and dominates the acceleration signal.

In order to smooth and differentiate position signals, the classical approach of convolution by a gaussian kernel and by its first and second derivatives is used. It gives access to the filtered position, velocity, and acceleration respectively (Mordant et al., 2004). It is key to chose the width of the gaussian kernels in order to filter most of the noise while keeping most of the signal. This is traditionally achieved by looking at the evolution of the acceleration variance estimated over the ensemble of available trajectories as a function of the filter width (Figure 5.2(a)). Ideally this trend shall exhibit a rapid decrease for small values of the filter width (indicating that most of the noise contribution to the second derivative variance is effectively reduced by the filtering) followed by a plateau with no significant influence of the filtering (indicating that the small scale signal has been retrieved with no major influence of the noise). At very large values of the filter width, the acceleration variance then starts to decrease again as relevant dynamical scales get filtered. The optimal choice for the filtering is then taken near the transition between the rapid initial decrease and the plateau. Figure 5.2(a) shows the

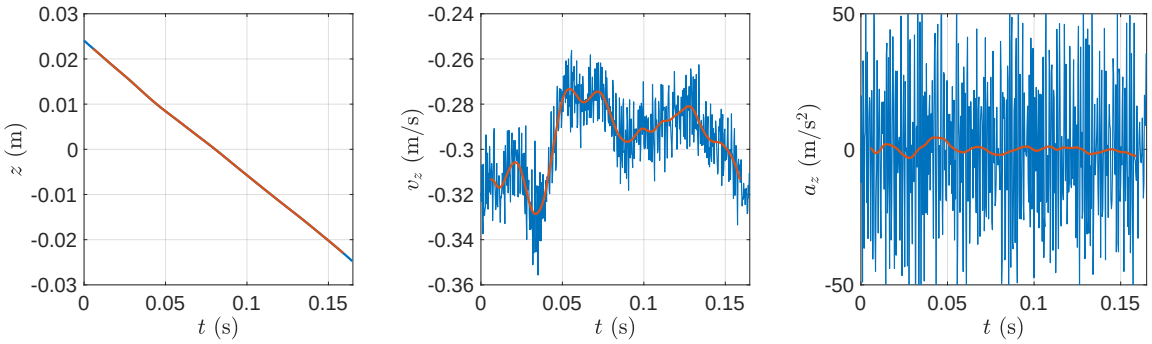

Figure 5.1: Time evolution of the vertical position of a sample trajectory (left), corresponding velocity component (middle) and acceleration (right). Blue lines correspond to the raw position, velocity (estimated from a simple finite difference scheme) and acceleration (double finite difference). Red lines correspond to the position, velocity and acceleration estimated by convolution of gaussian kernels of width 10 time steps.

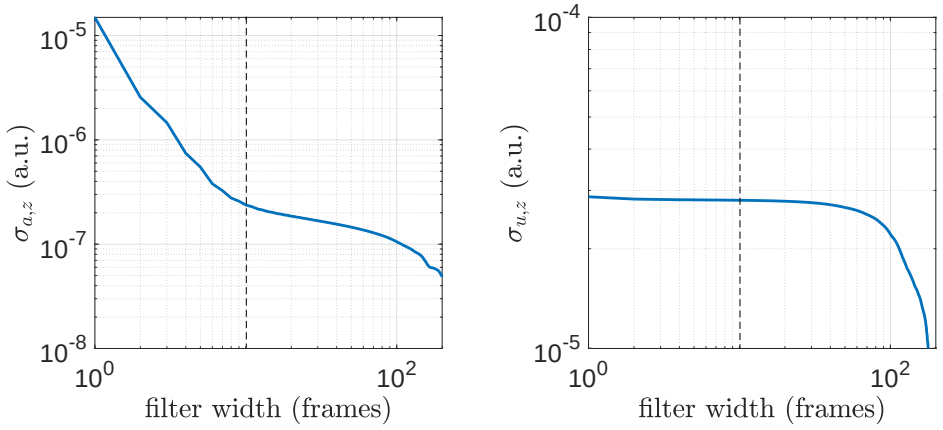

Figure 5.2: Variance of acceleration (left) and velocity (right) for the z component of the ensemble of trajectories recorded at $g^* = 1$ as a function of the gaussian kernel filter width used to smooth the trajectories and their derivatives (trends are similar for other components and effective gravities). The vertical dashed line indicates the optimal chosen filter width (10 frames in the present case).

evolution of the vertical acceleration variance as a function of the filter width for the case of particles settling at normal gravity ($g^* = 1$), which do exhibit the expected behavior. In the present case, the optimal filter width corresponds to 10 time steps. Although not shown, analysis of other components and other values of the effective gravity lead to similar optimal filtering parameters. Figure 5.2(b) shows the velocity variance as a function of the filter width. As expected, velocity (first derivative of position) is much less sensitive to filtering than acceleration (second derivative). A mild reduction of the velocity variance is visible for small filter width before a plateau and a strong reduction at large filter width where the dynamics gets strongly filtered. The important observation is that the velocity variance is not sensitive to filtering near the optimal filter width given by the acceleration analysis.

Red curves in Figure 5.1 show the corresponding filtered position, velocity and acceleration using the optimal filter width of 10 time steps, showing the performance of the filtering procedure.

Finally, it is worth to remark that the level of noise on acceleration fluctuations was found, for certain data sets to be significantly higher for the horizontal components compared to the vertical component. Figure 5.3 shows, for instance, the variance of acceleration as a function of the gaussian filter width for the z (vertical) and y (horizontal) component in the case $g^* = 1$. It can be seen that a much broader filter width would be required to reasonably smooth the horizontal acceleration signal (note however that velocity remains well filtered for all components with the filter width of 10 frames previously discussed). Figure 5.3 shows though that at large filter width (typically for a filter width larger than about 40 frames), both components behave similarly, hence suggesting a good isotropy level of acceleration fluctuations. In the sequel, when addressing acceleration fluctuations only results for the vertical component are going to be presented. It will be interesting to improve the resolution of horizontal components in future experiments. Finally, note that the smaller level of noise on the vertical component can be related to the optical arrangement of the cameras that resolves with higher redundancy the vertical direction.

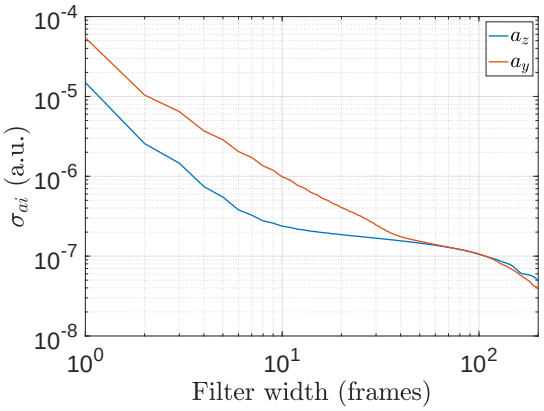

Figure 5.3: Variance of acceleration for the z (vertical) and y (horizontal) components of the ensemble of trajectories recorded at $g^* = 1$ as a function of the gaussian kernel filter.

5.3 Position statistics

Figures 5.4-5.5 present the probability density functions of recorded particle positions for the different data sets. The goal here is mainly to evaluate the region in which particles actually settle and hence the zone of the background flow that they explore. These PDFs show that particles settle close to the center of the cylinder: y component PDF is well peaked, around 1 cm

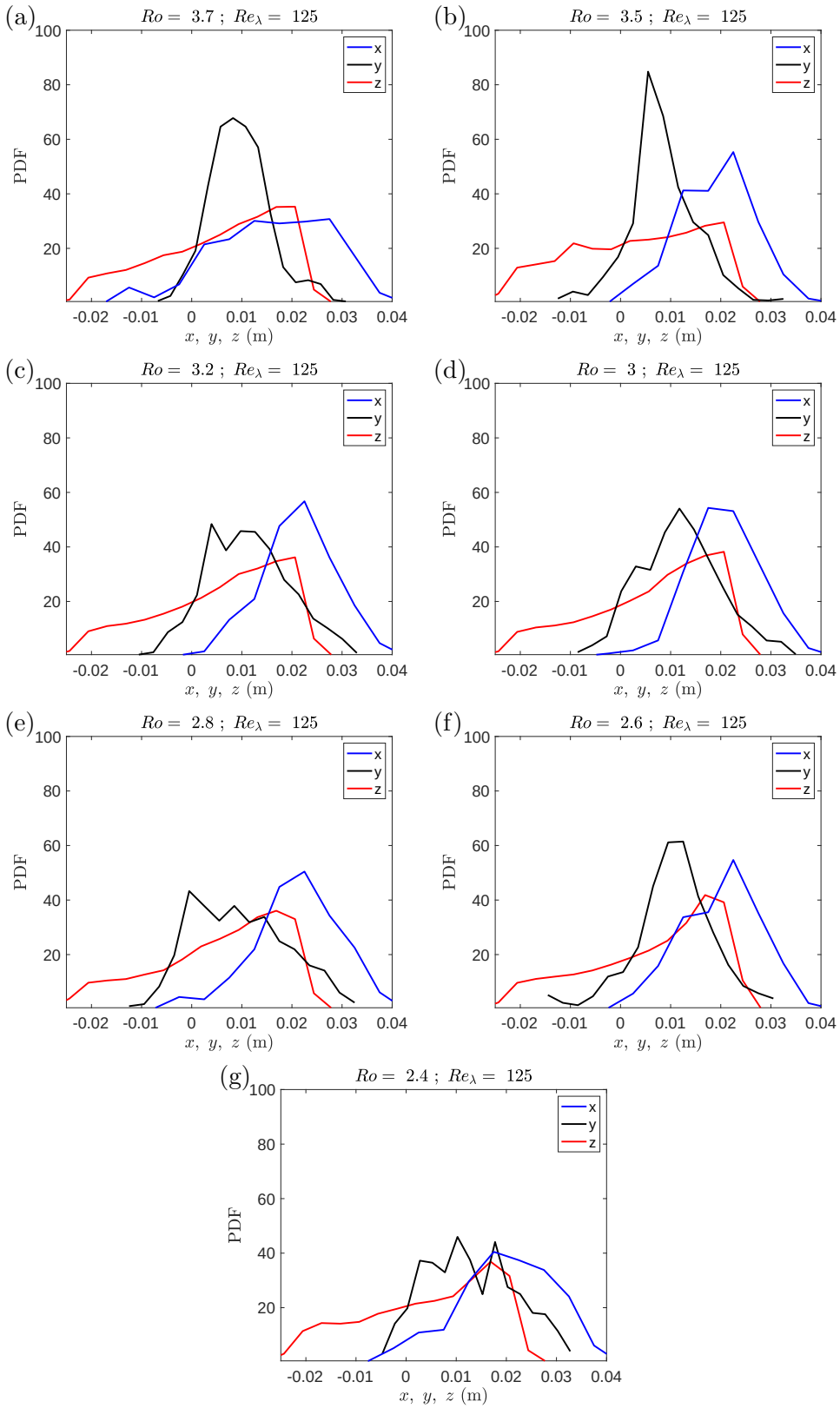

Figure 5.4: Particle's positions PDFs in the case $Re_\lambda = 125$. Each sub-panel presents a different Rouse number at the particle position Ro, or equivalently, a different effective gravity value in decreasing order.

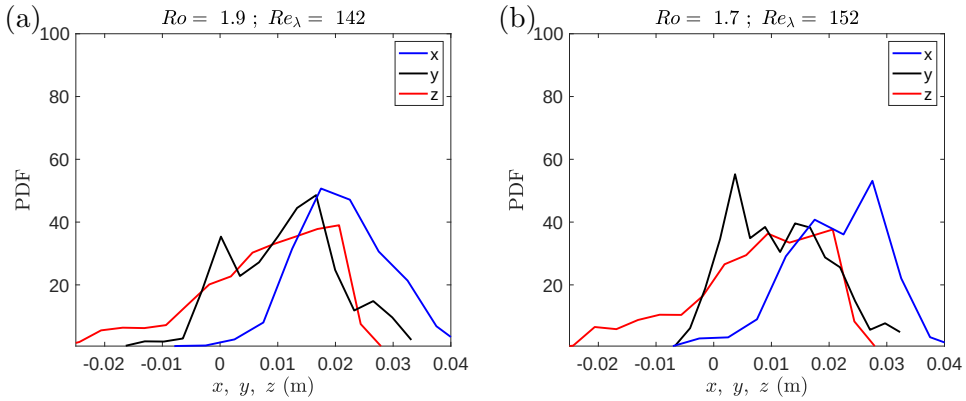

Figure 5.5: Particle's positions PDFs in the cases $Re_\lambda = 142$ and 152, and $g^* = 0.49$. Each sub-panel presents a different Rouse number at the particle position Ro, and a different Re_λ.

off-center with a typical extension of ± 0.5 cm; x component PDF peaks around 2 cm off-center with a typical extension of the order of ± 1 cm. The broader extension of the z component is expected and simply reflects the vertical extent of the trajectories as particles settle. The asymmetry of the z-PDF is noticeable, with a higher probability of detecting particles on the top part of the experiment (positive values of z). This is also expected as all the particles are detected when they enter the measurement volume (from the top) and they leave it as they settle, due to turbulent fluctuations.
Note that these observations are valid for all Re_λ and g^*.

5.4 Velocity statistics

5.4.1 Velocity PDFs

Figures 5.6-5.7 present the velocity probability density functions for all the cases explored. Note that the considered velocity is that of the particles to which the local mean flow $\langle u \rangle_{@p}$ at the position of the particle along its trajectory is subtracted.

Although full convergence of the PDFs is difficult with a number of drops limited to about 100, these PDfs show that:

- velocity fluctuations are reasonably gaussian (the PDFs have a reasonable parabolic shape in semi-log representation).
- horizontal components are reasonably isotropic with no significant mean value.
- the PDFs for the vertical component are shifted to negative values as a result of the settling velocity.

Figure 5.8 presents the PDFs of vertical velocity for the data-sets with $Re_\lambda = 125$ (obtained with the pumps operating at their nominal voltage of 12V) in continuous lines. While the dotted and dashed lines present the result for the two points obtained with the pumps operated at higher voltage, corresponding to higher Reynolds number and smaller Rouse numbers.
This plot shows a tendency of the PDFs peaks to shift to more negative values as Ro increases, as naturally expected due to the increase of effective gravity. Interestingly, this trend is not so pronounced at the smaller values of Ro (even if only $Re_\lambda = 125$ configurations are considered). Besides, no clear evolution of the width of the PDFs (reflecting any eventual evolution with Ro of the settling velocity variance) is visible. These questions will be addressed more carefully in the following Subsections.

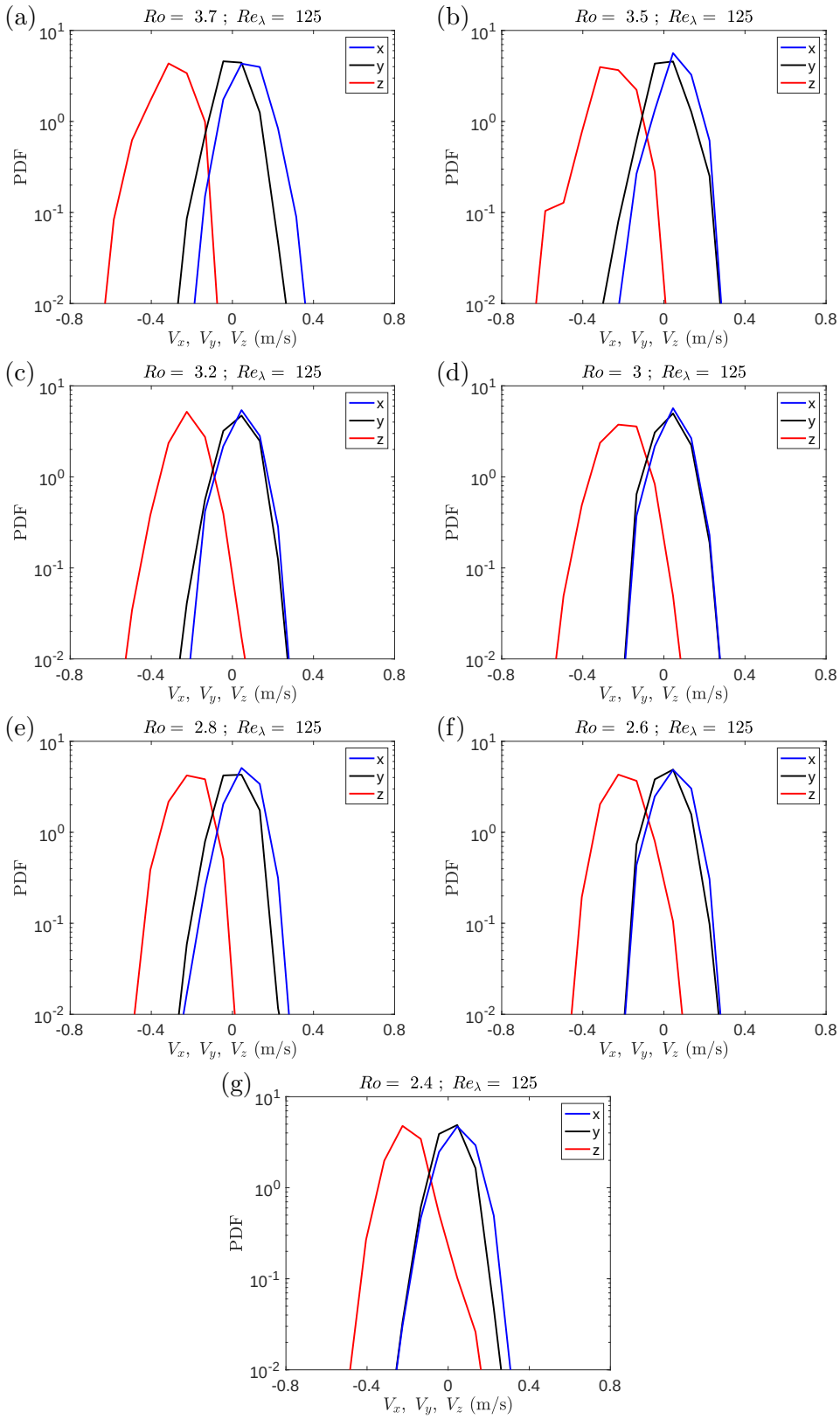

Figure 5.6: Particle's velocity PDFs in the case $Re_\lambda = 125$. Each sub-panel presents a different Rouse number at the particle position Ro, or equivalently, a different effective gravity value in decreasing order.

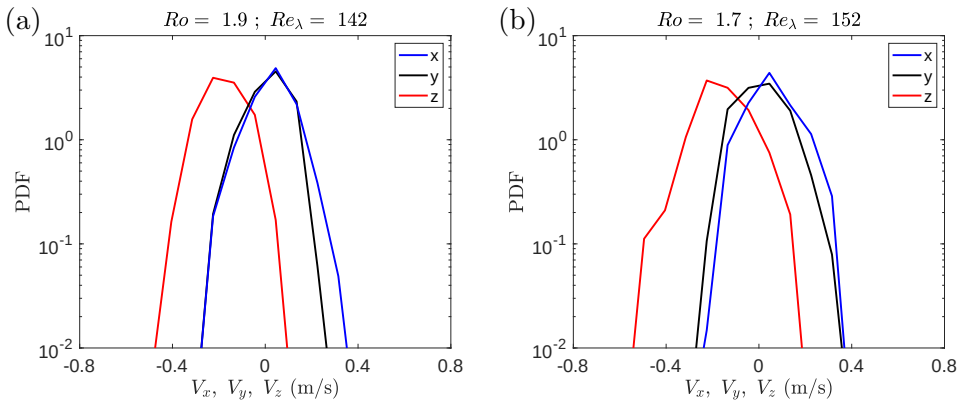

Figure 5.7: Particle's velocity PDFs in the cases $Re_\lambda = 142$ and 152, and $g^* = 0.49$. Each sub-panel presents a different Rouse number at the particle position Ro, and a different Re_λ.

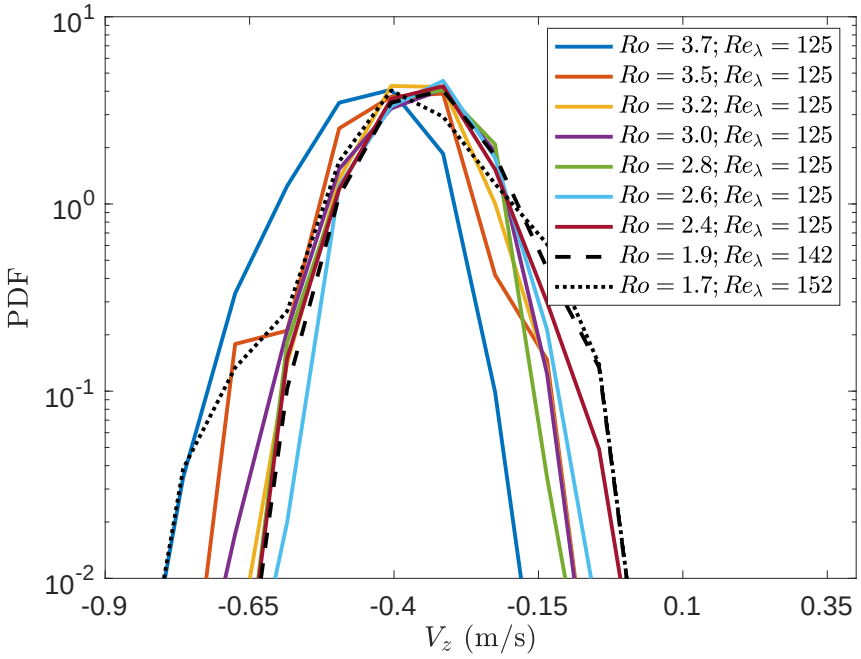

Figure 5.8: Particle's vertical velocity PDFs with the mean flow subtracted. The different colors represent different Ro values, while the two realisations with $Re_\lambda = 142$ and 152 are denoted in black lines.

5.4.2 Mean settling velocity

Figure 5.9 presents the mean settling velocity $\langle v_z \rangle = v_s$ as a function of the effective dimensionless gravity $g^* = \tilde{g}/9.8$ m s^{-2}. Black diamonds correspond to the settling velocity v_s^0 in the quiescent fluid, whereas coloured symbols correspond to the turbulent settling case. Interestingly, this Figure shows that for lower gravity conditions, turbulent settling is enhanced compared to the quiescent case, whereas turbulent settling seems to asymptotically tend to the quiescent value for the highest values of g^* explored. A surprising effect is that this enhancement is such that, for the smallest values of effective gravity investigated, the enhancement of settling by turbulence as gravity is reduced almost compensates the reduced settling by lower gravity, leading to an almost constant settling velocity of the order of 0.35 m/s.
Naturally, it is expected that $v_s = 0$ in the limit of vanishing Ro. It would be interesting in future studies to improve the present capabilities of the magnetic compensation of gravity in order to explore the trend towards this limit and the behavior at lower values of the effective gravity.

The aforementioned settling enhancement is emphasized in Figure 5.10 which represents the turbulent-to-quiescent settling velocity ratio as a function of Ro. An enhancement of up to 40% percent is observed for the measurements at the lowest Ro investigated. It is also interesting to note that, although with some scatter, the two points for the experiments at higher Re_λ in the low Ro range reasonably follow the Rouse number trend of experiments at $Re_\lambda = 125$, what suggests that the observed trend might be robust to moderate variations of the turbulent Reynolds number.
The turbulent-to-quiescent settling velocity ratio then decreases to order unity as Ro increases. The point at the largest Ro investigated, which corresponds to natural gravity ($g^* = 1$, without any magnetic compensation), seems, surprisingly, to exhibit an enhanced settling. Further measurements would be required to confirm this trend.

Overall, these results are consistent with the turbulent enhancement of settling, generally attributed to preferential sweeping (Wang and Maxey, 1993), as observed in previous experiments (Aliseda et al., 2002; Berk and Coletti, 2021b; Sumbekova, 2016) and point particle simulations (Good et al., 2014; Rosa et al., 2016). The tendency of enhancement to reduce at large values of the Ro number is also consistent with the numerical simulations by Good et al. (2014) and Rosa et al. (2016).
It is not observed however any regime where settling would be hinder by turbulence, reminiscent of loitering effect (Nielsen, 1993) and, as reported in simulations by Good et al. (2014), as a result of non-linear drag onset. In this regard, the present results seem more in the line with the simulations by Rosa et al. (2016) who did not observe settling hindering (unless particle transverse motion is blocked), than with those of Good et al. (2014) who did observe hindering at large values of Ro. Note however that the simulations in those studies are in the context of point particles, while in the present case $d_p/\eta \simeq 10$ is probably out of the range of validity of this approximation. Simulations of fully resolved particles by Chouippe and Uhlmann (2019) report a small effect of turbulence on settling (mostly a hindering of a few percent). Direct comparison with those results is however not straightforward as those simulations concern particles with smaller density ratio ($\Gamma = 1.5$), and the Rouse number (actually the inverse of the Rouse number, called the turbulence intensity I in Chouippe and Uhlmann (2019)) was varied by changing the turbulence intensity at fixed gravity. That is the counterpart of the strategy in the present work where Ro was varied by changing the effective gravity. Future experiments are planned to complete the data sets at the two higher values of Reynolds number for which only one value of effective gravity could be explored so far.

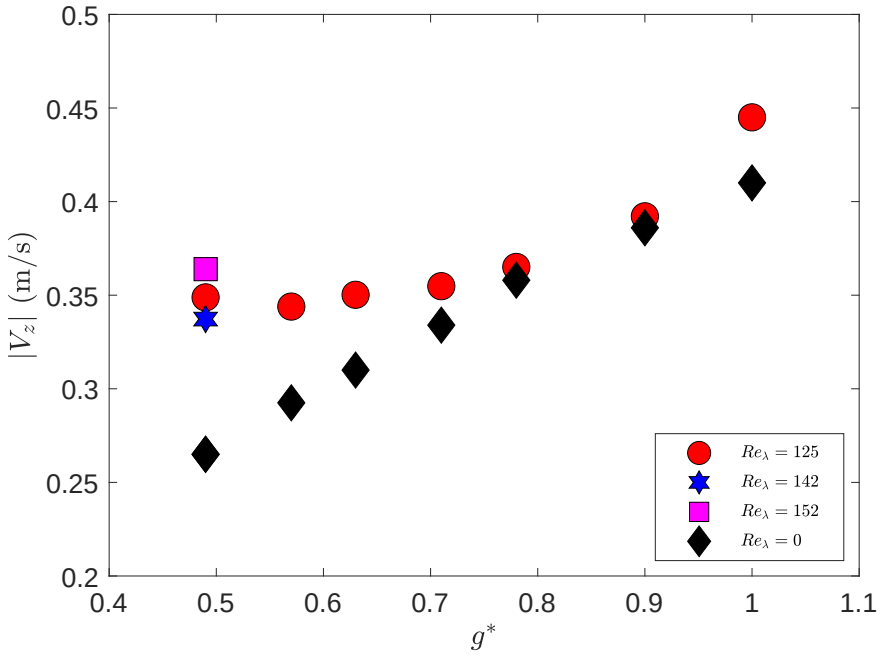

Figure 5.9: Mean settling velocity $\langle v_z \rangle$ as a function of the dimensionless gravity g^*. Black diamonds correspond to the settling velocity vs0 in the quiescent fluid, whereas coloured symbols correspond to the turbulent settling case.

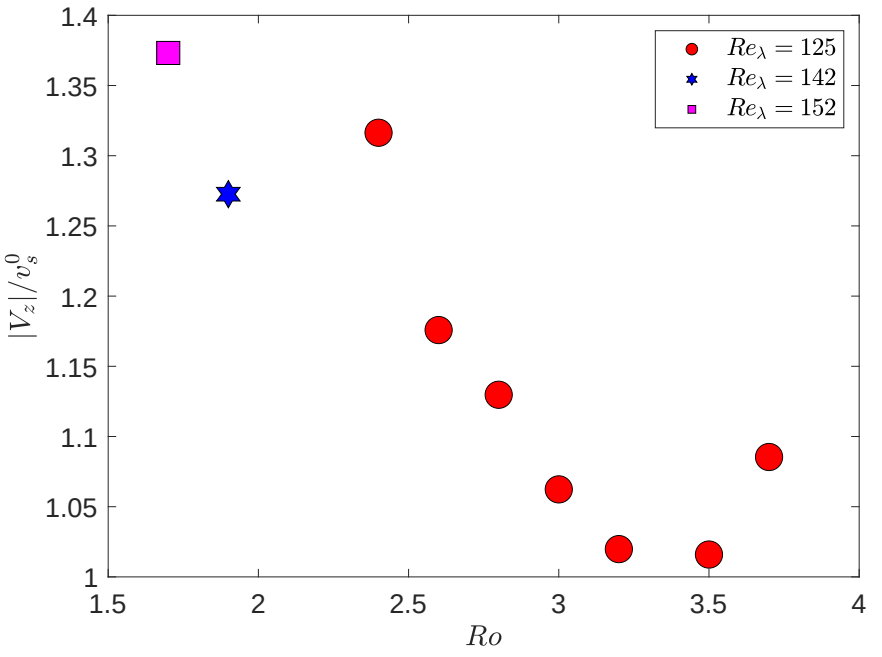

Figure 5.10: Turbulent-to-quiescent settling velocity ratio as a function of Ro. Black diamonds correspond to the settling velocity v_s^0 in the quiescent fluid, whereas coloured symbols correspond to the turbulent settling case.

5.4.3 Velocity fluctuating statistics

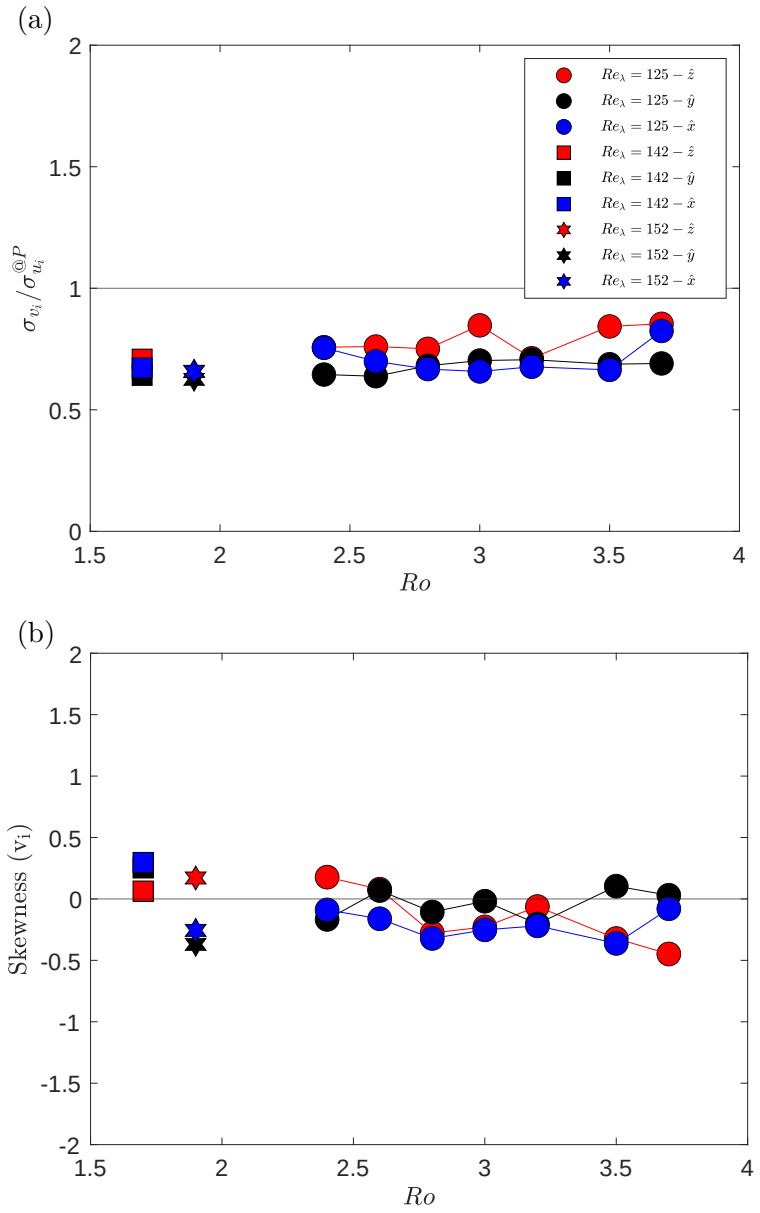

Figure 5.11: Second and third order moments of particle velocity versus Ro. The colors represent the velocity component, whereas the symbols represent the different values of Re_λ.

Figure 5.11 reports higher order statistics of velocity fluctuations (standard deviation and skewness) and their evolution with Ro. In particular, Figure 5.11(a) shows the standard deviation of velocity, normalized by the mean standard deviation of the background flow explored by the particles. It can be seen the standard deviation of the particles velocity is within 70%-85% of the fluid velocity fluctuations for all cases (and all components) investigated, with no noticeable trend with Ro. The lower fluctuations of particles velocity compared to fluid's is expected and can be interpreted as a Stokes number effect related filtering effect due to particles inertia. The absence of a significant trend with Ro is more surprising as the modification of the crossing trajectory effect (Berk and Coletti, 2021a; Csanady, 1963) under different effective gravity conditions is expected to modify the typical Lagrangian time scales "view by the particles" (see Eq. 1.15), which in turn affects the particle-to-fluid velocity variance ratio. This point will be

further discussed in Section 5.6, after the time scales of the particle's Lagrangian dynamics will be addressed.

On the other hand, Figure 5.11(b) show the velocity skewness. Although this higher order moment is marginally converged, due to the limited number of drops, the Figure suggest that velocity fluctuations are reasonably symmetric (skewness is null).

5.5 Acceleration statistics

As previously detailed, acceleration statistics will be only discussed for the vertical component which exhibit a lesser level of noise.

Figures 5.12-5.13 show the acceleration PDFs for all measurements. The PDFs appear symmetric and centered around zero (no mean acceleration) with wide tails. Most plots show a indistinguishable acceleration statistics regardless of the considered component, supporting the isotropy of particles small scale dynamics. The cases of $Ro = 3.7$ and $Ro = 2.5$ show however discrepancies depending on the component. This is due to a larger level of noise on the horizontal components associated to these two measurements, as already pointed in Section 5.2, which results in an overestimation of the horizontal acceleration variance with the chosen filtering parameters. The origin of this increased level of noise is not clear. Considering the good level of isotropy observed for most measurements, acceleration statistics will therefore be discussed only for the vertical component, which does not suffer from this spurious increase of noise.

5.5.1 Mean acceleration

Figure 5.14 shows the average vertical acceleration of the particles normalized by gravity for all experiments performed. It mostly shows that particles have statistically reached a regime of terminal settling with no significant mean vertical acceleration (although a mild trend with a small negative slope can be seen). This validates that the mean vertical velocity previously discussed in Figure 5.9 can be interpreted as a terminal velocity and compared in the turbulence case to the terminal velocity in quiescent fluid.

5.5.2 Acceleration fluctuations

Figure 5.15 shows higher order acceleration statistics and their dependency on Ro. The lack of statistical convergence for skewness (Fig. 5.15(b)) and kurtosis (Fig. 5.15(c)) does not allow to draw major conclusions other than an overall small skweness (reflecting the symmetry of acceleration fluctuations) and a kurtosis generally much larger than 3, typical of the intermittent dynamics of turbulence. Regarding this last point, it is worth recalling that while point-particle models (in the absence of gravity) predict a gaussianisation of acceleration statistics of inertial particles (Bec et al., 2006), finite size particle simulations (Chouippe and Uhlmann, 2015) and experiments (Qureshi et al., 2008) do see persistent non-gaussian statistics of finite size particles acceleration.

Figures 5.15(a) presents the evolution with Ro of particles acceleration variance normalised by the fluid acceleration variance estimated from the Heisenberg-Yaglom relation $\sigma_a^{tracer} = a_0^{1/2}\epsilon^{3/4}\nu^{-1/4}$, where the constant a_0 has a value of the order of 3 in the range of turbulent Reynolds number at which the experiment is operated (more precisely, the empirical relation $a_0 = 0.13Re_\lambda^{0.64}$ from Sawford (1991) is used to estimate its value as a function of Re_λ).
Not surprisingly the acceleration of the particles is found to be lower than that of the fluid, what can be attributed to a filtering effect due to inertia (Stokes number effect) and/or finite particle size effects (Chouippe and Uhlmann, 2015; Qureshi et al., 2008, 2007). The trend with Ro, where acceleration standard deviation gets closer to that of the fluid at higher values of effective

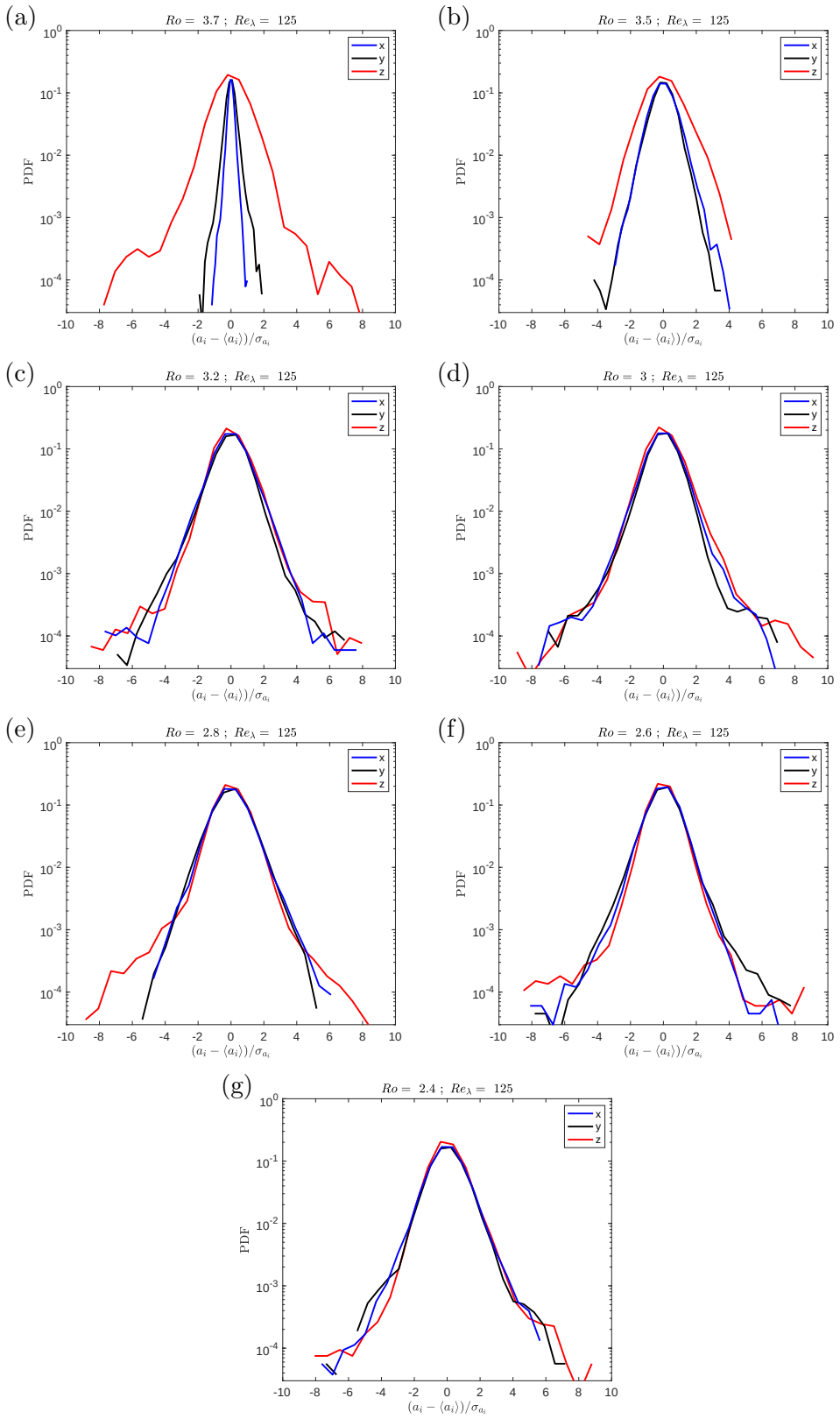

Figure 5.12: Particle's acceleration PDFs in the case $Re_\lambda = 125$. Each sub-panel presents a different Rouse number at the particle position Ro, or equivalently, a different effective gravity value in decreasing order.

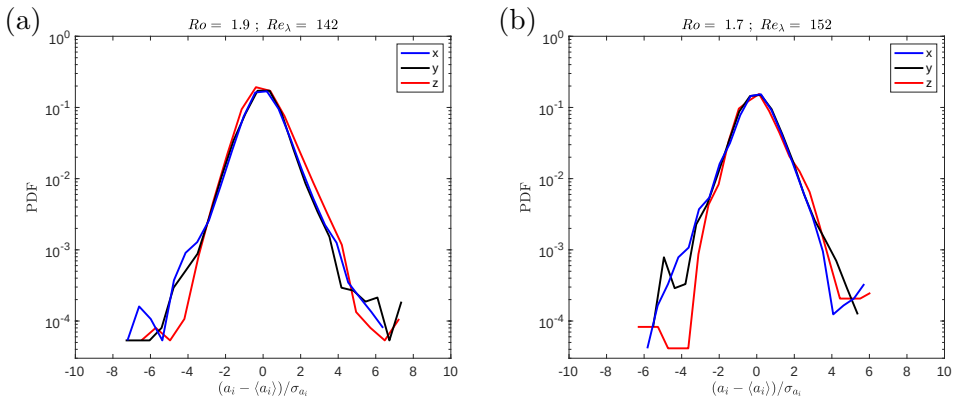

Figure 5.13: Particle's acceleration PDFs in the cases $Re_\lambda = 142$ and 152, and $g^* = 0.49$. Each sub-panel presents a different Rouse number at the particle position Ro, and a different Re_λ.

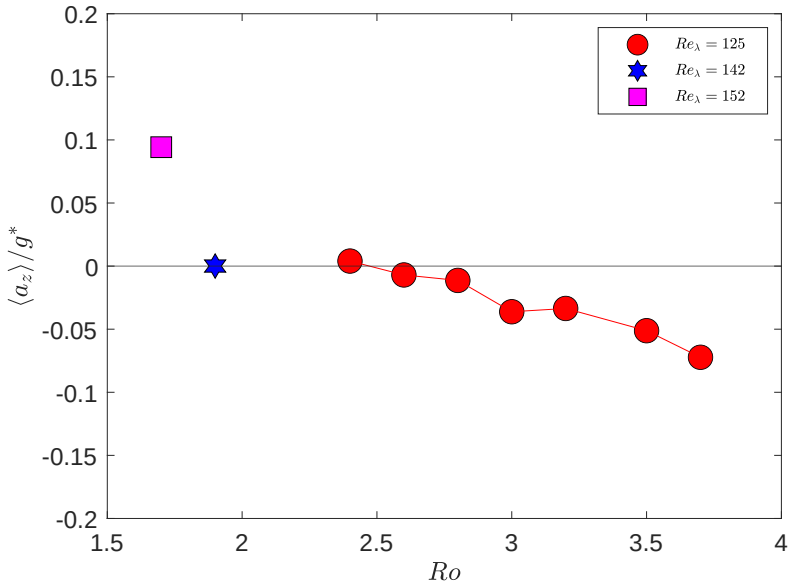

Figure 5.14: Average vertical acceleration of the particles, normalized by gravity for all experiments performed.

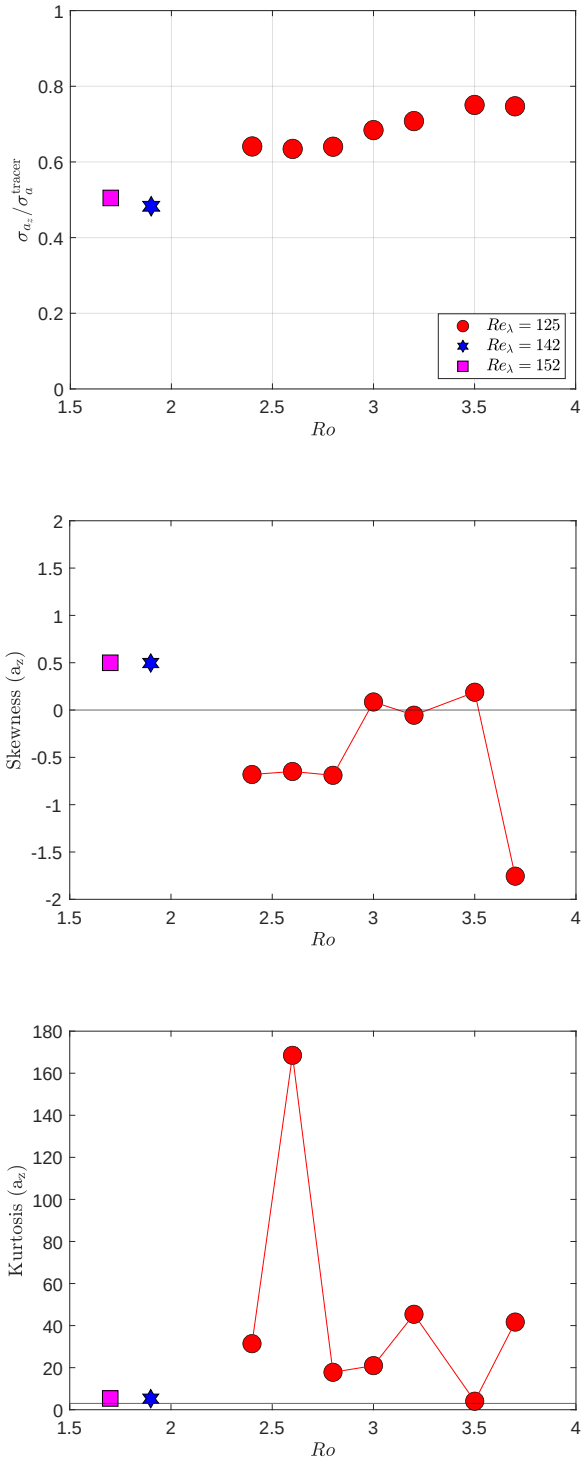

Figure 5.15: Acceleration fluctuations statistical moments: acceleration standard deviation normalized by the standard deviation of tracers estimated from Heisenberg-Yaglom relation $\sigma_a^{\text{tracer}} = a_0^{1/2}\eta/\tau_\eta^2$ (Top); acceleration skewness (Middle); acceleration kurtosis (Bottom).

gravity may however seem somehow counter-intuitive, as one may expect that the enhanced crossing trajectory effect at higher gravity induces a stronger deviation of particles dynamics compared to fluid tracers. This point will be further discussed in section 5.6.

5.6 Lagrangian timescales of settling particles

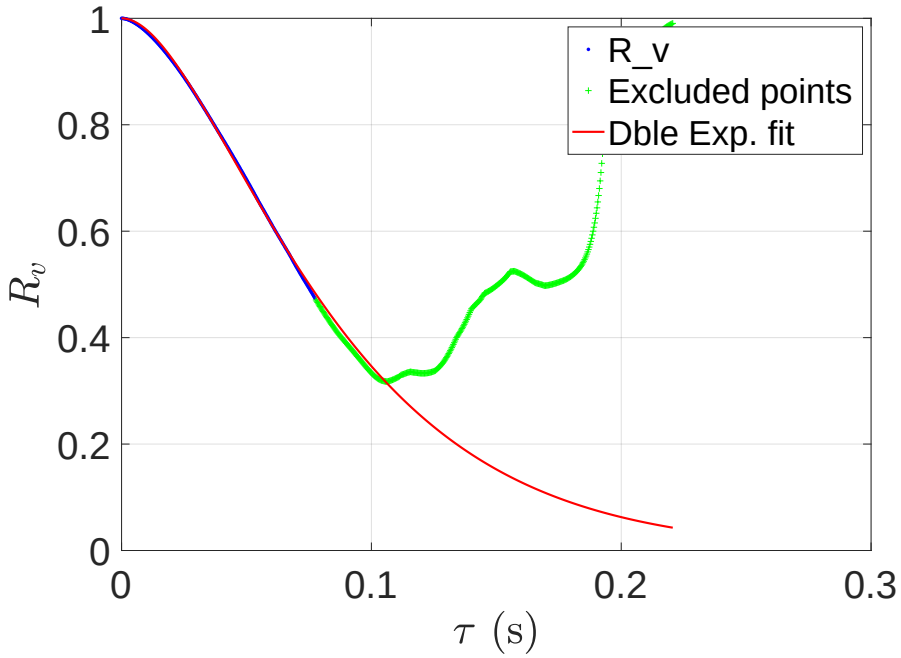

Figure 5.16: Auto-correlation function of the particles vertical velocity for the case $g^* = 1$. Blue and Green points correspond to the experimentally measured auto-correlation function. Red line is the fit by the the double exponential model (Eq. 5.1) where the fit is performed only on the blue points.

In this section some relevant time scales of the Lagrangian dynamics of the particles are estimated. Recall that a measurement of the Lagrangian dynamics of the fluid itself was not performed in this work. To this end, the framework of two time description of Lagrangian stochastic dynamics, as introduced by Sawford (1991) is considered. In this framework, the Lagrangian auto-correlation function of the particle velocity components can be expressed as a double exponential function:

$$R_v(\tau) = \langle v(t+\tau)v(t)\rangle = \frac{\frac{1}{T_2}e^{-\tau/T_L^*} - \frac{1}{T_L^*}e^{-\tau/T_2}}{\frac{1}{T_2} - \frac{1}{T_L^*}}, \tag{5.1}$$

where T_L^* is a large scale time (characterizing the long term fluctuating dynamics) and T_2 is a small scale Lagrangian time, characteristic of acceleration dynamics (Sawford, 1991; Viggiano et al., 2020). The Lagrangian correlation time $T_L = \int_0^\infty R_v(\tau)\mathrm{d}\tau$ is then given by:

$$T_L = T_L^*\left(1 + \frac{T_2}{T_L}\right). \tag{5.2}$$

The Lagrangian Taylor microscale $\tau_\lambda = \sigma_u/\sigma_a$ can also be defined, which corresponds to the curvature at the origin of $R_v(\tau)$ which in the limit of small time lags can be Taylor expanded

as:

$$R_v(\tau) \approx 1 - \frac{\sigma_a^2}{2\sigma_u^2}\tau^2 + \mathcal{O}(t^3) = 1 - \frac{1}{2}\left(\frac{\tau}{\tau_\lambda}\right)^2.$$

The Lagrangian taylor microscale therefore defines the osculatory parabola of R_v at the origin and it simply corresponds to the geometric average of T_L and T_2 :

$$\tau_\lambda = \sqrt{T_L T_2}. \tag{5.3}$$

In the next subsections the different Lagrangian timescales for the particle settling velocity are estimated.

5.6.1 Velocity auto-correlation function

Figure 5.16 shows, as an example, the Lagrangian correlation function of the particles vertical velocity for the case $g^* = 1$ (normal gravity) and $Re_\lambda = 125$. This is estimated by averaging the individual correlation function of all dropped particles in the given dataset. The experimental estimate of the auto-correlation loses statistical convergence for time lags $\tau > 0.1$. This is due to the fact that recorded trajectories do not all have the same duration: some particles tend to leave the measurement zone as they settle, resulting in a lesser number of long trajectories, required to estimate long term correlations.
A fit of the experimental auto-correlation function by the double exponential model (Eq. 5.1) is performed only on the first part of the curve (blue points in the Figure). The fit is shown by the red line, which perfectly matches the shape of the experimental auto-correlation function. Based on this fit, the long and short time scales T_L and T_2, as well as the Taylor microscale $\tau_\lambda = \sqrt{T_L T_2}$ can be estimated. Since the Taylor microscale can be independently obtained from the velocity and acceleration variance presented in previous sections, this quantity will be presented first.

5.6.2 Lagrangian timescales of settling particles dynamics

Figure 5.17 shows the different characteristic timescales (T_2, τ_λ and T_L) estimated for the vertical particle dynamics from the velocity autocorrelation functions. Times are given normalized by the turbulent dissipation scale τ_η.

For clarity, the alternative estimate of the Taylor microscale based on velocity and acceleration variance is not presented, although it is found in excellent agreement with the estimate from the correlation functions. It can be noted that 3 points (at $Ro = 2.4$, 2.8 and 3.7) show a pathological behavior where $T_2 = \tau_{lambda}$ (also equal to T_L^*) what results in an ovestimate of T_2 and an underestimate of T_L. This problem seems to be related to an inappropriate fitting of the correlation functions and will be corrected in future analysis.

Lagrangian dissipation scale T_2. Without considering those outliers, the ratio T_2/τ_η is found to remain relatively constant and approximately equal to 2.5. The black dashed line indicates the equivalent ratio predicted for fluid tracers in the context of two-time stochastic model by Sawford (1991): $T_2^{tracers}/\tau_\eta = C_0/2a_0$ which here is of order 1. This estimate from Sawford (1991)'s model is however known from experiments and numerical simulations to underestimate the the actual Lagrangian time scale of tracers by at least a factor of 2 (Viggiano et al., 2020). It is possible then to conclude that the small Lagrangian time scale of the particles is comparable to the Lagrangian dissipative time scale of the flow itself. This result contrasts with usual point particle predictions, where Lagrangian acceleration time scale of inertial particles is reported to be significantly larger than the fluid's and to increase with particles inertia (Calzavarini et al., 2009). It is however in line with experimental results of finite size inertial particles by Qureshi where the characteristic acceleration time scale of dense particles in wind-tunnel experiments

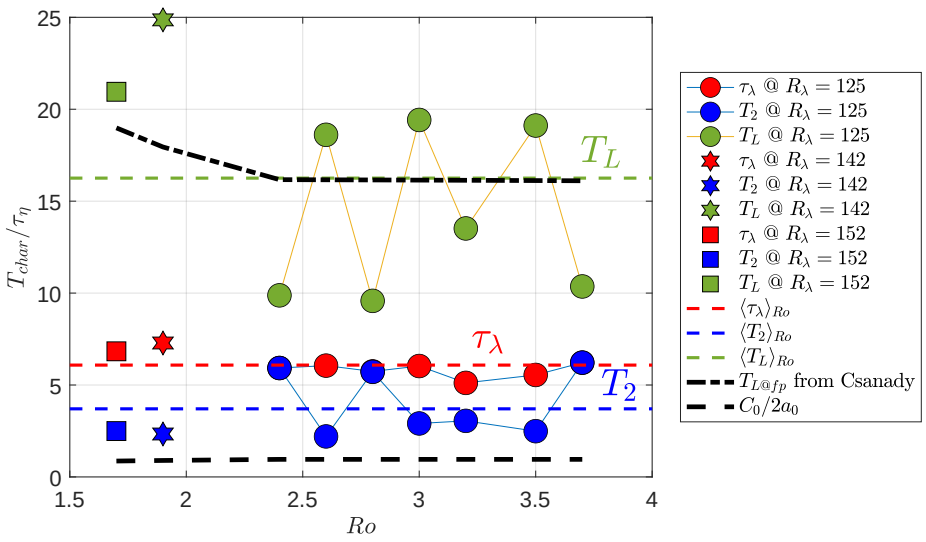

Figure 5.17: Lagrangian timescales of particles vertical dynamics as a function of Ro. The integral timescale T_L and T_2 are estimated by fitting the auto-correlation function with the double exponential model. Note that T_L is not the fitting parameter T_L^* but the integral timescale, given by relation 5.2. The Taylor microscale is estimated as $\tau_\lambda = \sqrt{T_L^* T_2}$. Circles correspond to data at $Re_\lambda = 125$, hexagram to data at $Re_\lambda = 142$ and square to data at $Re_\lambda = 152$. The dashed line shows the prediction from two-times stochastic models for $T_2^{tracers}/\tau_\eta = C_0/2a_0$. The dotted dashed line shows the prediction by Csanady (1963) for $T_{L@p}/\tau_\eta$ given by Eq. 5.4.

was found to remain comparable to the fluid Lagrangian dissipation time-scale of the background turbulence (with $T_2/\tau_\eta \simeq 2-3$), regardless of particles Stokes number (note that Rouse number effects were not addressed in this previous work).

Lagrangian integral scale T_L. Concerning the integral Lagrangian time scale T_L, not considering the aforementioned outliers, a mild trend is observed with an increase of T_L for the experiments carried at the lowest values of Ro (corresponding to the higher values of Re_λ and the higher values of Stokes number St). As previously discussed, usual crossing trajectory considerations à la Csanady predict a modification of the turbulent Lagrangian time scale of the flow sampled by the particles, $T_{L@p}$, depending on particles Rouse number and turbulence Reynolds number (see Eq. 1.15 in the introductory section here rewritten as in Berk and Coletti (2021a)):

$$\frac{T_L^{@p}}{\tau_\eta} = \frac{2(Re_\lambda + 32)}{\sqrt{15}C_0} \frac{1}{\left[1 + \alpha(5/C_0)^2 Ro^2 15 Re_\lambda^2\right]^{1/2}}, \tag{5.4}$$

whare $\alpha = 1$ for the case of vertical velocity dynamics, as considered here, and C_0 is the second order Lagrangian structure function constant, which can be estimated using the empirical relation $C_0 = C_0^\infty/((1 + 7.5 * C_O^{\infty 2} * Re_\lambda.^{-1.64}))$ with $C_0^\infty \approx 6$ (Sawford, 1991).

The dotted dashed line in Figure 5.17 shows this prediction for the present experiments. Interestingly (and maybe even quite surprisingly considering that the measured values of T_L in this plot are for the Lagrangian dynamics of the inertial particles, while Csanady prediction is for the fluid "seen by the particles") the agreement with the values of T_L determined from the auto-correlation function of the settling particles is very good. This suggests that Lagrangian correlation time scale of the particles directly reflects that of the sampled flow, regardless of particles own inertia.

5.6.3 Consequences on the filtering effect of particles Lagrangian dynamics

Csanady (1963) proposed that the modification of the integral Lagrangian timescale experienced by the particles due to settling and crossing trajectory (Rouse number effect) according to the previous Equation 5.4 modifies in turn the inertial filtering (Stokes number effect). The revisit of this problem by Berk and Coletti (2021a), extending the original Tchen-Hinze filtering theory (based on single time Lagrangian auto-correlation function) to include double-exponential auto-correlation function, leads to the following prediction for the modification of particles velocity and acceleration standard deviation (Eqs. 4.10 and 4.11 in (Berk and Coletti, 2021a)) :

$$\frac{\sigma_v}{\sigma_{u^{@p}}} = \frac{St^2}{\left(\frac{T_{L@p}}{\tau_\eta} + St\right)\left(\frac{T_{2@p}}{\tau_\eta} + St\right)}, \tag{5.5}$$

$$\frac{\sigma_a}{\sigma_{u^{@p}}\tau_\eta} = \frac{1}{\left(\frac{T_{L@p}}{\tau_\eta} + St\right)\left(\frac{T_{2@p}}{\tau_\eta} + St\right)} \tag{5.6}$$

In this expressions $\sigma_{u^{@p}}$ represents the standard deviation of the velocity of the turbulence explored by the particles. Ideally, it should be estimated by considering based on simultaneous measurements of particles and tracers dynamics. As already explained, in the present study tracers were not tracked and $\sigma_{u^{@p}}$ is estimated based on the averaged Eulerian field of velocity standard deviation from PIV measurements, interpolated at the particles position instantaneous position.

Velocity fluctuations. Figure 5.18 recalls the data-points for the standard deviation of the vertical component of velocity previously discussed in Figure 5.11(a). The dashed line indicates the prediction from the Berk-Coletti-Csanady theory (Eq. 5.5), which is found in very good agreement, retrieving in particular the seemingly counter-intuitive trend where the fluctuating velocity of the particles approaches that of the fluid as Ro increases. This trend can now be interpreted as an effect of inertial filtering. Indeed, points at the lowest values of Ro in this plot (magenta and blue symbols) correspond to experiments at higher values of Re_λ and hence highest values of St (see table 5.1). Their lower value of fluctuating velocity is mainly due to the larger inertia of the particles associated to their larger Stokes number. Red symbols correspond to experiments as fixed Re_λ, where the Stokes number of the particles only changes marginally (it slowly decreases with increasing Ro) due to non-linear drag corrections in the estimation of the particle response time τ_p. This results in a slight reduction of inertial filtering as Ro increases. The effect of the moderate $T_{L@p}$ modification seen in Figure 5.17 is mild and only tends to marginally accentuate the bending of the prediction at small Ro. Note that the prediction plotted in Figure 5.18 has been calculated using the usual dissipation time scale Stokes number $St = \tau_p/\tau_\eta$. If the Stokes number corrected for finite size effects St_d is used, the theory over-estimates the fluctuating particle velocity (dotted-dashed line in Figure 5.18).

Overall, the Berk-Coletti-Csanady theory accounts very well for the combined effect of Ro, St and Re_λ on the filtering of velocity fluctuations. Future experiments are planned in order to take advantage of the magnetic modification of effective gravity to systematically (and independently) vary these 3 parameters and further validate the theory.

Acceleration fluctuations. Figure 5.19 recalls the data-points for the standard deviation of the vertical component of acceleration, but normalized according to Eq. 5.6. The dashed line shows the prediction of the Berk-Coletti-Csanady theory for vertical acceleration (Eq. 5.6). The theory reasonably captures the trend and the order of magnitude of acceleration fluctuations

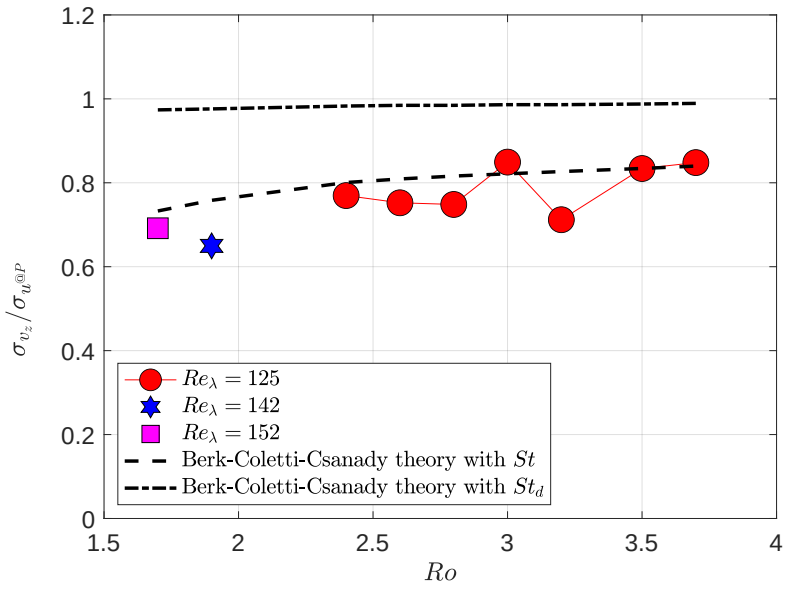

Figure 5.18: Particle-to-fluid standard deviation velocity ratio as a function of Ro. Dashed line shows the prediction from the Berk-Coletti-Csanady theory according to Eq. 5.5, based on the usual dissipation time scale Stokes number $St = \tau_p/\tau_e ta$. Dotted-dashed line shows the same prediction when the Stokes number corrected for particle finite size effects, St_d, is used instead of St (see table 5.1).

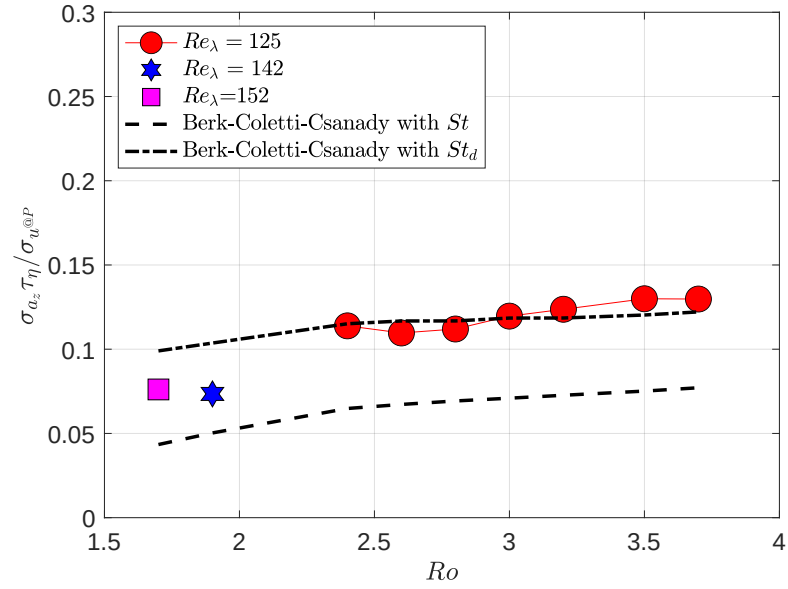

Figure 5.19: Standard deviation of particle acceleration normalized by $\sigma_{u@p}/\tau_\eta$. Dashed line shows the prediction from the Berk-Coletti-Csanady theory according to Eq. 5.6, based on the usual dissipation time scale Stokes number $St = \tau_p/\tau_e ta$. Dotted-dashed line shows the same prediction when the Stokes number corrected for particle finite size effects, St_d, is used instead of St (see table 5.1).

when Eq. 5.6 is used with the dissipation scale Stokes number St, although it slightly underestimates the amplitude of particles acceleration fluctuations. Contrary to velocity fluctuations, the agreement is improved here if the Stokes number corrected for particles finite size St_d is used.

Overall the Berk-Coletti-Csanady theory reasonably captures the trend with Ro, Re_λ and St for acceleration and velocity fluctuations.

5.7 Conclusion

This section presented a first series of experiments using magnetic compensation of effective gravity to disentangle the effects of inertia and gravity on the coupling between settling particles and turbulence. This study shows that the strategy of magnetic control of effective gravity is operational to vary the Rouse number independently of Re_λ and St, although a small intertwine between Ro and St still remains due to non-linear drag corrections in the estimate of particles response time, which are affected by the modification of settling (even in quiescent flow) when effective gravity is modified. This could be improved in future studies by considering smaller magnetic particles.

In the explored regimes, enhancement of settling by turbulence was evidenced, where particles could settle up to 40% faster in presence of turbulence compared to the quiescent flow case. The enhancement was found to be reduced as the Rouse number was increased, but no regime of settling hindering was observed, even at the largest valued of Rouse number explored. In future experiments, it would be relevant to use the magnetic field to increase the effective gravity and hence explore regimes of even higher valued of Rouse number.

Finally, the fluctuating Lagrangian dynamics of settling particles was investigated and analysed at the light of the classical crossing trajectory theory by (Csanady, 1963) and its recent revisit by (Berk and Coletti, 2021a). The small Lagrangian time scale (T_2, characteristic of acceleration correlation) was found not to significantly depend on particles and effective gravity properties and to remain of the order of the carrier flow Lagrangian dissipative time scale. The integral time scale of particles Lagrangian dynamics was found to mildly change with experimental conditions, in particular when the Reynolds number was varied. The observed trend is in reasonable agreement with Csanady crossing-trajectory prediction for the Lagrangian correlation time scale associated to the flow sampled by the particles. Combining this with the filtering prediction (in the framework of double exponential correlation model) for Stokes number effects, a reasonable agreement is found for the overall trends measured for velocity and acceleration standard deviations.

After this proof of concept of the magnetic control of effective gravity to explore particle/turbulence interaction, this study could now be pushed further by systematically varying Re_λ (by varying the power driving the pumps in the experiment) and St (by varying for instance the diameter of the magnetic particles) together with Ro. Also, measuring the dynamics of the flow together with the dynamics of the particles would give a deeper insight by actually giving the flow properties along particle tracks.

Finally, the experiments in micro-gravity, to be carried in the Dryden Drop Tower in Portland, will allow to explore the limit of vanishing Ro impossible to access with the magnetic control of effective gravity.

Conclusions and Perspectives

5.8 Conclusions

Our goal was to investigate several aspects of the coupling between settling particles (spheres, cubes, and rods) in quiescent and turbulent conditions, with a particular effort to identify and explore the relevant control parameters of the problem.
We presented experimental studies of single inertial particles in two main water fluid configurations: Quiescent Flow and Turbulent Flow (see Fig. 1.9 for an outline of the experiments).
In particular, the Quiescent Flow studies can be split in two subcategories:

- Creeping Flow.
- Moderate Reynolds Number Flow.

The Turbulent Flow studies can be split in two categories as well:

- Ground Experiments
- Drop Tower Experiments

Our experiments regarding slender particles settling in a Quiescent Creeping Flow were in the regime where the particle angular dynamics is overdamped, so the torque and the force acting on the object could be readily determined from the settling and from the angular velocities, which was made possible via a 4D-LPT method. We considered two particles, with aspect ratios $\beta = 8$ and $\beta = 16$. In the two cases, the Reynolds numbers were small, making comparisons with predictions at low particle Reynolds numbers ($\mathrm{Re_p} \ll 1$) meaningful.
We compared the measured force with theoretical predictions in the slender-rod limit, and in the case of spheroids. Our results show that both models qualitatively predict the translational dynamics, in particular the slender-rod theory was found to represent better the experimental data.
Regarding the rod angular dynamics, the models took a simpler form as the rotational dynamics was found to be planar and overdamped. The particles were seen to orient broadside on, i.e. with the maximal drag orientation. We found the torque to be qualitatively well described by a $\sin 2\phi$ functional form, and differences in the torque pre-factor that both models provide were seen. The spheroid theory was found to describe correctly the dynamics of the rods with aspect ratio $\beta = 16$, whereas for the case $\beta = 8$ the agreement is less satisfactory, the experimental pre-factor being roughly twice as large as the theory predictions. On the other hand, the slender-rod theory happens to quantitatively agree with the data in the case $\beta = 8$ and, for $\beta = 16$, tends to over-predict the magnitude of fluid-inertia torque.

Regarding spherical and cubic particles settling in a Quiescent Flow at moderated Reynolds numbers, we found a very rich dynamics in the ranges of Galileo number between 100 and

350. We found the two control parameters (Ga and Γ) to influence the trajectories dynamics (obliquity, spectral content, and planarity) in a way in quantitatively agreement with numerical predictions from the literature (Seyed-Ahmadi and Wachs, 2019; Zhou and Dusek, 2015), in particular in the regimes of large density ratios which were not explored in previous studies. With this respect, our study confirms the existence for dense spherical of a multi-stable region of the parameter space where in the range $Ga = 210 - 230$.

We used the spherical particle case as a benchmark to test a method to compensate gravity on spherical magnetic particles via the application of an external magnetic field. This method is based on the idea of counteracting the gravitational force by a magnetic force on the particles, yielding a controllable effective gravitational acceleration. In particular, we proved that the configurations used in this thesis allow to reduce the effective gravity down to 4.8 m s^{-2}. Apart from the gravity compensation, such a method also blocks the particle rotation as the particle magnetic moment has to be aligned with the external field.
We applied the method to the spherical particle settling in a Quiescent Flow at moderated Re_p case with the objectives of: (i) testing the magnetic gravity compensation method and (ii) exploring the effects of blocking particle rotation on its dynamics. Our studies demonstrate that the gravity compensation method performs well as we were able to modify the particle Galileo number of the particles by magnetically tuning the effective gravity what lead to equivalent results as tuning the Galileo number by changing the fluid viscosity. On the other hand, we proved that magnetically blocking the particle rotation has no influence on the trajectory obliquity and planarity and its overall dynamics as the results of the benchmark case are retrieved. Regarding the trajectory oscillations, our study also suggests that blocking the particle rotation does not significantly affect the trajectory spectral content.
As discussed extensively in Chapter 1, both inertia and gravity affect how particles interact with a turbulent flow and these effects are usually intertwined what complicates the interpretation and modelling of the turbulent transport of particles based on the different control parameters (Re, Γ, Ro, St) of the problem. In this sense, the principal goal of the magnetic gravity compensation method just mentioned was to propose a new strategy to disentangle the effects of particle inertia (Stokes number effects) and gravity (Rouse number effects) in the dynamics of particles in a turbulent flow. A first series of experiments was carried where the Rouse number was varied by magnetically changing the gravity, while keeping particles and turbulence properties unchanged. This series was completed with two additional (although limited to a single value of the effective gravity for the moment) experiments where Reynolds number Re (and hence St) were also varied. Important results of this study concern (i) the evidence turbulent settling enhancement and its dependency on Rouse number and (ii) the consistency of the influence of Rouse and Stokes number effects on the fluctuating dynamics of the particles with the crossing trajectory phenomenology by Csanady and the revisited filtering theory by Berk and Coletti. The proof of concept of the magnetic control of effective gravity to vary Rouse number, opens now the way to a more complete exploration of parameter space, in particular by completing the additional experiments at different Reynolds number with a systematic variation of effective gravity. This should to further test the combined Ro and St dependencies on the turbulent settling enhancement/hindering and on the filtering effects.

Finally, we anticipated the utilisation of a Drop Tower at Portland State University (PSU) to further separate the gravity and inertia effects, by performing experiments in micro-gravity conditions. It is worth to remark that both turbulent experiments (magnetic gravity compensation and Drop Tower) use the same Turbulent Flow that was designed, constructed and fully characterised via PIV, to respect the constrains of the Drop Tower. This shall allow to directly include the micro-gravity results as part of the study with magnetically tuned effective gravity. We expect to have results in this zero-gravity case shortly as I will be at PSU using the drop tower from October 2021.

5.9 Perspectives

The results obtained during this thesis open many perspectives for future studies. We point out here the most straightforward future work that I think should be done to advance the areas of research that this thesis explored.

- Slender particles:
  - In the creeping flow case, decrease even more Re_p to be closer to the model's limits and clarify their actual range of validity;
  - Produce experimental data with this kind of anisotropic particles in the turbulent case, where no models exist;
  - Apply the magnetic gravity compensation method to anisotropic particles where orientation is an important additional parameter that can be magnetically controlled, allowing for instance to explore regimes where particles do not settle according to their natural self-orientation.
  - Magnetic control of orientation and rotation blockage/release could also be used to investigate the rotational relaxation of anisotropic particles.
- Spherical particles in quiescent flow:
  - The experimental exploration of (Γ, Ga) parameter space for settling regimes can be further refined by reducing the uncertainty in Ga, in particular in the tri-stable region. This could be achieved for instance by a systematic finely tuned magnetic variation of effective gravity in this range of Ga.
  - Further increase particle-to-fluid density ratios Γ where no literature data exist regarding path instabilities.
  - Measure the particle settling drag and terminal velocity over a larger range of Ga to study the effect on Γ.
  - Characterize the wake at the same time as the settling regimes (by simultaneously measuring the fluid motion around the particle).
- Cubic particles in quiescent flow:
  - Increase particle-to-fluid density ratios, where no literature exists.
  - Set an optical arrangement (higher magnification) that allows to resolve the temporal evolution of particle orientation.
  - Apply the magnetic gravity compensation method to this case were particle orientation is an important parameter and explore settling regimes at arbitrarily fixed orientations;
  - Complete the exploration of (Γ, Ga) parameter space over a broader range.
- Magnetic gravity compensation method
  - Explore magnetic fields with constant gradient but with a change of sign, to force particles rotation at known locations and investigate the effects of a magnetic torque and orientation relaxation.

  - Explore the magnetic coupling in the case of 2 of more particles and its competition with turbulence interactions;
  - Explore the version of the method where gravity is enhanced instead of reduced, what would allow to further increase the range of accessible effective gravity and Rouse numbers.

- Spherical particles in turbulent flow:
  - Complete the initiated study by systematically varying Ro with effective magnetically controlled gravity for various particle types and turbulence forcing, in order to independently vary St and Re_λ in addition of Ro. This shall allow to further explore the coupling between inertial and gravity effects as crossing trajectory and filtering effects, as well as the settling enhancement/hindering.
  - Use smaller magnets to diminish finite size effects and non-linear corrections on τ_p inducing a small residual dependence of St with Ro.
  - Measure flow and particles simultaneously to better characterise the local coupling between particle and turbulence and explore the eventual role of preferential sampling effects.
  - Explore collective effects with the magnetic method. How the magnetic interactions between particles affect the particle preferential concentration/clustering and overall coupling with turbulence ? Note that, although interactions maybe of different nature, similar question are important for instance for water droplets in clouds which may interact via electrostatic interactions;
  - Finally, the Drop Tower facility opens a myriad of other questions to be addressed regarding the particle/turbulence coupling problem, such as studying low and high particle concentration to investigate 2 and 4 way coupling.

Bibliography

4d-lpt. https://4d-ptv.readthedocs.io/en/latest/index.html. Accessed: 2020-08-30.

Ronald J. Adrian. Particle-imaging techniques for experimental fluid mechanics. Annual Review of Fluid Mechanics, 23(1):261–304, 1991. doi: 10.1146/annurev.fl.23.010191.001401. URL https://doi.org/10.1146/annurev.fl.23.010191.001401.

A. Aliseda, A. Cartellier, F. Hainaux, and J. C. Lasheras. Effect of preferential concentration on the settling velocity of heavy particles in homogeneous isotropic turbulence. Journal of Fluid Mechanics, 468:77–105, 2002. doi: 10.1017/S0022112002001593.

Analog Devices. Digital Accelerometer ADXL345. https://www.analog.com/media/en/technical-documentation/data-sheets/ADXL345.pdf, 2021a.

Analog Devices. Synchronous step-down regulator - lt8646s. https://www.analog.com/media/en/technical-documentation/data-sheets/lt8645s-8646s.pdf, 2021b.

P. Anand, S. S. Ray, and G. Subramanian. Orientation dynamics of sedimenting anisotropic particles in turbulence. Phys. Rev. lett., 125:034501, 2020.

H. I. Andersson and F. Jiang. Forces and torques on a prolate spheroid: Low-reynolds number and attack angle effects. Acta Mech., 230:431, 2019.

Arduino. Arduino UNO REV3. https://store.arduino.cc/arduino-uno-rev3, 2021.

Franck Auguste and Jacques Magnaudet. Path oscillations and enhanced drag of light rising spheres. Journal of Fluid Mechanics, 841:228–266, 2018. doi: 10.1017/jfm.2018.100.

G. K. Batchelor. The application of the similarity theory of turbulence to atmospheric diffusion. Quarterly Journal of the Royal Meteorological Society, 76(328):133–146, 1950. doi: https://doi.org/10.1002/qj.49707632804. URL https://rmets.onlinelibrary.wiley.com/doi/abs/10.1002/qj.49707632804.

E Beaugnon and R Tournier. Levitation of organic materials. Nature, 349(6309):470, 1991. ISSN 1476-4687. doi: 10.1038/349470a0. URL https://doi.org/10.1038/349470a0.

J. Bec, L. Biferale, G. Boffetta, A. Celani, M. Cencini, A. Lanotte, S. Musacchio, and F. Toschi. Acceleration statistics of heavy particles in turbulence. Journal of Fluid Mechanics, 550:349–358, 2006. doi: 10.1017/S002211200500844X.

Tim Berk and Filippo Coletti. Dynamics of small heavy particles in homogeneous turbulence: a lagrangian experimental study. Journal of Fluid Mechanics, 917:A47, 2021a. doi: 10.1017/jfm.2021.280.

Tim Berk and Filippo Coletti. Dynamics of small heavy particles in homogeneous turbulence: a lagrangian experimental study. Journal of Fluid Mechanics, 917:A47, 2021b. doi: 10.1017/jfm.2021.280.

G. Bouchet, M. Mebarek, and J. Dušek. Hydrodynamic forces acting on a rigid fixed sphere in early transitional regimes. European Journal of Mechanics - B/Fluids, 25(3):321–336, 2006. ISSN 0997-7546. doi: https://doi.org/10.1016/j.euromechflu.2005.10.001. URL https://www.sciencedirect.com/science/article/pii/S0997754605000968.

M. Bourgoin and S. G. Huisman. Using ray-traversal for 3d particle matching in the context of particle tracking velocimetry in fluid mechanics. Rev. Sci. Instr., 91(8):085105, 2020. doi: 10.1063/5.0009357. URL https://doi.org/10.1063/5.0009357.

Mickaël Bourgoin. Turbulent pair dispersion as a ballistic cascade phenomenology. Journal of Fluid Mechanics, 772:678–704, 2015. doi: 10.1017/jfm.2015.206.

Mickaël Bourgoin and Haitao Xu. Focus on dynamics of particles in turbulence. New Journal of Physics, 16(8):085010, aug 2014. doi: 10.1088/1367-2630/16/8/085010. URL https://doi.org/10.1088/1367-2630/16/8/085010.

F Box, E Han, C R Tipton, and T Mullin. On the motion of linked spheres in a Stokes flow. Experiments in Fluids, 58(4):29, 2017. ISSN 1432-1114. doi: 10.1007/s00348-017-2321-2. URL https://doi.org/10.1007/s00348-017-2321-2.

Andrew D. Bragg, Peter J. Ireland, and Lance R. Collins. Mechanisms for the clustering of inertial particles in the inertial range of isotropic turbulence. Phys. Rev. E, 92:023029, Aug 2015a. doi: 10.1103/PhysRevE.92.023029. URL https://link.aps.org/doi/10.1103/PhysRevE.92.023029.

Andrew D. Bragg, Peter J. Ireland, and Lance R. Collins. On the relationship between the non-local clustering mechanism and preferential concentration. Journal of Fluid Mechanics, 780:327–343, 2015b. doi: 10.1017/jfm.2015.474.

G.M. Bragg, L. van Zuiden, and C.E. Hermance. The free fall of cylinders at intermediate reynold's numbers. Atmospheric Environment (1967), 8(7):755–764, 1974.

Phillip P. Brown and Desmond F. Lawler. Sphere drag and settling velocity revisited. Journal of Environmental Engineering, 129(3):222–231, 2003. doi: 10.1061/(ASCE)0733-9372(2003)129:3(222).

Facundo Cabrera and Pablo J Cobelli. Design, construction and validation of an instrumented particle for the Lagrangian characterization of flows. Experiments in Fluids, 62(1):19, 2021. ISSN 1432-1114. doi: 10.1007/s00348-020-03121-3. URL https://doi.org/10.1007/s00348-020-03121-3.

E. Calzavarini, R. Volk, M. Bourgoin, E. Leveque, J.-F. Pinton, and F. Toschi. Acceleration statistics of finite-sized particles in turbulent flow: the role of faxén forces. Journal of Fluid Mechanics, 630:179–189, 2009. doi: 10.1017/S0022112009006880.

F. Candelier and B. Mehlig. Settling of an asymmetric dumbbell in a quiescent fluid. Journal of Fluid Mechanics, 802:174–185, 2016. doi: 10.1017/jfm.2016.350.

Kelken Chang, Benedict J Malec, and Raymond A Shaw. Turbulent pair dispersion in the presence of gravity. New Journal of Physics, 17(3):033010, mar 2015. doi: 10.1088/1367-2630/17/3/033010. URL https://doi.org/10.1088/1367-2630/17/3/033010.

D Chatain, D Beysens, K Madet, V Nikolayev, and A Mailfert. Study of fluid behaviour under gravity compensated by a magnetic field. Microgravity - Science and Technology, 18(3):196–199, 2006. ISSN 1875-0494. doi: 10.1007/BF02870408. URL https://doi.org/10.1007/BF02870408.

R.P Chhabra, S Agarwal, and K Chaudhary. A note on wall effect on the terminal falling velocity of a sphere in quiescent newtonian media in cylindrical tubes. Powder Technology, 129(1):53–58, 2003. ISSN 0032-5910. doi: https://doi.org/10.1016/S0032-5910(02)00164-X. URL https://www.sciencedirect.com/science/article/pii/S003259100200164X.

Agathe Chouippe and Markus Uhlmann. Forcing homogeneous turbulence in direct numerical simulation of particulate flow with interface resolution and gravity. Physics of Fluids, 27(12): 123301, dec 2015. ISSN 1070-6631. doi: 10.1063/1.4936274. URL http://aip.scitation.org/doi/10.1063/1.4936274.

Agathe Chouippe and Markus Uhlmann. On the influence of forced homogeneous-isotropic turbulence on the settling and clustering of finite-size particles. Acta Mechanica, 230(2): 387–412, feb 2019. ISSN 0001-5970. doi: 10.1007/s00707-018-2271-7. URL http://link.springer.com/10.1007/s00707-018-2271-7.

R. Clift, J. Grace, and M. Weber. Bubbles, drops, and particles. 1978a.

R. Clift, J. Grace, and Martin E. Weber. Bubbles, drops, and particles. 1978b.

S. W. Coleman and J. C. Vassilicos. A unified sweep-stick mechanism to explain particle clustering in two- and three-dimensional homogeneous, isotropic turbulence. Physics of Fluids, 21(11):113301, 2009. doi: 10.1063/1.3257638. URL https://doi.org/10.1063/1.3257638.

R. G. Cox. The steady motion of a particle of arbitrary shape at small reynolds numbers. J. Fluid Mech., 23(4):625–643, 1965.

G. T. Csanady. Turbulent diffusion of heavy particles in the atmosphere. Journal of Atmospheric Sciences, 20(0):201–208, 1963. doi: https://doi.org/10.1175/1520-0469(1963)020⟨0201:TDOHPI⟩2.0.CO;2.

V. Dabade, N. K Marath, and G. Subramanian. Effects of inertia and viscoelasticity on sedimenting anisotropic particles. J. Fluid Mech., 778:133, 2015.

H. M. De La Rosa Zambrano, G. Verhille, and P. Le Gal. Fragmentation of magnetic particle aggregates in turbulence. Phys. Rev.s Fluids, 3:084605, Aug 2018. doi: 10.1103/PhysRevFluids.3.084605. URL https://link.aps.org/doi/10.1103/PhysRevFluids.3.084605.

Deutsch E. Dispersion de particules dans une turbulence homogéne isotrope stationnaire calculée par simulation numérique des grandes échelles. École Centrale de Lyon, France, 1992.

Rohit Dhariwal and Andrew D. Bragg. Enhanced and suppressed multiscale dispersion of bidisperse inertial particles due to gravity. Phys. Rev. Fluids, 4:034302, Mar 2019. doi: 10.1103/PhysRevFluids.4.034302. URL https://link.aps.org/doi/10.1103/PhysRevFluids.4.034302.

Stefano Discetti and Filippo Coletti. Volumetric velocimetry for fluid flows. Measurement Science and Technology, 29(4):042001, mar 2018. doi: 10.1088/1361-6501/aaa571. URL https://doi.org/10.1088/1361-6501/aaa571.

W. M. Durham, E. Climent, M. Barry, F. De Lillo, G. Boffetta, M. Cencini, and R. Stocker. Turbulence drives microscale patches of motile phytoplankton. Nature Comm., 4(1):1–7, 2013.

Earnshaw. S. Trans. Camb. Phil. Soc., 7:97–112, 1842. URL https://doi.org/10.1038/349470a0.

J. Einarsson, F. Candelier, F. Lundell, J. R. Angillela, and B. Mehlig. Rotation of a spheroid in a simple shearat small reynolds number. Phys. Rev. Lett., 27:063301, 2015.

S. Elghobashi and G. C. Truesdell. Direct simulation of particle dispersion in a decaying isotropic turbulence. Journal of Fluid Mechanics, 242:655–700, 1992. doi: 10.1017/S0022112092002532.

Patricia Ern, Frédéric Risso, David Fabre, and Jacques Magnaudet. Wake-induced oscillatory paths of bodies freely rising or falling in fluids. Annual Review of Fluid Mechanics, 44(1): 97–121, 2012. doi: 10.1146/annurev-fluid-120710-101250.

Expert Power. 12v 10ah lifepo4 - ep1210. https://www.expertpower.us/products/ep1210-10ah, 2021.

David Fabre, Franck Auguste, and Jacques Magnaudet. Bifurcations and symmetry breaking in the wake of axisymmetric bodies. Physics of Fluids, 20(5):051702, 2008. doi: 10.1063/1.2909609.

David Fabre, Joel Tchoufag, and Jacques Magnaudet. The steady oblique path of buoyancy-driven disks and spheres. Journal of Fluid Mechanics, 707:24–36, 2012. doi: 10.1017/jfm.2012.231.

F. Falkinhoff, M. Obligado, M. Bourgoin, and P. D. Mininni. Preferential concentration of free-falling heavy particles in turbulence. Phys. Rev. Lett., 125:064504, Aug 2020. doi: 10.1103/PhysRevLett.125.064504. URL https://link.aps.org/doi/10.1103/PhysRevLett.125.064504.

T Fallon and C B Rogers. Turbulence-induced preferential concentration of solid particles in microgravity conditions. Experiments in Fluids, 33(2):233–241, 2002. ISSN 1432-1114. doi: 10.1007/s00348-001-0394-3. URL https://doi.org/10.1007/s00348-001-0394-3.

Jeremy Ferrand. Écoulements et écrasements de fluides : effet du mouillage et de la rhéologie. Theses, Université de Lyon, September 2017. URL https://tel.archives-ouvertes.fr/tel-01599934.

L. Fiabane, R. Zimmermann, R. Volk, J.-F. Pinton, and M. Bourgoin. Clustering of finite-size particles in turbulence. Phys. Rev. E, 86:035301, Sep 2012. doi: 10.1103/PhysRevE.86.035301. URL https://link.aps.org/doi/10.1103/PhysRevE.86.035301.

Walter Fornari, Francesco Picano, and Luca Brandt. Sedimentation of finite-size spheres in quiescent and turbulent environments. Journal of Fluid Mechanics, 788:640–669, 2016. doi: 10.1017/jfm.2015.698.

Uriel Frisch. Turbulence: The Legacy of A. N. Kolmogorov. Cambridge University Press, 1995. doi: 10.1017/CBO9781139170666.

K. Fröhlich, M. Meinke, and W. Schröder. Derivation of drag and lift forces and torque coefficients for non-spherical particles in a flow. J. Fluid Mech., 901:A5, 2020.

R. Gatignol. The faxén formulae for a rigid particle in an unsteady non-uniform stokes flow. J. Méc. Theor. Appl., 1(143), 1983. doi: 10.1063/1.864230. URL https://aip.scitation.org/doi/abs/10.1063/1.864230.

William K. George. Lectures in turbulence for the 21st century, 2013.

Bradut Ghidersa and Jan Dusek. Breaking of axisymmetry and onset of unsteadiness in the wake of a sphere. Journal of Fluid Mechanics, 423:33–69, 2000. doi: 10.1017/S0022112000001701.

G. H. Good, P. J. Ireland, G. P. Bewley, E. Bodenschatz, L. R. Collins, and Z. Warhaft. Settling regimes of inertial particles in isotropic turbulence. Journal of Fluid Mechanics, 759:R3, 2014. doi: 10.1017/jfm.2014.602.

K. Gumowski, J. Miedzik, S. Goujon-Durand, P. Jenffer, and J. E. Wesfreid. Transition to a time-dependent state of fluid flow in the wake of a sphere. Phys. Rev. E, 77:055308, May 2008. doi: 10.1103/PhysRevE.77.055308. URL https://link.aps.org/doi/10.1103/PhysRevE.77.055308.

K. Gustavsson, J. Jucha, A. Naso, E. Lévêque, A. Pumir, and B. Mehlig. Statistical model for the orientation of nonspherical particles settling in turbulence. Phys. Rev. Lett., 119(25): 254501, 2017.

K. Gustavsson, M. Z. Sheikh, D. Lopez, A. Naso, A. Pumir, and B. Mehlig. Effect of fluid inertia on the orientation of a small prolate spheroid settling in turbulence. New Journal of Physics, 21(8):083008, 2019.

K. Gustavsson, M. Z. Sheikh, A. Naso, A. Pumir, and B. Mehlig. Effect of particle inertia on the alignment of small ice crystals in turbulent clouds. J. Atmos. Sci., in press, 2021.

A. Haider and O. Levenspiel. Drag coefficient and terminal velocity of spherical and nonspherical particles. Powder Technology, 58(1):63–70, 1989. ISSN 0032-5910. doi: https://doi.org/10.1016/0032-5910(89)80008-7. URL https://www.sciencedirect.com/science/article/pii/0032591089800087.

Richard Hartley and Andrew Zisserman. Multiple View Geometry in Computer Vision. Cambridge University Press, 2 edition, 2004. doi: 10.1017/CBO9780511811685.

Jincan He, Meiying Huang, Dongmei Wang, Zhuomin Zhang, and Gongke Li. Magnetic separation techniques in sample preparation for biological analysis: A review. Journal of Pharmaceutical and Biomedical Analysis, 101:84–101, 2014. ISSN 0731-7085. doi: https://doi.org/10.1016/j.jpba.2014.04.017. URL https://www.sciencedirect.com/science/article/pii/S0731708514002088. JPBA Reviews 2014.

S.S. Hidalgo-Tobon. Theory of gradient coil design methods for magnetic resonance imaging. Concepts in Magnetic Resonance Part A, 36A(4):223–242, 2010. doi: https://doi.org/10.1002/cmr.a.20163. URL https://onlinelibrary.wiley.com/doi/abs/10.1002/cmr.a.20163.

J. Hinze. Turbulence. McGraw-Hill, 421:3, 1959.

Sighard F Hoerner. Fluid-dynamic drag : practical information on aerodynamic drag and hydrodynamic resistance, 1965.

A. Hölzer and M. Sommerfeld. Lattice boltzmann simulations to determine drag, lift and torque acting on non-spherical particles. Comput. Fluids, 38:572, 2009.

Holger Homann and Jeremie Bec. Finite-size effects in the dynamics of neutrally buoyant particles in turbulent flow. Journal of Fluid Mechanics, 651:81–91, 2010. doi: 10.1017/S0022112010000923.

M. Horowitz and C. H. K. Williamson. The effect of reynolds number on the dynamics and wakes of freely rising and falling spheres. Journal of Fluid Mechanics, 651:251–294, 2010. doi: 10.1017/S0022112009993934.

J. B. Huang, Z. Chen, and T. L. Chia. Pose determination of a cylinder using reprojection transformation. Pattern Recognition Letters, 17(10):1089 – 1099, 1996. ISSN 0167-8655. doi: https://doi.org/10.1016/0167-8655(96)00061-X. URL http://www.sciencedirect.com/science/article/pii/016786559600061X.

Sander G. Huisman, Thomas Barois, Mickaël Bourgoin, Agathe Chouippe, Todor Doychev, Peter Huck, Carla E. Bello Morales, Markus Uhlmann, and Romain Volk. Columnar structure formation of a dilute suspension of settling spherical particles in a quiescent fluid. Phys. Rev. Fluids, 1:074204, Nov 2016. doi: 10.1103/PhysRevFluids.1.074204. URL https://link.aps.org/doi/10.1103/PhysRevFluids.1.074204.

W. Hwang and J.K. Eaton. Turbulence attenuation by small particles in the absence of gravity. International Journal of Multiphase Flow, 32(12):1386–1396, 2006. ISSN 0301-9322. doi: https://doi.org/10.1016/j.ijmultiphaseflow.2006.06.008. URL https://www.sciencedirect.com/science/article/pii/S0301932206001157.

Andreas Hölzer and Martin Sommerfeld. New simple correlation formula for the drag coefficient of non-spherical particles. Powder Technology, 184(3):361–365, 2008. ISSN 0032-5910. doi: https://doi.org/10.1016/j.powtec.2007.08.021. URL https://www.sciencedirect.com/science/article/pii/S0032591007004792.

John David Jackson. Classical electrodynamics. Wiley, New York, NY, 3rd ed. edition, 1999. ISBN 9780471309321. URL http://cdsweb.cern.ch/record/490457.

K. O. L. F. Jayaweera and B. J. Mason. The behaviour of freely falling cylinders and cones in a viscous fluid. J. Fluid Mech., 22(4):709–720, 1965.

G. B. Jeffery. The motion of ellipsoidal particles immersed in a viscous fluid. Proc. Royal Soc. London. Ser. A, 102(715):161–179, 1922.

M. Jenny, J. Dusek, and G. Bouchet. Instabilities and transition of a sphere falling or ascending freely in a newtonian fluid. Journal of Fluid Mechanics, 508:201–239, 2004. doi: 10.1017/S0022112004009164.

Mathieu Jenny, Gilles Bouchet, and Jan Dusek. Nonvertical ascension or fall of a free sphere in a newtonian fluid. Physics of Fluids, 15(1):L9–L12, 2003. doi: 10.1063/1.1529179.

F. Jiang, J. P. Gallardo, and H. I. Andersson. The laminar wake behind a 6:1 prolage spheroid at 45° incidence angle. Phys. Fluids, 26:113601, 2014.

F Jiang, L Zhao, H Andersson, K Gustavsson, A Pumir, and B Mehlig. Inertial torque on a small spheroid in a uniform flow. Phys. Rev. Fluids, 6, 2021.

T. A. Johnson and V. C. Patel. Flow past a sphere up to a reynolds number of 300. Journal of Fluid Mechanics, 378:19–70, 1999. doi: 10.1017/S0022112098003206.

J. Jucha, A. Naso, E. Lévêque, and A. Pumir. Settling and collision between small ice crystals in turbulent flows. Phys. Rev. Fluids, 3(1):014604, 2018.

Y. Kamotani and S. Ostrach. Effect of g-jitter on liquid free surfaces in microgravity. In Hans Josef Rath, editor, Microgravity Fluid Mechanics, pages 175–183, Berlin, Heidelberg, 1992. Springer Berlin Heidelberg. ISBN 978-3-642-50091-6.

Dimitar G. Karamanev and Ludmil N. Nikolov. Free rising spheres do not obey newton's law for free settling. AIChE Journal, 38(11):1843–1846, 1992. doi: https://doi.org/10.1002/aic.690381116.

Eric E. Keaveny and Martin R. Maxey. Spiral swimming of an artificial micro-swimmer. Journal of Fluid Mechanics, 598:293–319, 2008. doi: 10.1017/S0022112007009949.

Majid Hassan Khan, P. Sooraj, Atul Sharma, and Amit Agrawal. Flow around a cube for reynolds numbers between 500 and 55,000. Experimental Thermal and Fluid Science, 93: 257–271, 2018. ISSN 0894-1777. doi: https://doi.org/10.1016/j.expthermflusci.2017.12.013. URL https://www.sciencedirect.com/science/article/pii/S0894177717303965.

Majid Hassan Khan, Atul Sharma, and Amit Agrawal. Simulation of Flow Around a Cube at Moderate Reynolds Numbers Using the Lattice Boltzmann Method. Journal of Fluids Engineering, 142(1), 10 2019. ISSN 0098-2202. doi: 10.1115/1.4044821. URL https://doi.org/10.1115/1.4044821. 011301.

Majid Hassan Khan, P. Sooraj, Atul Sharma, and Amit Agrawal. Experimental investigation of flow around a 45° oriented cube for reynolds numbers between 500 and 50 000. Phys. Rev. Fluids, 6:074606, Jul 2021. doi: 10.1103/PhysRevFluids.6.074606. URL https://link.aps.org/doi/10.1103/PhysRevFluids.6.074606.

M. Kharrouba, J.-L. Pierson, and J. Magnaudet. Flow structure and loads over inclined cylindrical rodlike particles and fibers. Phys. Rev. Fluids, 6:044308, 2021.

R. E. Khayat and R. G. Cox. Inertia effects on the motion of long slender bodies. J. Fluid Mech., 209:435–462, 1989.

Sangtae Kim and Seppo J. Karrila. Microhydrodynamics: principles and selected applications. Butterworth-Heinemann, Boston, 1991.

L. Klotz, S. Goujon-Durand, J. Rokicki, and J. E. Wesfreid. Experimental investigation of flow behind a cube for moderate reynolds numbers. Journal of Fluid Mechanics, 750:73–98, 2014. doi: 10.1017/jfm.2014.236.

A.N. Kolmogorov. The local structure of turbulence in incompressible viscous fluid for very large reynolds numbers. Doklady Akademii Nauk SSSR, 30:301–304, 1941.

S. Kramel. Non-Spherical Particle Dynamics in Turbulence. PhD thesis, Wesleyan College, 2017.

Krontech. Chronos 2.1-HD High Speed Camera.

V. Kumaran. Rheology of a suspension of conducting particles in a magnetic field. Journal of Fluid Mechanics, 871:139–185, 2019. doi: 10.1017/jfm.2019.295.

Raymond Lau and Hong Kai Lawrence Chuah. Dynamic shape factor for particles of various shapes in the intermediate settling regime. Advanced Powder Technology, 24(1):306–310, 2013. ISSN 0921-8831. doi: https://doi.org/10.1016/j.apt.2012.08.001. URL https://www.sciencedirect.com/science/article/pii/S0921883112001276.

Legi Grenoble. UVMAT Particle Image velocimetry program. http://servforge.legi.grenoble-inp.fr/projects/soft-uvmat.

Lensagon. Lensagon CK10M5020S43.

Olivier Liot, David Martin-Calle, Amélie Gay, Julien Salort, Francesca Chillà, and Mickaël Bourgoin. Pair dispersion in inhomogeneous turbulent thermal convection. Physical Review Fluids, 4(9):94603, 2019. ISSN 2469990X. doi: 10.1103/PhysRevFluids.4.094603. URL https://doi.org/10.1103/PhysRevFluids.4.094603.

D. Lopez and E. Guazzelli. Inertial effects on fibers settling in a vortical flow. Phys. Rev. Fluids, 2(2):024306, 2017.

Clément Lorin, Alain Mailfert, Christian Jeandey, and Philippe J. Masson. Perfect magnetic compensation of gravity along a vertical axis. Journal of Applied Physics, 113(14):143909, 2013. doi: 10.1063/1.4801529. URL https://doi.org/10.1063/1.4801529.

Francesco Lucci, Antonino Ferrante, and Said Elghobashi. Is stokes number an appropriate indicator for turbulence modulation by particles of taylor-length-scale size? Physics of Fluids, 23(2):025101, 2011. doi: 10.1063/1.3553279. URL https://doi.org/10.1063/1.3553279.

Nikolay Lukerchenko, Yury Kvurt, Alexander Kharlamov, Zdenek Chara, and Pavel Vlasak. Experimental evaluation of the drag force and drag torque acting on a rotating spherical particle moving in fluid. Journal of Hydrology and Hydromechanics, 56:88–94, 01 2008.

F. Lundell, L. D. Söderberg, and P. H. Alfredsson. Fluid mechanics of papermaking. Ann. Rev. Fluid Mechanics, 43:195–217, 2011.

N. Machicoane, A. Aliseda, R. Volk, and M. Bourgoin. A simplified and versatile calibration method for multi-camera optical systems in 3d particle imaging. Review of Scientific Instruments, 90(3):035112, 2019. doi: 10.1063/1.5080743. URL https://doi.org/10.1063/1.5080743.

Mailfert, Alain, Beysens, Daniel, Chatain, Denis, and Lorin, Clément. Magnetic compensation of gravity in fluids: performance and constraints*. Eur. Phys. J. Appl. Phys., 71(1):10902, 2015. doi: 10.1051/epjap/2015150089. URL https://doi.org/10.1051/epjap/2015150089.

MATLAB. version version 9.7.0.1586710 (R2019b) Update 8. The MathWorks Inc., Natick, Massachusetts, 2019.

M. R. Maxey. The gravitational settling of aerosol particles in homogeneous turbulence and random flow fields. Journal of Fluid Mechanics, 174:441–465, 1987. doi: 10.1017/S0022112087000193.

Martin R. Maxey and James J. Riley. Equation of motion for a small rigid sphere in a nonuniform flow. The Physics of Fluids, 26(4):883–889, 1983a. doi: 10.1063/1.864230. URL https://aip.scitation.org/doi/abs/10.1063/1.864230.

Martin R. Maxey and James J. Riley. Equation of motion for a small rigid sphere in a nonuniform flow. The Physics of Fluids, 26(4):883–889, 1983b. doi: 10.1063/1.864230. URL https://aip.scitation.org/doi/abs/10.1063/1.864230.

Qingrui Meng, Hongwei An, Liang Cheng, and Mehrdad Kimiaei. Wake transitions behind a cube at low and moderate reynolds numbers. Journal of Fluid Mechanics, 919:A44, 2021. doi: 10.1017/jfm.2021.406.

Terunobu Miyazaki and Hanmin Jin. The Physics of Ferromagnetism. Springer, 2012.

Romain Monchaux, Mickael Bourgoin, and Alain Cartellier. Analyzing preferential concentration and clustering of inertial particles in turbulence. International Journal of Multiphase Flow, 40:1–18, 2012. ISSN 0301-9322. doi: https://doi.org/10.1016/j.ijmultiphaseflow.2011.12.001. URL https://www.sciencedirect.com/science/article/pii/S030193221100245X.

N. Mordant, P. Metz, O. Michel, and J.-F. Pinton. Measurement of lagrangian velocity in fully developed turbulence. Phys. Rev. Lett., 87:214501, Nov 2001. doi: 10.1103/PhysRevLett.87.214501. URL https://link.aps.org/doi/10.1103/PhysRevLett.87.214501.

Nicolas Mordant, Emmanuel Lévêque, and Jean-François Pinton. Experimental and numerical study of the lagrangian dynamics of high reynolds turbulence. New Journal of Physics, 6:116–116, sep 2004. doi: 10.1088/1367-2630/6/1/116. URL https://doi.org/10.1088/1367-2630/6/1/116.

Isao Nakamura. Steady wake behind a sphere. The Physics of Fluids, 19(1):5–8, 1976. doi: 10.1063/1.861328.

Aurore Naso and Andrea Prosperetti. The interaction between a solid particle and a turbulent flow. New Journal of Physics, 12(3):033040, mar 2010. doi: 10.1088/1367-2630/12/3/033040. URL https://doi.org/10.1088/1367-2630/12/3/033040.

Ramesh Natarajan and Andreas Acrivos. The instability of the steady flow past spheres and disks. Journal of Fluid Mechanics, 254:323–344, 1993. doi: 10.1017/S0022112093002150.

Peter Nielsen. Turbulence effects on the settling of suspended particles. Journal of Sedimentary Research, 63(5):835–838, 09 1993. ISSN 1527-1404. doi: 10.1306/D4267C1C-2B26-11D7-8648000102C1865D. URL https://doi.org/10.1306/D4267C1C-2B26-11D7-8648000102C1865D.

V S Nikolayev, D Chatain, D Beysens, and G Pichavant. Magnetic Gravity Compensation. Microgravity Science and Technology, 23(2):113–122, 2011. ISSN 1875-0494. doi: 10.1007/s12217-010-9217-6. URL https://doi.org/10.1007/s12217-010-9217-6.

A. Oberbeck. Über stationäre Flüssigkeitsbewegungen mit Berücksichtigung der inneren Reibung. J. reine angew. Math., 81:62–80, 1876.

A Obukhov. Spectral energy distribution in a turbulent flow. Izv. Akad. Nauk. SSSR. Ser.Geogr. i. Geofiz, 5:453–466, 1941. URL https://ci.nii.ac.jp/naid/10012382304/en/.

Robert C. O'Handley. Modern Magnetic Materials: Principles and Applications. Wiley, New York, NY, 1st ed. edition, 2000. ISBN 978-0-471-15566-9. URL https://www.wiley.com/en-us/Modern+Magnetic+Materials%3A+Principles+and+Applications-p-9780471155669.

H. Okada, H. Okuyama, M. Uda, and N. Hirota. Removal of aerosol by magnetic separation. IEEE Transactions on Applied Superconductivity, 16(2):1084–1087, 2006. doi: 10.1109/TASC.2006.870000.

Delphine Ormières and Michel Provansal. Transition to turbulence in the wake of a sphere. Phys. Rev. Lett., 83:80–83, Jul 1999. doi: 10.1103/PhysRevLett.83.80. URL https://link.aps.org/doi/10.1103/PhysRevLett.83.80.

R. Ouchene, M. Khalij, A. Taniére, and B. Arcen. Lattice boltzmann simulations to determine drag, lift and torque acting on non-spherical particles. Comput. Fluids, 113:53, 2015.

R. Ouchene, M. Khalij, B. Arcen, and A. Taniére. A new set of correlations of drag, lift and torque coefficients for non-spherical particles at large reynolds numbers. Powder Technol., 303:33, 2016.

Nicholas T Ouellette, Haitao Xu, Mickaël Bourgoin, and Eberhard Bodenschatz. An experimental study of turbulent relative dispersion models. New Journal of Physics, 8(6):109–109, jun 2006. doi: 10.1088/1367-2630/8/6/109. URL https://doi.org/10.1088/1367-2630/8/6/109.

Jun-Hua Pan, Nian-Mei Zhang, and Ming-Jiu Ni. Instability and transition of a vertical ascension or fall of a free sphere affected by a vertical magnetic field. Journal of Fluid Mechanics, 859: 33–48, 2019. doi: 10.1017/jfm.2018.803.

Neepa Paul, Simon Biggs, Jessica Shiels, Robert B. Hammond, Michael Edmondson, Lisa Maxwell, David Harbottle, and Timothy N. Hunter. Influence of shape and surface charge on the sedimentation of spheroidal, cubic and rectangular cuboid particles. Powder Technology, 322:75–83, 2017. ISSN 0032-5910. doi: https://doi.org/10.1016/j.powtec.2017.09.002. URL https://www.sciencedirect.com/science/article/pii/S0032591017307234.

B. R. Pearson, P.-Å. Krogstad, and W. van de Water. Measurements of the turbulent energy dissipation rate. Physics of Fluids, 14(3):1288–1290, 2002. doi: 10.1063/1.1445422. URL https://doi.org/10.1063/1.1445422.

T. J. Pedley and J. O. Kessler. Hydrodynamic phenomena in suspensions of swimming microorganisms. Ann. Rev. Fluid Mechanics, 24(1):313–358, 1992.

Benoit Pier. Local and global instabilities in the wake of a sphere. Journal of Fluid Mechanics, 603:39–61, 2008. doi: 10.1017/S0022112008000736.

PIVMat. Frédéric Moisy. http://www.fast.u-psud.fr/pivmat/, 2015.

Stephen B Pope. Turbulent flows. Cambridge Univ. Press, Cambridge, 2011. URL https://cds.cern.ch/record/1346971.

H. R. Pruppacher and J. D. Klett. Microphysics of clouds and precipitation. Nature, 284(5751): 88–88, 1980.

A. Przadka, J. Miedzik, K. Gumowski, S. Goujon-Durand, and J. Wesfreid. The wake behind the sphere; analysis of vortices during transition from steadiness to unsteadiness /). Archives of Mechanics, 60:467–474, 2008.

N M Qureshi, U Arrieta, C Baudet, A Cartellier, Y Gagne, and M Bourgoin. Acceleration statistics of inertial particles in turbulent flow. The European Physical Journal B, 66(4): 531–536, 2008. ISSN 1434-6036. doi: 10.1140/epjb/e2008-00460-x. URL https://doi.org/10.1140/epjb/e2008-00460-x.

Nauman Qureshi. Investigation of Finite Sized Inertial Particles Dynamics in Wind Tunnel Grid Generated Turbulence. PhD thesis, Université Joseph Fourier - Grenoble I.

Nauman M. Qureshi, Mickaël Bourgoin, Christophe Baudet, Alain Cartellier, and Yves Gagne. Turbulent transport of material particles: An experimental study of finite size effects. Phys. Rev. Lett., 99:184502, Oct 2007. doi: 10.1103/PhysRevLett.99.184502. URL https://link.aps.org/doi/10.1103/PhysRevLett.99.184502.

M. Rahmani and A. Wachs. Free falling and rising of spherical and angular particles. Physics of Fluids, 26(8):083301, 2014. doi: 10.1063/1.4892840. URL https://doi.org/10.1063/1.4892840.

Indresh Rampall, Jeffrey R. Smart, and David T. Lighton. The influence of surface roughness on the particle-pair distribution function of dilute suspensions of non-colloidal spheres in simple shear flow. Journal of Fluid Mechanics, 339:1–24, 1997. doi: 10.1017/S002211209600479X.

Robin Raul, Peter S. Bernard, and Frank T. Buckley Jr. An application of the vorticity–vector potential method to laminar cube flow. International Journal for Numerical Methods in Fluids, 10(8):875–888, 1990. doi: https://doi.org/10.1002/fld.1650100803. URL https://onlinelibrary.wiley.com/doi/abs/10.1002/fld.1650100803.

Lewis Fry Richardson and Gilbert Thomas Walker. Atmospheric diffusion shown on a distance-neighbour graph. Proceedings of the Royal Society of London. Series A, Containing Papers of a Mathematical and Physical Character, 110(756):709–737, 1926. doi: 10.1098/rspa.1926.0043. URL https://royalsocietypublishing.org/doi/abs/10.1098/rspa.1926.0043.

Andreas Richter and Petr A. Nikrityuk. Drag forces and heat transfer coefficients for spherical, cuboidal and ellipsoidal particles in cross flow at sub-critical reynolds numbers. International Journal of Heat and Mass Transfer, 55(4):1343–1354, 2012. ISSN 0017-9310. doi: https://doi.org/10.1016/j.ijheatmasstransfer.2011.09.005. URL https://www.sciencedirect.com/science/article/pii/S0017931011005023.

Bogdan Rosa, Hossein Parishani, Orlando Ayala, and Lian-Ping Wang. Settling velocity of small inertial particles in homogeneous isotropic turbulence from high-resolution dns. International Journal of Multiphase Flow, 83:217–231, 2016. ISSN 0301-9322. doi: https://doi.org/10.1016/j.ijmultiphaseflow.2016.04.005. URL https://www.sciencedirect.com/science/article/pii/S0301932215301543.

A. Roy, R. J. Hamati, L. Tierney, D. L. Koch, and G. A. Voth. Inertial torques and a symmetry breaking orientational transition in the sedimentation of slender fibres. J. Fluid Mech., 875: 576–596, 2019.

J. Ruiz, D. Macías, and F. Peters. Turbulence increases the average settling velocity of phytoplankton cells. Proceedings of the National Academy of Sciences, 101(51):17720–17724, 2004.

A. K. Saha. Three-dimensional numerical simulations of the transition of flow past a cube. Physics of Fluids, 16(5):1630–1646, 2004. doi: 10.1063/1.1688324. URL https://doi.org/10.1063/1.1688324.

A.K. Saha. Three-dimensional numerical study of flow and heat transfer from a cube placed in a uniform flow. International Journal of Heat and Fluid Flow, 27(1):80–94, 2006. ISSN 0142-727X. doi: https://doi.org/10.1016/j.ijheatfluidflow.2005.05.002. URL https://www.sciencedirect.com/science/article/pii/S0142727X05000561.

H. Sakamoto and H. Haniu. A Study on Vortex Shedding From Spheres in a Uniform Flow. Journal of Fluids Engineering, 112(4):386–392, 12 1990. ISSN 0098-2202. doi: 10.1115/1.2909415. URL https://doi.org/10.1115/1.2909415.

B. L. Sawford. Reynolds number effects in lagrangian stochastic models of turbulent dispersion. Physics of Fluids A: Fluid Dynamics, 3(6):1577–1586, 1991. doi: 10.1063/1.857937. URL https://doi.org/10.1063/1.857937.

Arman Seyed-Ahmadi and Anthony Wachs. Dynamics and wakes of freely settling and rising cubes. Phys. Rev. Fluids, 4:074304, Jul 2019. doi: 10.1103/PhysRevFluids.4.074304. URL https://link.aps.org/doi/10.1103/PhysRevFluids.4.074304.

Arman Seyed-Ahmadi and Anthony Wachs. Sedimentation of inertial monodisperse suspensions of cubes and spheres. Phys. Rev. Fluids, 6:044306, Apr 2021. doi: 10.1103/PhysRevFluids.6.044306. URL https://link.aps.org/doi/10.1103/PhysRevFluids.6.044306.

M. Z. Sheikh, K. Gustavsson, D. Lopez, E. Lévèque, B. Mehlig, A. Pumir, and A. Naso. Importance of fluid inertia for the orientation of spheroids settling in turbulent flow. J. Fluid Mech., 886:A9, 2020. doi: 10.1017/jfm.2019.1041.

C. Siewert, R. P. J. Kunnen, M. Meinke, and W. Schröder. Orientation statistics and settling velocity of ellipsoids in decaying turbulence. Atmospheric research, 142:45–56, 2014.

M. D. Simon and A. K. Geim. Diamagnetic levitation: Flying frogs and floating magnets (invited). Journal of Applied Physics, 87(9):6200–6204, 2000. doi: 10.1063/1.372654. URL https://doi.org/10.1063/1.372654.

Kyle D. Squires and John K. Eaton. Preferential concentration of particles by turbulence. Physics of Fluids A: Fluid Dynamics, 3(5):1169–1178, 1991. doi: 10.1063/1.858045. URL https://doi.org/10.1063/1.858045.

Katepalli R. Sreenivasan. An update on the energy dissipation rate in isotropic turbulence. Physics of Fluids, 10(2):528–529, 1998. doi: 10.1063/1.869575. URL https://doi.org/10.1063/1.869575.

G. G. Stokes. On the effect of the internal friction of fluids on the motion of pendulums. Transactions of the Cambridge Philosophical Society, 9:8, 1851. URL https://doi.org/10.1063/1.1445422.

G. Subramanian and D. L. Koch. Inertial effects on fibre motion in simple shear flow. J. Fluid Mech., 535:383, 2005.

Sholpan Sumbekova. Clustering of inertial sub-Kolmogorov particles : structure of clusters and their dynamics. PhD thesis, 2016. URL http://www.theses.fr/2016GREAI093. Thèse de doctorat dirigée par Cartellier, Alain et Bourgoin, Mickaël Mécanique des fluides Energétique, Procédés Université Grenoble Alpes (ComUE) 2016.

Sadatoshi Taneda. Experimental investigation of the wake behind a sphere at low reynolds numbers. Journal of the Physical Society of Japan, 11(10):1104–1108, 1956. doi: 10.1143/JPSJ.11.1104. URL https://doi.org/10.1143/JPSJ.11.1104.

Roger I. Tanner and Shaocong Dai. Particle roughness and rheology in noncolloidal suspensions. Journal of Rheology, 60(4):809–818, 2016. doi: 10.1122/1.4954643. URL https://doi.org/10.1122/1.4954643.

C. M. Tchen. Mean value and correlation problems connected with the motion of small particles suspended in a turbulent fluid. PhD thesis, TU Delft, 1947.

J. Ross Thomson, Francois Drolet, and Jorge Vinals. Fluid physics in a fluctuating acceleration environment. Third Microgravity Fluid Physics Conference, 1996. URL https://ntrs.nasa.gov/citations/19970000426.

Thorlabs. KC1/M - Kinematic 30 mm-Cage-Compatible Mount, Metric.

Ananias G. Tomboulides and Steven Orszag. Numerical investigation of transitional and weak turbulent flow past a sphere. Journal of Fluid Mechanics, 416:45–73, 2000. doi: 10.1017/S0022112000008880.

Federico Toschi and Eberhard Bodenschatz. Lagrangian properties of particles in turbulence. Annual Review of Fluid Mechanics, 41(1):375–404, 2009. doi: 10.1146/annurev.fluid.010908.165210. URL https://doi.org/10.1146/annurev.fluid.010908.165210.

C. Toupoint, P. Ern, and V. Roig. Kinematics and wake of freely falling cylinders at moderate reynolds numbers. J. Fluid Mech., 866:82–111, 2019. doi: 10.1017/jfm.2019.77.

Clément Toupoint. Path and wake of cylinders falling in a liquid at rest or in a bubble swarm towards the hydrodynamical modeling of ebullated bed reactors. PhD thesis, 2018. URL http://www.theses.fr/2018INPT0126. Thèse de doctorat dirigée par Ern, Patricia et Roig, Véronique Dynamique des Fluides Toulouse, INPT 2018.

Sabine Tran-Cong, Michael Gay, and Efstathios E Michaelides. Drag coefficients of irregularly shaped particles. Powder Technology, 139(1):21–32, 2004a. ISSN 0032-5910. doi: https://doi.org/10.1016/j.powtec.2003.10.002. URL https://www.sciencedirect.com/science/article/pii/S0032591003002973.

Sabine Tran-Cong, Michael Gay, and Efstathios E Michaelides. Drag coefficients of irregularly shaped particles. Powder Technology, 139(1):21–32, 2004b. ISSN 0032-5910. doi: https://doi.org/10.1016/j.powtec.2003.10.002. URL https://www.sciencedirect.com/science/article/pii/S0032591003002973.

R. Tsai. A versatile camera calibration technique for high-accuracy 3d machine vision metrology using off-the-shelf tv cameras and lenses. IEEE Journal on Robotics and Automation, 3(4): 323–344, 1987. doi: 10.1109/JRA.1987.1087109.

Robert Turner. Gradient coil design: A review of methods. Magnetic Resonance Imaging, 11(7): 903–920, 1993. ISSN 0730-725X. doi: https://doi.org/10.1016/0730-725X(93)90209-V. URL https://www.sciencedirect.com/science/article/pii/0730725X9390209V.

Markus Uhlmann. An immersed boundary method with direct forcing for the simulation of particulate flows. Journal of Computational Physics, 209(2):448–476, 2005. ISSN 0021-9991. doi: https://doi.org/10.1016/j.jcp.2005.03.017. URL https://www.sciencedirect.com/science/article/pii/S0021999105001385.

Markus Uhlmann and Todor Doychev. Sedimentation of a dilute suspension of rigid spheres at intermediate galileo numbers: the effect of clustering upon the particle motion. Journal of Fluid Mechanics, 752:310–348, 2014. doi: 10.1017/jfm.2014.330.

J. Christos Vassilicos. Dissipation in turbulent flows. Annual Review of Fluid Mechanics, 47(1): 95–114, 2015. doi: 10.1146/annurev-fluid-010814-014637. URL https://doi.org/10.1146/annurev-fluid-010814-014637.

C.H.J. Veldhuis and A. Biesheuvel. An experimental study of the regimes of motion of spheres falling or ascending freely in a newtonian fluid. International journal of multiphase flow, 33 (10):1074–1087, 2007. ISSN 0301-9322. doi: 10.1016/j.ijmultiphaseflow.2007.05.002.

Jérémy Vessaire, Nicolas Plihon, Romain Volk, and Mickaël Bourgoin. Sedimentation of a suspension of paramagnetic particles in an external magnetic field. Phys. Rev. E, 102:023101, Aug 2020. doi: 10.1103/PhysRevE.102.023101. URL https://link.aps.org/doi/10.1103/PhysRevE.102.023101.

Bianca Viggiano, Jan Friedrich, Romain Volk, Mickael Bourgoin, Raul Bayoan Cal, and Laurent Chevillard. Modeling Lagrangian velocity and acceleration in turbulent flows as infinitely differentiable stochastic processes. Journal of Fluid Mechanics, 900:A27, 2020. doi: 10.1017/jfm.2020.495. URL http://arxiv.org/abs/1909.09489.

Andreas Volk and Christian J Kähler. Density model for aqueous glycerol solutions. Experiments in Fluids, 59(5):75, 2018. ISSN 1432-1114. doi: 10.1007/s00348-018-2527-y. URL https://doi.org/10.1007/s00348-018-2527-y.

Lian-Ping Wang and Martin R. Maxey. Settling velocity and concentration distribution of heavy particles in homogeneous isotropic turbulence. Journal of Fluid Mechanics, 256:27–68, 1993. doi: 10.1017/S0022112093002708.

Yanan Wang, David Thompson, and Zhiwei Hu. Effect of wall proximity on the flow over a cube and the implications for the noise emitted. Physics of Fluids, 31(7):077101, 2019. doi: 10.1063/1.5096072. URL https://doi.org/10.1063/1.5096072.

Yanan Wang, Zhiwei Hu, and David Thompson. Numerical investigations on the flow over cubes with rounded corners and the noise emitted. Computers and Fluids, 202:104521, 2020. ISSN 0045-7930. doi: https://doi.org/10.1016/j.compfluid.2020.104521. URL https://www.sciencedirect.com/science/article/pii/S0045793020300943.

Jelle B. Will, Varghese Mathai, Sander G. Huisman, Detlef Lohse, Chao Sun, and Dominik Krug. Kinematics and dynamics of freely rising spheroids at high reynolds numbers. Journal of Fluid Mechanics, 912:A16, 2021. doi: 10.1017/jfm.2020.1104.

Haitao Xu and Eberhard Bodenschatz. Motion of inertial particles with size larger than kolmogorov scale in turbulent flows. Physica D: Nonlinear Phenomena, 237(14):2095–2100, 2008. ISSN 0167-2789. doi: https://doi.org/10.1016/j.physd.2008.04.022. URL https://www.sciencedirect.com/science/article/pii/S0167278908001863. Euler Equations: 250 Years On.

M. Zastawny, G. Mallouppas, F. Zhao, and B. van Wachem. Derivation of drag and lift forces and torque coefficients for non-spherical particles in a flow. Int. J. Multiphase Flow, 39:227, 2012.

Jisheng Zhao, John Sheridan, Kerry Hourigan, and Mark C. Thompson. Flow-induced vibration of a cube orientated at different incidence angles. Journal of Fluids and Structures, 91:102701, 2019. ISSN 0889-9746. doi: https://doi.org/10.1016/j.jfluidstructs.2019.102701. URL https://www.sciencedirect.com/science/article/pii/S0889974618305905.

Peng Zhao, Jun Xie, Fu Gu, Nusrat Sharmin, Philip Hall, and Jianzhong Fu. Separation of mixed waste plastics via magnetic levitation. Waste Management, 76:46–54, 2018. ISSN 0956-053X. doi: https://doi.org/10.1016/j.wasman.2018.02.051. URL https://www.sciencedirect.com/science/article/pii/S0956053X18301405.

Yu Zhao and Robert H. Davis. Interaction of sedimenting spheres with multiple surface roughness scales. Journal of Fluid Mechanics, 492:101–129, 2003. doi: 10.1017/S0022112003005652.

W. Zhou and J. Dusek. Chaotic states and order in the chaos of the paths of freely falling and ascending spheres. International Journal of Multiphase Flow, 75:205–223, 2015. doi: https://doi.org/10.1016/j.ijmultiphaseflow.2015.05.010.

Wei Zhou. Instabilités de trajectoires de spheres, ellipsoides et bulles. PhD thesis, 2016.

Appendices

Appendix A

Pair Dispersion

The problem of how a pair of tracers particles drift apart in turbulence has been studied by Richardson (Richardson and Walker, 1926), Obukhov (Obukhov, 1941) and Batchelor (Batchelor, 1950), yielding the Richardson−Obukhov and Batchelor's laws. Some subtleties were found after the aforementioned seminal works and the problem is not completely solved. The current understanding of the problem is that there are three pair dispersion regimes, that differ on the mean-square pair separation time dependence: Ballistic or Batchelor (t^2), Super Diffusive or Richardson (t^3) and Diffusive (t). If one defines $\mathbf{D}(t)$ as the distance between the particle pair at time t and $\mathbf{D}_0 = \mathbf{D}(t = 0)$, these three regimes take the following form (Bourgoin, 2015; Ouellette et al., 2006):

$$\langle|\mathbf{D}(t) - \mathbf{D}_0|^2\rangle = \begin{cases} S_2(D_0)t^2 & : t_\eta << t << t_0 \\ g\epsilon t^3 & : t_0 << t << T_L \\ \propto t & : t > T_L \end{cases}$$

Where $t_0 = (r_0^2/\epsilon)^{1/3}$ is the correlation time of an eddy with size D_0, i.e. the time for which the initial pair separation influences the dynamics. Note that $S_2(D_0)$, the trace of the second-order Eulerian structure function tensor, equals $\frac{11}{3}C_2(\epsilon D_0)^{2/3}$ in the context of Kolmogorov's 1941 theory (Kolmogorov, 1941). Furthermore, due to the 2D nature of the measurements, it is convenient to express the mean-square pair separation relation to S_2 in the following way: $\langle|\mathbf{D}(t)-\mathbf{D}_0|^2\rangle = (S_{2\perp}(D_0)+2\times S_{2\parallel}(D_0))t^2$. The latter allows to manually eliminate the out-of-laser-plane velocity component ($S_{2\perp}$), yielding $\langle|\mathbf{D}(t)-\mathbf{D}_0|^2\rangle = 2\times S_{2\parallel}(D_0)t^2 = \frac{8}{3}C_2(\epsilon D_0)^{2/3}t^2$, in the Ballistic regime.

The solid experimental evidence about the Ballistic regime (Berk and Coletti, 2021a; Ouellette et al., 2006) permits to indirectly measure $S_2(D_0)$, and therefore the energy dissipation ϵ, via the computation of pair separation. Moreover, an estimation of the integral scale L is possible as it matches the end of the Ballistic regime, i.e. the end of the inertial range.

Although the latter analysis is valid for tracer particles, the turbulent flow was seeded with glass particles with a mean size of 200 μm, that have $\tau_p = 4\times10^{-3}$. Although a particle with $\tau_p \leq 10^{-3}$ is usually considered a tracer, the flow characteristics extracted from these measurements are expected to be fairly close to the tracers' case. It was seen that the existence of the Ballistic regime is not greatly affected by small levels of particle inertia (Berk and Coletti, 2021a; Chang et al., 2015; Dhariwal and Bragg, 2019).

Appendix B

fps1000 Camera Synchronization

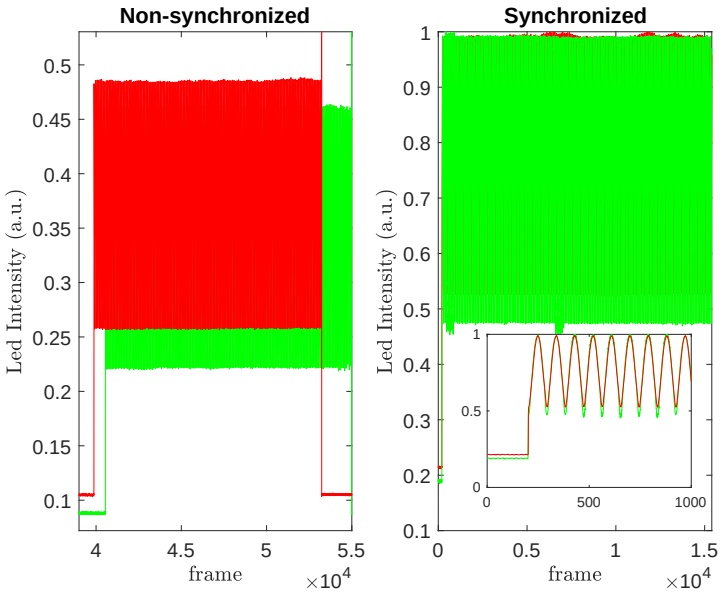

Figure B.1: Typical case of external led's intensity used to synchronize cameras. Left: led intensity from two non-synchronized cameras. Right: led intensity after synchronization.

In order to implement the particle tracking step of the 4D-LPT method, the cameras need to be synchronized. The software of the cameras Chronos 2.1HD from Krontech used in the Drop Tower experiments allows to do synchronize. On the other hand, the cameras fps1000 from the Slow Motion Company, used in the remaining experimental setups, have a software bug that inhibits the synchronization thus it was done externally.
A led was placed outside the water tank, in a position such that it was imaged by both cameras (usually in the upper corner of each image). The led was connected to a function generator that input a sinusoidal function. The protocol is as follows:

- the recording is started for both cameras (not at the same time);
- after approximately 1 sec, the function generator is turned on;
- the particle is released;
- and finally, the cameras are turned off.

The portion of the image from each camera imaging the led is then isolated and its intensity extracted. A typical plot of led intensity versus frame number, is presented in Figure B.1(left). From this plot, a correspondence between each period of the sinusoid seen by each camera is obtained. In that sense, a correspondence between each camera frame is obtained. Hence the images are be synchronized, as shown in Figure B.1(right), with an inset showing a zoom at the moment the led goes on.
Note that it is crucial to see the moment when the led goes on as that allows to set a time origin.